1-1-1992

An optical study of the faint end of the stellar luminosity function.

Thomas Harold Jarrett
University of Massachusetts Amherst

AN OPTICAL STUDY OF THE FAINT END OF THE STELLAR LUMINOSITY FUNCTION

A Dissertation Presented

by

THOMAS HAROLD JARRETT

Submitted to the Graduate School of the
University of Massachusetts in partial fulfillment
of the requirements for the degree of

DOCTOR OF PHILOSOPHY

February 1992

Department of Physics and Astronomy

AN OPTICAL STUDY OF THE FAINT END OF THE
STELLAR LUMINOSITY FUNCTION

A Dissertation Presented

by

THOMAS HAROLD JARRETT

Approved as to style and content by:

Robert L. Dickman, Chairman

William Herbst, Member

Michael Skrutskie, Member

Edward Chang, Member

Robert B. Hallock, Department Head
Department of Physics and Astronomy

ACKNOWLEDGEMENTS

This dissertation is the culmination of many a long (and mostly) wonderful journey through the American educational and intellectual jungle. I owe gratitude to many people who have added critical support through friendship, emotional, intellectual, and financial means. First and foremost, I would like to thank my family, for their patience and understanding in my cosmic follies. I must also extend my deepest appreciation to my advisor at UMASS, Bob Dickman. No person has had a more profound influence on my intellectual and scientific development; frankly, my career in astronomy would have probably collapsed during the early days of graduate school if Bob had not provided support and encouragement. It was surely an extraordinary and fortunate stroke of luck that our paths crossed some 4 years ago. I am equally indebted to Suzan Edwards for her guidance and (especially) patience towards my error-prone ways. The two years that I worked for Suzan were both humbling and satisfying, AND were never dull. Fortune ... indeed. And speaking of luck -- KISMET ! -- I have been twice blessed to be able to work for (and with) Susan Kleinmann. Along with Suzan Edwards, Susan taught much of what I know about the art (and *zen*) of infrared astronomy. She also provided crucial financial support over the last 18 months or so. And of course, a study of this kind could not have been pulled off without the vast computer resources that Susan kindly provided (at no cost! ... well ...). It has been most illuminating to be privy to the workings and sorcery of one who can only be described as an awesome mover and shaker. Thanks, Suz! I would also like to thank Steve Strom for his many helpful suggestions — especially his advice to supplement our photometric data with a proper motion analysis.

I would like to thank the other members of my thesis committee, including Ed Chang from physics, who also taught one of my favorite classes at UMASS (Atoms and Molecules), Mike Skrutskie, who provided many helpful suggestions and served as the critical contact with Terry Herter at Cornell Univ. (who obtained the optical spectra presented in chapter 6), and Bill Herbst at Wesleyan University. Bill is predominantly responsible for the idea behind this dissertation; quite simply, his vision has shaped the direction of my research interests for some time to come. In actuality, my good fortune began prior to graduate school. I am indebted to my undergraduate advisor at Pomona College, Bob Chambers, for his guidance and unwavering enthusiasm for my pursuit in the fields of physics and astronomy. He is truly an inspiration, for Bob is one of those rare people that you meet in life who is both abundantly successful in his career and is genuinely a nice guy. I would also like to thank my mentor at Harvey Mudd College, William Sandman, for taking me under his tutelage and showing me the ropes in astronomical photometry.

Graduate school has been for the most part a rich and fulfilling experience. The many friendships that I've made over these last 6 years are principally responsible for this positive experience. I will miss my 'astro' pals, and my *OOZE* drinking buddies. I will wax nostalgic for the days of WALLEYBALL and the great wars with my compatriot Harry Miles. To the good times with Lori Allen, Dave Taylor, Jeff Kenney, Wayne Kinzel, Lowell and Linda Tacconi-Garman, Steve Lord, Mark Heyer, Bill Waller, Carolyn Jordan, and Stacey Bork. I am especially thankful for having as good of friends as Jim Morgan, Jeff Seeley, Kent Nierendorf, Rich Lempicki, Neil Lacey, and my best pal, Kevin Olson.

Last but not least, I would like to thank my fiance RoseLynn. Her foremost virtues, patience and understanding, were the key to surviving the two week span in which the thesis defense, wedding, and relocation to SoCal were *all* scheduled.

ABSTRACT

AN OPTICAL STUDY OF THE FAINT END OF THE
STELLAR LUMINOSITY FUNCTION

FEBRUARY 1992

THOMAS HAROLD JARRETT, B.A., POMONA COLLEGE

Ph.D., UNIVERSITY OF MASSACHUSETTS

Directed by: Professor Robert L. Dickman

We implement a new method by which to study the faint end of the field star luminosity function. The method relies on deep, multicolor photometry of fields projected against highly obscured, nearby molecular clouds. The clouds act as nearly opaque screens and delimit a well-defined survey sample volume free of the problem of distinguishing nearby, intrinsically faint dwarf stars from more distant red giants. We demonstrate that with this technique it is possible to probe the faint end of the field star luminosity function down to the hydrogen-burning main sequence out to distances much further than have been previously attempted.

This study is based upon deep photographic and CCD photometry at optical (V, R, I) bandpasses towards the most obscured portions of the Taurus and Ophiuchus molecular clouds. The fields comprise a total area of ~0.63 square degrees, and the total volume delimited by the cloud distances is ~198 pc^3. Within this volume, the survey is complete for all stars brighter than M_V = 16 - 17 mag; at R and I, the survey is complete down to the lowest mass stars capable of sustaining core hydrogen burning.

Color-color criteria are used to distinguish between background, highly reddened stars and stars located in front of the clouds. The method of photometric parallax is used to deduce the absolute magnitude and spectral type of those stars found to lie in front of

the clouds. To help further resolve foreground/background ambiguities we supplement the photometry and color-color results with proper motion measurements of the candidate foreground sample. These are obtained from the photographic and CCD data, and from the circa 1950 Palomar Sky Survey.

As a test of our ability to distinguish foreground dwarfs from heavily reddened background stars, we obtained redband (6000 - 9000 Å) spectra of three Taurus foreground candidate stars. Two of the stars are found to be foreground M dwarfs, but the third appears to be a reddened, high velocity background star, possibly belonging to the spheroid population. Although such objects should be quite rare, the least biased conclusion regarding the integrity of our foreground sample is that there may be 33% contamination from reddened background stars and/or associated cloud members. This is most likely confined to the faintest magnitudes, $M_V > 14$.

We estimate the faint end of the field star luminosity function for the composite Taurus and Ophiuchus foreground sample and find that it resembles the *local* luminosity function down to $M_V \sim 16$. At still fainter magnitudes we find at least 15% more stars than do photometric parallax studies of the polar regions. This difference widens dramatically if even the simplest correction for incompleteness is applied to our data. We therefore tentatively conclude that the luminosity function rises beyond $M_V \sim 16$; even if we discard our attempts to correct for incompleteness in the faintest magnitude bins, there appears to be little doubt that the luminosity function at least remains flat for the lowest mass stars.

Our provisional finding that the luminosity function rises again beyond its well-known peak at $M_V \sim 12$ - 13, also implies that the IMF probably rises beyond the turnover point associated with this peak. Even if our most conservative estimate for the faint end of the luminosity function is used — in which no corrections are made for incompleteness — the IMF must at least remain flat down to the edge of the hydrogen-burning main sequence.

TABLE OF CONTENTS

LIST OF TABLES

LIST OF FIGURES

CHAPTER 1

INTRODUCTION

1.1 Overview

The initial mass function (IMF) describes the relative number of stars of various masses born within a given region of space. Usually expressed as a stellar frequency distribution representing the number of main-sequence stars born at coformation in a given volume as a function of logarithmic stellar mass interval (Salpeter 1955), few astrophysical quantities are as fundamental as the mass function. For example, in concert with an overall stellar birth rate, the stellar mass function predicts the frequency of events such as planetary nebula or supernova formation, along with the birth rate of their remnants, white dwarfs, neutron stars and black holes (Scalo 1986). On Galactic scales, the mass function is believed to govern the compositional evolution of interstellar atomic and molecular gas (Dearborn *et al.* 1978; Scalo 1988), and it is the mass function which dictates the degree to which various kinds of stars dominate the dynamics of our own and other galaxies.

Notwithstanding its basic importance, the IMF is poorly known in a number of ways, and as Scalo (1986) has emphasized, the very existence of a widely applicable mass function remains more assumption than observationally established fact. While the general hope is that the physics of star formation is sufficiently universal to promote the existence of a mass distribution which varies only gently with the various factors known to influence star formation (such as metallicity and cloud mass), the bulk of what we know concerning

the IMF — particularly at the low mass end which governs the dynamical behavior of galaxies — is based upon observations of field stars in the immediate solar neighborhood.

This raises the related issue of the extent to which the solar neighborhood can be deemed "typical" insofar as the star formation process is concerned. It is well known that the population of stars comprising the Milky Way, the disk field stars, association and open cluster members, halo field stars and globular cluster members, have dramatically contrasting metal abundances, dynamics and ages. It is possible, even probable, that these very different populations possess distinct IMF's as well. The solar neighborhood contains a mixture of older stars that have drifted away from their parent associations and clusters. Thus, the local IMF reflects an *average* over a mixed ensemble of stars, some as old as the Galactic disk, which formed in different parts of the Galaxy and in diverse environments.

Fundamental ambiguities plague the determination of the IMF at both the high and low mass ends. At the high end, obvious difficulties stem from the great rarity of massive, very luminous stars. At the low-mass end the difficulties are of a different sort: very low mass main-sequence stars ($M < 0.4\ M_\odot$) have cool photospheres; consequently, they are very faint and can only be observed in relatively close proximity to the Sun. Moreover, the IMF is itself not directly observable, but rather is computed from the relation (*e.g.* Scalo 1986):

$$IMF = \phi(M_V) \times \left(\frac{dM_V}{dL}\right) \times \left(\frac{dL}{dM}\right) \times (scale\text{-}height\ factors)$$

where (dM_V / dL) is the bolometric correction, (dL/dM) is the mass-luminosity relation, and $\phi(M_V)$ is the luminosity function. Ignoring the (formidable!) problems associated with determining the mass-luminosity relation, it should be noted that the luminosity function, $\phi(M_V)$, is the fundamental *observable* quantity for studies of the mass function. It is

usually expressed as the frequency distribution of stars per unit volume per unit absolute visual magnitude.

Constructing statistically complete samples of faint (and thus low-mass) main sequence stars in order to estimate the corresponding behavior of the luminosity function has proven to be extremely difficult, even for the immediate solar neighborhood. Studies relying only on stars with measurable trigonometric parallaxes (*cf.* Henry and McCarthy 1990; Wielen *et al.* 1983) have been carried out and necessarily pertain to only the closest (d ~ 25 pc) stars. Other approaches, including those employing kinematic and proper motion constraints (*cf.* Dahn *et al.* 1986; Luyten 1963 & 1976), and optical/infrared photometric surveys (*cf.* Reid and Gilmore 1982; Boeshaar and Tyson 1985; Leggett and Hawkins 1988) have attempted to extend sample volumes to distances ~100 pc. Nonetheless, all these studies are plagued by selection biasing, and most possess limiting absolute magnitudes of only 14 - 15 mag at V (which roughly marks the boundary of what in many ways is the most interesting mass range — see below) and poor statistics. There is no doubt that the luminosity function is poorly understood — and therefore somewhat controversial — for stars with absolute visual magnitudes exceeding 13.

The lower portion ($M < 0.4\ M_{\odot}$) of the IMF describes the frequency with which the most common stars occur in the Galaxy (because such stars live much longer than the age of the Galaxy, their abundance at birth must equal their present abundance). These stars dominate the stellar contribution to the Milky Way's dynamics and are of special interest in regard to the so called "missing mass" problem for the Galactic disk. As first pointed out by Oort (1960; see Bahcall 1984) there appears to be a discrepancy between the Galactic disk's mass density inferred from dynamical arguments and the aggregate mass density determined from observed Galactic disk constituents (this value is sometimes referred to the "Oort limit"). Regardless of current theoretical prejudices (which suggest

that as much as 90% of all matter in the universe may be invisible to astronomers), a great deal of observational evidence (though see Gilmore, Wyse, and Kuijken 1989 for a differing view) does indicate that a large fraction, perhaps 50%, of the self-gravitating matter in the Galaxy cannot be accounted for in the form of observed stars and interstellar gas. Note that unlike the dark matter associated with the largest cosmological scales, which is frequently assumed to interact only very weakly with normal matter, any non-luminous material associated with the Oort problem is generally expected to be baryonic — the kinematic studies which point to the presence of the missing mass in the Galactic disk also suggest that this material possesses a scale-height of ~ few hundred pc (Bahcall 1984), and thus had to be subject to substantial viscous dissipation as the disk evolved. Low-mass stars, or cooling sub-stellar "brown" dwarfs having masses below ~0.08 $M_\odot$ hydrogen-burning main sequence limit are attractive guises for the alleged missing matter because such objects are extraordinarily faint — even ten 0.1 $M_\odot$ stars give only 1% of the Sun's light output — and the luminosity function is very poorly known below about 0.4 $M_\odot$. To examine this possibility — which would represent the least exotic but most natural resolution of the dark matter problem in the Galactic disk — one must establish the IMF reliably down to masses significantly less than 0.4 $M_\odot$, and 0.08 $M_\odot$ (brown dwarfs).

Recent work in this area is conflicting, largely because of uncertainties in the luminosity function. The IMF computed by Scalo (1986), for example, declines rapidly for masses below ~0.3 $M_\odot$. Similarly, the Reid and Gilmore luminosity function peaks in the range $11 < M_V < 13$, exhibiting a steep decline at higher magnitudes (and thus lower masses). This trend is not encouraging because in order for very low mass stars (either red or brown dwarfs) to contribute substantially to any local missing-mass, the luminosity function must *rise* beyond $M_V \sim 15 - 16$ ($M < 0.2\ M_\odot$). Interestingly, the Reid and Gilmore luminosity function does suggest a rising trend at the extreme low mass end

($M_V > 17$) — although there is considerable uncertainty in these values — and the luminosity functions of Hawkins and Bessell (1988) and Leggett and Hawkins (1988) also appear to rise or at least remain flat for masses near the hydrogen-burning limit. A rising trend in the IMF is intriguing, since it suggests an alternative mode of star formation, perhaps consistent with Larson's (1986) 'bimodal' mechanism in which a second class of low mass stars forms, possibly in a burst very early in the existence of the Galaxy. A rising mass function that extends beyond the limit of the minimum mass required to sustain hydrogen-burning would also suggest that there may be a staggering number of degenerate brown dwarf objects in the Galactic disk. (Given the absence of *any* confirmed brown dwarf candidates, however, it is difficult to avoid the conclusion that even if the IMF continues to rise for masses $< 0.08\ M_\odot$, it must soon thereafter steeply decline.) In any case, the recent results suggest that previous surveys which found a decline at the faint end of the luminosity function may simply not have been sensitive to a subsequent 'bump' or rise in the IMF for stellar masses approaching the hydrogen burning limit. It is essential to verify the reality of this result.

1.2 This Research

In this dissertation we describe a research program that addresses some of the issues raised here. The core of the program is a study of the field star luminosity function down to the very faint limiting magnitudes which correspond to masses near the hydrogen-burning main sequence, in regions considerably beyond the Solar vicinity. This effort represents an implementation of a new method by which to study the faint end of the luminosity function first suggested by Herbst (see Herbst and Dickman 1983), which relies on deep, multicolor photometry of fields projected against heavily obscured, nearby molecular clouds. The clouds act as distance-limiting opaque screens, accurately confining

the sample of foreground field stars and minimizing the confusion caused by background field dwarfs and late-type giants.

In order to obtain reasonable statistics with the "screen" method, one must choose a set of molecular clouds having highly obscured regions of large angular extent; further, while the search volume probed varies as the cube of the cloud's distance (for an opaque region of constant angular area), the requirement that one be able to observe the faintest possible stars with the smallest possible telescope dictates that relatively nearby clouds be selected for study. Previous work by Jarrett, Dickman and Herbst (1989), providing deep multicolor 4-m photography of the Heiles' Cloud 2 region in the Taurus molecular cloud complex, and of L1689 in the ρ Ophiuchi cloud, has revealed the locations and extents of filaments and cores with extinctions exceeding 15 mag at V. Another prime area for study lies toward the molecular cloud, Barnard 5, since it also appears to be endowed with an extended, very high extinction core (Langer *et al.* 1989), yet lies ~2 times further from the Sun than the Taurus or Oph clouds. All three regions were chosen for this study, but poor weather prevented us from obtaining the B5 data; observation of this field is now scheduled for 1991 December on the KPNO 4-m telescope.

The observations, described in detail in Chapter 2, consist of deep CCD multicolor (V, R, I) photometry using the KPNO 0.9-m and 4-m telescopes and one of the new generation large format CCD arrays. Our goal was to achieve complete coverage extending to the distance limits of the clouds for stars as faint as $M_V \sim 16 - 18$. This requires photometry with limiting visual magnitudes of ~22 - 23 for the Taurus and Oph fields (and ~24-25 for the B5 field).

Despite their very large extinctions, the clouds are not totally opaque. Given the very faint limiting magnitudes of the observations, some stars invariably shine through the clouds. Color-color criteria are thus applied to the optical data in order to distinguish

between background, reddened stars and stars located in front of the clouds. Since the method relies on cloud obscuration as the primary discriminator, it is necessary to accurately determine the visual extinctions due to the molecular clouds. We employ the method of star counts to accomplish this. We describe this effort in Chapter 3. The method of photometric parallax is used to deduce the absolute magnitude and spectral type of those stars found to lie in front of the clouds. A description of the color-color analysis and photometric parallax results are given in Chapter 4.

To help further resolve foreground/background ambiguities we supplement the photometry and color-color results with proper motion measurements of the candidate foreground sample. The proper motion study compares the CCD and photographic data with circa 1950 Palomar Sky Survey fields. Using a two-dimensional fitting algorithm, the movement of stars can be determined over ~40 year baselines. In Chapter 5, we describe the method used to compute proper motions, and present the results of this analysis.

As a test of our ability to distinguish between foreground dwarfs and heavily, reddened background stars, we obtained optical spectra of three Taurus foreground candidate stars. This enables us to make a crude estimate of the effectiveness of the techniques used to select foreground stars. The results are summarized in Chapter 6.

Finally, we estimate the field star luminosity function from the Taurus and Ophiuchus fields, and constrain the low mass end of the initial mass function corresponding to the Solar neighborhood. We present these results along with a discussion of their implications in Chapter 7.

The appendices contain images of the CCD fields (Appendix A), and discussions of various tools used in the proper motion (Appendices B and D) and color-color analyses (appendices C and E), including a detailed description of a model developed to simulate the Galactic stellar distribution at multiple wavelengths (Appendix F).

CHAPTER 2

OBSERVATIONS AND DATA

The data collected in this program consist of optical photography and CCD images of fields toward the Taurus and ρ Ophiuchi molecular cloud complexes. In addition, ^{12}CO and ^{13}CO radio data were collected for the ρ Ophiuchi field. Finally, we also acquired digitized Palomar Sky Survey data for the two fields mentioned above, and for the Barnard 5 molecular cloud. A description of the observations and reductions is presented in the following sections.

2.1 Photography

Deep prime focus plates in three optical bands were taken using the 4-m telescopes at CTIO and Kitt Peak. The fields observed at CTIO were two ~50′ diameter areas toward the ρ Ophiuchi molecular cloud complex, one region lying in the southeast filament of the cloud, L1689 [$\alpha(1950) = 16^h\ 30^m\ 00^s$, $\delta(1950) = -24°\ 30'\ 00''$], and the second in a nearby, nearly extinction-free region [$\alpha(1950) = 16^h\ 32^m\ 30^s$, $\delta(1950) = -25°\ 00'\ 00''$]. One ~50′ diameter field toward Heiles' Cloud 2 in the Taurus molecular cloud [$\alpha(1950) = 4^h\ 37^m\ 55^s$, $\delta(1950) = +25°\ 46'$] was observed with the KPNO 4-m telescope. Plates were exposed at the Kron J, F and N bands (Bruzual 1966; Kron 1980) using a Racine prism. Densitometry of the Oph and Taurus plates were carried out on the YALE and University of Minnesota PDS machines, respectively. A summary of the properties of the Kron system is listed in Table 2.1 (which is taken from Dickman and Herbst 1990).

Table 2.1

Properties of Kron J, F, and N Bands

Band	Emulsion	Filter	λ_0(Å)[a]	$\Delta\lambda$(Å)[a]	(A_v/A_λ)[b]
J	IIIa-J	GG385	4627	487	0.80
F	IIIa-F	GG495	6167	599	1.18
N	IV-N[c]	RG695	7941	562	1.69

[a] Bruzual 1966; Kron 1980.
[b] Savage and Mathis 1979.
[c] Hypered.

Calibration of the plates was carried out as follows. BVR_cI_c photoelectric photometry[1] was also obtained for a number of stars in the cloud and reference regions having apparent magnitudes as faint as 17, using a single-channel photometer on the 60″ (1.5-m) CTIO and 50″ (1.3-m) KPNO telescopes. The BVI magnitudes were converted to their J, F, N equivalents using the transformations given by Kron (1980):

$$J = B - 0.23(B - V), \quad F = V - 0.40(B - V), \quad N = I_c \qquad (2.1)$$

The resulting J, F, and N magnitudes for each star were then used to calibrate densitometric diameter-brightness sequences at each color. Because a Racine wedge was used for the 4-m photography[2], calibration of the fields was secured to the plate limit in each color. We estimate the accuracy of the magnitude determination in each band to be ~0.2 mag or better.

The end result of this process was a catalog containing the coordinates and J, F, N magnitudes of each star brighter than the plate limits in the cloud and reference fields. A

[1] Cousins (1976) photometric system.

[2] A Racine wedge creates a secondary image of each star, fainter by ~6.9 mag than each primary image and displaced from it by some 30".

summary of the *conservative* limiting magnitudes adopted in this work at each color is provided in Table 2.2. Although the limiting magnitudes in Table 2.2 are not as deep as the plate limits, they are values at which all detected stars are likely to be real and have apparent magnitudes determined to ~0.2 mag or better.

Table 2.2

Limiting Magnitudes of Exposures

Object	Band	m_{lim}
L1689	J	23.5
L1689	F	22.0
L1689	N	19.5
Heiles' Cloud 2	J	22.0
Heiles' Cloud 2	F	21.5
Heiles' Cloud 2	N	18.5

2.2 CCD Observations

Observations of several fields in the Taurus and ρ Ophiuchi regions photographed were also carried out using CCD[3] cameras at Kitt Peak National Observatory and the Toronto Southern Observatory in Las Campanas Chile.

[3] A charge-coupled device (CCD) is a silicon semiconductor sub-divided into an array of detectors (pixels), each a tiny photodiode. An incident photon striking a pixel on the chip strips an electron inside the semiconductor. The negative charge is subsequently trapped in the potential well created by a capacitance across the semiconductor. As one integrates over time, the potential wells fill with electrons, leaving an array of negative charges that is in linear proportion to the number of incident photons. The charge is "coupled" in the sense that the array is read out by shifting the charge of each pixel to its nearest neighbor (e.g. horizontally, to the right) by passing a periodically changing voltage across the array. The charges from each pixel migrate across the chip until the array is completely cleared. For a more detailed discussion, see Lena (1986).

2.2.1 Kitt Peak

A large portion of the optical data for this project are derived from CCD images of the areas defined by the prime focus plates of Taurus and ρ Oph (described in section 2.1), which were made using a Tek 2048 CCD camera aboard the Kitt Peak #1 0.9-m telescope. The Taurus observations were carried out in October of 1989, and the Ophiuchus observations were made during May of 1990. An attempt was also made to obtain CCD observations of the B5 molecular cloud using the 4-m telescope during December 1990. Unfortunately, the weather did not cooperate. A summary of the Kitt Peak observations is presented in Table 2.3.

Between the 1989 and 1990 dates, two different Tek 2048 CCD cameras were in service[4]. The main difference in the two cameras is that the second has poorer cosmetic quality, whereas the first had a higher read noise (25 versus 13 electrons). A summary of the physical characteristics of the second Tek 2048 CCD is provided in Table 2.4 (NOAO Newsletter #23, 1990). The observing characteristics of the 0.9-m and 4-m telescopes are given in Table 2.5[5].

---

[4] During 1990, an engineering mishap resulted in the unfortunate death of the only Tek 2048 CCD camera in service at KPNO. Just before the May observing run, a new camera was installed; the physical specifications of this camera are described in the text.

[5] Information comes from the 1990 manual *Operation of the CCD Direct Imaging Camera for the 0.9 Meter Telescope Kitt Peak National Observatory*, by B. Shoening, P. Massey, T. Armandroff, G. Jacoby, C. Neese and J. Salzer.

Table 2.3

Kitt Peak Observations

Date	Telescope	Instrument CCD	Seeing Conditions	Weather
10-24-89	#1 0.9-m	#1 Tek 2048	1″	Clear
10-25-89	#1 0.9-m	#1 Tek 2048	1″ - 1.5″	Clear
10-26-89	#1 0.9-m	#1 Tek 2048	2″ - 3″	Poor
10-24-89	#1 0.9-m	#1 Tek 2048	1.5″ - 2″	Clear, Hazy
10-28-89	#1 0.9-m	#1 Tek 2048	0.5″ - 1″	Clear
10-29-89	#1 0.9-m	#1 Tek 2048	2″	Hazy
10-30-89	#1 0.9-m	#1 Tek 2048	1″ - 1.5″	Clear
5-22-90	#1 0.9-m	#2 Tek 2048	1.5″	Clear
5-23-90	#1 0.9-m	#2 Tek 2048	N/A	Clouded out
5-24-90	#1 0.9-m	#2 Tek 2048	2″	Clear, Hazy
5-25-90	#1 0.9-m	#2 Tek 2048	1″ - 1.5″	Clear
5-26-90	#1 0.9-m	#2 Tek 2048	1″ - 1.5″	Clear
12-21-90	4-m	#2 Tek 2048	N/A	Snowed out
12-22-90	4-m	#2 Tek 2048	N/A	Snowed out
12-23-90	4-m	#2 Tek 2048	N/A	Snowed out

Table 2.4

Tek 2048 Characteristics at the 0.9-m Telescope

read noise (electrons)	13
gain (electrons / ADU)	4.4, 8.2, or 11
linearity (electrons)	500K
QE at 3200Å	12%
QE at 3650Å	12%
QE at 4050Å	12%
QE at 5000Å	16%
QE at 6000Å	35%
QE at 7000Å	16%
QE at 8000Å	37%
QE at 9000Å	17%
effective chip size	1800 × 2048
pixel size	27μm

Table 2.5

Scale and Field of View for the Tek 2048 CCD

Telescope	Scale (″/pixel)	Field of View
0.9-m (f/7.5)	0.77	23′ × 26′
4-m (f/2.8)	0.54	16.2′ × 18.3′

Three CCD fields were imaged in Taurus using V, R and I filters. The CCD areas cover 26′ × 26′ each, centered at locations (epoch 1990): 1) $\alpha = 4^h\ 40^m\ 46^s$, $\delta = 25°\ 40'\ 28''$, 2) $\alpha = 4^h\ 38^m\ 59^s$, $\delta = 25°\ 41'\ 26''$, and 3) $\alpha = 4^h\ 40^m\ 37^s$, $\delta = 26°\ 00'\ 43''$. The Ophiuchus data set is composed of one CCD field exposed using V, R and I filters. The field size is 23′ × 26′, centered at α (1990) = $16^h\ 32^m\ 09^s$, δ (1990) = -24° 27′ 19″. The V

and R filters used are KPNO standard Harris filters (*cf.* KPNO 4-m Telescope manual), and the I filter is an RG715 interference filter (Beckert and Newberry 1989). A list of the filter properties is shown in Table 2.6.

Table 2.6

Properties of Harris B,V,R and I RG715

Filter	λ_0(Å)	FWHM (Å)	Bandpass (Å)
B	4419	949	732
V	5399	987	703
R	6352	1060	937
I	8151	1744	1373

2.2.2 CCD Data Reduction for Kitt Peak

Along with the fields mentioned above, a set of Landolt standard stars (Landolt 1983) were observed in order to calibrate the data. In addition, the same set of standard stars used in the photographic photometry reductions (see section 2.1) were imaged using the CCD. These standards are critical to the calibration since Landolt standards are generally not red or faint enough for the calibration of heavily reddened stars who lie background to the targeted molecular clouds, whereas the Taurus and Oph standards have (V-R) and (R-I) colors as red as ~2 magnitudes.

Reduction of a raw CCD image follows three basic steps per filter:

1. Subtract the bias[6] counts and dark current[7] from the CCD image,

---

[6] Bias refers to the electrons added to the data upon chip readout by the CCD electronics.

[7] Rate at which electrons are stripped (and eventually trapped) from the surface of the chip by events other than photons originating from astronomical sources. The dark current is controlled by thermal sources within the detector itself, which is why CCDs are typically cooled to liquid nitrogen temperatures (~ -100 C).

2. Divide image by a "flat-field" image,
3. Apply atmospheric extinction corrections.

Flat-fielding is carried out in order to correct for slight pixel to pixel sensitivity and illumination variations. Flat-field images are either obtained from viewing a white screen mounted to the dome of the observatory (these are known as "dome flats"), viewing the twilight/dawn sky ("dawn flats"), or from observing fields near or within the targeted region ("sky flats"). Sky flats are made by imaging a field with multiple exposures, where each exposure corresponds to a slightly different location. For example, after each exposure, one offsets the telescope by ~50 pixels. The resultant images are then combined using a median filter routine. Since each pixel per exposure is looking at a different location on the sky, the median filter automatically culls extreme pixels (i.e. due to starlight and cosmic rays), leaving an image that represents the surface sensitivity of the CCD detector.

Each exposure is subject to a degree of atmospheric extinction. The extinction, measured in magnitudes, depends linearly on the airmass between the telescope and the direction that it is pointed. The attenuation is wavelength dependent, with the shorter (blue) wavelengths affected the most. It is desirable to measure the extinction for each filter.

In order to correct the CCD exposures for atmospheric extinction, one observes a pair of standards (e.g. Landolt standards) that are spatially close together but which have very different colors (*i.e.*, blue-red pairs provide a second order extinction correction). One follows the pair as they rise, transit across the sky, and set; a full range of airmasses is then covered. One then plots their magnitude as a function of airmass, fitting a linear function to the data. The slope of the line is the extinction coefficient. The atmospheric extinction-

corrected magnitude is simply:

$$m = m_0 - (kX) \tag{2.2}$$

where m_o is the raw magnitude, X is the airmass and k is the extinction coefficient.

In this study, to the accuracy of the photometry, the extinction coefficients were found to be in agreement (within ~20%) with mean values determined at the Kitt Peak location (George Jacoby, private communication) as follows:

$$\begin{aligned} k_V &\approx 0.13 \\ k_R &\approx 0.08 \\ k_I &\approx 0.05 \end{aligned} \tag{2.3}$$

The correction was particularly important to the Ophiuchus data because this field lies below the celestial equator; therefore, from Kitt Peak (~31° latitude) we always view Ophiuchus through at least 1.7 airmasses. In this study Ophiuchus was imaged only when the airmass was less than ~2, translating to observing less than ~2 hours before and after transit.

Using the IRAF astronomical software package, the CCD data were reduced according to the four steps outlined above (using sky flats), cleaned of cosmic ray "hits" and cosmetic anomalies intrinsic to the chip[8], and finally combined into deep, long-exposure images for each filter.

The next step was to detect, isolate and measure stellar profiles. IRAF has a number of routines to aid in this tricky procedure (*e.g.*, routines DAOPHOT, DAOFIND, TVMARK, PHOT). Care must be taken to flag sources that are confused (due to spatial orientation), which are then treated separately from the rest of the sample. PHOT can automatically compute the flux from a stellar image detected using the DAOFIND routine.

[8] Bad pixels were replaced by a linear or polynomial interpolation of nearest neighbor pixels (if and only if they were not bad pixels themselves).

The total flux is calculated by summing the pixels within a circular aperture of a given size centered on the star. The flux due to the star only is then computed by subtracting a "sky" flux which is measured by computing the median (or mode) of a set of pixels within an annular ring aperture of a given size centered on the star.

Along with the flux of a star, we may also compute its signal to noise ratio. For example, suppose we have a star with total flux N (measured in counts or electrons per second), total integration time t (seconds), and sky flux Σ (electrons per pixel); the signal to noise, S/N, is then

$$\frac{S}{N} = \frac{Nt}{\sqrt{Nt + n\Sigma t + nR^2}} \tag{2.4}$$

where n is the total number of pixels within the circular aperture, and R is the read noise (electrons) of the detector.

Machine magnitudes are next assigned to all stars based on their computed fluxes. The *expected* photometric 'accuracy' of each measure is essentially

$$\delta m \approx \left[\frac{S}{N}\right]^{-1} \tag{2.5}$$

Once a list of stars with fluxes and magnitudes is compiled, the next phase is to reduce the machine magnitudes to a standard photometric system using the observations of Landolt standards and field object standards (*i.e.*, standard stars within the Taurus and Ophiuchus fields). In this study, the standard system adopted is that of Cousins (1976). The filter response characteristics of the Cousins photometric system are listed in Table 2.7.

Table 2.7

Properties of the Cousins Filter System

Filter	λ_0(Å)	FWHM (Å)	Bandpass (Å)
R	4417	960	724
V	5505	827	735
R	6690	1744	1347
I	8000	1425	855

Transformation to the Cousins system is carried out as follows. For each standard star, we plot the machine colors, (v-r) and (r-i), *versus* the Cousins colors, (V-R) and (R-I). The two are related by a simple linear expression:

$$(V-R) = \frac{\left[(v-r) - \zeta_{vr}\right]}{\psi_{vr}}$$
$$(R-I) = \frac{\left[(r-i) - \zeta_{ri}\right]}{\psi_{ri}} \qquad (2.6)$$

where ζ_{vr}, ψ_{vr}, ζ_{ri} and ψ_{ri} are the coefficients to be solved for. The Taurus standards are shown in Figure 2.1 and the Ophiuchus standards in Figure 2.2. Landolt stars are represented by filled squares and filled circles represent standards located within the Taurus and Ophiuchus fields. Best fits to the data are drawn with solid lines. The transformation coefficients and their corresponding formal errors are listed in Table 2.8.

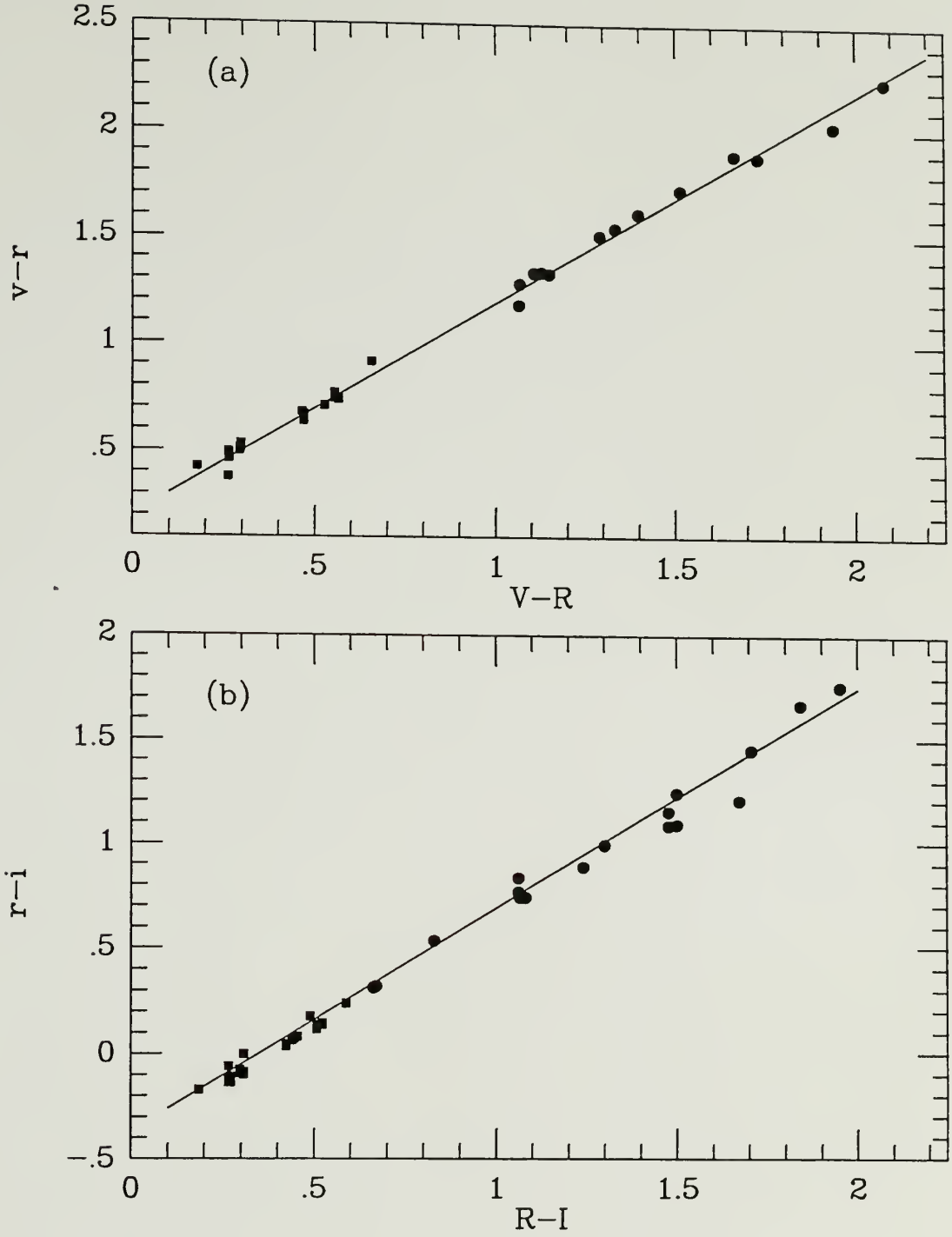

Figure 2.1 Machine colors versus Cousins colors for the Taurus field standards and Landolt standards. Taurus standards are represented by filled circles, and the Landolt standards by filled squares. The best fit to the data is also shown.

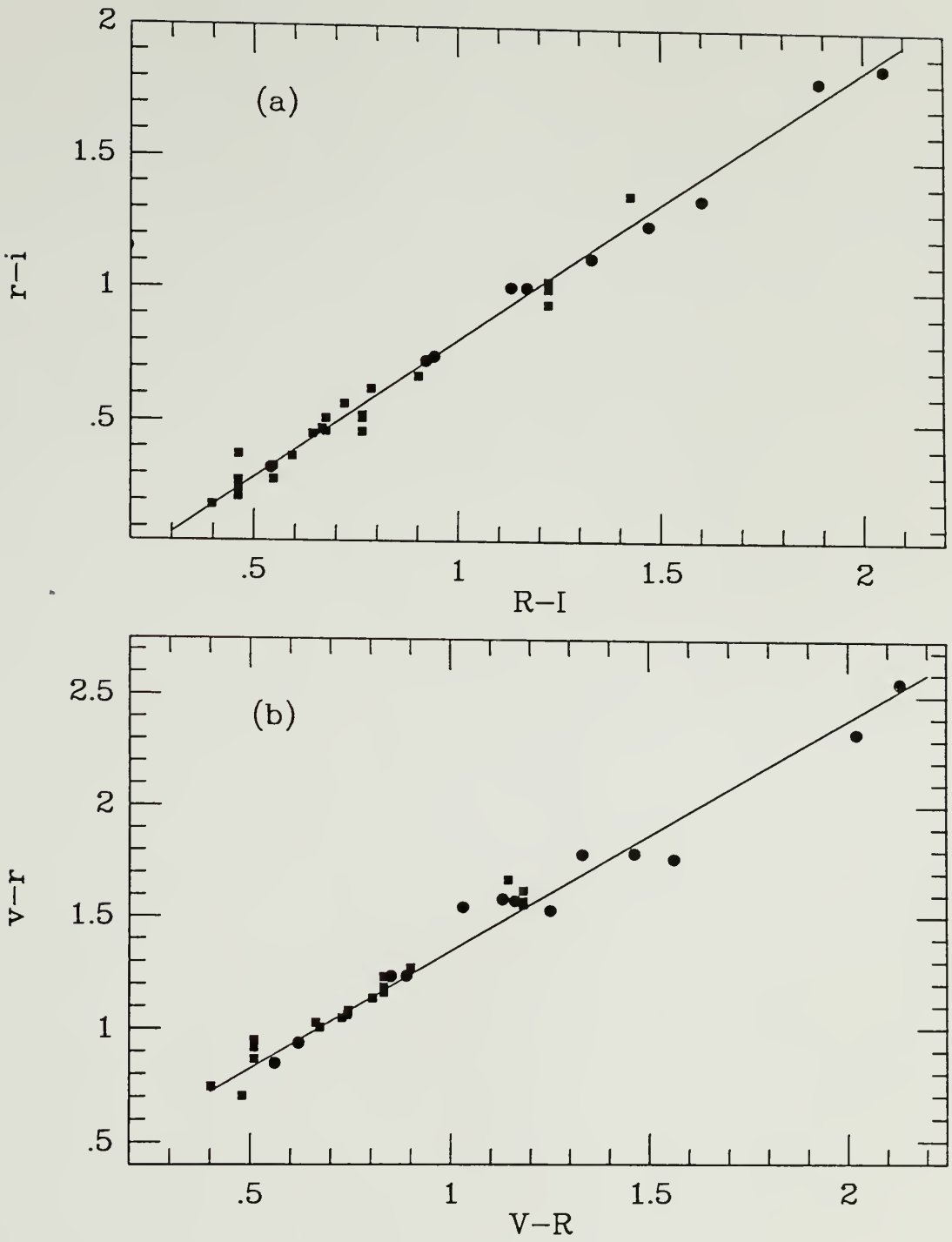

Figure 2.2 Machine colors versus Cousins colors for the Ophiuchus field standards and Landolt standards. Ophiuchi standards are represented by filled circles, and the Landolt standards by filled squares. The best fit to the data is also shown.

Table 2.8

Photometric Transformation Coefficients: v-r, r-i

Field	ζ_{vr}	ψ_{vr}	ψ_{ri}	ζ_{ri}
Taurus	0.22 ± 0.05	0.98 ± 0.01	-0.40 ± 0.07	1.07 ± 0.06
Ophiuchus	0.30 ± 0.03	1.06 ± 0.04	-0.23 ± 0.01	1.04 ± 0.02

The scatter in the fit parameters is due to a number of factors. Seeing conditions determine the size of the circular aperture used in the photometry. The larger the aperture, the more random error is introduced into the total flux of the star. Recall from Equation 2.4 that the read noise and the sky flux both depend on the total number of pixels contained within the aperture. As one can see from Table 2.3, the seeing conditions during the October and May observing runs were, for the most part, less than ideal. Moreover, in a related problem, a Tek 2048 CCD is so large that a field imaged onto the chip suffers from coma at its extreme edges. Thus, stellar profiles near the edges of the CCD field have a non-spherical, "teardrop" shape. It is then necessary to increase the aperture size to include the total stellar profile. A third problem that plagues users of CCDs is that the instruments are so sensitive that Landolt standards will typically saturate with an exposure of only a few seconds. The shorter the exposure, the greater the error introduced as a result of the finite instrument shutter speed. In some cases, shutter speed error can be corrected using pre-calibrated values tabulated by the observatory staff.

The observations of Landolt standards in this study were often very close to saturating, and thus many times were within the non-linear regime of the CCD[9].

[9] Though not used in this study, a trick employed by astronomers using the KPNO 4-m telescope is to configure the secondary so that stellar images are grossly out of focus, thereby spreading the profiles over many pixels -- and preventing over-filling of the CCD's potential wells.

Consequently, their measured fluxes were not as accurate as their corresponding signal to noise measure would indicate. However, there were several redundant observations of the Landolt standards which helped to minimize the errors due to non-linear saturation effects.

A final point to consider is that standard stars have intrinsic uncertainty in their colors and brightness. Although photometry by Landolt is generally quite precise, ~ 1%, and thus need not be concerned with, the photoelectric photometry of the Taurus and Ophiuchus standards have photometric accuracy ranging from 1% to 10%. In addition, in a couple of instances the Taurus and Ophiuchus standards exhibited photospheric variability on the order of 0.05 to 0.1 magnitudes. The fact that a few of our standards may be variables is not too surprising considering it is not uncommon for late-type M dwarfs, the most common star in the Galaxy, to display variability in their surface flux. The errors quoted in Tables 2.7 and 2.8 incorporate the effects described in this section. A further discussion of expected random and systematic errors effecting the photometry are contained in section 4.4, Chapter 4.

The transformation from colors to magnitudes follows a similar procedure to that for the machine magnitude conversion. For each standard star, we plot Cousins colors, (V-R) and (R-I), *versus* (v - R) and (V - r). As before, the two are related by a linear relation:

$$\begin{aligned} (V-r) &= \psi_{Vr}(V-R) + \zeta_{Vr} \\ (v-R) &= \psi_{vR}(v-R) + \zeta_{vR} \end{aligned} \qquad (2.7)$$

where ζ_{Vr}, ψ_{Vr}, ζ_{vR} and ψ_{vR} are the coefficients to be solved for. Though together both relations in Equation 2.7 are redundant, they can be used to minimize the transformation errors. For example, if the machine v magnitude has a lower signal to noise than the machine r magnitude, then the (V - r) relation is used; otherwise one implements the relation (v - R).

Results for the Taurus standards are shown in Figure 2.3, and those for the Ophiuchus standards are shown in Figure 2.4. As before, the Landolt stars are represented by filled squares and the field standards are filled circles. Best fits to the data are drawn with solid lines. The transformation coefficients and their corresponding errors are listed in Table 2.9.

Table 2.9

Photometric Transformation Coefficients: (V - r), (v - R)

Field	ζ_{Vr}	Ψ_{Vr}	Ψ_{vR}	ζ_{vR}
Taurus	-5.89 ± 0.05	1.00 ± 0.05	6.15 ± 0.03	0.97 ± 0.05
Ophiuchi	-5.68 ± 0.02	1.11 ± 0.02	-5.90 ± 0.03	1.04 ± 0.03

To estimate the errors associated with the transformed colors and magnitudes, we compute the root mean square of the transformations. For example,

$$\Delta(V-R)^2 = \left[\frac{(v-r) - \zeta_{vr}}{\Psi^2_{vr}}\right]^2 \Delta\Psi^2_{vr} + \left[\frac{\Delta\zeta_{vr}}{\Psi_{vr}}\right]^2 + \left[\frac{\Delta(v-r)}{\Psi_{vr}}\right]^2 \qquad (2.8)$$

$$\Delta V^2 = [(V-R)\Delta\Psi_{Vr}]^2 + [\Delta(V-R)\zeta_{Vr}]^2 + \Delta r^2 + \Delta\zeta^2_{Vr}$$

where Δ(v-r) and Δr are computed from the signal to noise ratio, Equation 2.5.

As with the photographic photometry, the end result of the CCD data reduction process is a catalog containing the coordinates and Cousins V, R, and I magnitudes and their associated errors of each star brighter than the adopted CCD limits in the cloud fields. The limits correspond to a signal to noise ratio greater than 10 to 1 in the final, processed exposures. A summary of the limiting magnitude for each color is provided in Table 2.10.

Table 2.10

10% Limiting Magnitudes of CCD Images

Object	Filter	m_{lim}
L1689	V	21.8
L1689	R_c	21.8
L1689	I_c	20.4
Heiles' Cloud 2	V	22.9
Heiles' Cloud 2	R_c	21.8
Heiles' Cloud 2	I_c	20.8

2.2.3 Las Campanas CCD Observations

Relatively unobscured portions of the Taurus photographic plates and CCD images have an associated interstellar extinction that is small, but non-zero. The purpose of the observations discussed in this section was to determine the residual extinction *offset* within the Heiles' Cloud 2 photographic field. The technique used to solve this problem was to compare the number of stars per limiting magnitude located in an unobscured region well offset from the Heiles' Cloud 2 field, with the corresponding star counts from a portion of the Taurus photographic plate (see section 2.1) that has the least amount of obscuration resulting from the intervening molecular cloud.

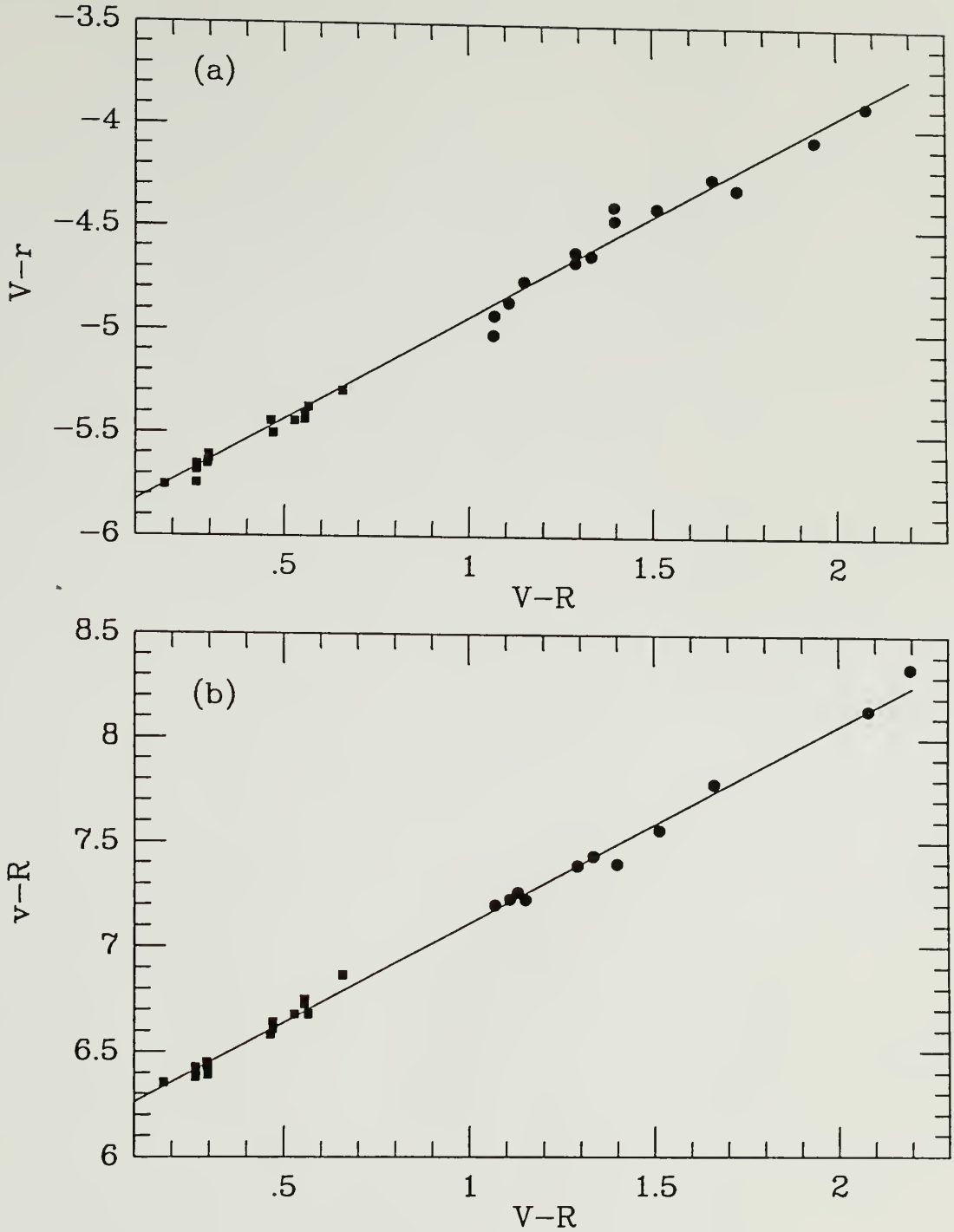

Figure 2.3 Machine magnitude *versus* Cousins colors for the Taurus and Landolt standards. Taurus standards are represented by filled circles, and the Landolt standards by filled squares. The best fit to the data is also shown.

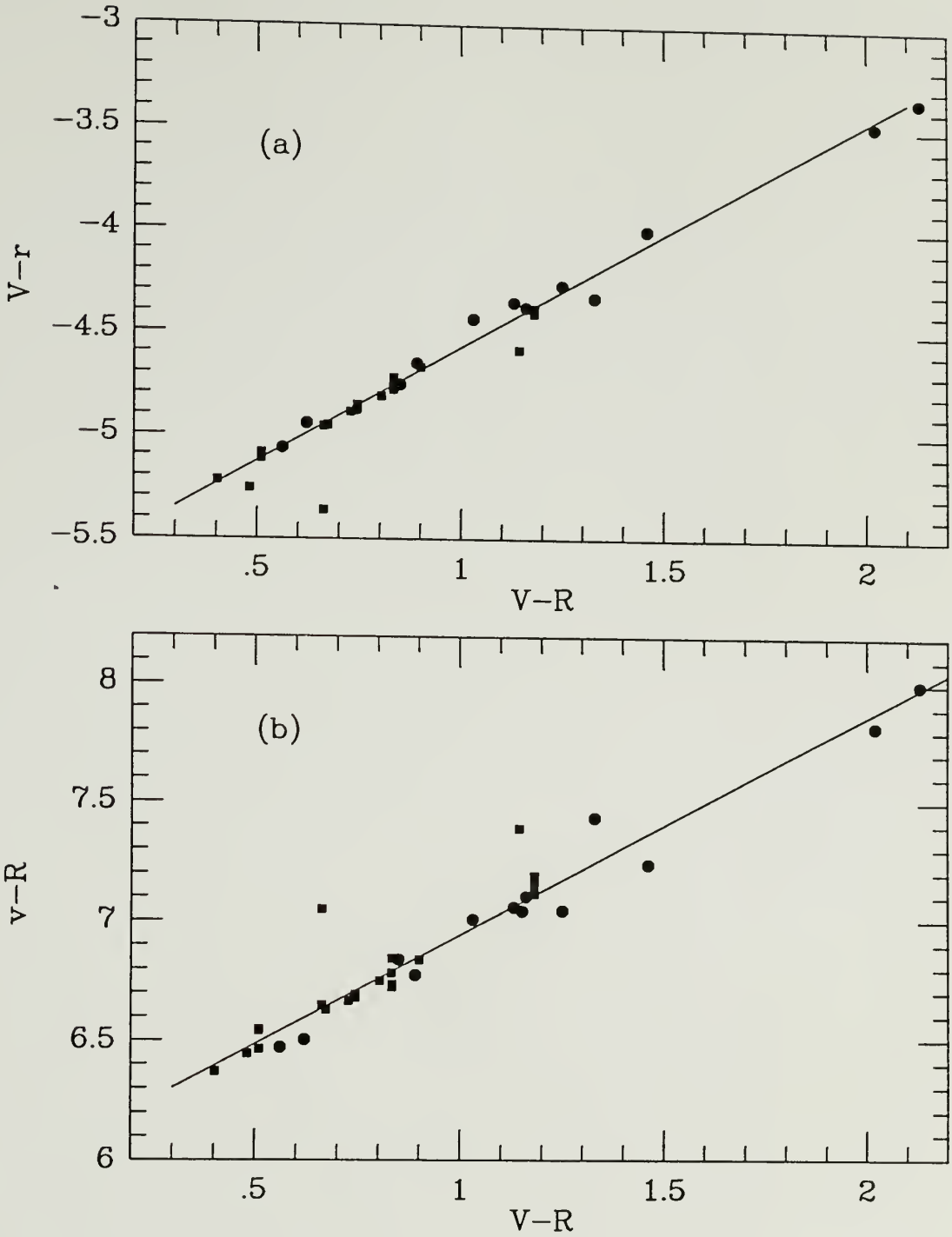

Figure 2.4 Machine magnitude *versus* Cousins colors for the Ophiuchus and Landolt standards. Ophiuchus standards are represented by filled circles, and the Landolt standards by filled squares. The best fit to the data is also shown.

Optical, B, V, R, I, photometry of a 3.3′ × 5.0′ field in Heiles Cloud 2 and a 16.5′ × 5.0′ field lying a few degrees east of the cloud along the same Galactic latitude were carried out in 1988 using a Thomson CCD camera mounted on the University of Toronto Southern Observatory 24″ telescope located in Las Campanas, Chile. The coordinates of the Cloud 2 field are $\alpha(1950) = 4^h\ 39^m\ 45^s$, $\delta = 25°\ 45'$, and the reference field coordinates are $\alpha(1950) = 4^h\ 55^m\ 00^s$, $\delta = 22°\ 10'$. The Thomson CCD has 384 × 576 pixels, each of size 0.52″, giving a total field of view of 3.3′ × 5.0′. A summary of the observations is presented in Table 2.11.

Multicolor photometry was conducted for Landolt standards and the Taurus field standard stars (see section 2.1), as well as for the reference and Cloud 2 fields. In addition, deep-long-exposure V-band images were taken of the Cloud 2 and reference fields. Reductions of the raw CCD images followed the same procedure as that of the Kitt Peak data (see section 2.2.3), namely, bias subtraction, flat-fielding and atmospheric extinction corrections. Stars were identified, their flux was computed, and their machine magnitudes were transformed to the standard Cousins system (see section 2.2.3 for more details).

Table 2.11

Las Campanas Observations

Date	Telescope	Instrument CCD	Seeing Conditions	Weather
12-29-88	TSO 24″	Thomson	1.7″	Clear
12-30-88	TSO 24″	Thomson	2″	Variable
1-01-89	TSO 24″	Thomson	2″ - 3″	Poor
1-02-89	TSO 24″	Thomson	1.5″ - 2″	Clear
1-03-89	TSO 24″	Thomson	0.5″ - 1″	Clear
1-04-89	TSO 24″	Thomson	2.3″	Hazy
1-05-89	TSO 24″	Thomson	1″	Clear

The limiting V magnitude achieved for the reference and object fields was ~19.1. The total number of stars within the reference field with magnitudes brighter than this limit was 221. A plot of the cumulative star counts for the reference field is shown in Figure 2.5 (for a description of cumulative star count techniques applied to this problem, see Dickman and Herbst 1990). Within the object field, a total number of stars with magnitudes brighter than the limit was 18. Factoring in the total area of the two CCD fields (2.31×10^{-2} deg^2 *versus* 4.62×10^{-3} deg^2), we find that the extinction offset between the object field in Heiles' Cloud 2 and the reference field is ~1.7 mag. Therefore we conclude that one must add about 1.7 magnitudes of extinction at V to all star count - based extinction which we obtain in Chapter 3.

2.3 Palomar Sky Survey

As part of the proper motion analysis carried out in Chapter 5, we obtained digitized images of the Taurus, Ophiuchus and B5 cloud regions. We used glass plate copies of the National Geographic Palomar Observatory Sky Survey (POSS) at the National Optical Astronomy Observatories in Tucson, Arizona.

Since the object fields are all heavily obscured by the molecular clouds, we chose the red E-plates of the survey to maximize the coverage depth. The plates were as follows:

Taurus	—	E-228,	epoch 1950.9
B5	—	E-301,	epoch 1955.8
Ophiuchus	—	E-1105,	epoch 1954.5

Stars within a 1.5° square area centered on the clouds were identified and their machine magnitudes computed using the "Monet Machine" automatic measuring engine. The result was a catalog of several thousand stars within the Taurus, B5 and Ophiuchus fields with cartesian coordinates and machine magnitudes.

The accuracy of the coordinates obtained depends in part upon the actual location of the star on the glass plate. Distortion due to buckling of the glass as it is placed in the holder of the telescope, amount to 0.5″ - 1.3″, for the most part, less than 1″ in position error can be expected (*cf.* Bowen 1960). Relative magnitudes of the scanned stellar images are accurate to ~0.5 magnitudes, which is adequate for out purposes, but there is a non-linear relation between actual and machine magnitudes. Since our goal was to extract all stars on the plate with magnitudes brighter than the plate limit ($R_{lim} \sim 20.0$), the machine was set to an extreme brightness intensity threshold. Unfortunately, this technique also resulted in the unavoidable side effect of numerous, false detections of imperfections on the glass plates. For the most part, these pseudo-stars were easily culled using a magnitude criterion (their apparent brightness is typically very low).

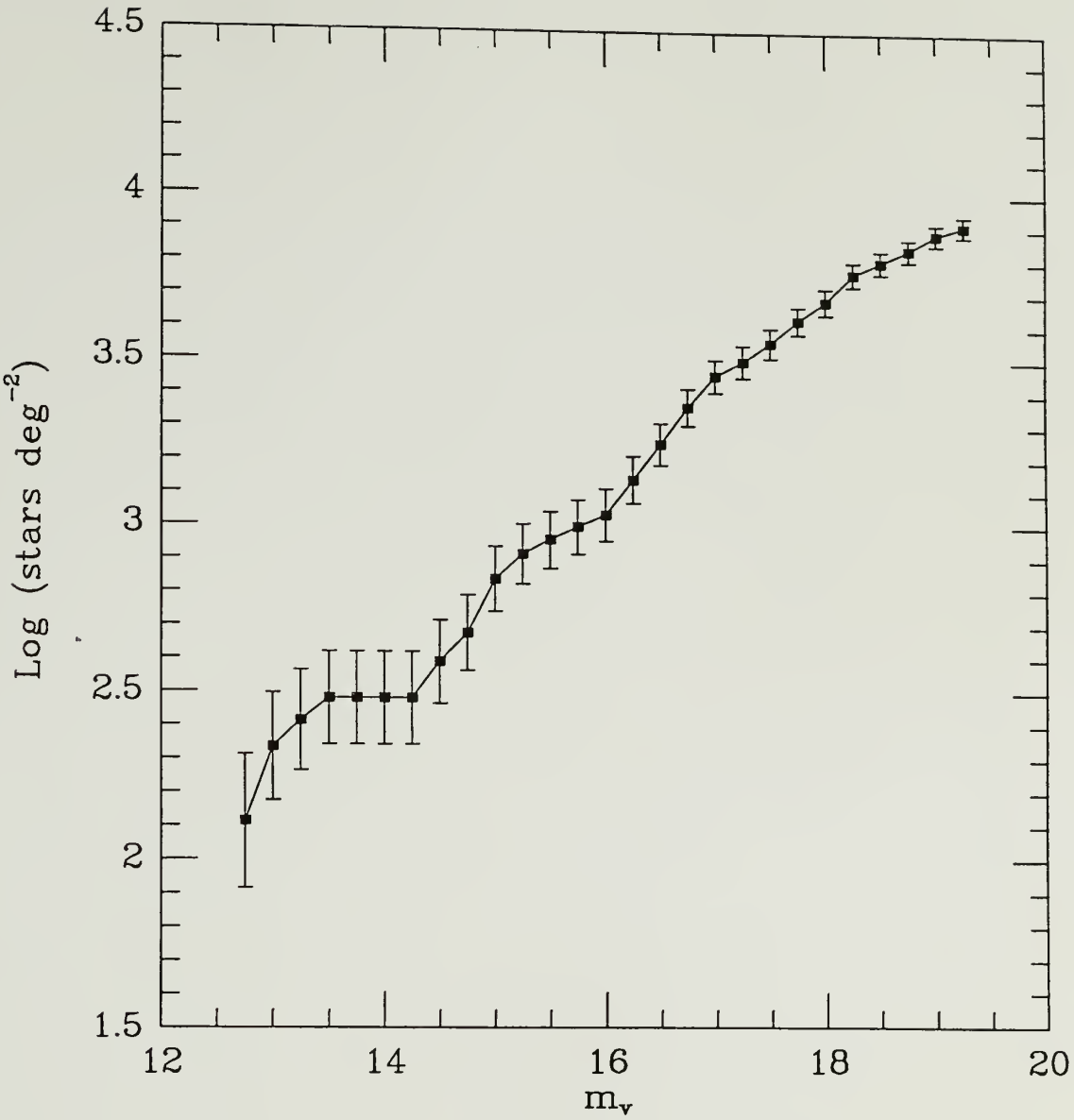

Figure 2.5 Cumulative star counts *versus* visual apparent magnitude for the Taurus reference field. Poisson error bars,$\sqrt{n}$, are included with the star counts.

CHAPTER 3

STAR COUNTS AND VISUAL EXTINCTION

In this study it is of central importance to determine the visual extinction due to molecular clouds. This information provides a gauge of the cloud's gas and dust mass distribution, which is critical to locating the darkest and most extensive parts of the clouds so that they can be used effectively as opaque screens. In addition, visual extinction can be employed as a color discriminator between foreground and background stars: in most cases, the only difference in colors between a red dwarf star near the Sun and a distant, luminous, late-type giant is the degree of interstellar reddening affecting the more distant star. If the visual extinction is known, then a background star's colors can be dereddened, thereby allowing constraints on its corresponding spectral type, and possibly, luminosity class. Further, stars foreground to the molecular clouds will have little or no reddening; therefore, attempting to deredden their colors will place them in unphysical regions of the color-color plane.

In this chapter we review a simple, yet effective method to determine the visual extinction toward molecular clouds. Using this technique, the method of star counts, we estimate the extinction in the Taurus and Ophiuchus photographic and CCD fields. The results are presented in section 3.2.

3.1 The Method of Star Counts

The most conspicuous visual feature of a molecular cloud is its apparent paucity of stars: compared to the surrounding starry sky, a molecular cloud looks acutely dark. The degree of darkness depends on the amount of obscuring dust and gas within the cloud, which in turn is gauged by its visual extinction. We can calibrate the degree of obscuration by comparing the number of stars counted within a field located toward the cloud, with the number of stars counted toward a nearby, relatively unobscured region of the sky. Briefly, this is the method of star counts effectively employed by Bok (1956), and most recently treated by Dickman (1978).

The extinction in a molecular cloud varies over spatial scales set by the physical structure of filaments, envelopes and cores comprising the cloud. Therefore, in order to resolve the structure of the cloud, it is necessary to divide it into a fine grid of "reseau" squares, where for each square the method of star counts is applied. In addition to the physical structure of the cloud, the size of the reseau squares are also constrained by the photographic plate scale, CCD stellar profile scale, and small sample statistics. For example, if the cloud grid is divided into reseau squares that are too small such that, on average, there is one star counted per square, then the associated expected Poisson error[1] is exactly one star per reseau square. Clearly, this would be a poor measure of the extinction (this is illustrated later in the text). On the other hand, a reseau square that is too large would degrade the resolution of the cloud physical structure. In practice, reseau sizes vary from 1′ to 2′ (*cf.* Dickman 1978).

The counting procedure is as follows. Within each reseau cell, count the number of stars with apparent magnitudes, m_λ, brighter than the photographic plate or CCD image limiting magnitude, m_λ^{lim}. Normalize the star counts by scaling the reseau cells to

[1] The statistical error expected within a reseau grid with N star counts is $\sqrt{N}$ (Bok 1937).

correspond to a one degree square area. The resultant quantity, the total number of stars per square degree, brighter than limiting magnitude M_λ^{lim}, is designated $N_\lambda(m_\lambda)$. It is this quantity that is to be compared with the corresponding surface density of stars, $N_{ref}(m_\lambda)$, within the reference field — a relatively unobscured field located nearby to the targeted molecular cloud. To determine the reference field star counts, construct the cumulative surface density of stars as a function of apparent magnitude within this field and scale the counts to correspond to one square degree area. The reference field may have a small residual extinction, especially if the field is chosen too close to the molecular cloud. Nevertheless, the residual simply adds a linear offset to the final, reduced visual extinction and can be added at a later time (assuming one knows the residual offset). A nice feature of the reference field stellar density curves is that they are generally linear if plotted as a semi-logarithm. In any case, the reference stellar surface density is used to calibrate the molecular cloud star counts as outlined below.

Since the reference field star counts presumably represents the true stellar surface density in the direction of the targeted molecular cloud and since the star counts measured in any given reseau cell of the molecular cloud possesses some degree of extinction, it necessarily follows that $N_{ref}(m_\lambda^{lim}) > N_\lambda(m_\lambda)$. The difference between the two measures reflects the amount of extinction. Indeed, the reference stellar density curve, $N_{ref}(m_\lambda)$ versus m_λ, defines the extinction in the reseau cell. At some m_λ (hereafter referred to the effective wavelength), $N_\lambda(m_\lambda)$ lies on the true stellar density curve. The extinction within the reseau is simply

$$A_\lambda = m_\lambda^{lim} - m_\lambda \qquad (3.1)$$

Reduction to a visual extinction is carried out using the appropriate reddening law (see Appendix C, Interstellar Reddening). Equation 3.1 assumes that all obscuring material belongs to the molecular cloud, and that all stars counted are located behind the cloud. The

first assumption is sufficient given that the clouds are not too far away (the extinction associated with the Galactic disk follows roughly a law given by 1 - 2 magnitudes of visual extinction per kpc; see Appendix F, Spatial Distribution Models of the Galaxy). Similarly, the second assumption is adequate if the clouds are not too far away; in which case the foreground space volume is minimized with respect to the background volume. For example, the relative number of background stars to those located in the foreground of a molecular cloud lying distance d from the Sun is

$$\frac{N(d_{max})}{N(d)} \sim \left(\frac{d_{max}}{d}\right)^3 \qquad (3.2)$$

where d_{max} is the maximum distance stars are located in a particular direction of the Galaxy. Here we have assumed a uniform distribution of stars. If the molecular cloud is located, for example, 140 pc from the Sun, and the maximum distance the Galactic disk extends in this direction (this value, of course, depends on the Galactic coordinates and structure of the disk; see Chapter F for a better discussion), for example is 2 kpc, then the ratio of background to foreground stars is ~2920. Clearly, the background component dominates the total star counts.

Two special cases require further attention. First, consider the case when a reseau square has no stars brighter than the limiting magnitude. A count of zero stars implies that our limiting magnitude is not faint enough to observe stars leaking through a column of gas and dust that has *at least* an amount of extinction corresponding to a count of 1 star per reseau. For this reason and the fact that a count of zero stars has a statistical error of one star, reseau cells with zero star counts are assigned a value of one. The second case comprises several, > 1, simply connected reseau cells, each with zero star counts. The bias-free approach is to assume that the obscuration is uniform over the contiguous area. As in the first case, assign a star count of one to the set of reseau squares. For example, if the

total number of simply connected reseau squares with zero star counts is n, then the corresponding star counts assigned to the grid is

$$N(stars\ degree^{-2}) = \frac{1}{[n\gamma A]} \tag{3.3}$$

where A is the area of one reseau square and γ is the scale factor to convert A to square degrees.

3.2 Results

In this section we construct cumulative stellar surface density curves for the Taurus and Ophiuchus reference fields, and use the method of star counts to compute the visual extinction in the two cloud fields from the photographic data and CCD images described in Chapter 2.

3.2.1 Ophiuchus

The photographic data includes a 50′ diameter reference field, exposed at Kron J, F and N bands, that is a centered on $\alpha(1950) = 16^h\ 32^m\ 30^s$, $\delta = -25°\ 00'\ 00''$. Dickman and Herbst (1990) used this data to correct the residual extinction belonging to the outer areas of the cloud field where the obscuration is at a minimum. Plots of the cumulative stellar surface density curves, corrected for residual extinction, at all three colors can be seen in Dickman and Herbst (1990). In their study, the N-band star counts provided the deepest measure of the extinction, largely due to the longer wavelength ($\lambda_0 \sim 7941$ Å), where the N-band plate limit was conservatively adopted to be 19.5 mag (*cf.* Table 2.2). Therefore, we use the N-band star counts of the Ophiuchus reference field to calibrate the

corresponding CCD images exposed at Cousins I band[2]. As a matter of convenience, we express the N-band star counts (from Figure 3 in Dickman and Herbst 1990) with a linear relation,

$$\log N(m_N) \cong -0.88 + 0.287 m_N, \quad 12.5 \leq m_N \leq 20.4 \tag{3.4}$$

where we have extrapolated the photographic data to $m_N = 20.4$ since the CCD I-band data extends to this limiting magnitude. The extrapolation adds some uncertainty since there is hint of curvature at the faint end of the N-band star counts of Dickman and Herbst, which is probably related to incompleteness. On the other hand, 90% of the star count curve accurately constraints the linear fit given by Equation 3.4. Further, there does not seem to be any evidence that the star counts turn over at N ~ 19.5 based on a simulation using the stellar density distribution described in Appendix F (also, see section 3.2.2).

The I-band CCD field covers an area 23′ × 26′ centered at $\alpha(1950) = 16^h\ 29^m\ 45^s$, $\delta = -24°\ 24'\ 10''$. A location plot of the I-band stars is shown in Figure 3.1. The field was divided into a 21 × 19 reseau grid with cells of size 1.25′ × 1.25′. In each cell, the number of stars with apparent magnitude, m_I, brighter than 20.4 were counted and scaled to a corresponding area of 1 deg^2. Those reseau cells with no stars were assigned a count of 1, and contiguous areas of zero star counts were assigned, as a group, one count. The effective magnitude of each square is then given by Equation 3.4 and the I-band extinction is computed according to

$$m_N = \left[\frac{\log N(m_N) + 0.88}{0.287} \right] \tag{3.5}$$

$$A_I = 20.4 - m_N$$

[2] Kron N-band and Cousins I band are roughly equivalent.

Making use of the Savage and Mathis (1979) "universal" reddening law (see Appendix C, Table C.1 and Equation C.4), we convert to visual extinction using the relation

$$A_V \cong 1.69 A_I \tag{3.6}$$

The resultant map of visual extinction was then smoothed using a sharply peaked gaussian 3 × 3 filter,

$$\left\{ \begin{matrix} & & \\ 2 & 3 & 2 \\ 3 & 24 & 3 \\ 2 & 3 & 2 \end{matrix} \right\} \tag{3.7}$$

Use of the filter reduces the small sample statistical errors associated with the most obscured portions of the cloud, and effectively smooths the abrupt transition between regions with moderate extinction and those with extinction set by the lower limit. This sharp gradient is non-physical, and is due to the way that small sample statistics are treated and to the discrete nature of the method of star counts.

A fully-reduced gray-scale map of the visual extinction determined for the Ophiuchus CCD field is shown in Figure 3.2. An overlay of extinction contours, $A_v = 5$ and 10, is also shown in the figure. The range of visual extinction starts as low as 3-5 mag on the outer perimeter of the field, and extends as high as 21 mag within the interior. The darkest regions have contiguous cells with no stars brighter than the plate limit.

The statistical error associated with the computed visual extinction in each reseau cell follows from the star count Poisson error, $\sqrt{N}$, and is derived in the Appendix of

Dickman (1978) as,

$$\delta A_V = b_I^{-1} \left(\frac{A_V}{A_I} \right) \sqrt{\frac{n_0 + n}{n_0 n}} \tag{3.8}$$

where b_I is the slope of the reference field stellar density curve, expressed in Equation 3.4, n_0 is the *average* number of stars per reseau cell in the reference field, and n is the number of stars in a cloud reseau square. The corresponding relative error is given by

$$\frac{\delta A_V}{A_V} = \left[\log \left(\frac{n_0}{n} \right) \right]^{-1} \sqrt{\frac{n + n_0}{n n_0}} \tag{3.9}$$

When n is comparable to n_0, the associated error of the extinction estimate is negligible, while the relative error is large (because the corresponding extinction approaches zero). This effect can be seen in Figure 3.3, where a plot of the extinction error and relative error *versus* the ratio (n / n_0) is shown. When the extinction is large and n approaches zero, the associated error climbs rapidly and the relative error settles near zero. These statistical effects cause considerable (unphysical) discontinuities between areas with significant extinction and those with slightly smaller extinction (*e.g.*, as reflected in the star counts: n *vs.* n-1, and n-2).

3.2.2 Taurus

Both the photographic and CCD data have reference fields with non-zero residual extinction. In Figure 3.4 a location plot of the N-band stars for Heiles' Cloud 2 is shown. We have chosen the reference field to be a 5′ square area centered on location $\alpha(1950) = 4^h\ 39^h\ 45^s$, $\delta(1950) = 25°\ 45'$. The residual extinction within this boundary was determined to be $Av \approx 1.7$ mag (as described in Chapter 2, section 2.2.4). The CCD fields do not extend to this location, so we must use as a reference field an area slightly closer to the molecular

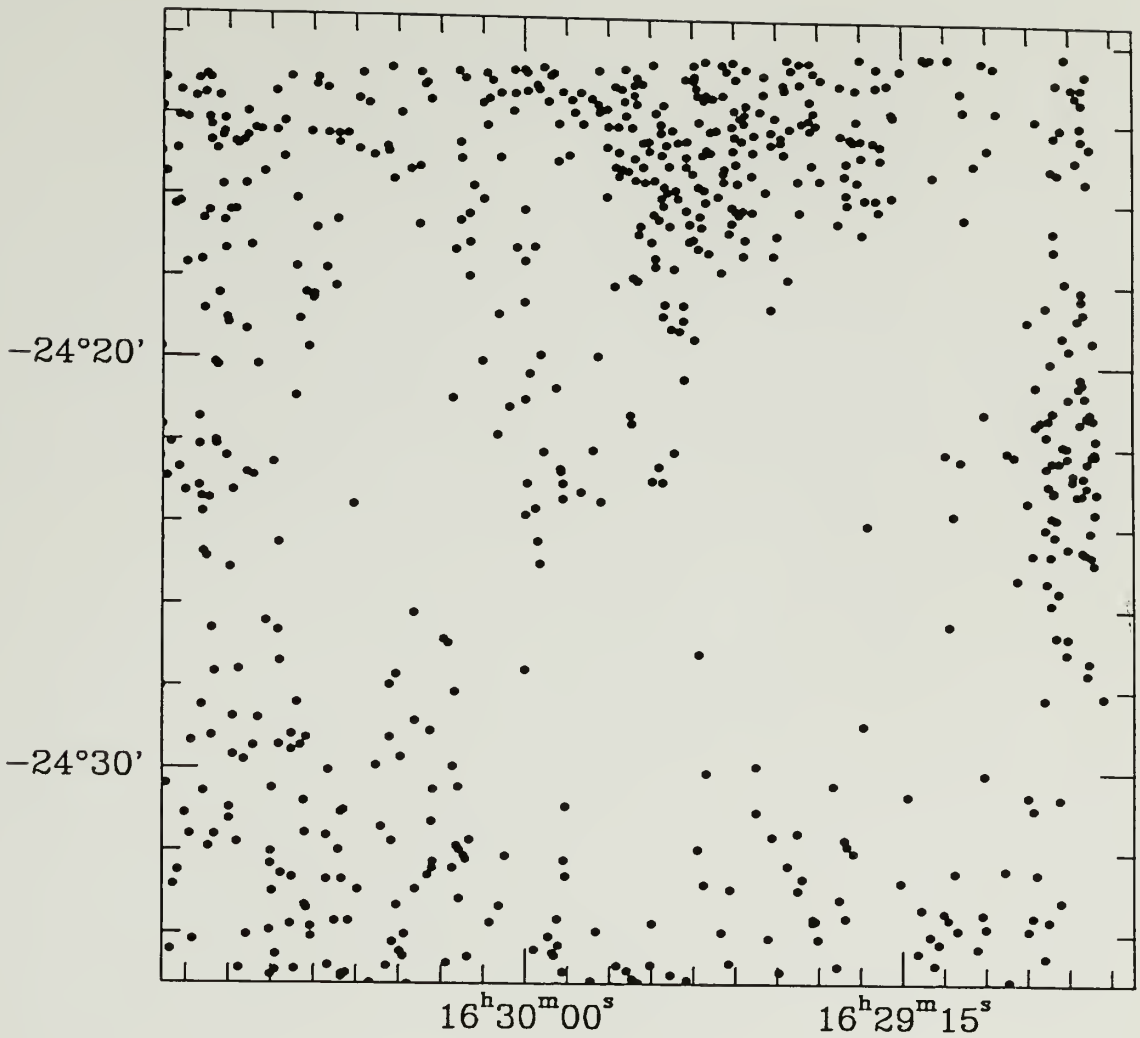

Figure 3.1 The Ophiuchus CCD field, shown in the Cousins I band ($\lambda_0 \sim 8000$ Å). All stars brighter than apparent magnitude $m_I = 20.4$ are plotted. The coordinates are epoch 1950.

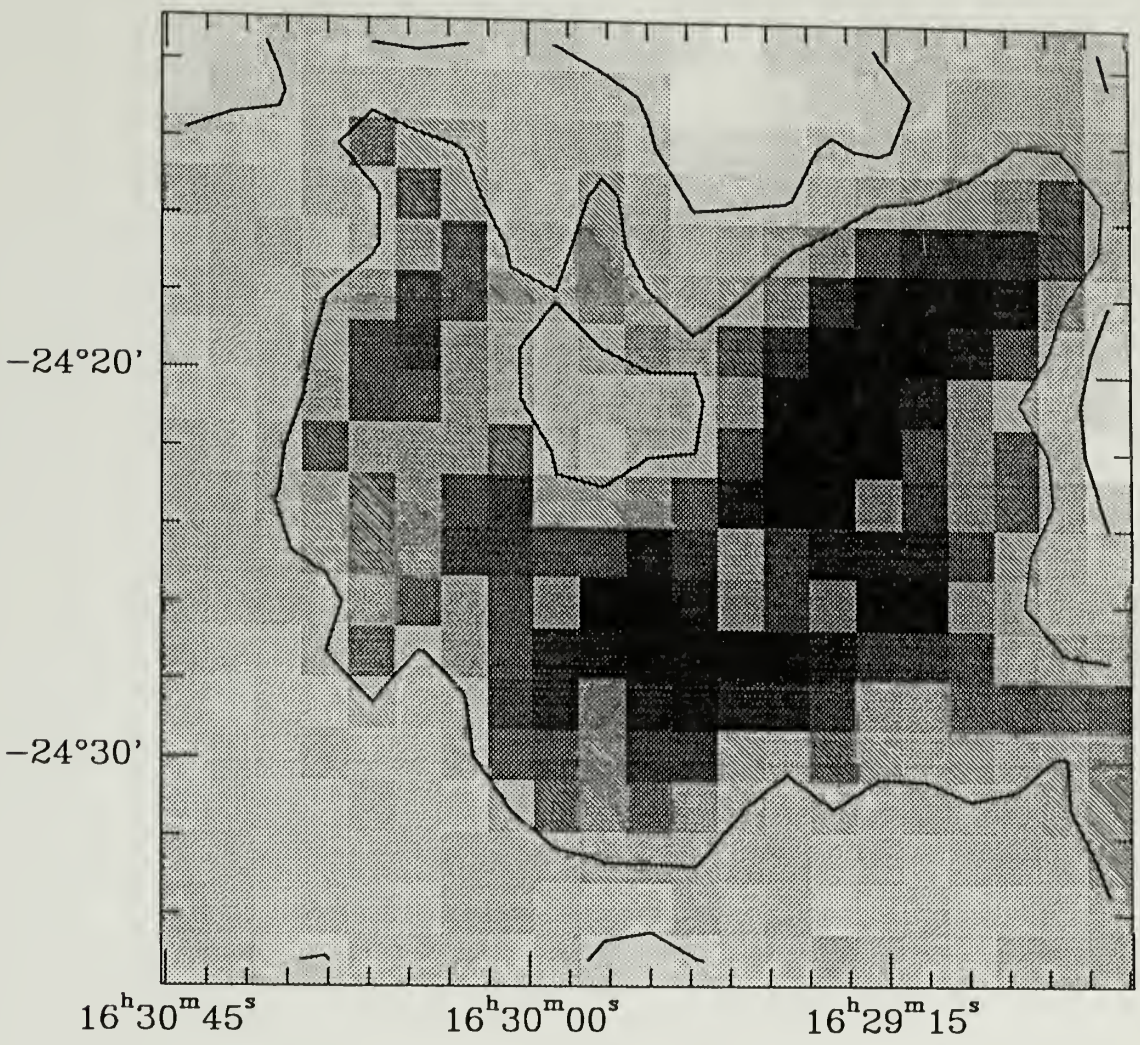

Figure 3.2 Visual extinction map of the Ophiuchus CCD field. There are 21 × 19 reseau cells, each of size 1.25′ square. Contour levels correspond to A_V = 5 and 10 mag. The A_V gray-scale values range from 3 to 21 mag (proportionately from white to black).

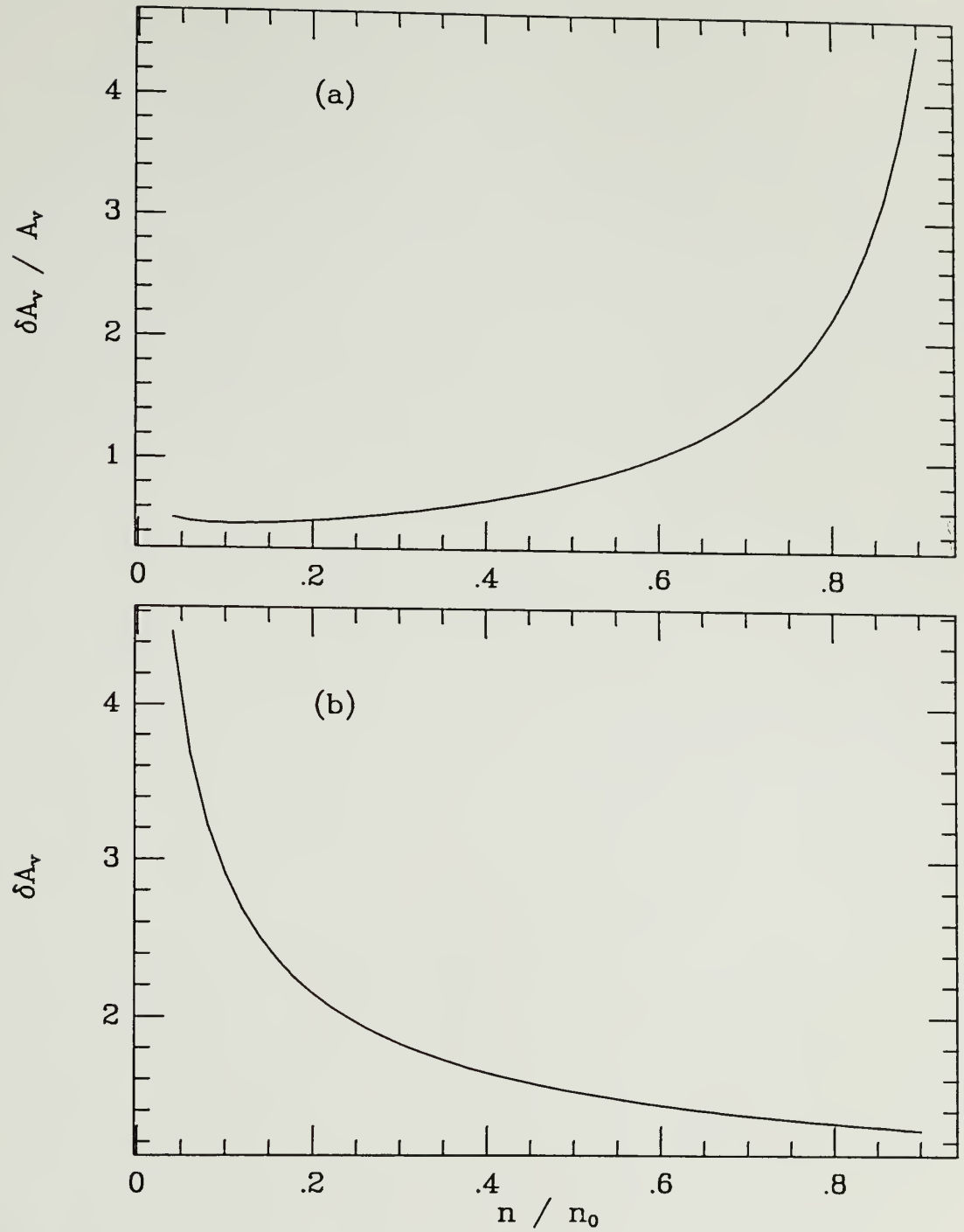

Figure 3.3 Statistical error associated with the visual extinction derived using the method of star counts. The relative error (a) and the visual extinction error (b) are plotted against the ratio of the number of stars in a reseau square, n, and the average number of stars in the reference reseau grid, n_0, of equivalent area.

cloud. A location plot of the I-band CCD stars is shown in Figure 3.5. We have chosen the CCD reference fields to be 4′ × 6′ boxes centered at locations $\alpha(1950) = 4^h\ 39^h\ 05^s$, $\delta(1950) = 25°\ 45'$, and $\alpha(1950) = 4^h\ 38^h\ 55^s$, $\delta(1950) = 26°\ 05'$. As a lower limit, we expect the residual extinction within these boundaries to be the same as that in the photographic reference field. We may verify this expectation by comparing the cumulative stellar surface density curves derived for the stars within the reference field boundaries with the corresponding predicted curves using a Galactic spatial distribution model. A description of the model is presented in Appendix F.

The expected distribution of stars located toward the Heiles' Cloud 2 (Galactic coordinates: $\ell = 173°$, $b = -15°$) of the Taurus Molecular cloud was determined at three bands, V, R and I, using the Galactic surface density model described in Appendix F. A residual extinction was added to the predicted model densities so that a best fit to the actual cumulative surface density was achieved. In Figure 3.6a, a plot of the constructed cumulative surface densities in the three bands, V, R and I, for the CCD reference fields is shown. Overlayed on these curves, Figure 3.6b, are the *predicted* densities using the spatial distribution model; a residual extinction of $A_v = 2.25$ is added to the curves so that they match the CCD data. We conclude that the visual extinction offset within the CCD reference fields is between 1.7 and 2.3 mag. The latter estimate is probably closer to the actual value since the CCD reference field is closer to the molecular cloud than the 4-m photographic reference field. As a matter of convenience, we adopt the model surface density curves (with $A_v = 0$ mag) as the calibrator for the cloud star counts. A plot of the V, R, and I surface density curves is shown in Figure 3.7. Rather than apply a linear fit to the curves (they are not linear over the dynamic range), we make use of them as "look-up" tables.

As with the Ophiuchus data, we divide the I band CCD field into a grid of reseau cells so that we may resolve the cloud's variation of extinction with position. We have chosen a mesh consisting of 41 × 37 cells of size 1.4′ × 1.4′. In each square, the number of stars with apparent magnitudes, m_I, brighter than 20.8 were counted and scaled to a corresponding area of 1 deg^2. Those reseau cells with no stars were assigned a count of 1, and contiguous areas of zero star counts were assigned, as a group, one count. The effective magnitude of each square is found from the reference field cumulative stellar density curves, Figure 3.7 and their associated look-up tables. The I and V band extinctions are then computed, similarly to Equations 3.5 and 3.6, according to

$$A_I = 20.8 - m_I$$
$$A_V \cong 1.69 A_I \qquad \textbf{(3.10)}$$

The resultant visual extinction map was then smoothed using a gaussian filter, Equation 3.7. A gray-scale image of the visual extinction determined for the Heiles' Cloud 2 CCD field is shown in Figure 3.8. Overlaying the map are contours given by A_v = 5 and 10. Extinction values range from 2 to 23 magnitudes, where the darkest regions have contiguous reseau cells with zero star counts. The statistical error associated with each extinction estimate is given by Equation 3.9 (see section 3.2.1 for a more detailed discussion).

In summary, the cloud extinctions derived using star counting techniques of the Taurus and Ophiuchus CCD fields indicate large extended areas (well over 60% of the fields) with considerable obscuration, $A_V >>$ a few; and thus, the cloud-fields chosen for this study are suitable objects for the opaque "screen" method introduced in the next chapter.

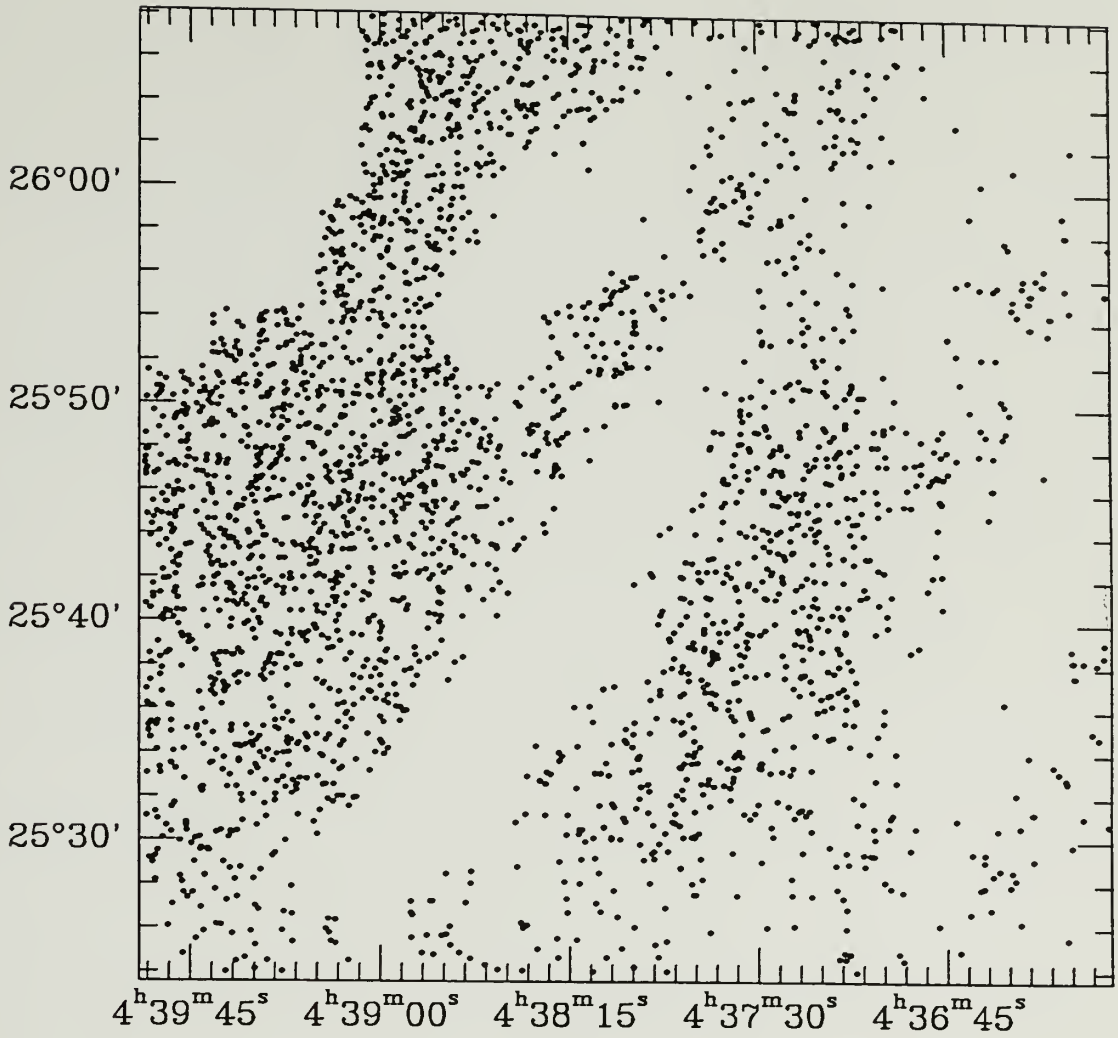

Figure 3.4 The Heiles' Cloud 2 photographic field, shown in the Kron N band ($\lambda_0 \sim 7941$ Å). All stars brighter than apparent magnitude $m_N = 18.5$ are plotted. The coordinates are epoch 1950. The star count reference field is a 5′ square area centered on location $\alpha(1950) = 4^h\ 39^h\ 45^s$, $\delta(1950) = 25°\ 45'$.

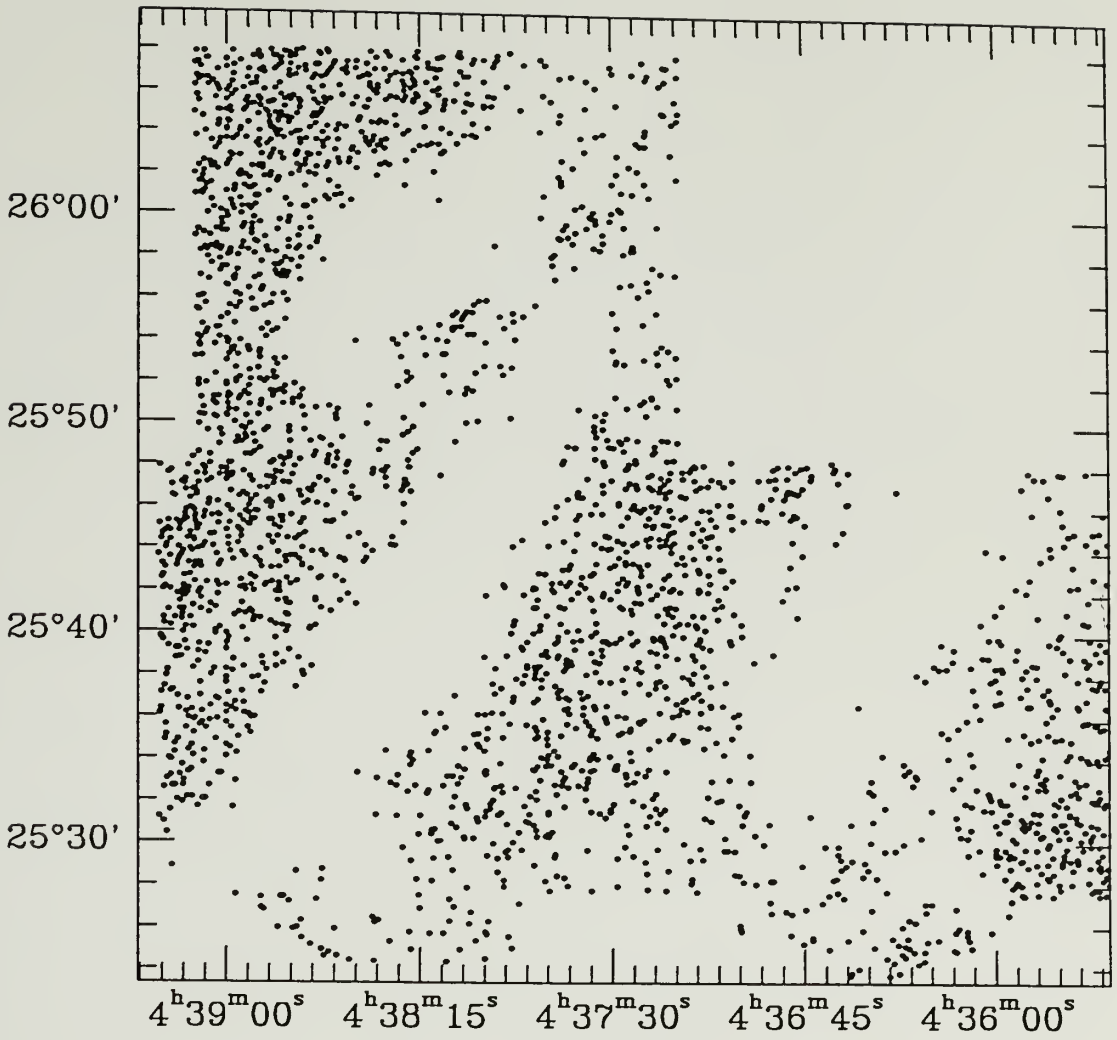

Figure 3.5 The Heiles' Cloud 2 CCD field, shown in the Cousins I band ($\lambda_0 \sim 8000$ Å). All stars brighter than apparent magnitude $m_I = 20.8$ are plotted. The CCD reference fields are $4' \times 6'$ boxes centered at locations $\alpha(1950) = 4^h\ 39^h\ 05^s$, $\delta(1950) = 25°\ 45'$, and $\alpha(1950) = 4^h\ 38^h\ 55^s$, $\delta(1950) = 26°\ 05'$.

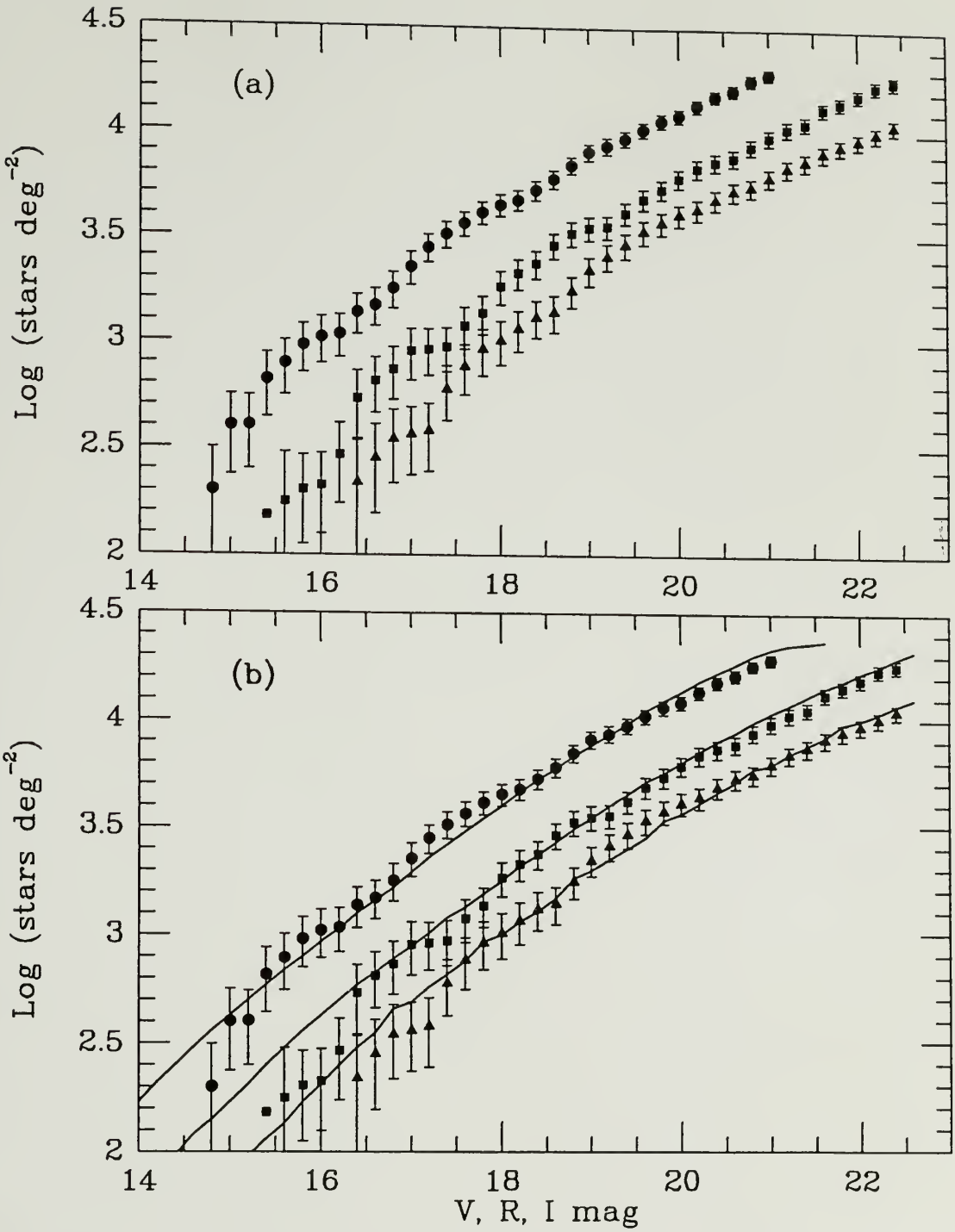

Figure 3.6 (a) Cumulative stellar surface densities in bands V, R and I for the CCD reference fields. The ordinate axis is the number of stars brighter per square degree of sky than apparent magnitude m_λ. Symbols are drawn as follows: filled circles denote the I band data, filled squares the R band and filled triangles the V band. Poisson error bars reflect the expected uncertainty of $\sqrt{N}$. In (b) the model predicted stellar surface densities are overlayed on the CCD data; a residual extinction offset of Av = 2.25 mag was added to the synthetic curves as a best fit to the CCD data.

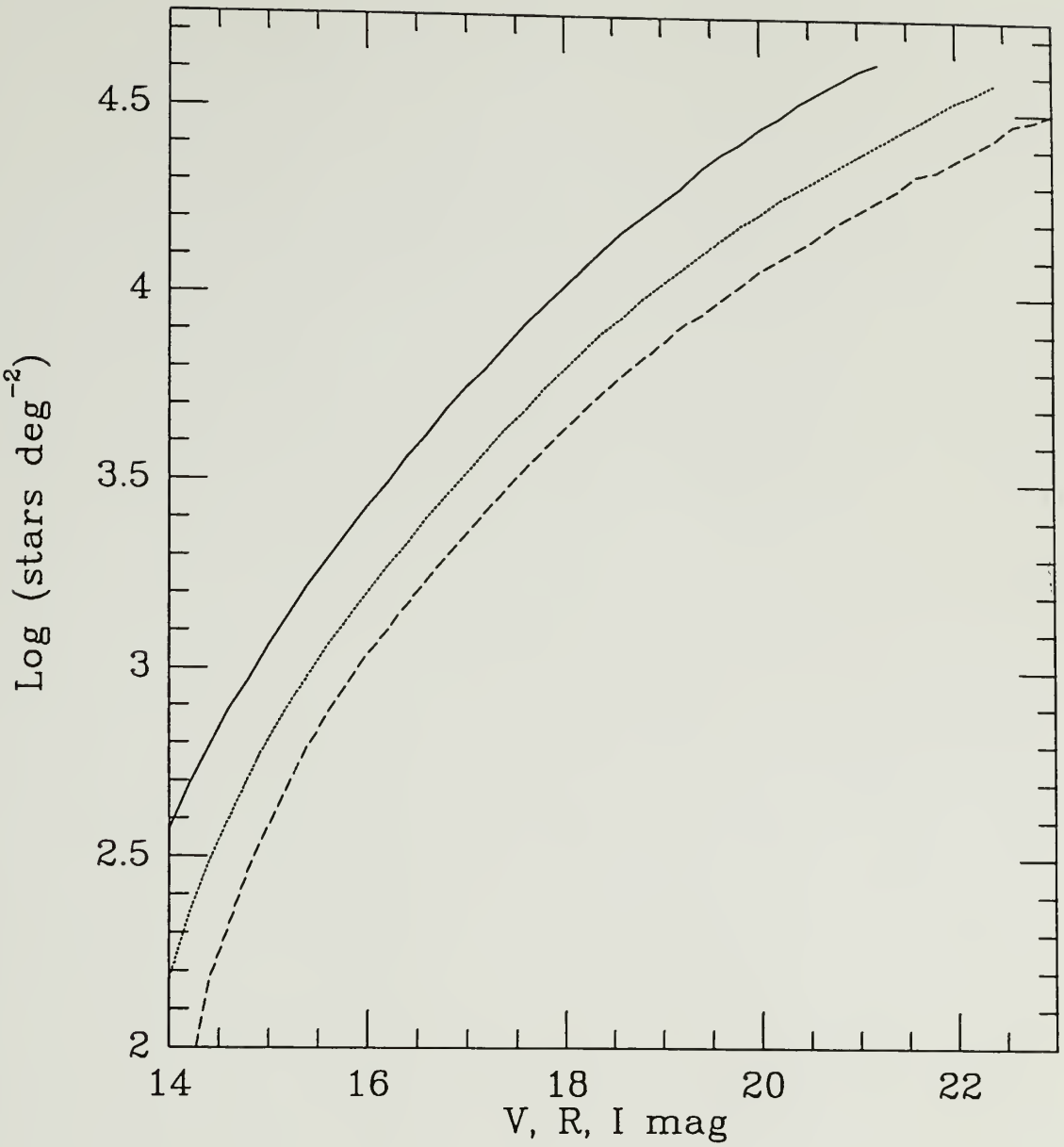

Figure 3.7 Predicted cumulative stellar surface densities in bands V, R and I for fields located toward the Taurus Molecular Cloud complex; Galactic coordinates l = 173°, b = -15°. Units are the same as those used in Figure 3.6. Drawn lines represent the following: solid denote the I band predictions, dotted the R band, and dashed the V band.

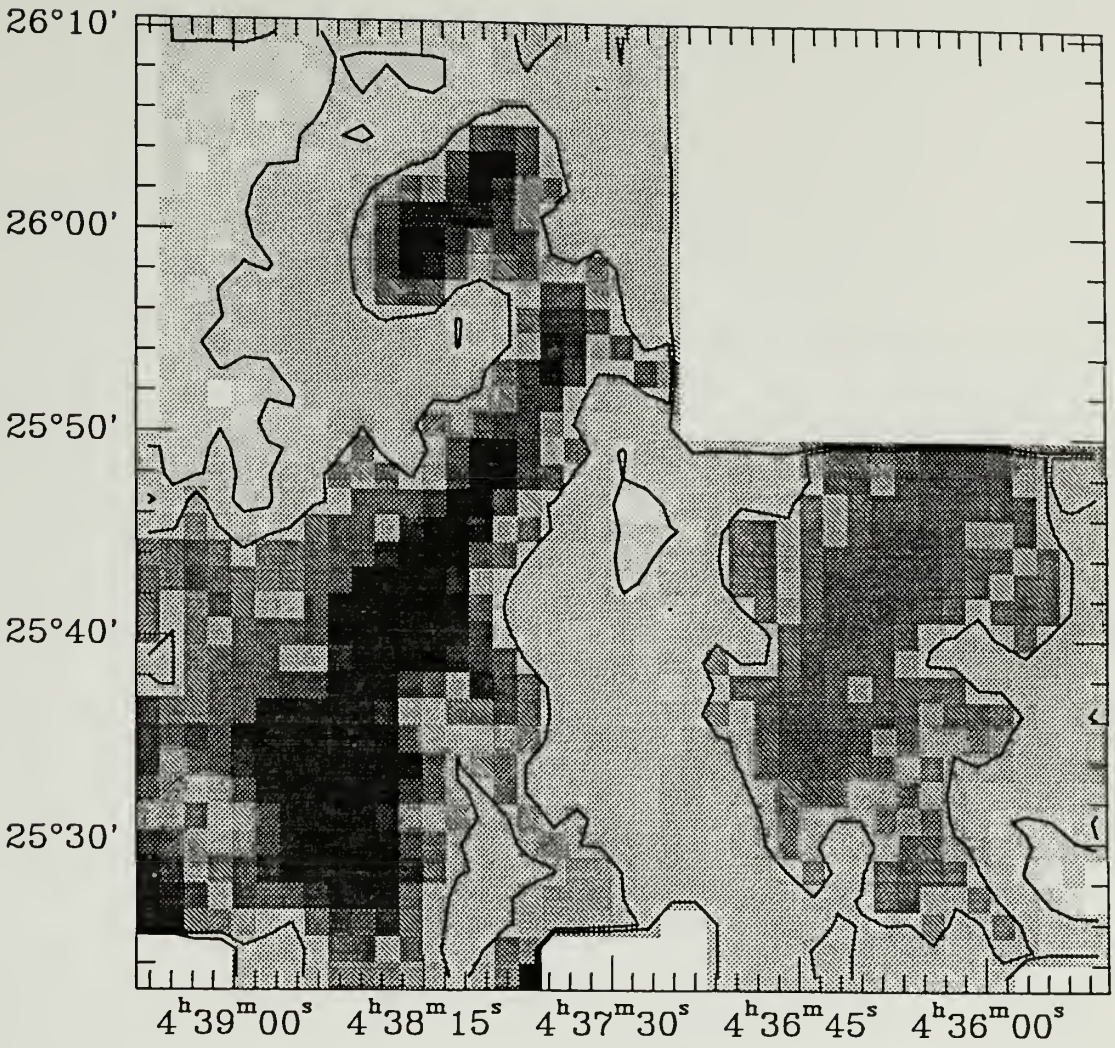

Figure 3.8 Visual extinction map of the Heiles' Cloud 2 CCD field. There are 41 × 37 reseau cells, each of size 1.4′ square. Contour levels correspond to A_V = 5 and 10 mag. The A_V gray-scale values range from 3 to 23 mag (proportionately white to black).

CHAPTER 4

COLOR - COLOR ANALYSIS

Traditionally astronomers have searched for low mass stars using parallax, proper motion and photometric techniques. The key advantage to using the last method is that it is free of the kinematic and population biases that are intrinsic to the astrometric techniques (*cf.* Hanson 1983). Another benefit of using photographic or CCD multi-color photometry is that large areas with deep limiting magnitudes can be surveyed. However, although photometric colors can be used to discriminate between stars of different spectral type, there may be some ambiguity, depending on the choice of colors, between luminosity classes. This is a major disadvantage of the photometric color-color technique.

In this study, we implement a method suggested by Herbst and Dickman (1983) in order to minimize this effect. By observing toward a nearby molecular cloud, stars that are behind the cloud are either completely blocked from view or are heavily reddened, in which case their colors reveal their location behind the cloud. Stars that lie in front of the cloud will have little or no reddening. In this way we may isolate a complete sample of low mass stars — provided the photometry is sufficiently deep — within the discrete volume defined by the survey area and the distance to the cloud. We will discuss this method in more detail in section 4.2.

Any luminosity function survey must be as sensitive as possible to the full range of stellar types and must offer a method of classifying the surveyed stars by spectral type. The idea behind photometric color-color analysis is that one can sample a range of stellar

surface temperatures, a quantity which is directly related to spectral type. The cool photospheric temperatures of low mass stars — the most common stellar objects — dictate the use of red, or better yet, near-infrared broad-band filters. Since only in the last few years have large-format near-infrared detectors been available, most photometry on M-dwarf stars has been carried out using V, R and I filters with photographic plates or CCD cameras (*cf.* Eggen 1980; Weis 1984; Bessell 1983, 1990, 1991).

In this study we apply photographic photometry at the Kron J, F and N bands (roughly equivalent to B, V and I; see Chapter 2), and CCD photometry with V, R and I filters toward heavily obscured regions of the Taurus and ρ Ophiuchi molecular clouds. In section 4.3 we present the results of this photometry via a color-color analysis. As a necessary preliminary to these results, we first discuss the spectral energy distribution of late-type stars and the convolution of their corresponding flux with red broad-band filters (section 4.1). The "opaque screen" method of Herbst and Dickman is then discussed in more detail in section 4.2. Finally, in section 4.4 we discuss the possible systematic errors that are associated with this technique.

4.1 Late Type Stars

Late type M dwarf stars have several unique properties that both aid and hinder their detection. First and foremost, they are intrinsically faint. Consequently, only examples in the Solar neighborhood are ever observed even though these are the most common stars in the Galaxy. Secondly, the cool atmospheres are blanketed by numerous atomic and molecular species. This severely complicates the radiative transfer, and leads to uncertainties in the evolutionary tracks of these stars (Liebert and Probst 1987). Further, since the effective surface temperatures and spectra[1] of dwarf M stars are similar to that of

[1] The Henry Draper (HD) Spectral Sequence is based on a color temperature scale.

evolved M giants, their respective red-band colors are the same. This makes it difficult to discriminate between the two luminosity classes when using only a red color constraint. Giant stars, however, have atmospheres that have greatly expanded since their main-sequence equilibrium state, and thus, possess a much lower surface gravity than that of dwarf stars. As a result, the atmospheric pressure of the two luminosity classes are quite different. Gas pressure in the atmosphere of a star can be written as

$$P(\tau) = \left(\frac{g}{\kappa}\right)\tau \quad , \tag{4.1}$$

where κ is the opacity, τ the optical depth and g the gravitational acceleration, given by (GM / R^2), R being the stellar radius. If we assume that the opacity is similar in both dwarf and giant stars[2], and that spectral lines begin to form at $\tau = 1$, then the dwarf to giant atmospheric pressure ratio is simply,

$$\left(\frac{M_{dwarf}}{M_{giant}}\right)\left(\frac{R_{giant}}{R_{dwarf}}\right)^2 \quad . \tag{4.2}$$

For example, an M5 V star has a mass ~ 0.2 $M_\odot$ and a radius ~ 0.3 $R_\odot$, while a class III M5 star has a mass ~ 10 $M_\odot$ and a radius ~ 50 $R_\odot$, so that the resulting atmospheric pressure ratio is ~ 560. The 3 orders of magnitude in pressure difference between these two classes of stars manifests itself in differences in both the depth and width of the absorption lines in the spectra of these stars. There are several atomic and molecular species in the visual, red and near-infrared wavebands sensitive to atmospheric pressure

[2] In reality, the opacity is greater in dwarf atmospheres compared to giant star atmospheres with the same surface temperature because of the greater number *density* of atoms and electrons. However, if the effective temperature of a giant star is slightly lower than the temperature of a dwarf star of identical spectral type, this opacity difference is minimized. For this reason the color temperatures, between stars of equivalent spectral type but differing luminosity class, are slightly different.

which can be used to discern between giants and dwarfs, as well as between subtypes at the late end (*i.e.*, low mass) of the M dwarf sequence.

Finally, the dynamics of old-disk M dwarfs set them apart from their younger main-sequence and giant counterparts (Wielen 1974; Reid 1987). Proper motion surveys exploit this property of red dwarfs, although, this introduces a kinematic bias toward stars with the greatest tangential velocities, including high velocity subdwarf stars of the Galactic halo or spheroid. However, since photometric surveys do not suffer this kinematic bias, the chance of detecting a subdwarf using photometric techniques is small because of their extreme rarity; the surface density of stars belonging to the Galactic spheroid is roughly three orders of magnitude smaller than the surface density of disk stars (*cf.* Bahcall and Soneira 1980). For our purposes we may thus ignore the contribution of the subdwarf population to the total population located within the Solar vicinity. The remainder of this section considers only disk M dwarfs. The space motions of subdwarfs are further discussed in Chapter 5.

Both visual and red broad-band filters are sensitive to differences in surface temperature between subclasses of M dwarfs. Bessell (1986, 1990, 1991) has done extensive photometry of late-type M dwarfs using Cousins V, R and I filters. In Table 4.1 we list several observational parameters of M dwarfs including colors, effective temperatures, I-band bolometric corrections and the wavelength at which the peak flux occurs (Wien's Law). This table is adapted from Table 2 in Bessell (1991). In Figure 4.1, we plot (V-R) *versus* (R-I) for the M dwarf sequence.

Table 4.1

Observational Parameters of the Old Disk M Dwarfs (adapted from Bessell 1991)

Type	$V-R_c$	$R-I_c$	V-K	BC_I	M_V	T_{eff}	λ_{max}(Å)	$M/M_\odot$
M0	0.89	0.91	3.65	0.59	8.86	3800	7630	0.5
M1	0.95	1.02	3.87	0.57	9.41	3650	7940	0.5
M2	1.00	1.16	4.11	0.55	10.16	3500	8280	0.4
M3	1.10	1.37	4.65	0.44	11.18	3350	8650	0.3
M4	1.23	1.63	5.28	0.30	12.71	3150	9200	0.2
M5	1.48	1.91	6.17	0.05	14.69	3000	9660	0.2
M5.5	1.69	2.06	6.71	-0.08	15.75	2900	9990	0.2
M6	1.91	2.22	7.37	-0.30	16.63	2800	10350	0.1
M6.5[a]	2.12	2.38	8.10	-0.60	17.70	2700	10730	0.1
M7.5[b]	2.10	2.30	8.45	-1.00	18.78	2600	11500	0.1
>M8[c]	2.1?	2.2?	9.1?	-1.50	19.6?	<2450	>11830	<0.1

[a] Based on the properties of VB 8 (Dahn *et al.* 1986).
[b] Based on the properties of VB 10 (Dahn *et al.* 1986).
[a] Based on the properties LHS 2924 (Probst and Liebert 1983).

As one can see from Figure 4.1, the (V-R) and (R-I) colors adequately delineate the M dwarf temperature sequence up to M5.5 - M6. The colors break down for the very late-type dwarfs, M6.5 and M7. Even with the I filter, most of the flux of these stars resides in the near-infrared (note λ_{max} in Table 4.1); consequently, (R-I) is much less sensitive to the surface temperature of very low mass dwarfs. In addition to these continuum properties, molecular line blanketing becomes severe at red wavebands for late-type M dwarfs. This effect is illustrated in Figure 4.2 (taken from Bessell 1986) where the red-band spectrum of an M7 dwarf is plotted with R and I Cousins and CCD passbands superimposed on the spectrum. The star's continuum flux peaks near ~1.2μm, while the Cousins I band response extends to only to ~0.9μm. Several molecular TiO features can be seen at 7100, 7600,

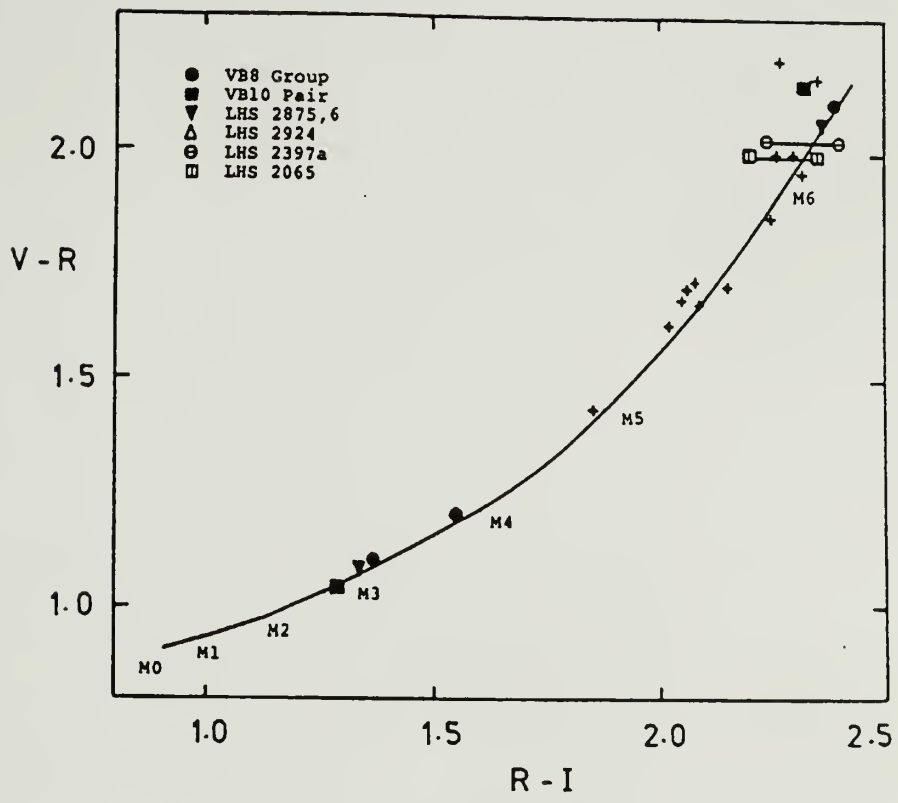

Figure 4.1 The $V\text{-}R_c$ *versus* $R\text{-}I_c$ color relation for M dwarfs. Subclasses M1 - M6 are indicated. The symbols represent known nearby late-type M dwarfs. This figure is taken from Bessell (1991).

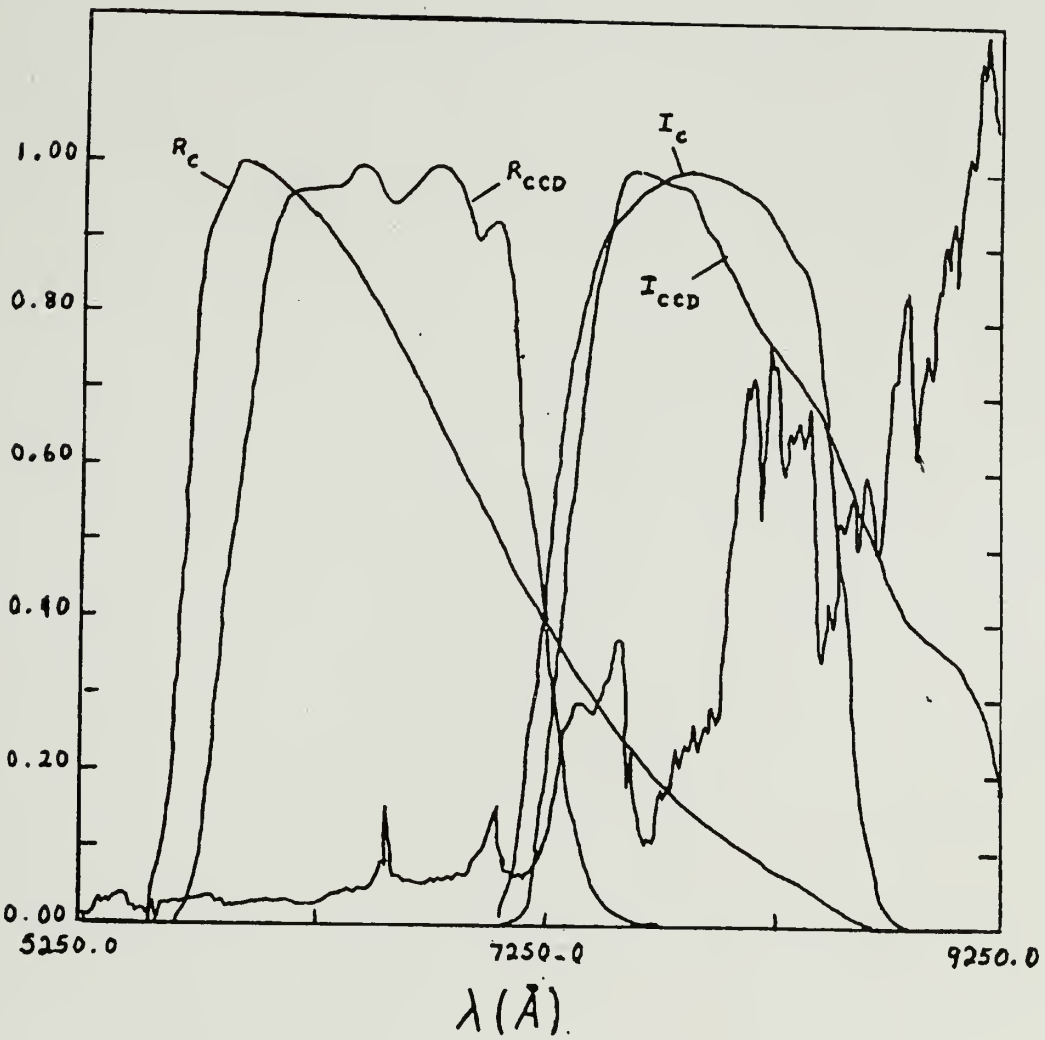

Figure 4.2 Red-band spectrum of an M7 dwarf star overlaid by the R and I bandpasses from the Cousins (1976) and Kitt Peak Harris CCD filters.

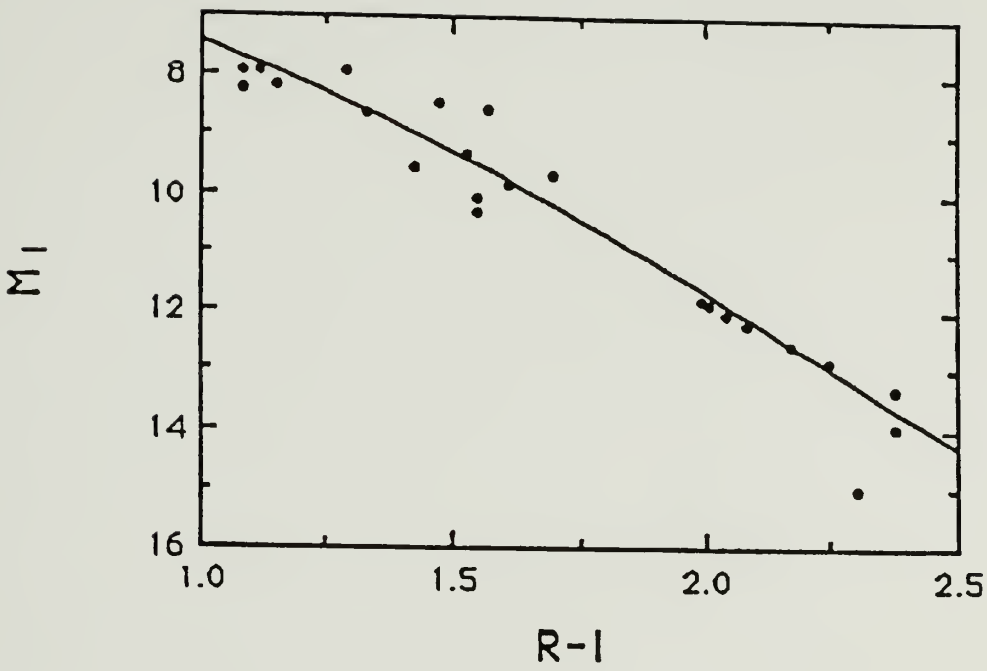

Figure 4.3 The M_I *versus* R-I_c color-magnitude relation for M dwarfs. This figure is taken from Bessell (1991).

8200, 8500 and 8900 Å. Several surface gravity features are visible in this spectrum, including CaOH at 5570 and 6250 Å, CaH at 6400 and 6800 Å, K I at 7700 Å and Na I at 8200 Å. Molecular VO bands are also present for the latest type M dwarfs. The latest spectral types also exhibit (not shown in figure) FeH at 9900-10100 Å. These surface gravity features and others are further addressed in Chapter 6.

Bessell (1991) points out that optical/near-infrared color (I-K) is a superior indicator of temperature for the latest M dwarfs (*i.e.*, M6, M7, M8, *etc*). However, of a more practical concern, optical photometry using large format CCDs is still more convenient than near-infrared photometry, given the current state of infrared semi-conductor detectors. Moreover, complete and deep K-band surveys are very difficult to achieve with angular coverage required for this kind of study (though it is feasible to conduct K-band photometry of a few dozen interesting candidates).

As a result of these features, it will unfortunately be impossible to separate the latest M dwarf candidates based on only their V, R and I colors. Nevertheless, most other K and M dwarfs can be classified based on their optical colors, and very late-type dwarfs will in any case have colors that are indicative of a spectral type at least as late as M5. At a future time supplemental infrared photometry can be carried out on stars with promising optical colors, with the goal of determining their spectral type more precisely.

The effective stellar temperature as a function of color (R-I), as determined by Bessell (1991), is

$$T_{eff} = 5990 - 3760(R-I) + 1790(R-I)^2 - 335(R-I)^3 \quad , \qquad 0.8 < (R-I) < 2.1 \quad , \tag{4.3}$$

where (R-I) is in the Cousins photometric system. Since most of the flux radiated by M dwarfs is in the near-infrared, a more useful measure of the absolute magnitude is given by

M_K, or, more generally, by the bolometric magnitude, m_{bol} (Reid 1987). Bessell (1991) provides a correction term that converts M_I to m_{bol} as follows

$$m_{bol} = M_I + BC_I ,$$
$$BC_I = 0.70 - 0.21(R-I) + 0.24(R-I)^2 - 0.16(R-I)^3 , \qquad (4.4)$$
$$0.8 < (R-I) < 2.1$$

Bolometric correction values for M dwarfs are shown in Table 4.1. Finally, the color-magnitude relation, M_I *vs.* (R-I), constructed by Bessell (1991) using photometry from nearby M stars identified from parallax surveys, is reproduced in Figure 4.3. This relation is particularly useful when only (R-I) color is available.

4.2 Opaque Screen Method

When undertaking the spectrophotometry of field stars, one is faced with the problem of separating nearby M dwarf stars from distant late-type evolved stars. As discussed in the last section, stars of similar temperature yet vastly different mass and luminosity, can exhibit spectra and colors that are difficult to distinguish. One solution to this problem is to direct the survey toward nearby dense molecular clouds. These clouds serve three distinct observational purposes: 1) to block the vast majority of stars located behind the cloud from view, 2) to heavily redden the colors of stars that are bright enough to "leak" through the intervening dust of the cloud, and 3) to isolate a foreground population of stars within a discrete volume defined by the solid angle and distance of the cloud.

We may demonstrate the opaque screen method using the ρ Ophiuchi extinction map presented in Chapter 3, (Figure 3.2), and the Galactic stellar distribution model described in Appendix F. The stellar distribution model predicts the surface density of stars for a given direction in the Galaxy, giving the expected total number of stars per spectral

type located within a given solid angle, as a function of limiting magnitude. We have assumed a local stellar number density based on previous determinations of the luminosity function (*e.g.*, Wielen *et al.* 1983). Information contained within a single simulation includes population type (type I: disk, and type II: spheroid or halo), spectral type, luminosity class (main sequence dwarf and evolved giants), apparent magnitudes, colors and locations. In this demonstration we would like to model the surface density of stars that are situated along the line of sight toward the Ophiuchus molecular cloud.

First consider the case in which the cloud does not interfere with the light from distant stars in the Galaxy. The predicted number of stars brighter than the CCD V-band limit, ~ 22, located in a volume constrained by the angular size of the Ophiuchi field, ~28 arc min, extending several kpc from the Sun in the direction of Ophiuchus (l = 353°, b = 17°), would be about 4000. A histogram showing the distribution of absolute magnitude, M_v, for these stars is displayed in Figure 4.4a. It is interesting to note that while M dwarfs are the most common stars in the Milky Way, most of the field stars shown in the histogram are G and K dwarfs. This effect is a reflection of a luminosity and volume bias: both the relative brightness of G and K dwarfs compared to the cooler M dwarfs, and the solid angle effect — volume increases as the distance cubed — causes more distant and less common stars to dominate the total number of stars located within the observer's solid angle.

Evolved giants, though extraordinarily luminous, are nevertheless very rare and thus greatly outnumbered by common dwarf stars; from Figure 4.4a it is evident that the apparent dwarf to giant number ratio is ~50:1. However, an important feature to note from the histogram is that late M dwarfs ($M_v > 12$) are predicted to be present in about the same numbers as evolved giant stars. Given that M giants have roughly the same colors as their

dwarf counterparts, it is clear that in the absence of a molecular cloud, it would be difficult to separate the two classes of stars based on photometric constraints alone.

Now consider the case in which the molecular cloud acts as an opaque screen to stars located behind the cloud. Here we make use of the extinction map of the center of the L1689 region of the ρ Ophiuchi molecular cloud described in the previous chapter. We adopt a distance of 160 pc to the ρ Ophiuchi cloud (Elias 1978; de Geus 1988). The visual extinction of a star located behind the cloud, distance d from the Sun, is given by:

$$A_V(d) = A_V^{cloud} + A_V^{\star}(d) \ , \quad d \geq 160\,pc \tag{4.5}$$

where the last term is the general extinction due to dust in the Galactic disk and is derived from Equation F.8 (see Appendix F). The visual extinction of the core of the L1689 cloud varies from 3 to at least 21 magnitudes, with an average of ~ 8 - 10 mag. At this level, most background stars will be blocked from view, while the remaining stars that manage to "leak" through the cloud will be heavily reddened.

The results of the model simulation can be seen in the histogram Figure 4.4b. The total number of stars brighter than the CCD limiting magnitude is now ~200. Evidently, about 95% of all the field stars in this direction are screened by the gas and dust of the molecular cloud. The cloud also directly affects the shape of the observed stellar distribution. The histogram of reddened field stars is now dominated by F and G dwarfs. In addition, luminous giant stars are dramatically elevated with respect to the dwarfs; evolved stars, in this case, account for about 25% of the total number of stars that have apparent (reddened) magnitudes brighter than the CCD limit. In effect, the cloud acts as a bias toward distant, luminous stars. Finally, and most importantly, the cloud isolates the unreddened population of stars located in front of the cloud. From Figure 4.4b it can be seen that there are very few K and early type M dwarfs, while the few late M dwarfs with $M_v > 12$ are distinctly separated from the luminous background field star population.

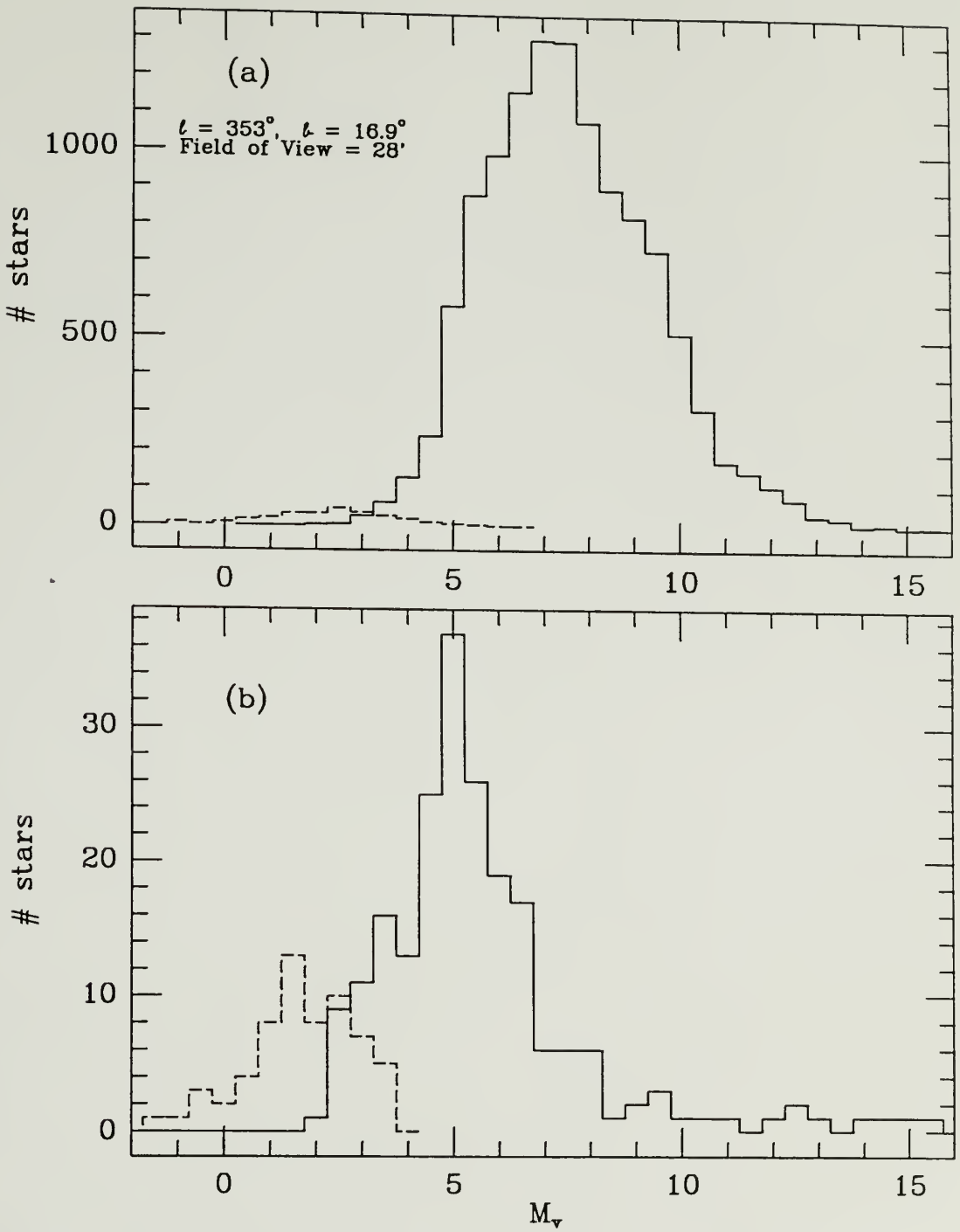

Figure 4.4 Absolute magnitude histogram of the stars located within a solid angle of angular width 28′, in the direction of the ρ Ophiuchi molecular cloud (ℓ = 353°, b = 16.9°). In case (a), $A_V^{cloud} = 0$ is assumed, *i.e.*, there is no obscuration due to the cloud; in case (b), the cloud, located at a distance of 160 pc, functions as a dark screen. The visual extinction of the cloud is taken from Figure 3.2. The solid line represents dwarf stars, and the dashed line evolved giant stars.

These stars will have little or no reddening, which should be reflected in their red band colors. Later in the following section, we will again employ the simulation described above, in order to illustrate the effects of color reddening, and we will ultimately compare the model results with the real CCD data.

In order to adequately constrain the luminosity function for late-type M dwarfs using photometric surveys, it is of critical importance for the survey to be *complete* in luminosity. Both the cloud distance and observational limiting magnitudes determine the degree of completeness of the survey, as follows. The latest M dwarf stars are believed to have masses extending down to the minimum limit at which hydrogen fusion burning is sustained by gravitational pressure, $M \sim 0.08\ M_{\odot}$ (Liebert and Probst 1987). Their corresponding absolute magnitudes at V and I are believed to be ~19.6 and 15 (*e.g.*, LHS 2924; see Probst and Liebert 1983), respectively. We can predict the apparent magnitude (via the distance modulus) these stars would have if they were located at the maximum distance within the survey volume (*i.e.*, at the distance to the cloud). In Figure 4.5 a plot of V and I apparent limiting magnitude as a function of cloud distance is shown. One can see that with a modest sized telescope and CCD detector system, the astronomer will be hard pressed to achieve the V-band limiting magnitude for cloud distances much beyond ~150 pc. The scenario is considerably better at I-band, given that M dwarfs radiate much of their energy in this wavelength range. In either case, cloud distances beyond 350 pc require limiting magnitudes that are untenable to achieve.

Of equal concern, we want to observe clouds at the greatest distance possible in order to maximize the survey volume. A cone of radius r and height d, has a volume given by $(1/3)\pi r^2 d$. If d is the distance to the cloud and α is the field of view angle, then the

survey volume is simply

$$V(\alpha, d) = \frac{\pi}{12}\alpha^2 d^3 \tag{4.6}$$

Even though we are severely restricted as to the choice of cloud distance, we may enlarge the volume by simply increasing α. This requires that the targeted molecular cloud have extensive, contiguous opaque sections. A visually opaque area of the cloud may, however, be unsuitable for the purposes of this study if it is also the site of vigorous star formation. This may be best ascertained at infrared wavelengths. Protostars and T-Tauri stars associated with such a region may contaminate the foreground sample in a variety of ways. Low mass young stars will have colors that are anomalous — being either blue shifted or red shifted with respect to main sequence stars (depending on the state of evolution; *cf.* Strom *et al.*, 1989) — variable, and possibly reddened depending on the amount of dust enshrouding the stars[3]. The colors, in some cases, will mimic those of very late-type M dwarfs.

Background stars will have V, R and I colors that are reddened by an amount given by the extinction of the molecular cloud (Chapter 3) and the Galactic dust distribution. In the simplest case, the reddening in a color-color plot follows a vector whose slope is given by the ratio of color excess, E(V-R)/E(R-I). Various reddening laws are shown in Table C.1 (see Appendix C). In Figure 4.6 a plot of main sequence stars and giant stars from spectral type G through M is shown in the V, R, I color-color plane. The data were obtained from Bessell (1991) and Johnson (1966), where conversion from the Johnson photometry system to that of Cousins (1980) was performed using calibrations of Fernie (1983). The colors represent typical values for each spectral class and are to be discern the

[3] There are three possible spatial components of dust associated with pre-main-sequence stars; intervening dust belonging to a circumstellar disk, the outer envelope and the general cloud environment.

relative location of the unreddened sequence. The linear reddening vector given by Schild is also shown in the figure. However, for the latest M type stars (dwarfs and giants), the reddening will not follow a simple vector, but rather a non-linear track that steepens with the degree of visual extinction (see Figures C.1 and C.2 in Appendix C). The reddening departs from a linear vector due to the way in which the stellar flux is convoluted with the cloud opacity and the broad-band filters used with the CCD. The reader is referred to Appendix C for a more detailed discussion of this phenomenon.

Once the extinction is known (determined using, for example, the method of star counts; see Chapter 3) a star plotted within the V,R,I color plane can be de-reddened onto the main-sequence or giant tracks, thereby yielding its spectral type and absolute magnitude. We may then compute the corresponding distance using the modified distance modulus, as follows:

$$m_V - M_V = 5\log D - 5 + A_V(cloud) + \left[\frac{D(pc)}{1000}\right] \qquad (4.7)$$

where the last term is due to interstellar absorption in the Galactic disk, ~ 1 mag per kpc (see Appendix F for more details). If the derived distance of a de-reddened star is too large (*i.e.*, beyond the Milky Way) or too small (*i.e.*, < cloud distance) then either the de-reddened spectral type is incorrect and/or the luminosity is erroneous. In either case, the star is flagged as having anomalous colors, and is investigated further. Stars with colors that do not appear to be reddened can be checked for self-consistency with Equation 4.7 and apparent spectral type, by setting $A_V^{cloud} = 0$.

In summary, the parameters that constrain the possible stellar spectral and luminosity type are the (V-R) and (R-I) colors, cloud extinction and distance. In the next section we describe the results of the Taurus and Ophiuchus surveys using the method presented here.

At this point, we have yet to consider one of the more integral components of this luminosity function study: the detection and classification of binary and other multiple stellar systems that are part of the total population of nearby field stars. We do expect a significant number of physical binaries in our foreground stellar sample, since, perhaps 30 - 50% of all stellar systems are multiple in nature (*cf.* Henry and McCarthy 1990). The binary stars that are located in front of the Taurus and Ophiuchus are, most likely, unresolved in our study given that most of the foreground stars lie at distances near the clouds (due to the solid angle effect) and the typical seeing for our CCD data was about 1-2″; thus, if a binary pair is, for example, separated by less than ~2″ and lies at distance of 140 pc, then the physical distance between the two stars is less than ~280 a.u., which is not an uncommon orbital separation for a low mass system. The optical colors of an unresolved binary system depend on the constituent pair. For example, two low mass stars of roughly the sample spectral type will have, as a system, a color typical of the spectral type, but will have a total brightness that exceeds the expected value of the spectral type. In contrast to this scenario, a binary system consisting of a bright star with a faint companion, for example, a G dwarf with an M dwarf companion, will have a color that is slightly redder than that of the primary itself (due to the M dwarf), but will have a total brightness that is nearly unchanged (note: the luminosity of the binary pair is minimally effected by the relatively faint M dwarf). In any case, since an unresolved binary pair will have anomalous colors (with respect to system total brightness), the pair can be discerned using the photometric techniques discussed in this section. Later, in Chapter 7, we will further consider the stellar binary problem, and in particular, the implications these systems have in our estimate of the faint end of the luminosity function.

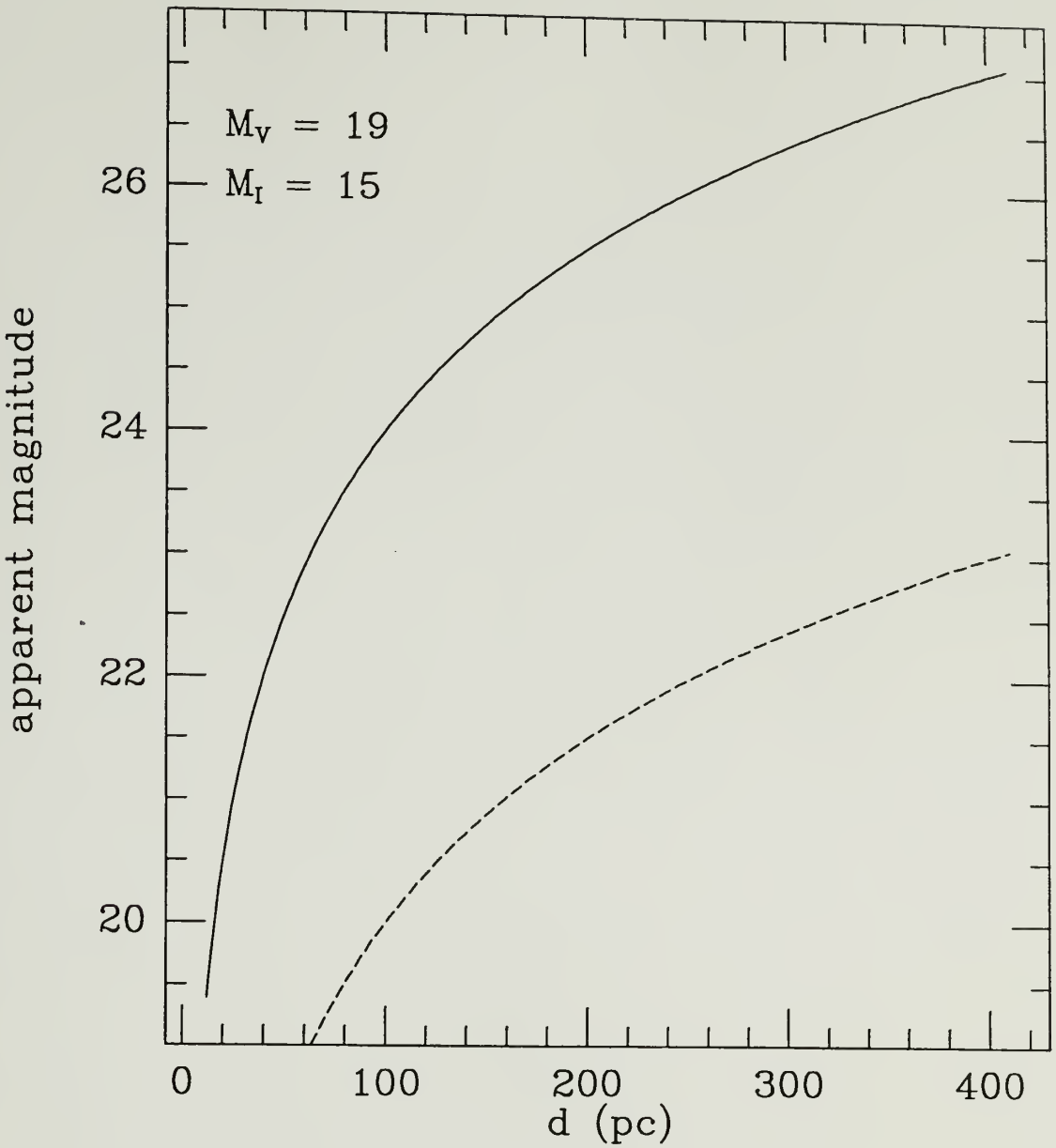

Figure 4.5 The apparent magnitude, M_λ + 5log(d) - 5, as a function of the distance. Two cases are shown: M_V = 19 (solid line) and M_I = 15 (dashed line).

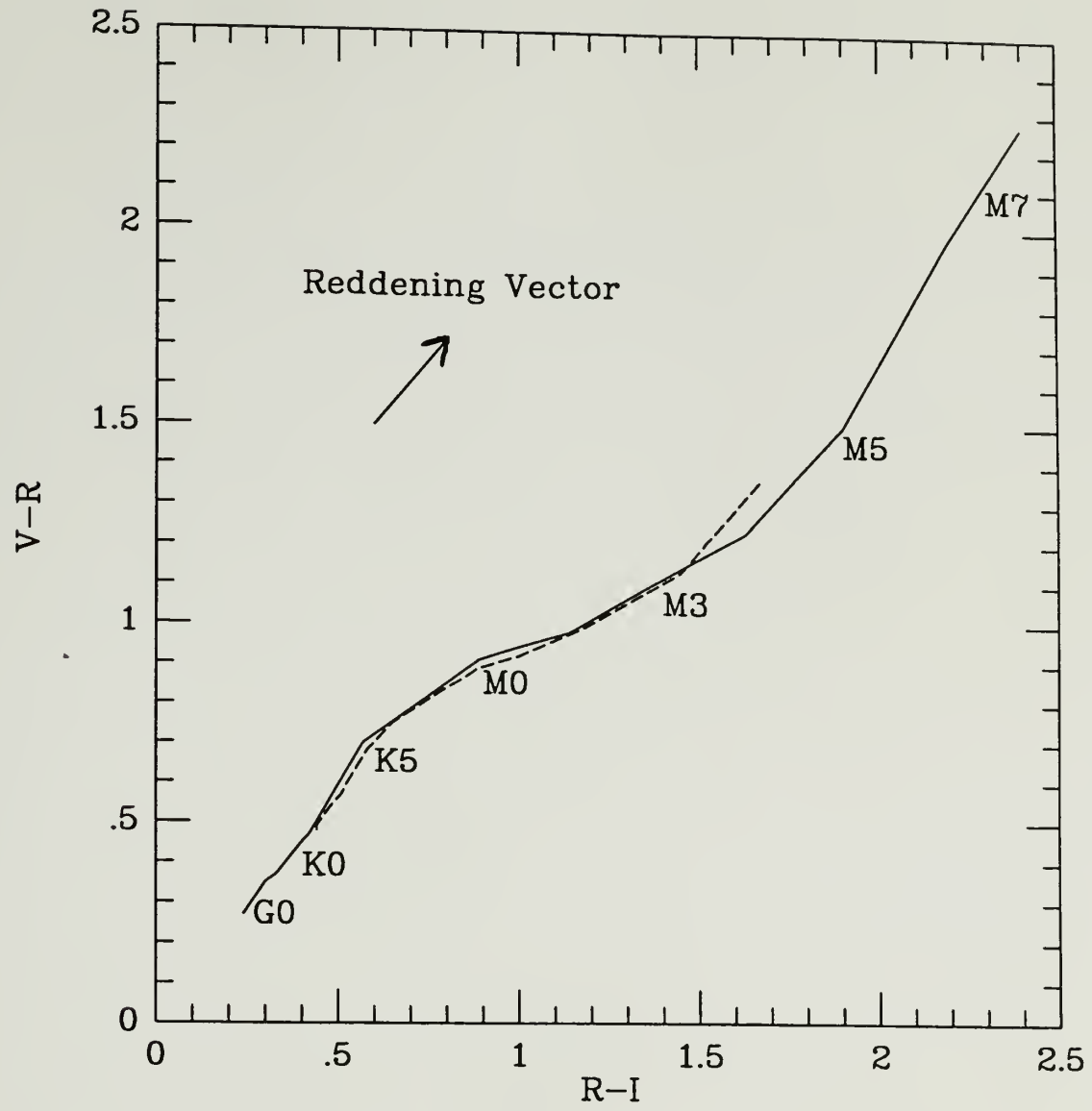

Figure 4.6 The V-R_c *versus* R-I_c color relation for G - M dwarfs (solid line) and giants (dashed line). Subclasses G0 - M7 are indicated. Also shown is the reddening vector corresponding to $A_V = 1$, given by Schild (1977), with slope 1.08.

4.3 Results

In this dissertation, we have chosen dark regions within the Taurus and Ophiuchi molecular clouds as our opaque screens. The clouds are relatively nearby, ~ 140 and 160 pc, respectively (Elias 1978), and have extensive, contiguous areas that are dark and apparently deficient in vigorous star formation[4]. Within the volume delimited by the cloud distances, the survey should be complete to $M_v \sim 16$ for Ophiuchus and $M_v \sim 17$ for Taurus. At the red wavebands, the completeness extends to the lowest mass stars capable of core hydrogen burning.

4.3.1 Ophiuchus Sample

The data obtained for the ρ Ophiuchi cloud consists of deep optical photography and CCD images. A summary of the observations are described in sections 2.1 and 2.2, Chapter 2. The limiting magnitudes for both data sets are comparable (see Tables 2.2 and 2.10). However, for the purposes of color-color analysis, the CCD data is superior to the photographic data because the limiting accuracy of the CCD photometry is about 10%, compared to an unwieldy 20-25% for the photographic photometry. The remaining analysis considers only the CCD data.

Within our one CCD field (size: 23′ × 26′) we detected ~200 stars with V, R and I magnitudes that had expected photometric errors of ~10%. Another 500 or so stars were detected only at R and I. Stars that were bright enough to saturate the CCD were discarded. The resultant range in apparent magnitude of the Ophiuchus stars was $14 < V$, $R < 22$, and $13 < I < 20.5$.

---

[4] Both the Taurus and Ophiuchus cloud complexes contain dense cores where low to intermediate star formation is occurring with a high degree of efficiency (*cf.* Myers et al. 1987; Wilking, Lada and Young 1989).

In Figure 4.7 we plot the colors of all stars detected at V, R, and I. Nearly all of the stars have colors that lie above the main-sequence and giant mean values (shown in the figure as the two tracks; the solid line denote the main-sequence; the dashed line denotes giants). The stars are scattered along the reddening curves expected for background field stars. As we demonstrated in the last section using a stellar surface density model, most of the stars in this plot are expected to be background dwarfs belonging to the G and K spectral types.

Cumulative stellar surface density curves at V, R and I, are plotted for the field in Figure 4.8. As one can see in the figure, stars at R and I stars dominate the total numbers in the sample. Moderate mass dwarf stars, spectral F, G and K, are bright enough to leak through the less opaque areas of the cloud (*i.e.*, $A_v < 10$ mag) and are relatively abundant compared to luminous, distant giants. At the shorter wavelength, visual bandwidth, evolved stars figure more prominently in the total sample of field stars. This effect can be seen in Figure 4.9 where we have plotted the expected V band cumulative stellar densities of the dwarf, giant and spheroid populations using our stellar distribution model (see section 4.2). The predicted star counts at V can be compared with those at R (Figure 4.10) and I (Figure 4.11). Our model indicates that stars with V magnitudes fainter than ~18 are most likely to be heavily reddened disk dwarfs located behind the cloud at distances < 1 kpc. Our task is to cull-out the background reddened stars and isolate a population of low mass stars lying in front of the Ophiuchi molecular cloud.

Most of the stars in Figure 4.7 are unambiguously reddened and, therefore, can be discarded from further consideration as foreground candidates. A few stars have colors that are distinctly anomalous for either reddened or unreddened main-sequence stars, in so far as they lie far below the main-sequence track, *i.e.*, their V-R index is too blue. It does not seem likely that these stars belong to the disk or giant populations, but given our

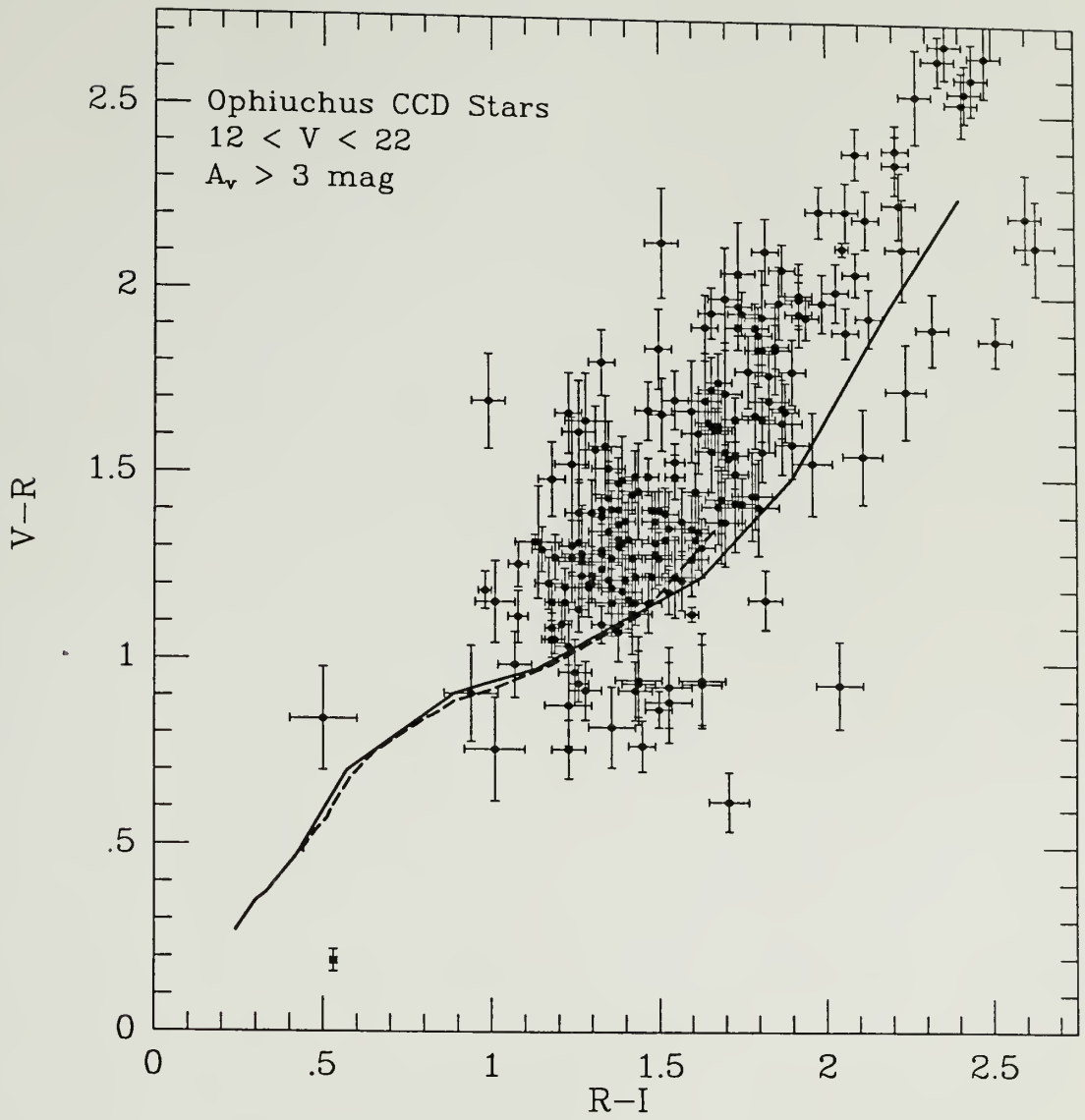

Figure 4.7 CCD photometry of the Ophiuchus sample, presented in the (V-R) *vs.* (R-I) plane. The V-band limiting magnitude is 22. Stars with visual magnitudes brighter than 12 are excluded. Color uncertainties, represented by 1σ error bars, are also shown. Stars with color uncertainties greater than 10% are excluded. All stars are located along a line of sight with at least 3 magnitudes of visual extinction. Mean colors of main-sequence G - M dwarfs are represented by a solid line, and giants by a dashed line.

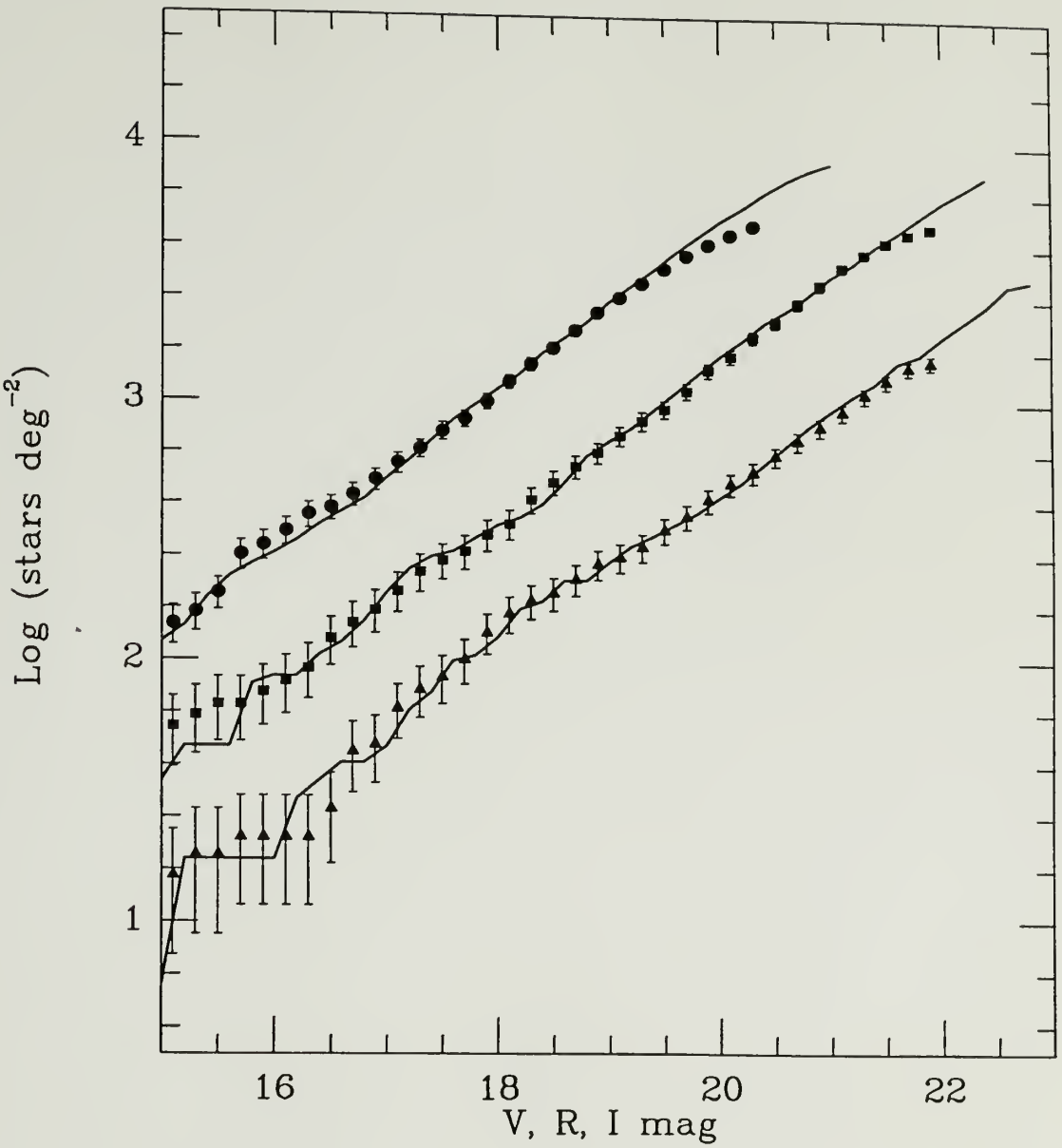

Figure 4.8 Cumulative stellar surface densities *vs.* limiting V,R,I magnitudes for the Ophiuchus CCD stars. The data are represented with the following symbols: filled triangles denote the V-band data; filled squares are the R-band; filled circles are the I-band. Expected $\sqrt{N}$ error bars are also shown. Synthetic model predictions, including contributions from disk dwarfs and giants, and spheroid stars, are represented by solid lines.

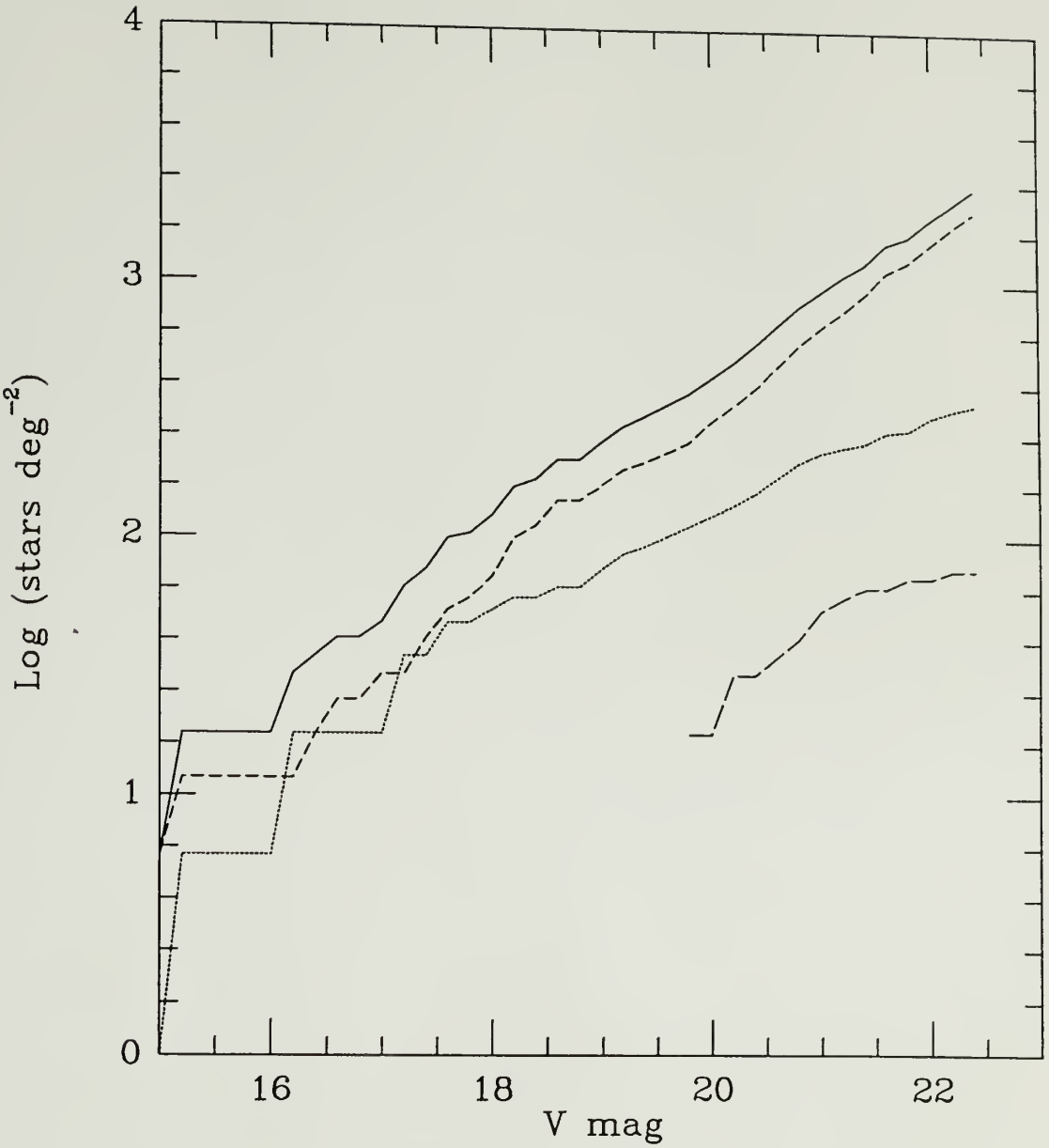

Figure 4.9 Synthetic model predictions at the visual waveband. Cumulative stellar surface densities *vs.* apparent visual magnitude for stars located behind the Ophiuchus molecular cloud. Contributions from dwarfs, giants and spheroid stars are drawn with the following line types: solid denotes the total contribution; short dashed are the disk dwarfs; dotted are the disk giants; long dashed are the spheroid stars.

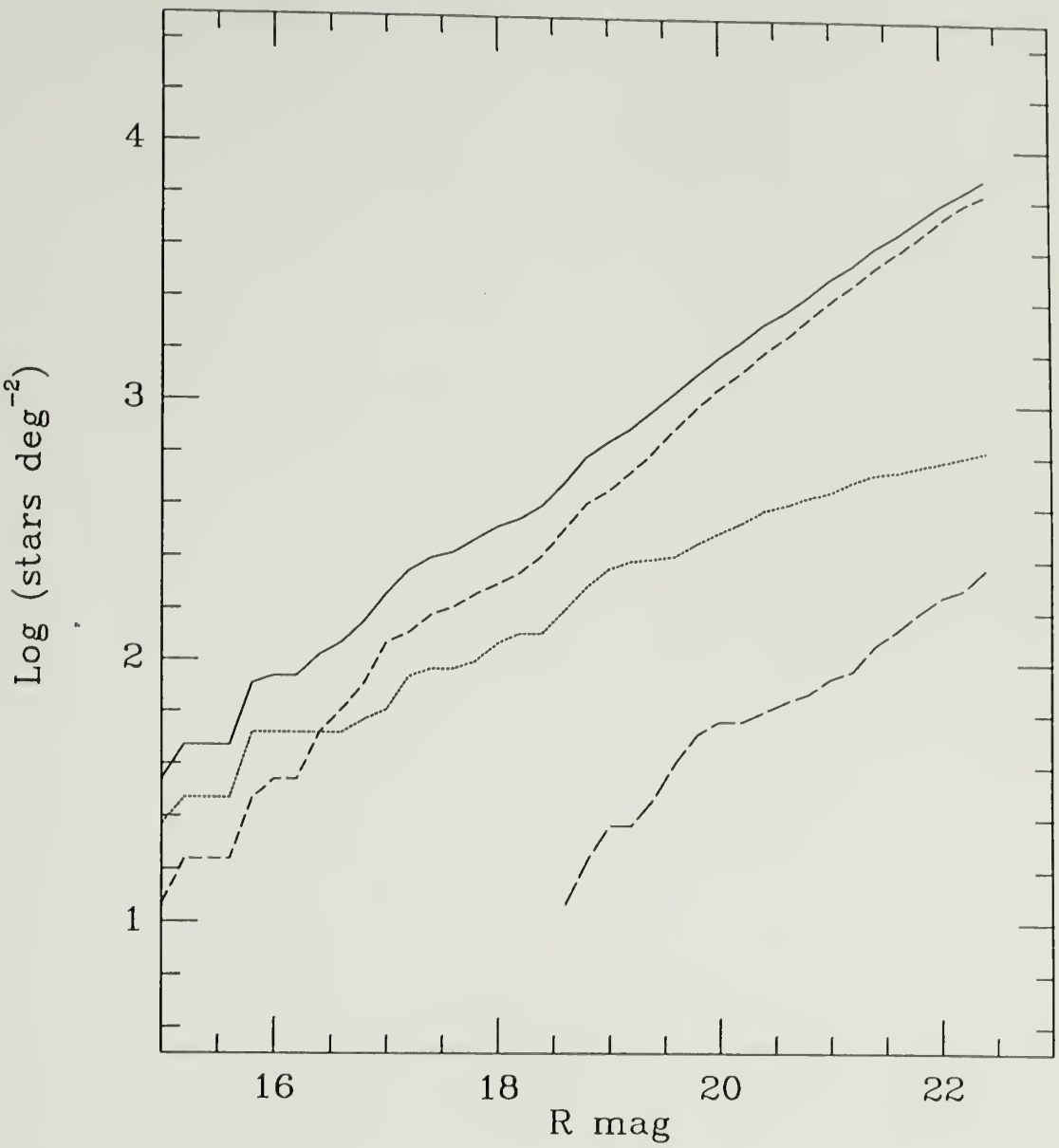

Figure 4.10 Synthetic model predictions at the red waveband. Cumulative stellar surface densities *vs.* apparent R magnitude for stars located behind the Ophiuchus molecular cloud. Contributions from dwarfs, giants and spheroid stars are drawn with the following line types: solid denotes the total contribution; short dashed are the disk dwarfs; dotted are the disk giants; long dashed are the spheroid stars.

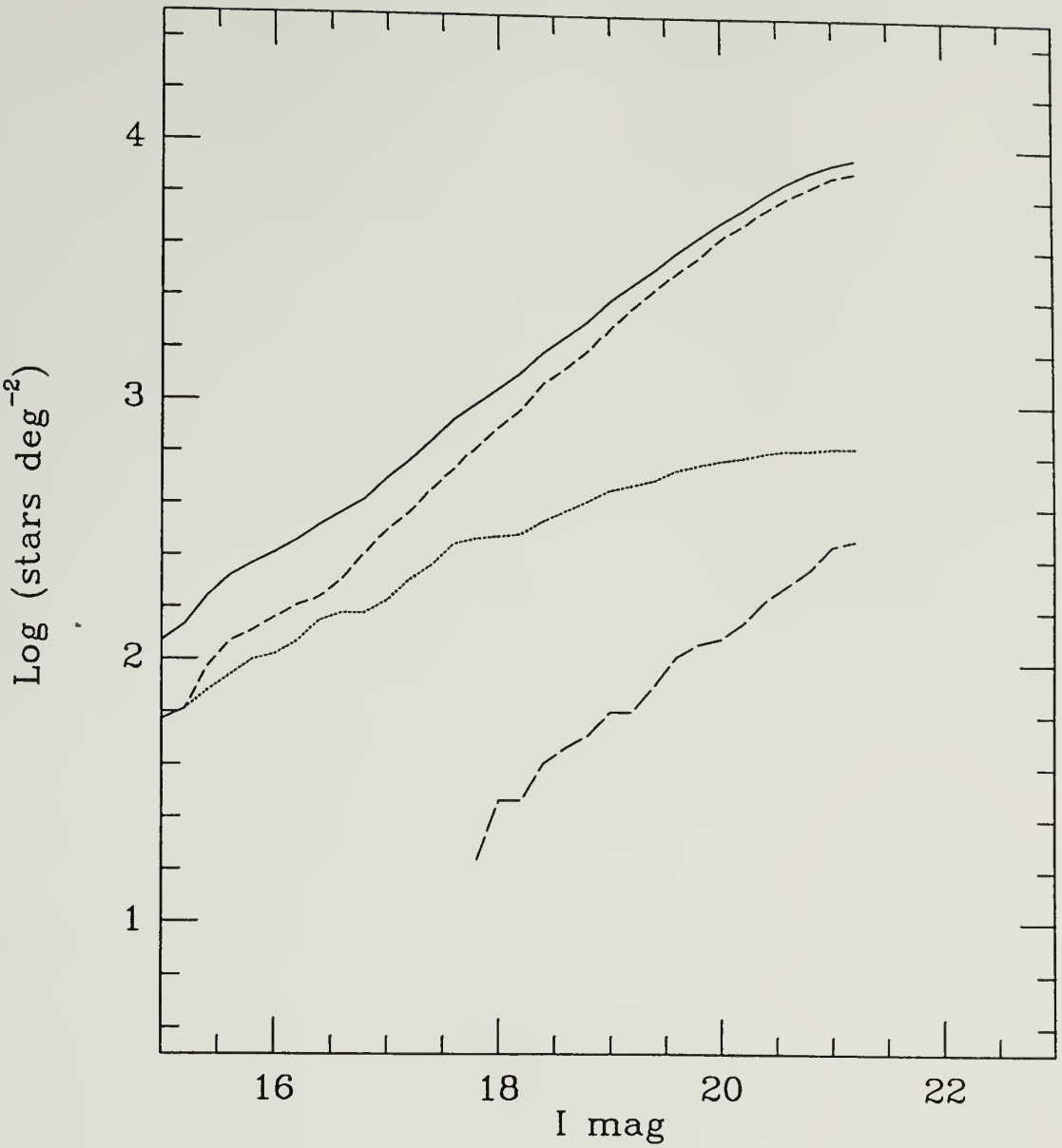

Figure 4.11 Synthetic model predictions at the far-red waveband. Cumulative stellar surface densities *vs.* apparent I magnitude for stars located behind the ρ Ophiuchi molecular cloud. Contributions from dwarfs, giants and spheroid stars are drawn with the following line types: solid denotes the total contribution; short dashed are the disk dwarfs; dotted are the disk giants; long dashed are the spheroid stars.

uncertainties regarding statistical errors (section 4.4) and the scatter about the mean color-color tracks of the main sequence and giant branches, which arises from the inherent scatter of the luminosity function, one cannot be sure without a detailed error model. Such a model is also necessary to address the extent to which a population of faint, red, foreground stars may be masked in the scatter of reddened background stars.

We thus consider the effect of random scatter in the color-color plane by, once again, employing our stellar surface density model. We consider three cases, in which we simulate the colors of the field stars leaking through the cloud with photometric scatter properties defined as follows. Case (1) assume photometric errors due solely to ordinary signal to noise criteria. Case (2) adds an additional, constant random error of 3%. Case (3) is the same as case 2, except that the excess noise is 10% instead of 3%. These additional noise fluctuations attempt to account for types of error (some of which may be systematic) which are expected to be present in the photometry and data reductions. We discuss these errors in more detail in the last section of this chapter.

In Figure 4.12 we show the results of the case (1). Here we have tried to duplicate the same observational parameters (*i.e.*, the field of view and limiting V, R and I magnitudes) constraining the actual Ophiuchus data. Only those stars with locations projected against areas with visual extinctions exceeding ~3 mag are considered. The simulated data is represented with symbols: crosses are disk dwarfs, filled squares are giants, filled triangles are spheroid or halo stars and filled circles are stars foreground to the cloud. One can see quite clearly the reddening of background stars as they scatter about a mean reddening curve. Very few (<10) background stars have colors that can be confused with those of stars located in front of the cloud. The situation becomes more complicated when we consider case (2), where an additional 3% random error has been introduced to the simulated data. Not surprisingly, the reddened stars populate a reddening curve that is

wider (due to the increased scatter) than in case (1). Some of the foreground stars appear to have colors that are too blue in (V-R) or too red in (R-I). It is interesting to note that this case appears to simulate the actual data better than case (1). Evidently the CCD data of Figure 4.7 must have an additional source of error that amounts to ~ 3%.

Finally, consider the extreme situation, case (3), where an additional 10% random error has been introduced to every star. The resultant distribution in the color-color plane, Figure 4.14, does not appear to simulate the real data (Figure 4.7) as well as case (2). However, unlike cases (1) or (2), several simulated stars (both foreground and background) now have colors that lie far below the main-sequence track, similar to the anomalous colors of a few stars in the Ophiuchus CCD data. This prompted further, more detailed inspection of these stars. It was found that many (~5%) were contaminated at one or two colors by nearby bright stars, bad (non-linear) pixels of the CCD, or transient phenomena (asteroid streaks, airplane tracks, etc). Therefore, stars in the data set Figure 4.7 whose anomalous colors were clearly due to visible contamination were discarded from further analysis. Of course, it is well known that some white dwarfs (Greenstein 1984) and protostars have V,R,I colors that are blue-shifted with respect to the average main-sequence values. For this reason, we *do* include the remaining stars in our sample with anomalous blue colors in our list of candidate foreground stars. We will attempt to unmask their true identity using the additional photometric and dynamic constraints described below.

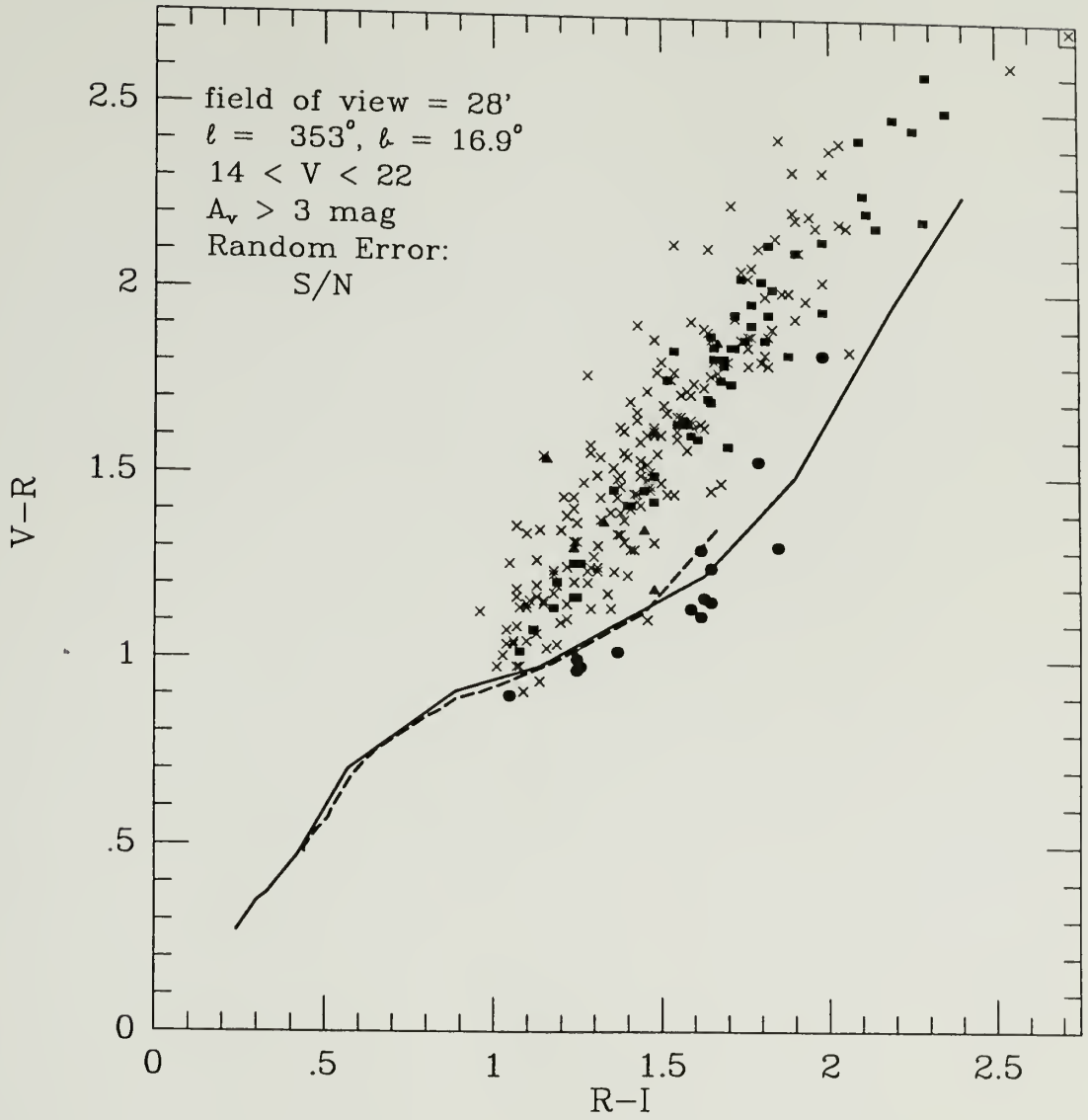

Figure 4.12 Synthetic model photometry of stars located in the direction of the ρ Ophiuchi molecular cloud, $\ell = 353°$, b = 16.9°, within a field of view of angular size 28′, presented in the (V-R) *vs.* (R-I) plane. The V-band magnitude range is from 14 to 22 mag. The extinction attributed to the cloud is taken from Figure 3.2. The scatter in the points is due to a random S/N uncertainty introduced into the synthetic colors. Point symbols represent the following stellar populations: crosses denote disk dwarfs; filled boxes denote disk giants; filled triangles denote spheroid stars; filled circles denote stars located in front of the molecular cloud. Mean colors of main-sequence G - M dwarfs are represented by a solid line, and giants by a dashed line.

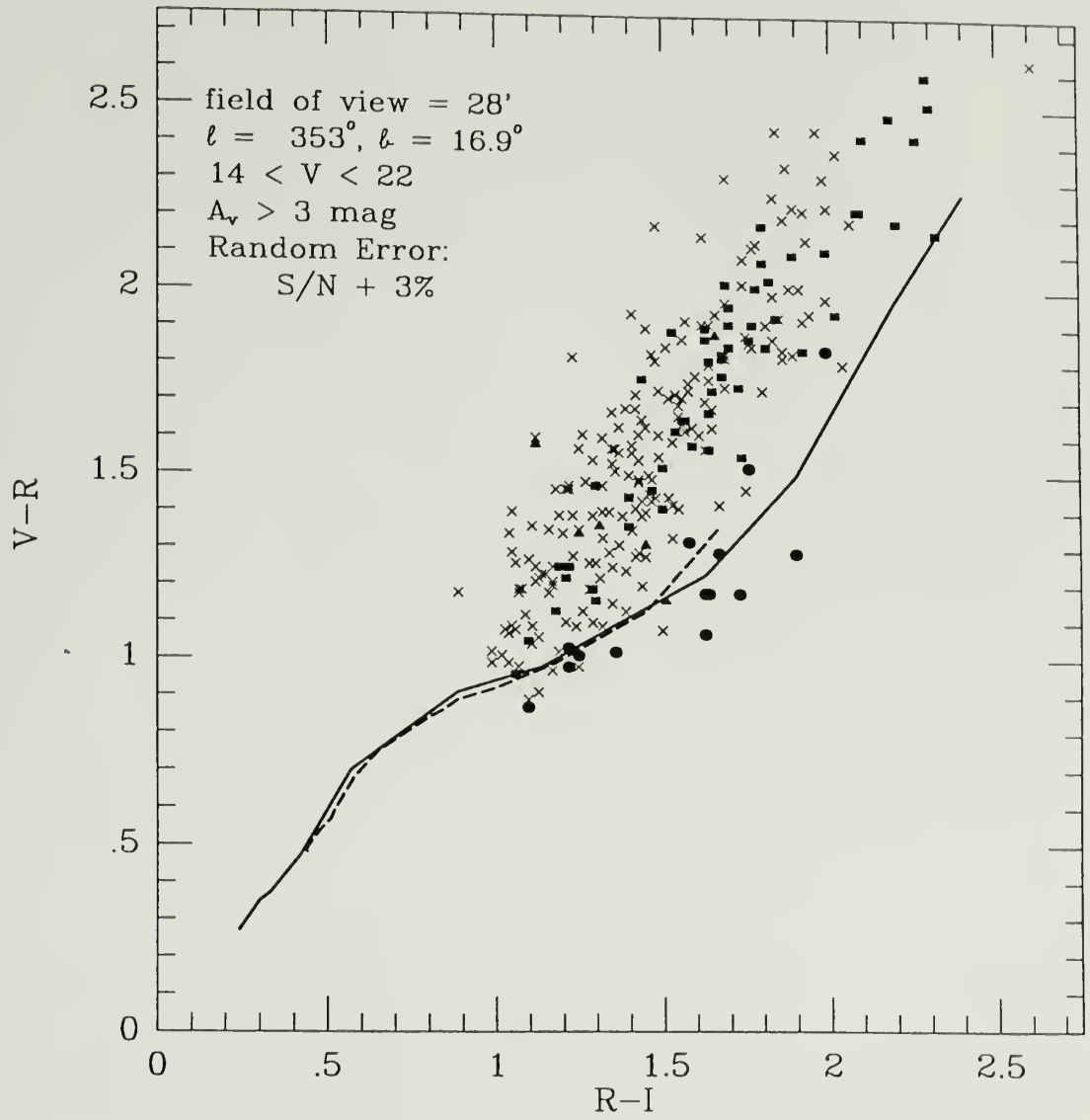

Figure 4.13 Synthetic model photometry of stars located in the direction of the ρ Ophiuchi molecular cloud, $\ell = 353°$, b = 16.9°, within a field of view of angular size 28′, presented in the (V-R) *vs.* (R-I) plane. The V-band magnitude range is from 14 to 22 mag. The extinction attributed to the cloud is taken from Figure 3.2. The scatter in the points is due to a random S/N uncertainty plus an added 3% uncertainty introduced into the synthetic colors. Point symbols represent the following stellar populations: crosses denote disk dwarfs; filled boxes denote disk giants; filled triangles denote spheroid stars; filled circles denote stars located in front of the molecular cloud. Mean colors of main-sequence G - M dwarfs are represented by a solid line, and giants by a dashed line.

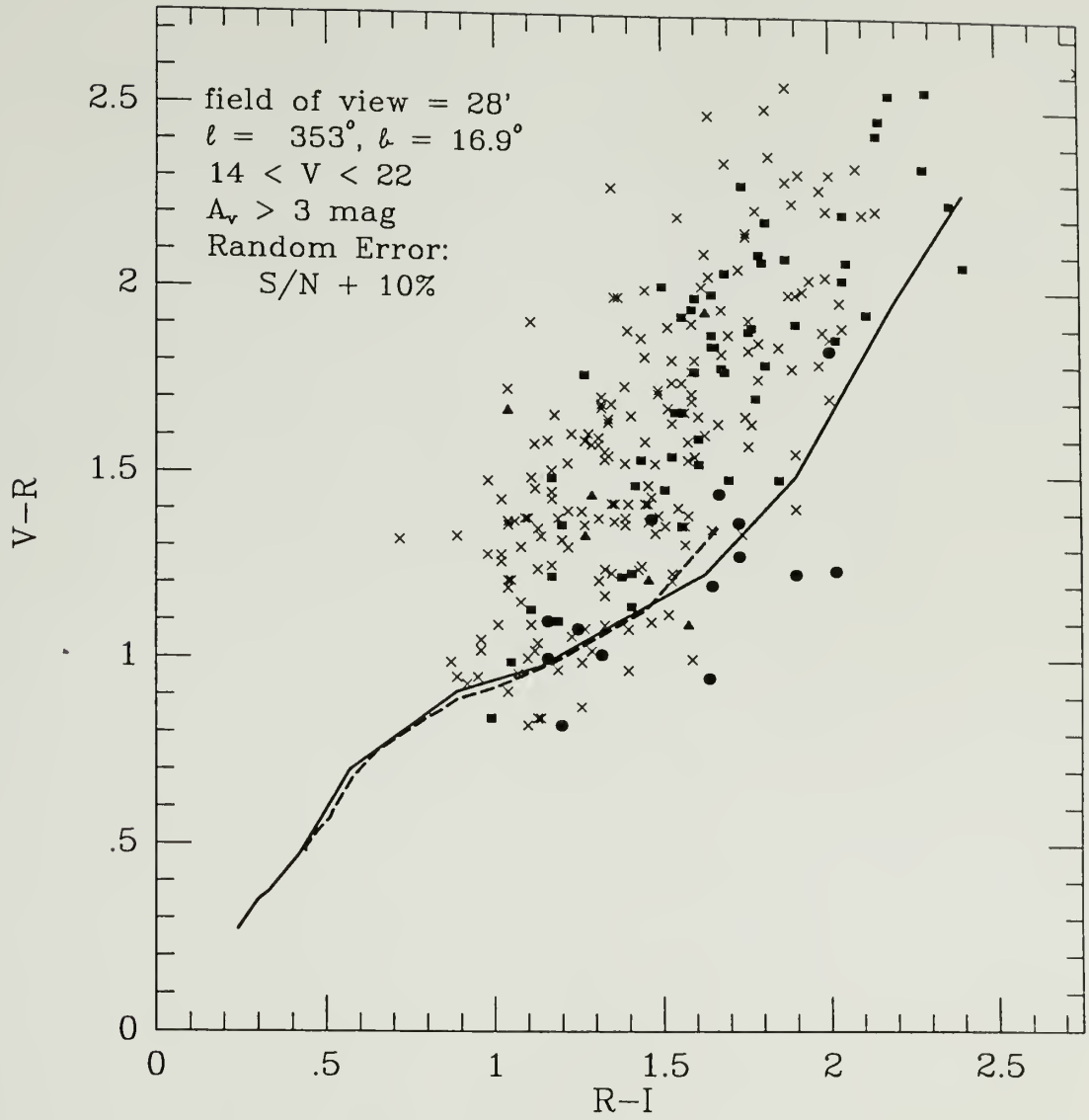

Figure 4.14 Synthetic model photometry of stars located in the direction of the ρ Ophiuchi molecular cloud, $\ell = 353°$, b = 16.9°, within a field of view of angular size 28′, presented in the (V-R) *vs.* (R-I) plane. The V-band magnitude range is from 14 to 22 mag. The extinction attributed to the cloud is taken from Figure 3.2. The scatter in the points is due to a random S/N uncertainty plus an added 10% uncertainty introduced into the synthetic colors. Point symbols represent the following stellar populations: crosses denote disk dwarfs; filled boxes denote disk giants; filled triangles denote spheroid stars; filled circles denote stars located in front of the molecular cloud. Mean colors of main-sequence G - M dwarfs are represented by a solid line, and giants by a dashed line.

In order to isolate the largest possible sample of candidate foreground stars from Figure 4.7, we assign two restrictions to their color properties. All foreground candidates must have one of the following photometric properties:

1. (V-R) colors that are blue with respect to the corresponding main sequence measure, $(V\text{-}R)_0$, or,
2. (V-R) and (R-I) colors that are within 2σ of the nearest point, $(V\text{-}R)_0$ and $(R\text{-}I)_0$, on the main-sequence track.

Where σ refers to the estimated photometric accuracy based on signal to noise and calibration measures. We feel a 2σ deviation toward the reddening side of the main-sequence track is sufficiently conservative for our purposes. Stars with colors deviating further than this value will lie clearly within the zone of reddening or will have unphysical colors.

In Figure 4.15 we plot the sample of stars with colors satisfying one of the two constraints listed above. From this group we next attempt to isolate those with colors and apparent magnitudes consistent with stars foreground to the L1689 portion of the ρ Ophiuchi molecular cloud.

Our consistency test uses the distances to the stars as the dependent variable and the corresponding absolute I-band magnitudes as the independent variable. Rewriting Equation 4.7 and setting $A_V(\text{cloud}) = 0$ (since the candidate stars are presumed to be located in front of the cloud) gives

$$D(pc) = 10^{(m_I - M_I + 5)/5} \tag{4.8}$$

The absolute magnitude is determined from the colors in Figure 4.15, that is, by assigning the most likely spectral type based on the observed (V-R) and (R-I) colors. The least biased approach to do so is to simply determine the nearest point on the main-sequence track in the color-color plane. For each star there is actually an associated error ellipse,

defined by the center and the four extrema:

$$\begin{aligned} (V-R)_0, (R-I)_0 &\rightarrow (V-R), (R-I) \\ (V-R)_0^{\pm} &\rightarrow (V-R) \pm \Delta(V-R) \\ (R-I)_0^{\pm} &\rightarrow (R-I) \pm \Delta(R-I) \end{aligned} \qquad (4.9)$$

where Δ(V-R) and Δ(R-I) are the expected color uncertainties. From these five points, three will determine the range of spectral type or absolute magnitude. We can assign a spectral type or absolute magnitude using the (R-I) color determined from Equation 4.9 and the M_I *vs.* (R-I) relation, Figure 4.3. As a matter of convenience, we fit a linear function to the color-magnitude plot, with the resulting solution:

$$M_I = 2.176 + 4.787(R-I), \qquad (R-I) > 1.75 \qquad (4.10)$$

If (R-I) < 1.7, we then use a look-up table from the mean values in Table F.1 (see Appendix F). If the derived distance is greater than the cloud distance, 160 pc, then the colors and apparent magnitudes are not consistent with a star foreground to the cloud, and thus, the star is removed from further analysis.

The results of this analysis are shown in Figure 4.16, where we have plotted only those stars with foreground solutions; that is to say, only those stars of the CCD sample CCD whose colors, apparent magnitudes and deduced spectral types are consistent with stars located in front of the Ophiuchus molecular cloud. A list of their photometric properties and deduced spectral types is shown in Table 4.2. The range in absolute magnitude is represented by M_I^0, M_I^+, M_I^-, where $M_I^- < M_I^0 < M_I^+$, and the corresponding range in distance (determined from Equation 4.8) is $d^- < d^0 < d^+$. A few of the candidates, particularly those with (V-R) > 2.5, may very well be reddened background stars. If they are indeed foreground stars, they would be very late M dwarfs, spectral type > M7, or even possibly brown dwarfs located in the immediate solar vicinity, d < 30 pc. Stars located this close to the Sun should have an easily measured proper motion. We will return to this

question in Chapter 5. One star, #113, is an obvious white dwarf candidate. It is relatively bright, V = 17.29 ± 0.03, and has colors that are too blue to be a main-sequence star. Both of these unusual properties are indicative of small, hot degenerate stars (Greenstein 1984).

Table 4.2

Ophiuchus Photometric Foreground Candidates

ID#	V	V-R	R-I	M_I^-	M_I^0	M_I^+	d^-(pc)	d^0(pc)	d^+(pc)
13	19.94	1.90 ± 0.07	2.06 ± 0.04	12.2	12.5	12.7	46	51	57
18	20.77	1.57 ± 0.08	1.88 ± 0.04	11.0	11.3	11.5	151	169	189
19	21.23	1.59 ± 0.09	1.90 ± 0.05	11.3	11.5	11.8	159	178	198
23	20.88	2.53 ± 0.09	2.41 ± 0.05	13.9	14.1	14.4	23	23	26
26	20.77	1.68 ± 0.08	1.88 ± 0.04	11.5	11.8	11.8	125	125	139
28	21.23	2.14 ± 0.13	2.63 ± 0.06	13.0	13.2	13.7	78	48	54
33	21.39	2.66 ± 0.11	2.48 ± 0.05	14.1	14.1	14.4	24	24	26
33	21.25	2.66 ± 0.11	2.44 ± 0.05	13.9	14.1	14.4	24	24	24
37	20.76	1.69 ± 0.08	1.87 ± 0.04	11.5	11.8	11.8	124	124	139
42*	21.60	2.22 ± 0.12	2.60 ± 0.05	13.0	13.7	13.9	38	48	48
33	17.45	1.33 ± 0.05	1.61 ± 0.03	9.8	10.1	10.1	78	78	87
48	20.88	1.94 ± 0.08	2.13 ± 0.04	12.5	12.7	13.0	66	66	74
59	20.50	2.56 ± 0.08	2.42 ± 0.05	13.9	14.1	14.4	19	19	21
76	21.81	1.74 ± 0.13	2.24 ± 0.06	12.2	12.5	12.7	107	119	133
76	19.09	1.55 ± 0.05	1.71 ± 0.03	10.8	10.8	11.0	91	102	102
80	21.81	2.13 ± 0.14	2.23 ± 0.05	13.9	13.2	14.4	66	78	81
113	17.29	0.19 ± 0.03	0.53 ± 0.02	?	?	?	?	?	?
183	19.01	1.88 ± 0.07	2.51 ± 0.05	13.0	13.0	13.2	20	22	22
223	21.53	1.91 ± 0.10	2.32 ± 0.05	12.7	13.0	13.0	75	75	84
908	16.60	1.13 ± 0.02	1.60 ± 0.02	9.4	9.6	9.8	64	73	80
909	11.99	0.62 ± 0.02	0.54 ± 0.02	6.0	6.1	6.1	80	87	87

* Optical binary; Faint I band companion separated by ~9″ from the primary star.

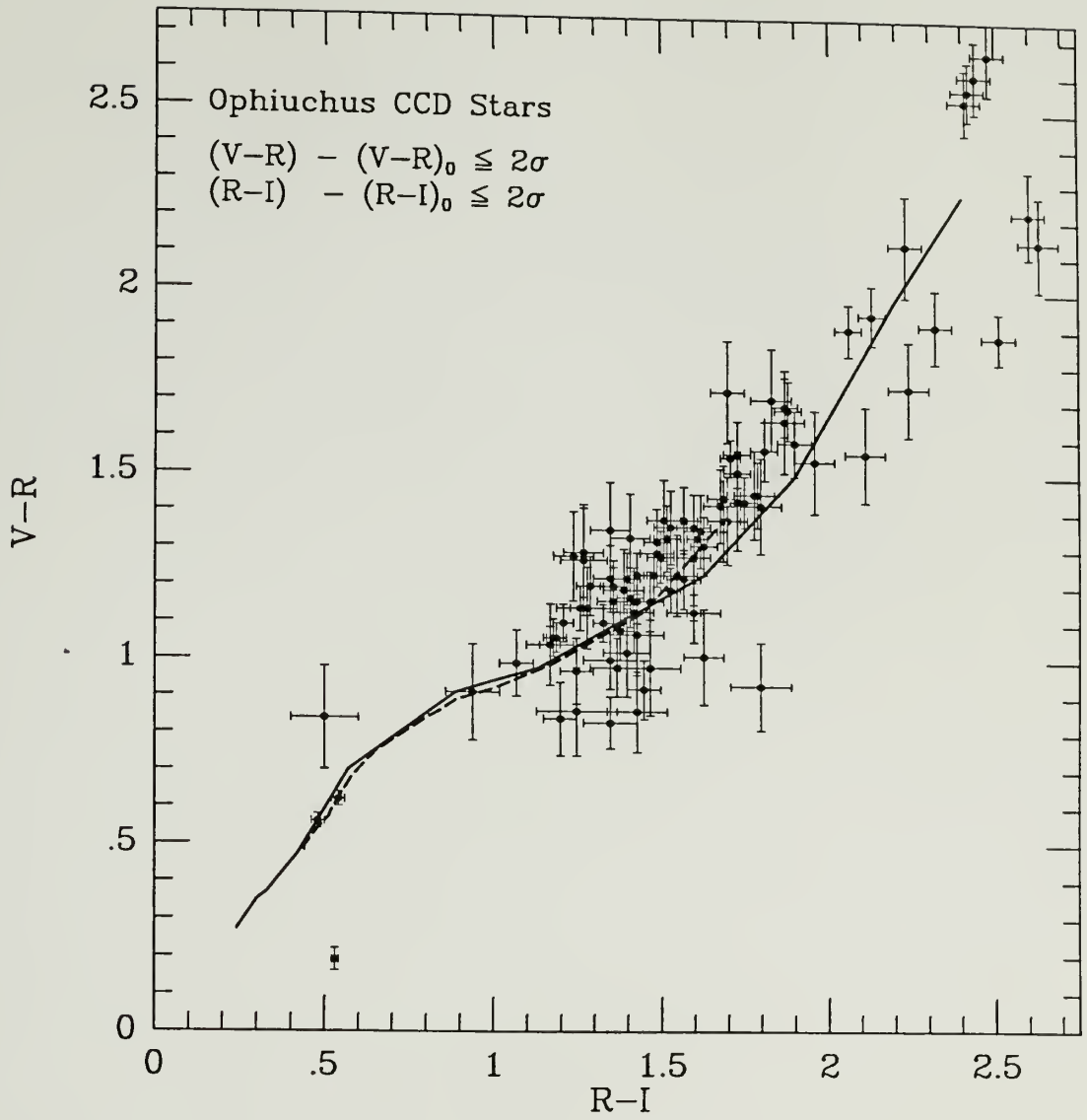

Figure 4.15 CCD photometry of the Ophiuchus candidate foreground stars presented in the (V-R) *vs.* (R-I) plane. These stars have colors that either lie below the mean tracks (mean colors of main-sequence G - M dwarfs are represented by the solid line, and giants by the dashed line), or lie within 2σ of the nearest point on the main-sequence track. The photometric properties are described in Figure 4.7. Color uncertainties, represented by 1σ error bars, are also shown.

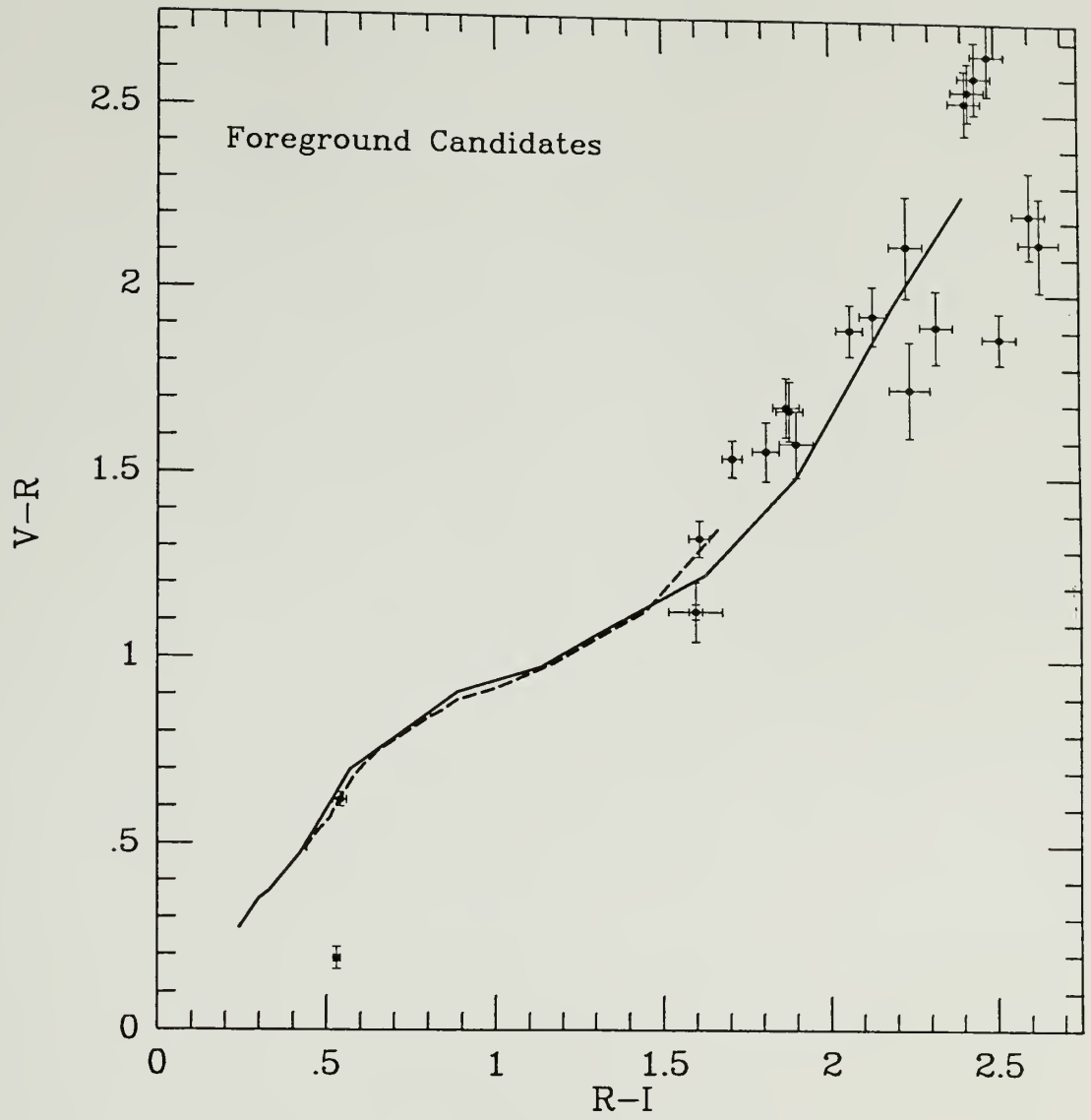

Figure 4.16 Ophiuchus photometric foreground candidates. The data is taken from Table 4.2. Mean colors of main-sequence G - M dwarfs are represented by the solid line, and giants by the dashed line.

It should be noted that nearly all of the stars with anomalous colors which satisfied our original photometric constraints (Figure 4.15) do not qualify as foreground candidates. However, their colors and relatively faint apparent luminosities *are* perhaps indicative of cloud membership. We therefore flag these stars for future study as possible T-Tauri objects or embedded protostars. In Table 4.3 we list the photometric properties of these stars.

Table 4.3

Possible Cloud Members

ID#	RA[a] (hh:mm:ss)	Dec[a] (° ′ ″)	V	V-R	R-I
5	16:29:05.1	-24:24:09	21.73	1.56 ± 0.13	2.11 ± 0.05
64	16:30:35.3	-24:22:42	21.62	1.01 ± 0.10	1.64 ± 0.07
170	16:30:35.5	-24:14:26	20.95	0.92 ± 0.07	1.45 ± 0.05
177	16:28:54.7	-24:13:21	20.49	0.83 ± 0.05	1.33 ± 0.03
198	16:29:04.1	-24:12:52	21.60	0.93 ± 0.12	1.80 ± 0.06
229	16:29:05.5	-24:12:45	21.48	0.86 ± 0.10	1.43 ± 0.07

[a] Epoch 1950

4.3.1.1 Stars with Only R and I Detections

The vast majority of stars detected in our CCD observations do not have V-band counterparts, mainly because the obscuring dust of the molecular cloud biases the survey toward detections of intrinsically red stars and stars whose colors are heavily reddened. Unfortunately, spectral classification is nearly impossible when only one color is available. Nevertheless, we may significantly cull the R,I sample of stars inconsistent with unreddened, late M dwarfs by using not only the (R-I) color, but also the I magnitude, cloud distance modulus and visual extinction.

The procedure follows a number of steps. Two observational properties constrain the R,I detections: (1) the limiting visual magnitude of the survey is ~22, and (2) the distance modulus to the ρ Ophiuchi molecular cloud is ~6. If any foreground stars are not detected at V, they are most likely located near the cloud since our conic search volume is quadratically biased toward foreground stars lying there (the "solid angle effect"). In other words, our survey is strictly complete to an absolute visual magnitude of ~16, corresponding to an M5.5 V star. From Table 4.1 we see that a star of this spectral type will have a mean (R-I) color ~2. A star with (R-I) color greater than this value will not be detected at V (unless it is located near the Sun), but will be detected at R and I because of its intrinsic redness (*e.g.*, V-I > 4). In addition, a star with (R-I) color greater than ~2.5 is probably not a red dwarf because the color index breaks down for the latest M dwarfs (as discussed in section 4.1). All stars satisfying the constraints specified above can be further culled by assigning an absolute magnitude, M_I, using the color index and Figure 4.10, and comparing the distance modulus of the cloud with the derived distance, Equation 4.8. Stars with deduced distances less than the cloud modulus have properties at least self-consistent with their being late-type M dwarfs.

In Figure 4.17 we show the results of this technique. Here we have plotted the (R-I) color and (V_{lim} - R) color limit. The arrows indicate the direction the (V-R) color would change if the survey was complete to M_V ~ 19 (instead of 16), or if the star were simply a heavily reddened background star too faint to be detected at V. Clearly, any star with a (V_{lim} - R) limit that is *above* the mean main-sequence track for M dwarfs is probably a reddened background star because its (V-R) color can only deviate *further* from the intrinsic (unreddened) main-sequence value.

Most of the stars in Figure 4.17 have properties not only consistent with their being foreground stars, but also with their being reddened background G and K dwarfs. This is

the major limitation of one-color analysis — there are usually two solutions. For example, consider the two solutions for star #329, listed here along with the star's photometric properties:

I	R-I	M_I^-	M_I^0	M_I^+	d^-(pc)	d^0(pc)	d^+(pc)	A_V	Type	d(pc)
18.79	2.35 ± 0.08	13.0	13.4	13.8	99	118	141	8.1	K5 V	275

In the first solution, star #329 is an M6.5 dwarf located about 120 pc from the Sun. It would have an apparent visual magnitude of ~23, or about 1 mag fainter than the limit of this study. In the second solution, star #329 appears to be a reddened K5 dwarf located about 275 pc behind the cloud. This solution was determined using the derived visual extinction (from Figure 3.2) and Equations 4.7 and 4.8. As we demonstrated using the Galactic stellar surface density model, we expect a majority of the stars detected in this survey to be nearby F, G and K dwarf stars whose starlight is leaking through less opaque areas of the cloud (see for example Figure 4.4). Since we cannot determine the true nature of star #329 or most other stars from Figure 4.17 using only photometric constraints, and since the R,I stars are most likely background objects, we elect not to include them in our list of candidate foreground stars. In Chapter 5 we will investigate whether these stars have measurable proper motions.

However, five stars from Figure 4.17 do not have second, background stellar solutions. Given that these stars do have a foreground solution, they are, therefore, included in the candidate list. In Table 4.4 we list the photometry and color solutions for these stars.

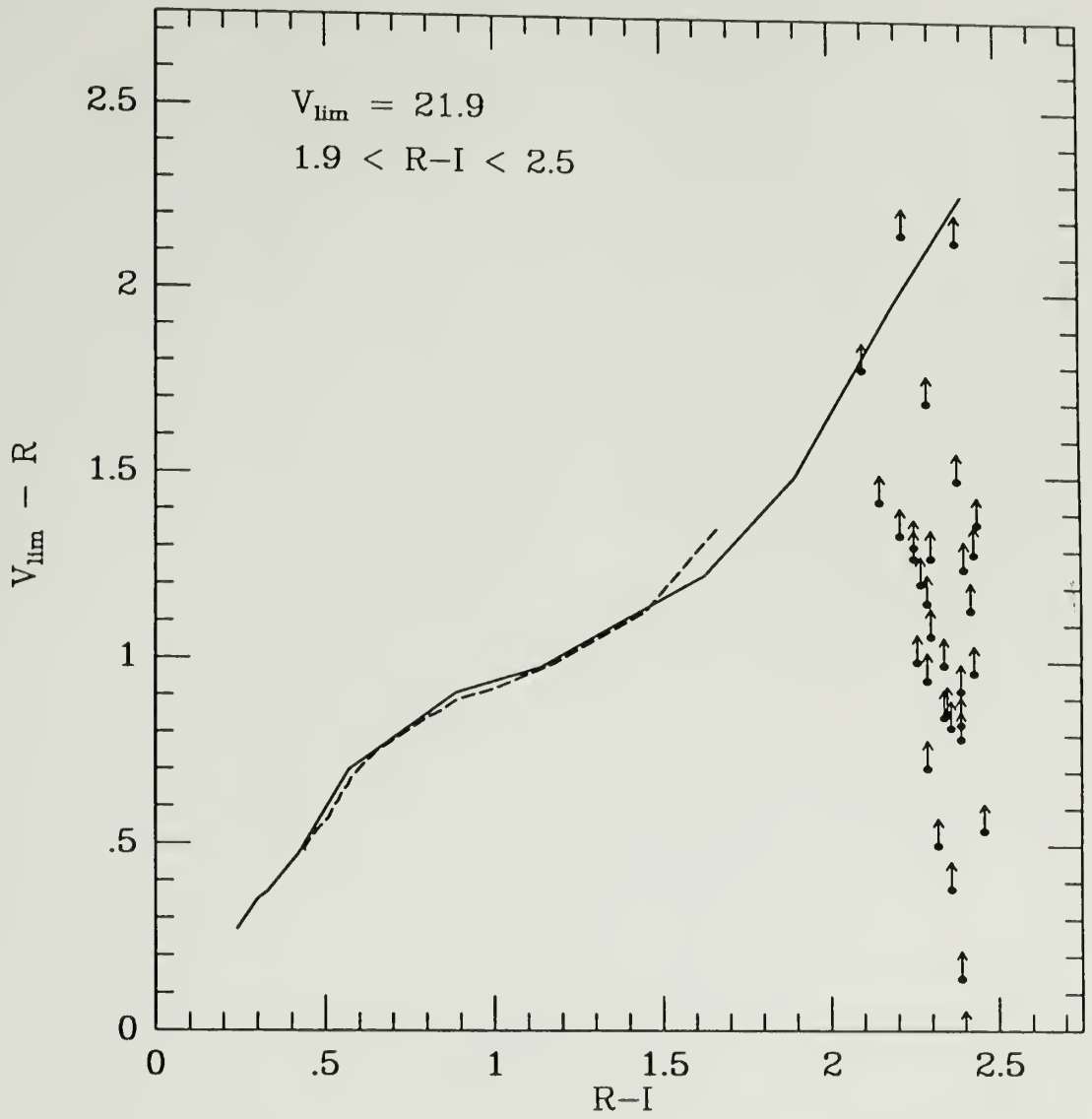

Figure 4.17 Ophiuchus R,I foreground candidates with R-I colors between 1.9 and 2.5. The y-axis is (V_{lim} - R), where V_{lim} = 21.9. The arrows signify the direction of the true V-R color if the survey were deeper at the visual waveband. Mean colors of main-sequence G - M dwarfs are represented by the solid line, and giants by the dashed line.

Table 4.4

R,I Analysis of Foreground Candidates

ID#	I	R-I	M_I^-	M_I^0	M_I^+	d^-(pc)	d^0(pc)	d^+(pc)	A_V
397	18.63	2.30 ± 0.07	12.9	13.2	13.5	105	123	143	11.2
398	18.79	2.39 ± 0.08	13.2	13.6	14.0	91	108	129	11.2
450	18.79	2.39 ± 0.08	13.2	13.6	14.0	87	104	129	13.3
465	18.55	2.29 ± 0.06	12.9	13.1	13.4	106	121	140	11.1
466	18.43	2.25 ± 0.06	12.7	13.0	13.2	109	125	143	11.4

4.3.1.2 Other Surveys of ρ Ophiuchi - Constraints on Foreground Stars

The color-color analysis presented in the previous sections assumes that there are generally two possible stellar solutions, namely, a foreground and/or a background solution. A major concern of this study is the possibility of contamination to the foreground candidate list by stars associated with the molecular cloud itself. This, if you will, is a third possible solution. Unfortunately, this solution is much more ill-determined than the foreground or background solutions, since A_V can only be said to be in the range of $0 \leq A_V \leq A_V^{cloud}$. Therefore, our optical data is somewhat limited for discerning T-Tauri objects and lightly embedded protostars from the intrinsically red foreground population. We may, however, turn to other surveys, and in particular the infrared studies, that are geared toward identifying association objects and protostars. In this section, we review recent work in this field.

Bruce Wilking and Tom Greene recently surveyed the northern portion of the L1689 filament of ρ Oph at J, H and K-bands, 1 - 2.2μm (private communication). The purpose of their study was to identify IRAS sources and to discover newly forming protostars deeply embedded within the molecular cloud. About 40% of their survey

overlaps our CCD field. Since their infrared survey was especially sensitive to stars associated with the cloud, including protostars and T-Tauri stars, we can check their detections with our optical foreground candidate list for contamination by pre-main-sequence stars. In Table 4.5, we list Wilking and Greene's IR stars that have optical counterparts from this study. The estimated accuracy of the Wilking and Greene photometry is generally about 10%.

Table 4.5

Optical and Infrared Detections of Ophiuchus Stars

Name	RA[a] hh:mm:ss	Dec[a] ° ′ ″	J mag	H mag	K mag	CCD ID#	I	V-R	R-I
IRS01a	16:28:57.3	-24:18:45	16.00	14.78	14.20	556	19.90	-	1.59 ± 0.13
IRS01b	16:28:59.7	-24:19:07	16.00	15.07	14.21	538	19.81	-	1.97 ± 0.16
IRS03	16:29:05.0	-24:21:25	15.25	14.23	13.54	514	19.19	-	1.88 ± 0.09
IRS05b	16:29:09.2	-24:25:46	16.00	14.23	9.18	443	17.63	-	3.08 ± 0.06
IRS06	16:29:07.8	-24:16:40	9.92	9.49	9.42	909	10.83	0.62 ± 0.01	0.54 ± 0.00
IRS07a	16:29:08.1	-24:22:35	11.17	9.22	8.33	59	15.51	2.56 ± 0.08	2.42 ± 0.05
IRS07b	16:29:09.3	-24:22:27	16.00	15.00	12.75	494	19.54	-	2.00 ± 0.12
IRS08b	16:29:09.6	-24:26:45	12.48	10.12	8.92	443	17.63	-	3.08 ± 0.08
IRS15a	16:29:19.4	-24:24:14	12.38	9.91	8.40	42a	16.81	2.22 ± 0.12	2.53 ± 0.10
IRS15b	16:29:19.1	-24:24:07	14.20	12.17	10.90	42b	19.16	-	2.89 ± 0.25
IRS16	16:29:20.1	-24:15:44	14.32	13.42	13.17	119	16.81	1.50 ± 0.05	1.47 ± 0.03
IRS19	16:29:29.8	-24:17:03	14.78	12.47	11.95	98	17.02	1.89 ± 0.04	1.80 ± 0.04
IRS21	16:29:32.7	-24:30:13	11.67	9.79	9.09	29	15.56	2.69 ± 0.09	2.36 ± 0.05
IRS22	16:29:33.6	-24:17:32	12.06	11.79	11.64	908	13.87	1.13 ± 0.02	1.60 ± 0.02
IRS24a	16:29:34.2	-24:16:30	11.79	11.50	11.27	598	15.28	-	3.28 ± 0.06
IRS24b	16:29:34.6	-24:16:26	9.70	9.54	9.35	600	13.68	-	1.15 ± 0.05
IRS27	16:29:39.4	-24:27:21	13.49	12.28	11.64	439	17.46	-	2.69 ± 0.06
IRS28b	16:29:42.4	-24:22:20	15.98	14.40	14.20	498	19.73	-	2.19 ± 0.17

[a] Epoch 1950

Of the stars in Table 4.5, IRS06, IRS07a, IRS15a,b and IRS22 are identified with optical foreground candidates #909, 59, 42a,b and #908 from this study. Stars 908 and 909 happen to be bright photoelectric standard stars (consequently, have accurate photometric V,R,I values) with deduced locations in front of the L1689 cloud, which, the near-IR photometry does not appear to contradict since there is no apparent reddening at these wavelengths. Star #59 has a (V-R) color that is too red to be an M dwarf star, although, it is within 2σ of the mean (V-R) value of a very late-type red dwarf. The fact that this star has colors consistent with being reddened and that it is associated with a bright infrared source, IRS07a, compels us to believe that this star is a lightly embedded protostar or T-Tauri type star. There are three other candidates from Table 4.2 which have colors similar to star #59. Two of the three, #25 and #33, are located outside of the region of the Wilking and Greene survey, while #34 is located within the boundaries of the survey. Since star #34 does not have a bright infrared counterpart, it must remain as a foreground stellar candidate. Little can be concluded about stars #25 and #33, since they lie outside the boundaries of the infrared survey; nevertheless, given that they have suspicious colors (similar to #59, which is most likely associated with Ophiuchus) they should be considered marginal foreground candidates at best.

The most interesting infrared star associated with optical foreground candidate is IRS15a,b, which is in fact, a double visual and infrared source. Curiously, this double star is also associated with a 25μm IRAS point source, IRAS 16293-2424, which, itself, lies 2′ south of point source IRAS 16293-2422. The latter infrared point source is identified with an energetic high-velocity bipolar molecular outflow (Walker *et al.* 1986 and 1988; Mundy *et al.* 1986). Bruce Wilking, intrigued by the close proximity of IRS15 to the IRAS and molecular outflow sources, conducted additional photometric observations of the double source at J, H, K, L, M, N and Q wavelengths (1.25 to 22μm), using telescopes at the IRTF

and CTIO during 1986 and 1989 (private communication). In Table 4.6 the infrared data is reproduced for IRS15a and IRS15b.

Table 4.6

Infrared Photometry of IRS15a,b (from Wilking, private communication)

Source	J (1.25μm)	H (1.6μm)	K (2.2μm)	L (3.4μm)	M (5μm)	N (10μm)	Q (22μm)
IRS15a	12.27	9.91	8.41	7.20	6.55	4.8	2.3
IRS15b	14.20	12.17	10.9	-	-	-	-

It is clear from the near to mid infrared photometry that IRS15a,b has an infrared excess indicative of either reradiated starlight or accretion from a circumstellar disk. This type of infrared excess is a common property of T-Tauri objects and protostars (Lada 1987). It is not clear whether the faint companion to IRS15a is a protostar since there is no mid-infrared photometry available for this star. Nevertheless, its close proximity to IRS15a (~9″, or ~1500 a.u.) and its sharply rising flux density, similar to IRS15a, strongly implies that this star is associated with the group of newly forming stars around the bipolar molecular outflow source, IRAS 1629a. In Appendix E, we consider the nature of this double star system in more detail.

In summary, the clue to the apparent nature of stars #59 and #42a,b lies in their association with recent star formation in the L1689 filament of ρ Ophiuchus.

In addition to the two IRAS point sources discussed above, there are four other very faint IRAS sources in our Ophiuchus field. None of these additional sources are associated with optical detections from this study or infrared detections from Wilking and Greene. In Table 4.7 a list of the positions (Epoch 1950) and fluxes of the six IRAS

sources located in L1689 is given (the information comes from the IRAS point source catalog).

Table 4.7

IRAS Point Sources

RA[a] (hh:mm:ss)	Dec[a] (° ′ ″)	12μm S_ν(Jy)	25μm S_ν(Jy)	60μm S_ν(Jy)	100μm S_ν(Jy)
16:29:18.7	-24:24:15	1	2.3	255	1031
16:29:21.0	-24:22:13	0.8	1.8	255	1031
16:30:20.5	-24:28:21	0.8	0.4	1	33
16:20:26.0	-24:33:04	0.3	0.4	3	22
16:30:33.0	-24:25:21	0.4	0.4	2	31
16:30:42.0	-24:35:06	0.3	0.8	3	23

[a] Epoch 1950

An optical photographic study by Ichikawa and Nishida (1989) attempted to identify IRAS stars in the ρ Oph region, including the L1689 cloud. Only one of their detections corresponds to a star in the foreground candidate and infrared samples of Tables 4.2 and 4.5. The star is none other than IRS15a (#42a). The I band magnitude (Kron - N) quoted by the aforementioned authors for this star is 17.00. This magnitude is about 0.2 mag fainter than the value derived in this study. The difference is consistent with the uncertainty associated with photographic photometry and our own in CCD photometry errors.

Several groups have searched for low-mass young stars in molecular clouds at the extremes of the energy spectrum thought to be associated with these stars. Most weak-line T-Tauri stars (a.k.a. naked T-Tauri stars) exhibit x-ray variability considered to be the result of solar-type chromospheric activity, including energetic flares (*cf.* Feigelson 1987). Numerous x-ray sources detected by the orbiting Einstein Observatory were found in the

Ophiuchus complex (Montmerle *et al.* 1983). None of the detections located in the L1689 cloud correspond to an optical foreground candidate of this study. However, it should be noted that only a small fraction of the L1689 filament of the Oph complex was surveyed by the Einstein Observatory. In the low energy regime, synchrotron radio emission has also been the focus of studies investigating low mass star formation in molecular clouds (Andre *et al.* 1987; Stine *et al.* 1988). This emission, presumably associated with x-ray flares, has been observed in only a small number of the x-ray detections. It is not clear whether radio emission is an adequate tracer of pre-main sequence stars in ρ Oph or other star formation sites. In any case, none of the 1.4 and 5 GHz radio detections in the Ophiuchus field are associated with an optical foreground candidate. It thus appears that the foreground candidates of Table 4.2 are not seriously contaminated by weak-line T-Tauri stars.

4.3.2 Taurus Sample

A summary of the Taurus observations are described in sections 2.1 and 2.2, Chapter 2. As in the case with the Ophiuchus color-color analysis, we consider only the CCD data for the remaining analysis of the Taurus stellar objects. The photometric data used for the color-color analysis is contained within three CCD fields, each of size 18′ × 26′. A total of ~2600 stars were detected at bands V, R, or I. Of this sample, a subset of ~1750 were detected at all three bands with at least a 10:1 S/N ratio. Due to non-linear CCD saturation effects (section 4.4), stars brighter than V ~ 12 were discarded from the sample. The resultant range in apparent magnitude of the Taurus stars was $14 < V, R < 22.5$, and $14 < I < 20.4$.

Since the opaque screen method functions best when the cloud extinction is high, we restrict our attention to areas of the cloud where the visual extinction is at least 3 mag. We have chosen this value so that the Taurus minimum extinction is identical to that for

the Oph field. The Taurus field, unlike the Ophiuchus CCD field, contains several areas with visual extinctions less than 3 mag (see the Taurus grayscale extinction map, Figure 3.8) and stars whose line-of-sight projection lie in areas of the cloud where $A_V < 3$ were discarded from further analysis. Of the total 1750 stars detected at V,R,and I, about 34% of the sample remained for study after this cut.

In Figure 4.18, we present the CCD photometry of these stars in the V,R,I color-color plane. As in the case of Ophiuchus (see Figure 4.7), three properties of this data are to be noted. First, most of the stars cluster about a reddening curve or set of reddening curves depending on spectral type (see Appendix C); second, there is a substantial amount of scatter seen in the plot; and third, there are a number of stars with colors too blue to be main-sequence stars. As before, in order to better understand these qualities, we simulate the color reddening of stars distributed along the line of sight in the direction of Taurus.

As in the Ophiuchus analysis in section 4.3.1, we may simulate the cumulative stellar surface densities at the V, R and I wavebands for a volume of stars given by the angular size of the Taurus CCD field and lying in the direction of Taurus (ℓ = 173°, b = -15°) by using the stellar distribution model described in Appendix F. In Figure 4.19 the model results are shown along with the observed densities. As expected, reddened background dwarfs dominate the observed star counts; about 10 times as many stars are detected at I-band than at V. The relative distribution of dwarfs, giants and spheroid stars as seen in the visual band is shown in Figure 4.20. At the V band limiting magnitude, the distribution is ~89% dwarfs, 8% giants and 3% spheroid stars. At the longer wavelengths, the distribution is almost totally dominated by nearby dwarf stars. This effect is illustrated in Figures 4.21 and 4.22, where we have plotted the simulated stellar densities at the R and I bands, respectively. At the R band limiting magnitude (~22), the dwarfs account for

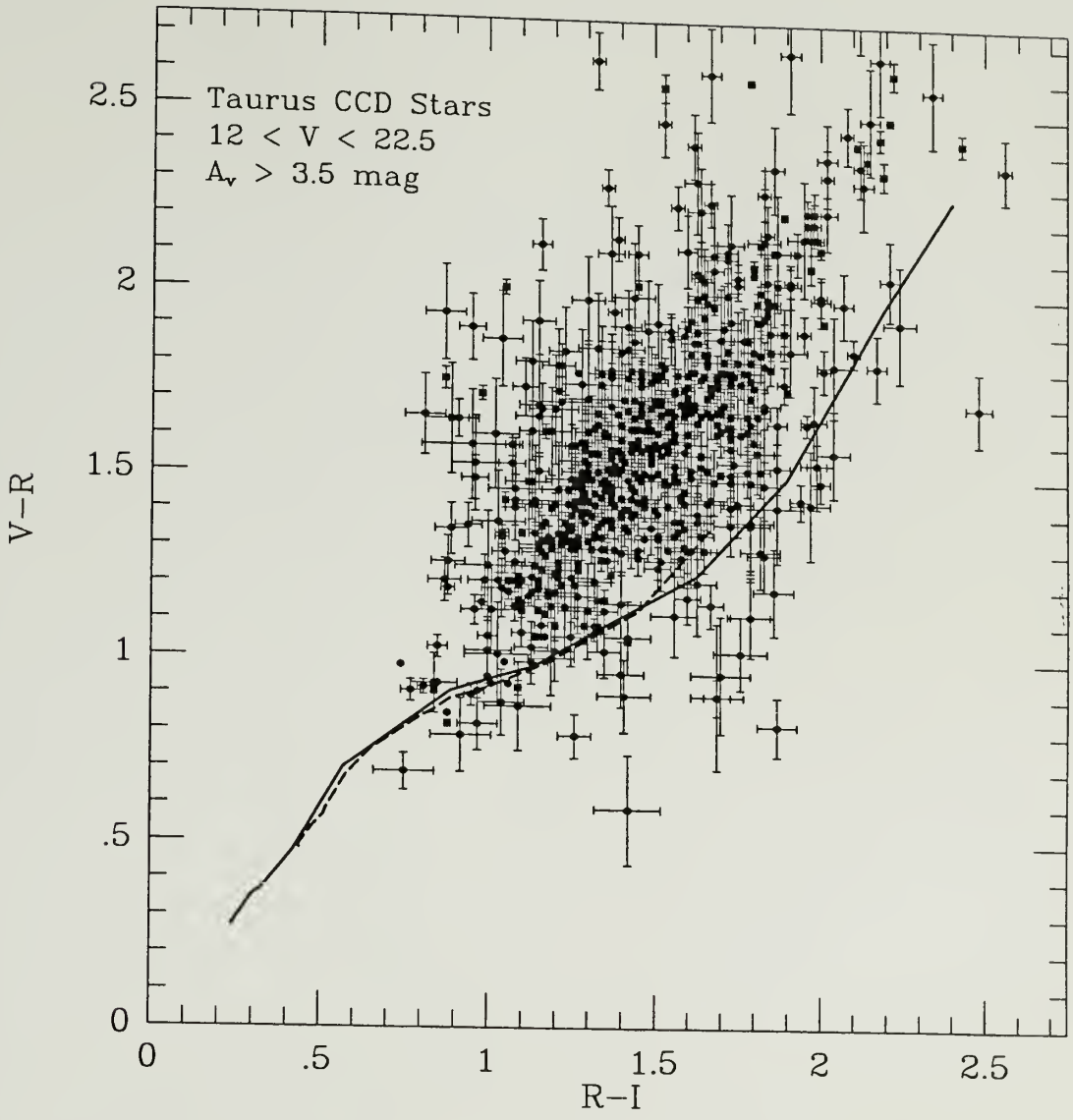

Figure 4.18 CCD photometry of the Taurus sample, presented in the (V-R) *vs.* (R-I) plane. The V-band limiting magnitude is 22.5. Stars with visual magnitudes brighter than 12 are excluded. Color uncertainties, represented by 1σ error bars, are also shown. Stars with color uncertainties greater than 10% are excluded. All stars are located along a line of sight with at least 3.5 magnitudes of visual extinction. Mean colors of main-sequence G - M dwarfs are represented by the solid line, and giants by the dashed line.

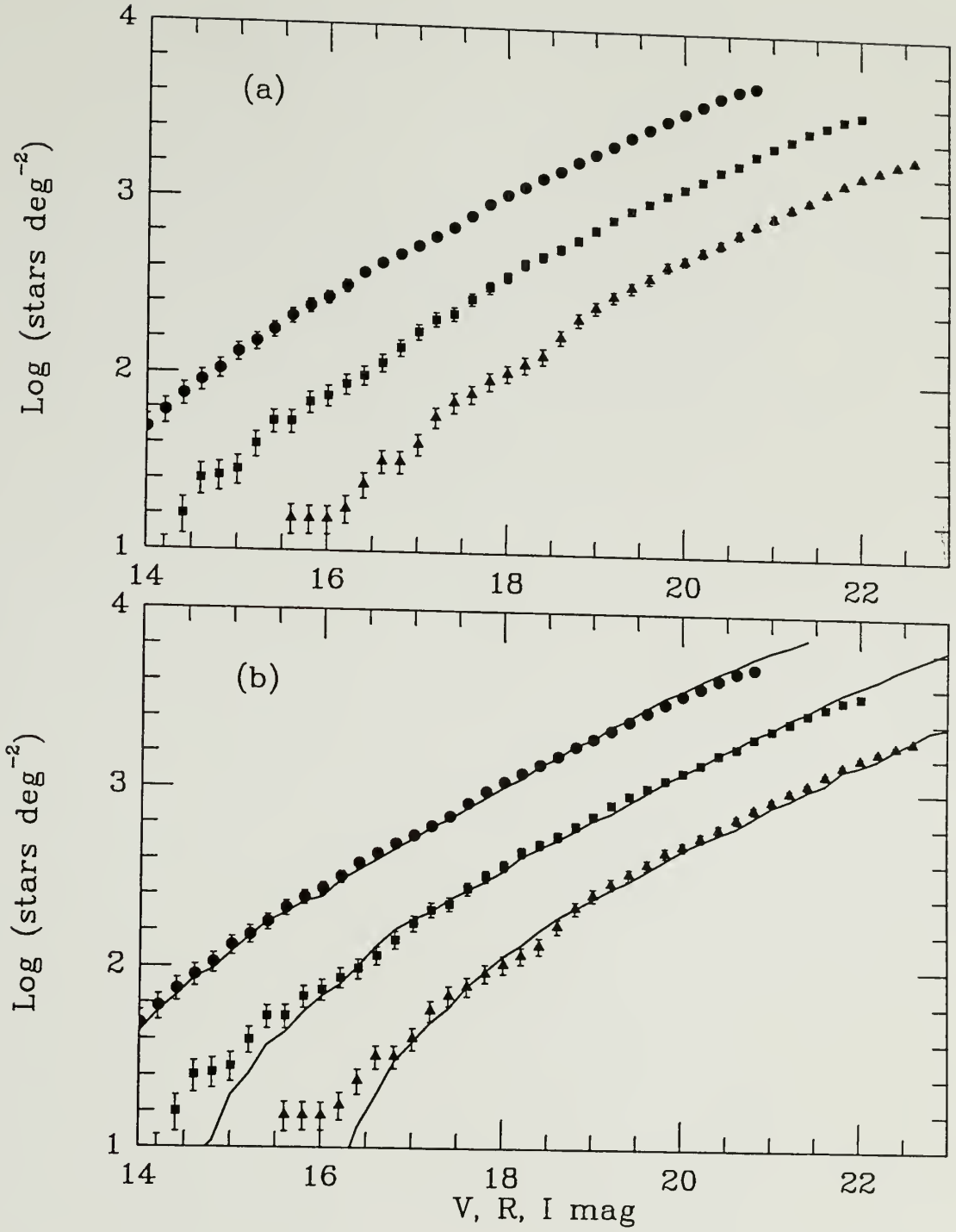

Figure 4.19 Cumulative stellar surface densities *vs.* apparent V,R,I magnitudes for the Taurus CCD stars. The data is represented with the following symbols: filled triangles denote the V-band data; filled squares are the R-band; filled circles are the I-band. Expected $\sqrt{N}$ error bars are shown. Synthetic model predictions, including contributions from disk dwarfs and giants, and spheroid stars, are represented with solid lines.

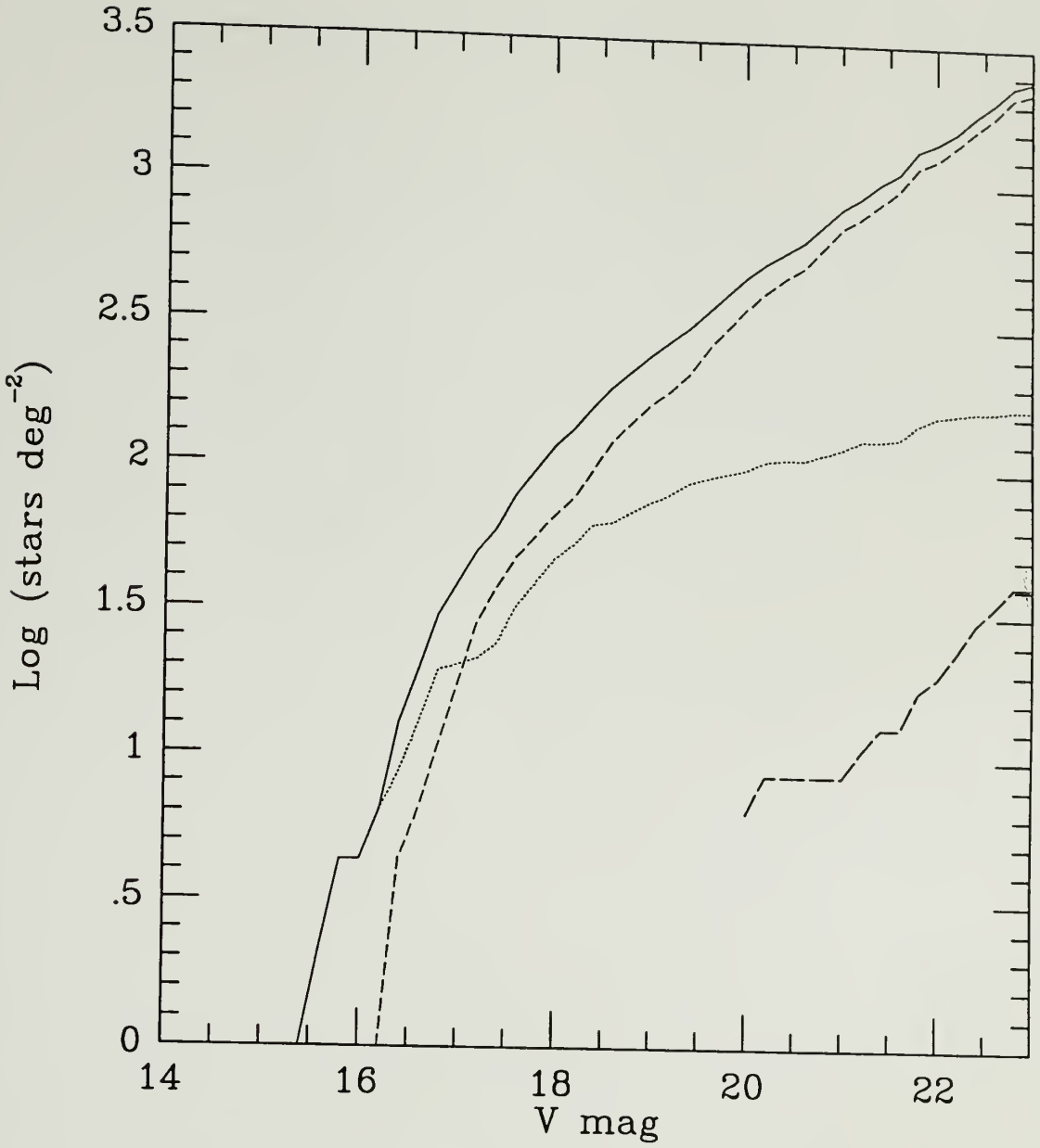

Figure 4.20 Synthetic model predictions at the visual waveband. Cumulative stellar surface densities *vs.* apparent visual magnitude for stars located behind the Taurus molecular cloud. Contributions from dwarfs, giants and spheroid stars are drawn with the following line types: solid denotes the total contribution; short dashed are the disk dwarfs; dotted are the disk giants; long dashed are the spheroid stars.

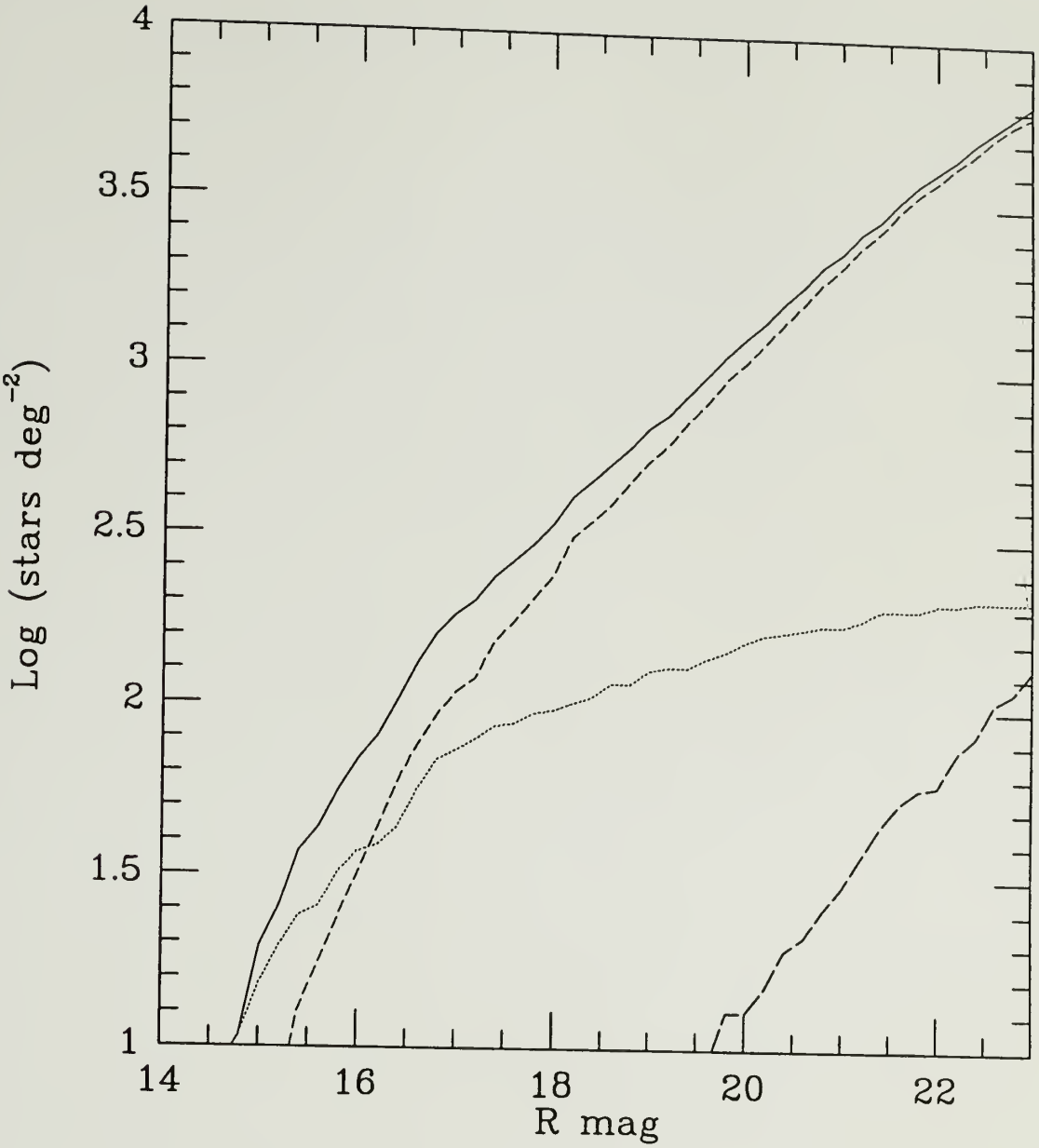

Figure 4.21 Synthetic model predictions at the red waveband. Cumulative stellar surface densities *vs.* apparent R magnitude for stars located behind the Taurus molecular cloud. Contributions from dwarfs, giants and spheroid stars are drawn with the following line types: solid denotes the total contribution; short dashed are the disk dwarfs; dotted are the disk giants; long dashed are the spheroid stars.

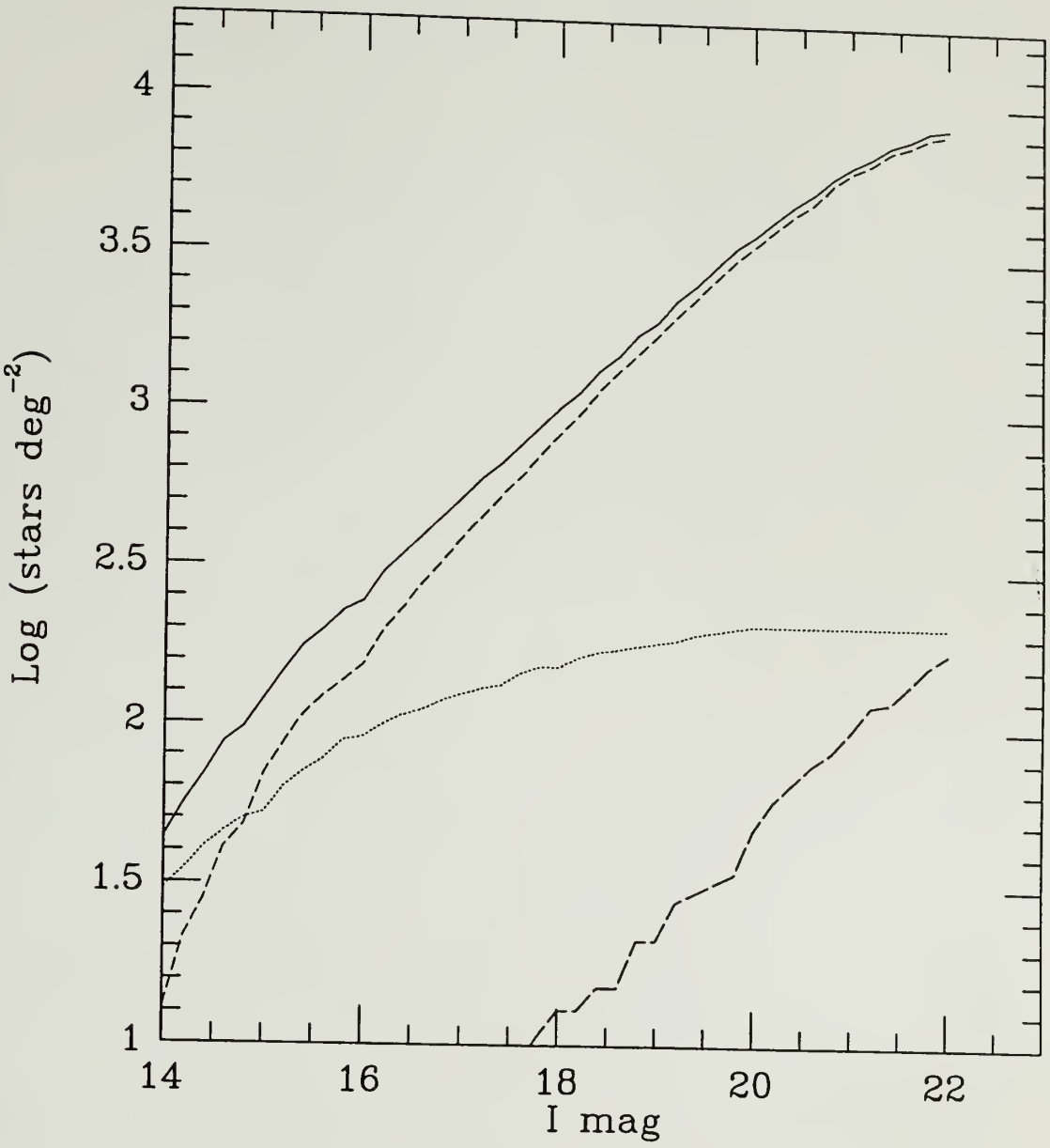

Figure 4.22 Synthetic model predictions at the far-red waveband. Cumulative stellar surface densities *vs.* apparent I magnitude for stars located behind the Taurus molecular cloud. Contributions from dwarfs, giants and spheroid stars are drawn with the following line types: solid denotes the total contribution; short dashed are the disk dwarfs; dotted are the disk giants; long dashed are the spheroid stars.

~95% of the total, and at the I-band limiting magnitude (~20.8), the dwarfs account for fully 97% of all background stars leaking through the cloud. Stars with V > 18 are most likely G - K dwarfs, and stars near the limits of the photometry are almost certainly dwarfs located behind the cloud, within 1 kpc of the Sun.

To help understand the photometric properties of the CCD data we simulate the colors of the stellar distribution, described above. As in the case of the Ophiuchus analysis, we consider three cases in which we convolve the model stellar distribution with the Taurus visual extinction map (Figure 3.8). The case studies are: simulated stellar colors with the expected random error due to S/N limitations, adding an additional 5% error, and including an additional 10% error. The first case is illustrated in Figure 4.23. The scatter shown in the simulated data appears too small compared to the actual CCD data. In the more extreme cases 2 and 3, shown in Figures 4.24 and 4.25, the respective 5 and 10% errors added to the expected S/N errors do replicate the scatter seen in the CCD data of Figure 4.18. This result suggests that the Taurus CCD data must have an additional source of error between 5 and 10%.

Note that this scatter is about a factor of 2 to 3 more severe than that of the Ophiuchus CCD data. This difference between the two data sets is not implausible considering that the Taurus and Ophiuchus fields were observed with two different CCD detectors, at separate times of the year, using entirely different sets of photometric standards. On the other hand, calibrations to the Cousins standards should minimize any differences between data sets. At the end of this chapter, we will discuss these points in more detail.

In order to cull the Taurus sample of stars that are clearly reddened, we follow the same procedure as described in the last section; namely, all stars with colors clearly in the reddening zone, or, outside a 2σ deviation from the main-sequence track, are eliminated

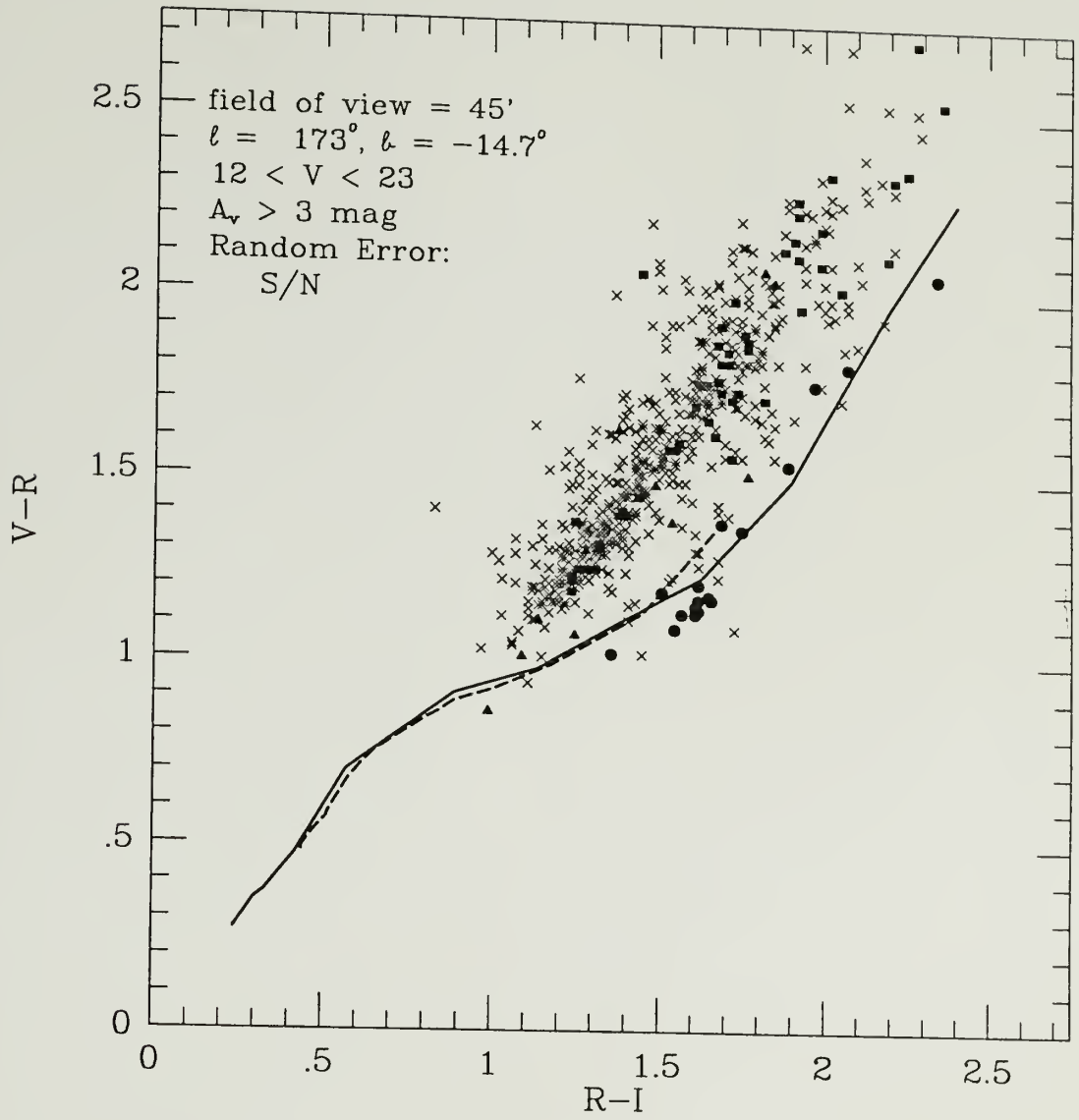

Figure 4.23 Synthetic model photometry of stars located in the direction of the Taurus molecular cloud, $\ell = 173°$, b = -15.0°, within a field of view of angular size 45′, presented in the (V-R) *vs.* (R-I) plane. The V-band magnitude range is from 14 to 23 mag. The extinction attributed to the cloud is taken from Figure 3.8. The scatter in the points is due to a random S/N uncertainty introduced into the synthetic colors. Point symbols represent the following stellar populations: crosses denote disk dwarfs; filled boxes are the disk giants; filled triangles are the spheroid stars; filled circles are the stars located in front of the molecular cloud. Mean colors of main-sequence G - M dwarfs are represented by the solid line, and giants by the dashed line.

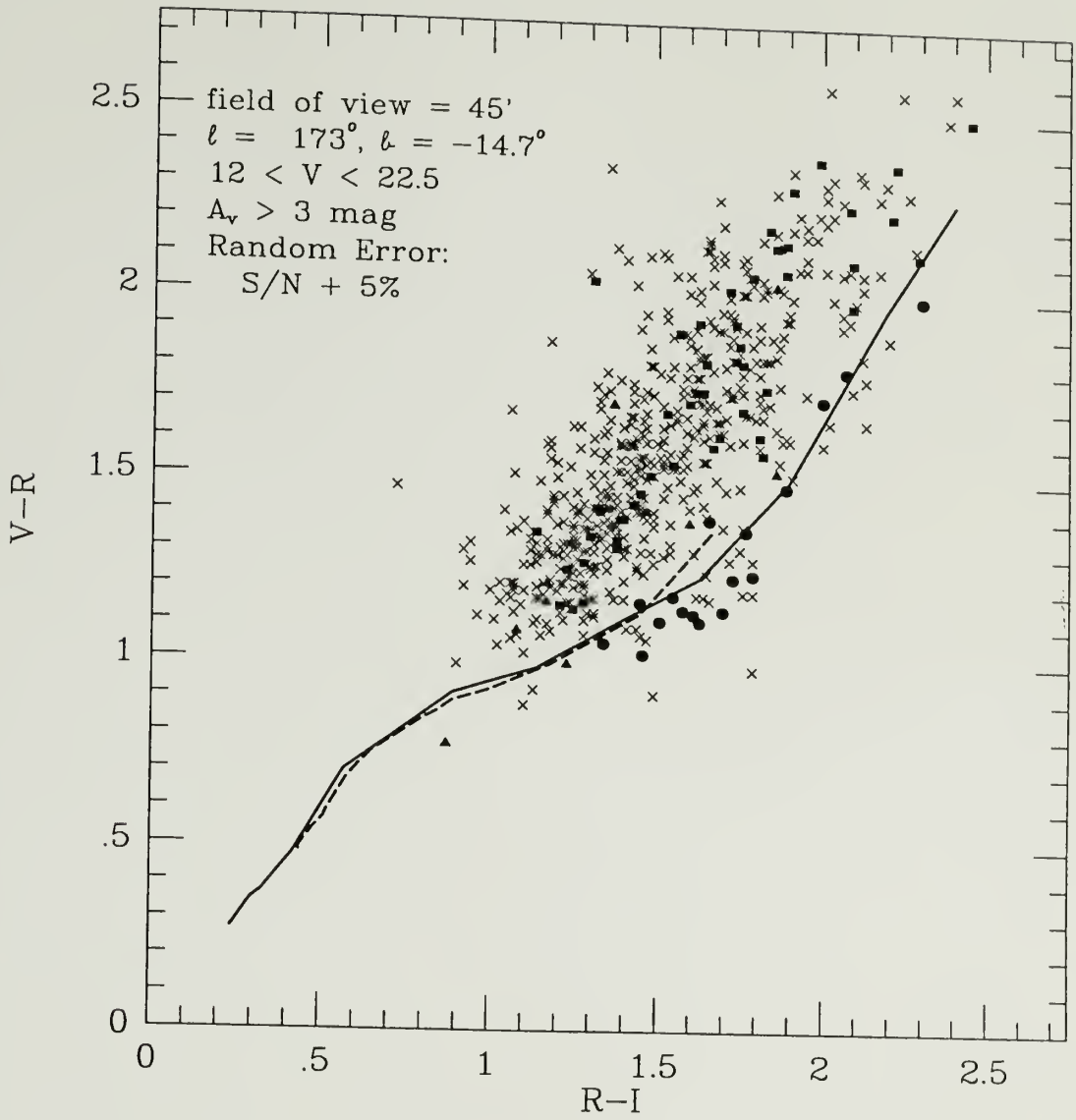

Figure 4.24 Synthetic model photometry of stars located in the direction of the Taurus molecular cloud, ℓ = 173°, b = -15°, within a field of view of angular size 45′, presented in the (V-R) *vs.* (R-I) plane. The V-band magnitude range is from 14 to 23 mag. The extinction attributed to the cloud is taken from Figure 3.8. The scatter in the points is due to a random S/N uncertainty plus an added 5% uncertainty introduced into the synthetic colors. Point symbols represent the following stellar populations: crosses denote disk dwarfs; filled boxes are the disk giants; filled triangles are the spheroid stars; filled circles are the stars located in front of the molecular cloud. Mean colors of main-sequence G - M dwarfs are represented by the solid line, and giants by the dashed line.

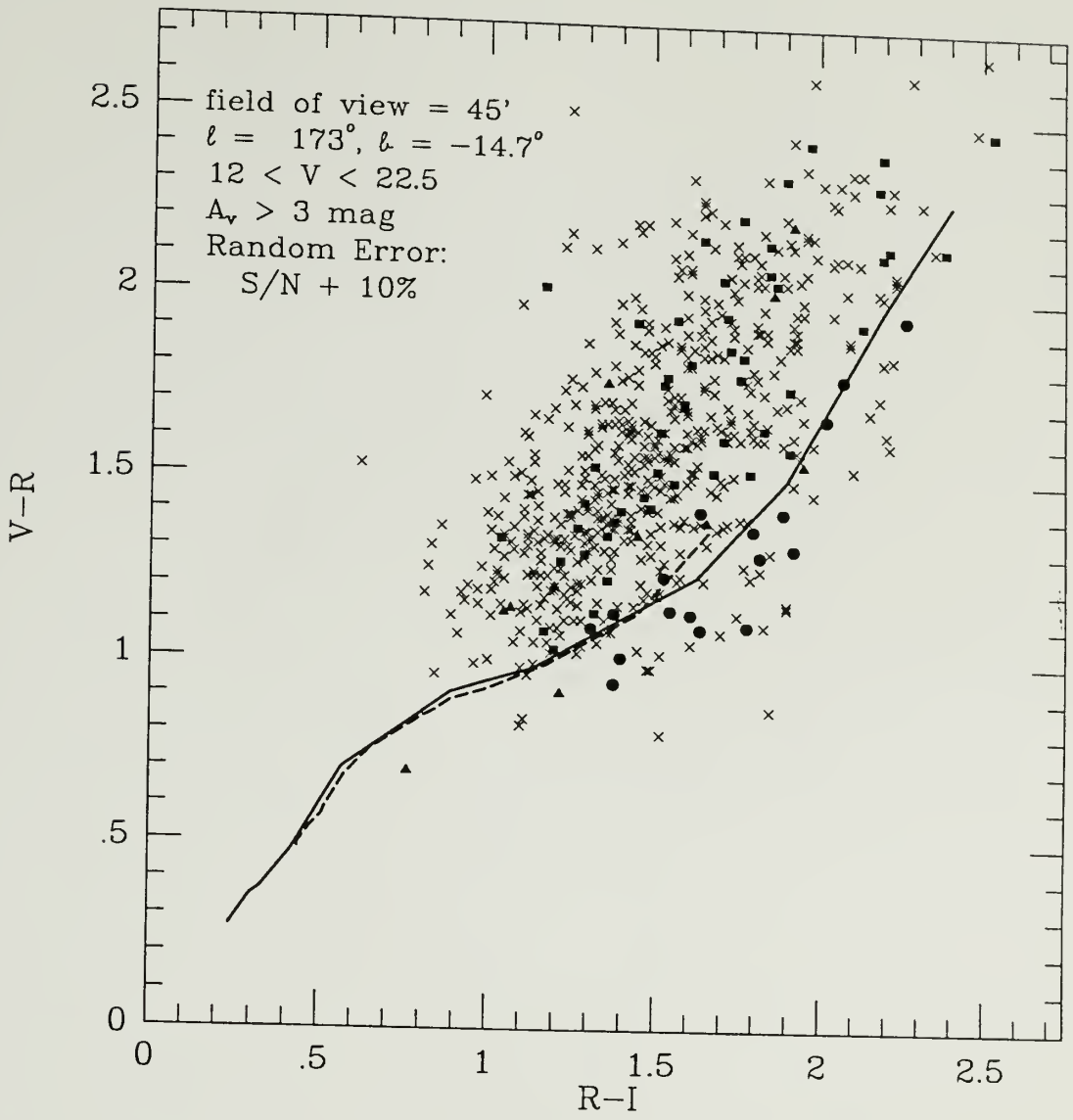

Figure 4.25 Synthetic model photometry of stars located in the direction of the Taurus molecular cloud, $\ell = 173°$, b = -15°, within a field of view of angular size 45′, presented in the (V-R) *vs.* (R-I) plane. The V-band magnitude range is from 14 to 23 mag. The extinction attributed to the cloud is taken from Figure 3.2. The scatter in the points is due to a random S/N uncertainty plus an added 10% uncertainty introduced into the synthetic colors. Point symbols represent the following stellar populations: crosses denote disk dwarfs; filled boxes are the disk giants; filled triangles are the spheroid stars; filled circles are the stars located in front of the molecular cloud. Mean colors of main-sequence G - M dwarfs are represented by the solid line, and giants by the dashed line.

from further analysis. We ease the latter restriction for the reddest stars in order to account for the additional scatter in the Taurus data as compared to the Oph data. Consequently, stars with V-R > 1.5, were required to lie outside a 3σ deviation from the main-sequence track before they were discarded. In Figure 4.26, the results of this culling process are shown. It is this sample from which we further test for self-consistency as foreground dwarfs.

The procedure to determine the range in spectral type of the candidate stars of Figure 4.26 is the same as described in section 4.3.1. First, for each star, we ascertain the nearest point on the main-sequence and assign appropriate mean colors according to Equation 4.9. Using the R-I index, we next compute the I-band absolute magnitude using Equation 4.10, or, for early type stars, using the look-up table, Table F.1. With this parameter along with the apparent I magnitude, it is a simple matter to compute the expected distance from the Sun using Equation 4.8. Stars with derived distances less than the maximum distance of the foreground volume — given by the distance to the Taurus molecular cloud, ~ 140 pc (Elias 1978) — have a consistent interpretation as foreground objects.

The results of this technique are shown in Figure 4.27. These stars have colors, apparent magnitudes, and deduced spectral types consistent with their being low-mass stars located in front of the Taurus molecular cloud. A list of the photometric properties and deduced spectral types of the candidate foreground stars is shown in Table 4.8. The symbols are the same as used in Table 4.2.

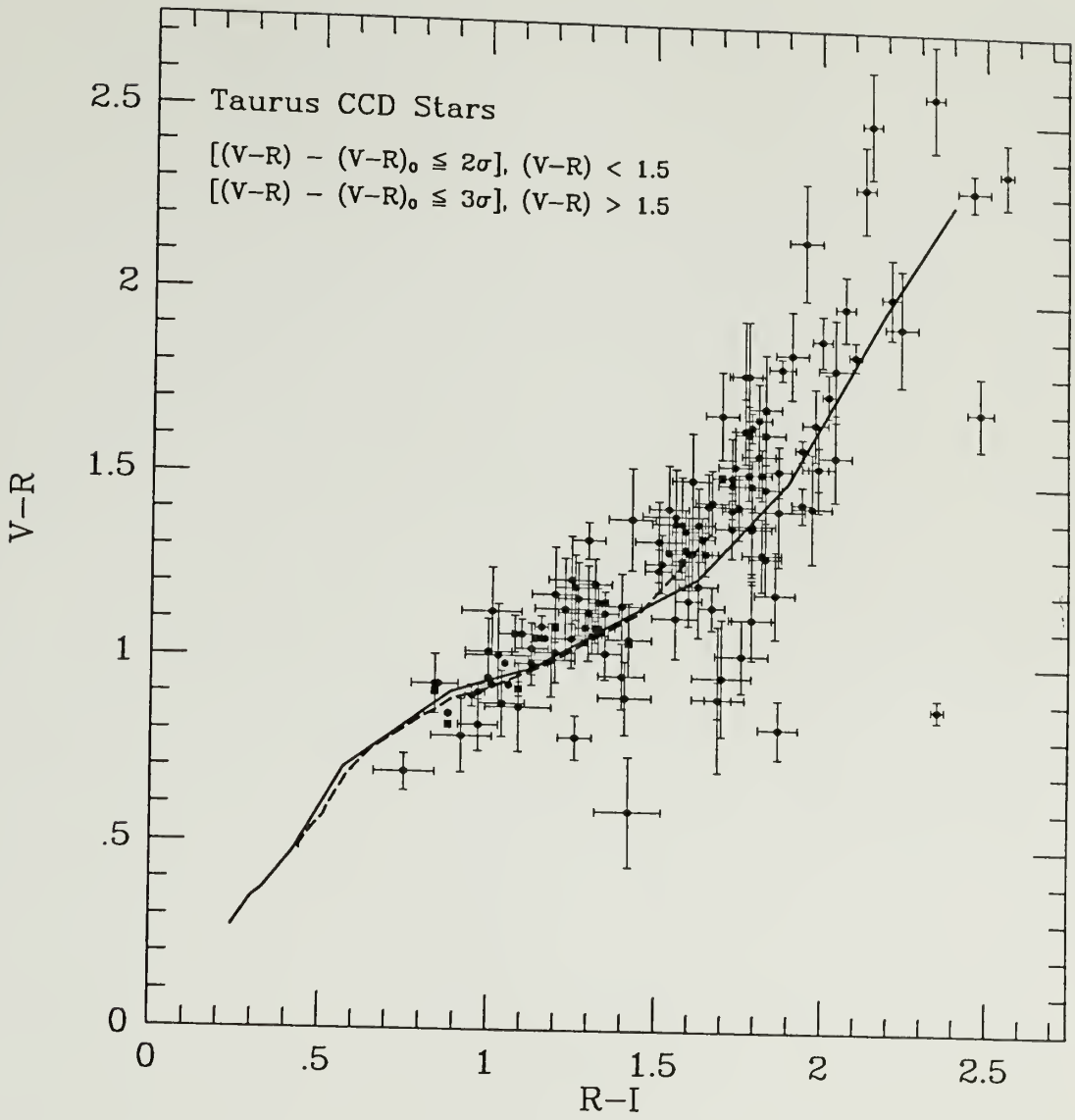

Figure 4.26 CCD photometry of the Taurus candidate foreground stars presented in the (V-R) *vs.* (R-I) plane. These stars have colors that either lie below the mean tracks (mean colors of main-sequence G - M dwarfs are represented by a solid line, and giants by a dashed line), or are within 2σ of the nearest point on the main-sequence track. The photometric properties are described in Figure 4.21. Color uncertainties, represented by 1σ error bars, are also shown.

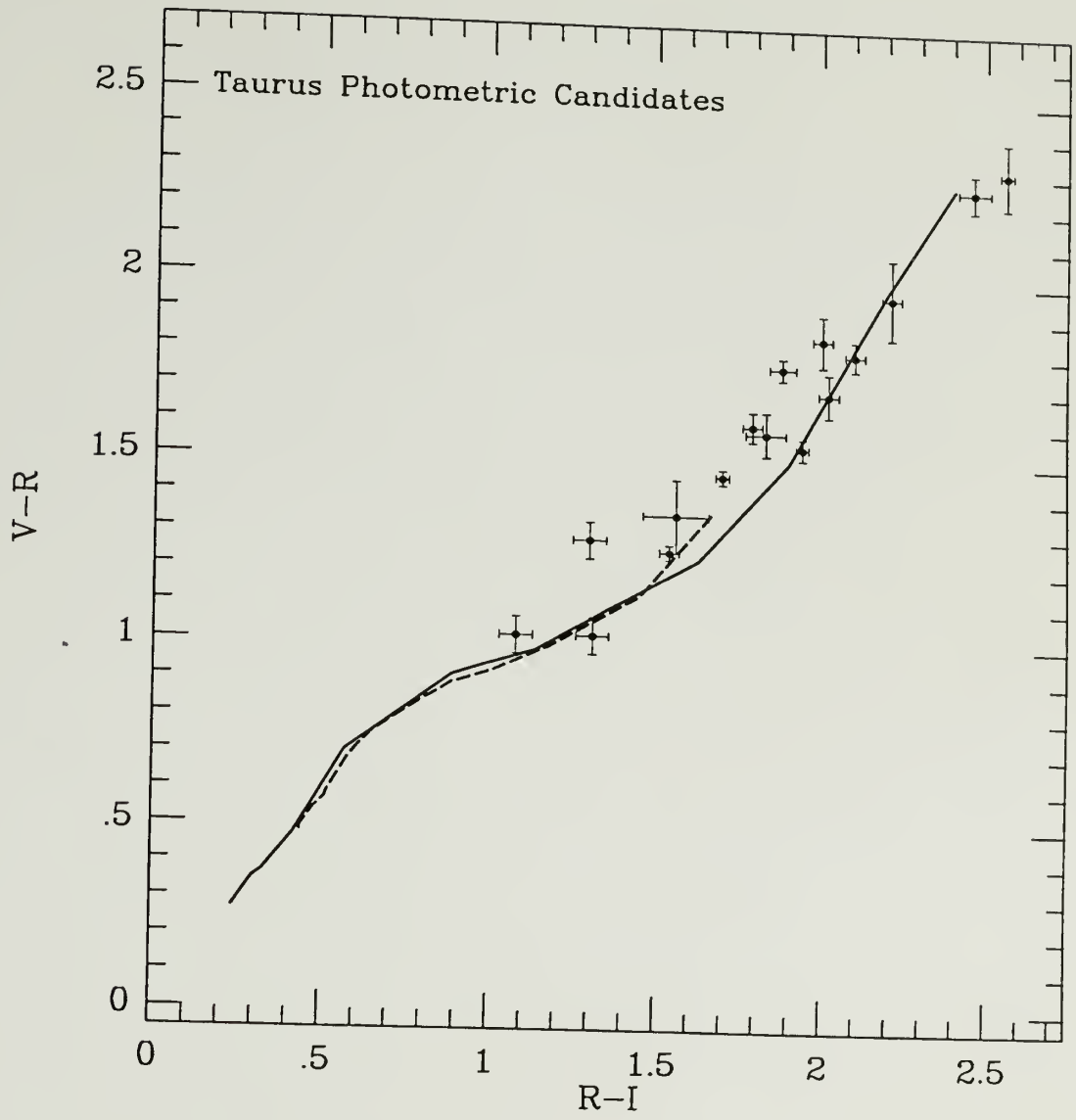

Figure 4.27 Taurus photometric foreground candidates. The data is taken from Table 4.8. Mean colors of main-sequence G - M dwarfs are represented by the solid line, and giants by the dashed line.

Table 4.8

Taurus Photometric Foreground Candidates

ID#	V	V-R	R-I	M_I^-	M_I^0	M_I^+	d^-(pc)	d^0(pc)	d^+(pc)
18	18.88	1.51 ± 0.02	1.70 ± 0.02	10.8	10.8	10.8	95	95	160
29	17.95	1.30 ± 0.01	1.54 ± 0.01	9.8	9.8	9.8	110	115	115
32	21.89	2.36 ± 0.09	2.56 ± 0.04	13.7	13.9	13.9	40	41	50
41	21.39	1.89 ± 0.07	2.00 ± 0.04	12.2	12.4	12.5	100	110	120
535	15.57	1.40 ± 0.10	1.56 ± 0.10	9.8	10.1	10.3	24	41	40
604	20.58	1.59 ± 0.03	1.94 ± 0.02	11.5	11.5	11.5	130	130	130
794	21.31	1.74 ± 0.06	2.02 ± 0.03	11.9	12.4	12.2	110	130	135
823	21.14	1.85 ± 0.04	2.10 ± 0.04	12.2	12.5	12.5	85	100	100
847	20.34	2.31 ± 0.05	2.46 ± 0.05	13.7	13.7	13.9	24	24	24
926	15.61	1.07 ± 0.05	1.08 ± 0.05	7.4	7.4	7.7	130	155	160
951	15.57	1.33 ± 0.05	1.30 ± 0.05	8.6	8.9	9.1	40	105	115
994	19.69	1.81 ± 0.03	1.88 ± 0.04	11.9	12.0	12.0	60	65	65
1173	22.13	2.01 ± 0.11	2.21 ± 0.04	12.7	13.9	13.2	85	100	110
1235	15.37	1.07 ± 0.05	1.31 ± 0.04	9.1	8.4	9.8	75	85	92
1372	20.90	1.65 ± 0.04	1.79 ± 0.03	11.3	11.3	11.5	150	170	175
1552	20.98	1.63 ± 0.06	1.83 ± 0.07	11.3	11.5	11.7	150	160	177

Most of the stars in our sample with anomalous blue colors were found to be compromised at one or both colors by, either nearby bright, saturated stars, transient phenomena (meteor streaks, asteroids, airplanes tracks, etc), or non-linear CCD pixels. Stars with magnitudes that could not be determined to better than 10% accuracy, due to these factors, were discarded from further analysis.

There still remains a fair number of stars with colors too blue to be main-sequence objects. The fact that three of these stars are optical counterparts to the Hα sources, Haro

6-31 (GN Tau), 6-32, and 6-33, tentatively places them in the T-Tauri (or weak-line T-Tauri) populations. Most of these stars are also very faint (V > 20 mag), which is probably why the Hα surveys did not detect them. It is interesting to note that many of these stars lie within 5′ of dense molecular (so called "ammonia") cores, TMC-1, TMC-1A and TMC-1C (molecular maps of these regions can be seen in Myers *et al.* 1983; Cernicharo and Guelin 1987). As Beichman *et al.* (1986) point out, nearly half of all dense cores in molecular clouds have associated T-Tauri stars and/or embedded protostars (as evident in the far-infrared IRAS sources). Moreover, less obscured pre-main sequence stars appear to lie further away from the core centers compared to embedded IRAS sources, presumably due to their relatively advanced age. Of the IRAS sources located within Heiles' Cloud 2, only 04385+2550 (Haro 6-33) has an optical counterpart in this study (#1041).

It would thus appear that the anomalous blue stars of this study are more likely unobscured (or nearly unobscured, $A_v < 2$) T-Tauri stars. One star, #1029 is a double source. In Table 4.9, we list the positions and photometric properties of known T-Tauri stars and candidate pre-main sequence stars. For completeness, we also list the IRAS sources located within Heiles' Cloud 2; Table 4.10. The IRAS point source catalog data is taken from Heyer *et al.* (1987), and the IRAS faint source data is from Beichman, Boulanger and Moshir (1991).

Table 4.9

Candidate and Known T-Tauri Stars

ID #	RA[a] (hh:mm:ss)	Dec[a] (° ′ ″)	V	V-R	R-I
111	4:37:24.1	25:33:41	20.66	1.02 ± 0.04	1.76 ± 0.03
121	4:37:37.4	25:33:57	21.49	0.96 ± 0.09	1.40 ± 0.08
893	4:35:51.0	25:42:41	22.02	1.70 ± 0.11	2.48 ± 0.05
1012	4:37:33.6	25:49:44	21.51	0.82 ± 0.08	1.87 ± 0.06
1029[b]	4:38:04.2	25:50:21	18.70	1.05 ± 0.10	1.42 ± 0.10
1041[c]	4:38:37.2	25:50:43	18.02	1.35 ± 0.05	1.53 ± 0.06
1046	4:37:31.5	25:50:54	21.07	0.96 ± 0.09	1.70 ± 0.04
1147	4:38:49.5	25:54:40	20.98	0.79 ± 0.06	1.26 ± 0.05
1338	4:38:37.2	26:01:09	21.83	0.90 ± 0.11	1.41 ± 0.06
1382	4:37:23.7	26:02:32	20.54	0.88 ± 0.13	2.35 ± 0.07
1467	4:38:18.8	26:04:11	21.89	1.18 ± 0.09	1.20 ± 0.07
5555[d]	4:38:00.0	25:52:12	16.81	1.73 ± 0.02	1.97 ± 0.02
5556[e]	4:36:17.0	25:39:11	15.7	?	?

[a] Epoch 1950
[b] Double I-band Source
[c] Haro 6-33
[d] Haro 6-32
[e] Haro 6-31; GN Tau

Table 4.10

IRAS Point Sources

IRAS #	Other	RA[a] (hh:mm:ss)	Dec[a] (° ′ ″)	12μm S_ν(Jy)	25μm S_ν(Jy)	60μm S_ν(Jy)	100μm S_ν(Jy)
04361+2547	47[b]	4:36:09.4	25:47:27	1.8	18.9	44.5	34.7
04362+2539	47[b]	4:36:17.2	25:39:10	0.4	0.4	-0.5	-25
04365+2535	50[b]	4:36:31.0	25:35:52	1.2	8.6	35.7	38.5
04368+2557	51[b]	4:36:49.3	25:57:16	0.3	0.8	17.6	72.2
04369+2539	IC 2087	4:36:54.6	25:39:17	5.0	6.8	7.2	17.7
04371+2559	53[b]	4:37:05.1	25:59:41	0.4	0.5	-2.5	-56
04380+2553		4:38:02.3	25:53:51	0.4	1.1	10.9	17.9
04381+2540	50[b]	4:38:07.6	25:40:48	0.4	2.7	10.2	13.6
04385+2550	Haro 6-33	4:38:34.2	25:50:43	0.5	1.6	2.8	7.8

[a] Epoch 1950
[b] Beichman, Boulanger and Moshir (1991)

4.3.2.1 Stars with Only R and I Detections

As in the case with the Ophiuchus data, most of the stars in the Taurus sample were detected at R and I, but not V. Although one color analysis is limited, we can significantly narrow the sample of R,I stars to those consistent with being foreground to the cloud by using (R-I) color, and apparent I magnitude. The procedure, outlined in section 4.3.1.1 for the Oph data, makes use of two critical properties of the survey, its limiting visual magnitude, ~22.5, and the Taurus distance modulus, ~5.7, in order to constrain the possible spectral types of the R,I data. The survey is complete, to the distance of the cloud, to $M_V \sim 16.8$, which corresponds to an M6 V spectral type. From Table 4.1, this spectral type will have a mean R-I color ~2.2. Therefore, stars located near the cloud (the most likely region in the search volume) having R-I colors greater than 2.2 will not be

detected at V band, but will be detected at R and I. Along with this color constraint, we can compare the expected absolute I magnitude, derived from Equation 4.10, with the apparent I magnitude, thus deducing the expected distance from the Sun, according to Equation 4.8. Stars with distances less than that of the cloud, and having a color satisfying the constraint $2.2 < R\text{-}I < 2.5$, are consistent with being late-type M dwarfs in the range M6 - M8 V.

In Figure 4.28, we show the results of this technique. As before, the arrows indicate the direction the (V-R) color of star would change if the survey was complete to $M_V \sim 19$, or, if the star were simply a faint, heavily-reddened background star. A few of the stars in Figure 4.28 have a $(V_{lim} - R)$ color that is above the main-sequence track, and therefore, are most likely reddened stars. Most of the R,I stars have more than one possible solution. This is, of course, the major limitation of one-color analysis, as discussed before. The background solutions range from spectral type A0 to M4, located at distances 0.17 to 1.8 kpc, with F and G dwarfs dominating the solution sample. One of the stars, #2532, has only a foreground solution, and thus, is the best red dwarf candidate of the R,I set. In Table 4.11, a list of the R,I candidates, their photometry and solutions is given.

Table 4.11

R,I Analysis of Taurus Foreground Candidates

ID#	I	R-I	M_I^-	M_I^0	M_I^+	d^-(pc)	d^0(pc)	d^+(pc)	A_V	Type	d(pc)
1859	18.36	2.39 ± 0.06	13.3	13.6	13.9	78	89	101	4.1	M4 V	170
2105	18.56	2.31 ± 0.07	12.9	13.2	13.6	106	116	130	9.5	G3 V	600
2147	18.16	2.29 ± 0.05	12.8	13.1	13.9	90	101	113	3.6	M4 V	175
2228	18.04	2.19 ± 0.04	12.5	12.7	12.9	110	120	130	7.1	K5 V	420
2262	19.06	2.33 ± 0.11	12.8	13.3	13.9	110	140	178	9.8	F5 V	1600
2347	18.00	2.13 ± 0.04	12.2	12.9	12.8	120	133	145	9.5	G3 V	600
2387	18.22	2.23 ± 0.05	12.6	12.9	13.1	106	119	130	8.3	F8 V	1300
2411	18.51	2.24 ± 0.06	12.6	12.9	13.2	116	130	153	7.5	G3 V	840
2429	18.61	2.25 ± 0.07	12.6	13.6	13.3	116	130	160	10.4	A0 V	1800
2430	18.57	2.31 ± 0.07	12.9	13.2	13.6	100	120	136	10.4	A3 V	1500
2532	18.10	2.37 ± 0.06	13.3	13.5	13.8	75	82	92	12.2	-	-

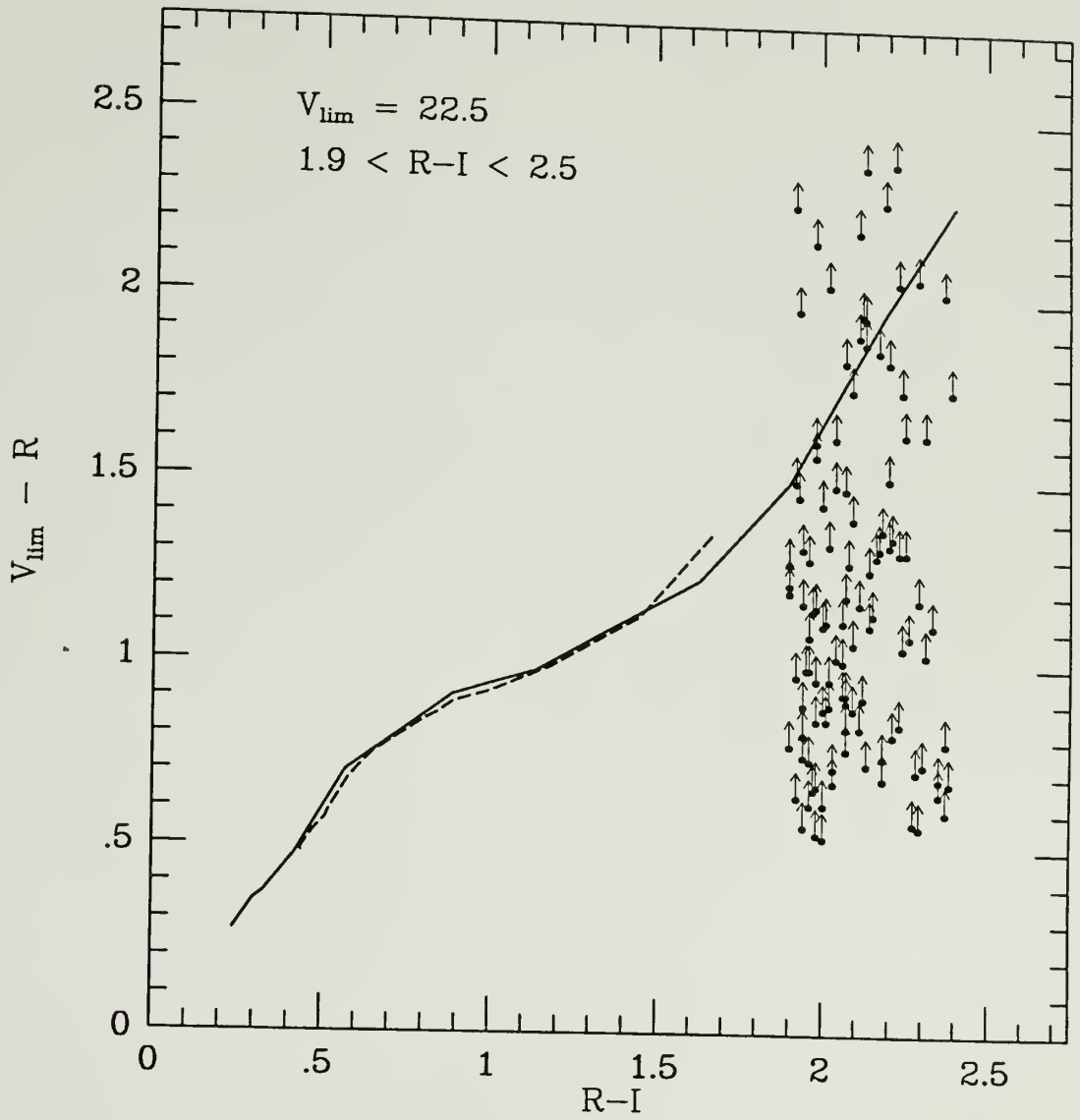

Figure 4.28 Taurus R,I foreground candidates with R-I colors between 2.2 and 2.5. The y-axis is (V_{lim} - R), where V_{lim} = 22.5. The arrows signify the direction of the true V-R color if the survey were deeper at the visual waveband. Mean colors of main-sequence G - M dwarfs are represented by a solid line, and giants by a dashed line.

4.4 Photometric Errors

In this section we will discuss in greater detail the types of errors that plague astronomical data, ranging from those of a stochastic nature, to the those of the less understood, more insidious, systematic genre. We will focus our attention to the kinds of errors that are specific to this study.

4.4.1 Random Errors

When undertaking astronomical photometry with CCD detectors, four basic factors constrain the *expected* accuracy of the data: sky brightness, seeing conditions, detector efficiency and the apparent brightness of the stars themselves. The flux due to the sky adds a random noise to the starlight. The seeing conditions, determined from the point spread function of a star or set of stars recorded on the CCD, control the size of the aperture used in the computation of the stellar flux. The worse the seeing conditions, the larger the aperture, and thus, the greater the random error due to the sky flux and detector read noise introduced into the photometry. Finally, the detector efficiency and the apparent brightness of the targeted stars determines the total exposure time needed to minimize the Poisson errors intrinsic to photon counting. We may quantify the expected accuracy of a photometric measurement, based on the factors mentioned here, using a signal to noise measure, as in Equation 2.4 (see Chapter 2, section 2.2.3, for additional information regarding S/N and the Tek 2048 detector).

As we discovered in the preceding sections regarding the Taurus and Ophiuchus photometry, there is, in all likelihood, an additional *unexpected* random error plaguing the stellar colors. We believe the errors are random because stars that are clearly reddened appear to symmetrically spread about the expected reddening curves. A certain amount of the scatter may also be due to systematic errors; see below. The scatter in the colors is

well modeled using a synthetic stellar density distribution subject to both expected signal to noise errors and additional random errors. It was found that the Ophiuchus data probably has an additional ~3% random error, and the Taurus data an additional 5 - 10% random error. It is not clear what the origin of this additional noise is. One possible culprit is the detector itself.

The CCD(s) used in this study is the Tek2048 (see Table 2.4 for a physical description), which is a first generation large format CCD[5]. Though its size may be wonderful, its cosmetic quality is frightful. Along with several bad pixel columns and blocks (which are easily avoided), there are literally thousands of non-linear response pixels (*a.k.a.* traps) which surface according to the degree of filling of the potential wells (the smaller the filling, the worse the problem). These pixel traps become important when they happen to be located within the point spread function of a star. Perhaps three hundred or so pixels are located within a typical aperture; a few bad pixels should not effect the total flux by more than one or two percent (this of course depends on the location of the trap in the point spread function, or in other words, on the statistical weight of the bad pixel). We have already seen that several stars in this study had photometric colors that were at least 10 - 20% in error due to their location near or within bad pixel columns or blocks. This does not mean to say that stars with bad pixel traps within their point spread function will also have grossly inaccurate colors; bad pixel columns/blocks are much more severe (that is, entirely unusable) than pixel traps, which tend to disappear as the wells fill.

These CCD cosmetic anomalies will add an additional error to the stellar flux computations, and this error should be mostly random since the degree of contamination

---

[5] Optical detectors of this size have been available for use by astronomers only since 1989 or so, however, I understand the Air Force and related defense contractors have been testing these types of detectors for some time now. The cutting edge of imaging technology is generally led by the military R & D network.

depends on the number and location of pixel traps in any given stellar spread function. The significant difference in the color spread between the Taurus and Ophiuchus data is consistent with the pixel trap scenario described here. The data sets were taken with two different detectors; The Taurus data using the original KPNO Tek2048, and the Oph data using a second ("poor cousin") detector. Although the second (and only surviving) Tek2048 was considered inferior -- mainly due to an ugly set of bad columns crowding one side of the detector -- it does in fact have a lower read noise than the first (by a factor of 2 - 3; note that the read noise is only important for short, ~ few minutes, exposures) and, once the bad columns are removed, is cosmetically respectable if the pixel wells are sufficiently filled (which is not a problem using V, R and I filters). The second Tek2048 detector, compared to the original, is thus the superior photon detector.

4.4.2 Systematic Errors

There are three general areas where systematic errors may have been introduced into the data: atmospheric extinction, transient sky conditions and photometric transformations. We will consider each factor separately, as they are distinct in origin and importance.

4.4.2.1 Atmospheric Extinction

Correcting for the dilution of starlight by the Earth's atmosphere is a simple matter if one knows the airmass and the extinction coefficients for each filter bandpass; see Equation 2.2. The airmass is easily (and accurately) determined from elevation of the targeted field. It is in the determination of the extinction coefficients where inaccuracies creep into the calculation of the atmospheric extinction.

Though we followed a number of blue-red standard stars through a range of airmasses during most nights of the Taurus and Oph observing runs, we were unable to determine the extinction coefficients to better than 15% at V, and 20% at R and I. The mean coefficient values were consistent with the "average" Kitt Peak coefficients, listed in Equation 2.3 (courtesy of Dr. George Jacoby). For the Taurus data, airmasses ranged from 1 to 1.4, and thus the extinction correction for this data is accurate to ~0.02 - 0.03 mags at V and R, and ~0.02 at I. (Note: the degree of atmospheric extinction at I band is about 40% that of V band). For the Ophiuchus data, the airmasses ranged from 1.7 to 2.2, and accordingly, the accuracy in the extinction corrections were about 0.01 mag worse than those of the Taurus data. If, for example, the extinction corrections are in error by +0.02 mag at V for the Taurus data, then there is a systematic *over*correction of the stellar magnitudes. Likewise, an error of magnitude -0.02 at V would result in a systematic *under*correction of the stellar magnitudes. In any case, systematic photometric errors of order 2 - 4% are well within the 10% bounds set for this study.

4.4.2.2 Transient Sky Conditions

When the atmosphere above the astronomer's telescope fills with clouds and water vapor, it usually (and sadly) marks the end of a night's work. Perfect weather conditions, in wonderful contrast, open the way for smooth and efficient data collecting. Most of the time, however, the astronomer is faced with a mix of the two extremes. As described in section 2.2.1 (see Table 2.3), the observing runs for this study were made under sky conditions that were generally "clear", with a few evenings during the Taurus run that were subject to short-term transient atmospheric conditions. Even if not visible to the naked eye, transient sky conditions are easily noticed when monitoring the flux of a star, or in the case of this study, when the magnitudes of stars between exposures differ by an amount

inconsistent with the change in airmass. If, for example, a cloud passes over the targeted field while exposing, the resultant flux of the stars detected by the CCD will be diminished by an amount depending on how *grey* the cloud was, and the corresponding magnitudes will be fainter than the true stellar magnitudes.

This condition is remedied by simply adding an offset to the cloud-contaminated CCD exposure, so that the stellar magnitudes match those of an uncontaminated exposure. In some cases, all the multiple exposures of a given CCD field may have some cloud contamination. In this case, it is important to have standard stars located in the CCD field so that transformation to a standard system is possible. In any case, self-consistency between multiple exposures is the key to minimizing errors due to grey sky conditions. This technique was applied to only a small fraction of the data.

Not only is the magnitude of transient sky extinction important, but so also is the time-scale of the changing atmospheric conditions. In this study, long exposures, ~20 to 30 minutes, were undertaken for the primary targeted fields. For sky conditions that changed slowly through the night (time-scale ~ 1 - 2 hours), the correction between multiple exposures amounted to about 0.02 - 0.04 magnitudes at all three bands; the estimated accuracy of these corrections is 2 - 3% (i.e., systematic magnitude errors no greater than 0.03 mag). In contrast to these generally pleasing conditions, the night of 10-26-89 was characterized by high humidity and rapidly varying sky conditions (a storm front had moved through earlier in the evening). Even correcting for grey - sky conditions there was a stellar brightness change that ranged from 0.1 to 0.3 magnitudes between each 20 minute I-band exposure, corresponding to an accuracy of 5 - 10%.

The accuracy of the grey-sky corrections is poor because the atmosphere was changing on a time-scale less than the 20 minute exposures; in effect, the exposures are no longer linear, but rather reflect the transient sky conditions. We elected to retain the data

from this evening, not withstanding its shortcomings, since it was crucial for the Taurus I-band data set. In any case, the remaining Taurus I-band observations from this run were obtained under more favorable conditions; despite the 10% systematic errors accrued in the I-band data from the 10-26-89 run, the total systematic error for all the Taurus I - band data is 4%.

In summary, though the atmospheric conditions during the Taurus observing runs were not ideal, they were sufficient for obtaining stellar fluxes with estimated systematic errors of about 2-3% at V and R, and 5% at I. The Ophiuchus run was subject to better weather conditions. We estimate the systematic errors due to transient sky conditions for this data set to be less than 2% at all three bands. In both cases, the errors are sufficiently less than the maximum ~10% photometric error necessary for this study.

4.4.2.3 Photometric Transformation

Photometric transformations calibrate raw or "machine" stellar magnitudes to a standard system familiar to professional astronomers around the globe. Several systems have been developed over the years, each with its unique advantages and drawbacks. In this study, we have utilized the Cousins (1976) VRI photometric system as it has a number of advantages keyed toward studies of this kind. Boeshaar and Tyson (1985) correctly point out that due to the complicated line blanketing in the spectra of late-type M dwarfs, photometric transformations between diverse standard systems can lead to systematic errors in the stellar magnitudes for these stars. For this reason it is desirable to use only one standard system for the photometric transformations. The standard stars used for calibration in this study, both Landolt stars and selected field stars, were previously calibrated within the Cousins system. Another advantage of the Cousins sequence is that the filter response functions of this system (see Table 2.7) closely resemble those of the

Kron system (1980) which were used in the calibration of the photographic data (see section 2.1). Finally, Bessell (1986) and Taylor (1986) have extensively studied the correlation of the Cousins filter response functions with stellar energy spectra of late-type dwarf stars. The differences between the CCD filter systems (and the quantum efficiency of the CCD itself) and the Cousins filter response functions, coupled with the red-band spectra of cool stars, is the primary source of systematic errors that are potentially introduced into the calibrations.

In section 4.1, we briefly discussed the convolution of the Cousins broad-band filters with the spectrum of late-type stars. We now consider the added complication of the CCD filter response functions within this scenario. As can be seen in Figure 4.2 (taken from Bessell 1986), the differences between the R and I filters used with CCD detectors at Kitt Peak National Observatory and the corresponding Cousins filter response functions is considerable. These differences are magnified in the case of convolution with a late-type dwarf spectrum, where deep molecular absorption features appear between the R and I filters and, particularly, within the I-band filter itself. In addition, most of the continuum flux of these cool stars lies longward of the I-band, which is why the R filter becomes much less sensitive to temperature differences along the late-type M dwarf sequence (section 4.1). The extended tail of the R_c filter response, ranging to ~8500 Å, compared to the relatively rectangular R_{ccd} filter response which cuts off at ~7300 Å, conspires to systematically brighten a cool red star measured using a Cousins R filter relative to what is measured using a Harris CCD filter. Therefore, the calibration of a machine red magnitude (*i.e.*, R_{ccd}) to a Cousins R magnitude, will involve a non-linear transformation that is a function of (R-I) color, such that the redder the stars, the greater difference between R_{ccd} and R_c. For the I filters, the situation is somewhat reversed. The Harris I filter has a tail

extending longward of the corresponding Cousins filter, which is more or less rectangular. A star measured at I_{ccd} will be systematically brighter than what is measured at I_c.

In this study we did not employ the standard Harris I-band CCD filter, but rather a RG715 interference filter (specifications listed in Table 2.6), because neither a Harris nor Cousins I filter was available at the time of the observing run (October 1989). The filter response function of the RG715 filter is not shown in Figure 4.2, but can be seen, for example, in Beckert and Newberry (1989). The filter has an I-band response characterized by a sharp cutoff at the blue end (~7000 - 7200 Å), behavior very similar to the Cousins I filter, peaks at ~7500 Å, and ramps downward all the way to ~10000 Å; this is clearly different from the Cousins I filter with its ~9000 Å sharp cutoff. Therefore, like the case with the R_c filter, the RG715 I band filter will be more sensitive to the flux of a cool star than the corresponding Cousins I filter. A star measured at I_{RG715} will be systematically brighter than the I_c measure. We are then left with the complicated situation where we are measuring the R-I color of a star using a R_{ccd} filter that records a systematically *fainter* magnitude than R_c, and an I_{RG715} filter that measures a systematically *brighter* magnitude than the corresponding I_c magnitude. It is not obvious what the functional relationship between the two colors should be. Here we turn to the data.

It can be seen in Figures 2.1 and 2.2 that the transformations between machine colors and standard Cousins colors generally follow linear relations. It is not clear whether a non-linear departure characterizes these relations at the reddest end of the plots (R-I ~ 2 - 2.2), as we might expect considering the differences in the filter response functions between the two systems. There are very few standard stars with very red colors (red Landolt stars are particularly scarce) and the scatter in the linear fit is large (~2-7%) for both the Taurus and Oph data sets. We have already discussed most of the dominant factors that lead toward this type of scatter (see sections 2.2.3 and 4.4.1). It is pertinent at this point to

reiterate one distinctive source of error belonging to the Taurus I-band transformations (as mentioned in section 2.2.3; see Figure 2.1b — many of the Taurus photometric standards did not have measurable I-band magnitudes because they are so bright that they saturated the CCD carrier potential wells. Both the nature of optical extinction (recall A_I is about 40% that of A_V) and the relative inexperience of the observer contributed to this unfortunate situation. Nevertheless, we were able to derive the fluxes of the saturated I-band standard stars by employing a technique in which we calibrated the point spread functions (the "wings" of the profiles where saturation did not occur) using profiles of non-saturated standard stars. This technique is considerably more difficult than simply performing aperture photometry, and consequently, the associated errors are 2 to 3 times greater than what would be expected based solely on signal to noise. The standard stars defining the reddest end of the Taurus (r-i) to (R-I) transformation relations reflect the uncertainties of this technique. Thus, although the linear fits are quite good, ~3%, at the bluer end of the color-color relation (R-I < 1.5), the linear relation redward of R-I ~ 1.5 has an uncertainty from 5 - 7%. Clearly any error belonging to the transformations would translate to a systematic miscalculation of the stellar magnitudes.

The lowest mass M dwarfs will have V-R and R-I colors that terminate around ~2.2 - 2.4 mag, which is redward of the linear calibrations seen in Figures 2.1 - 2.4. This of course means that we are left with little choice but to extrapolate the linear relations 0.1 - 0.3 magnitudes beyond their practical limit. The potential for a systematic error of order 5 - 10% for the reddest stars therefore cannot be ruled out. Of the three sources of systematic errors presented in this section, namely, atmospheric extinction, transient atmospheric conditions, and photometric transformation, we feel the last condition has the greatest potential for systematically distorting stellar magnitudes, even by ~10% for the reddest (and most interesting) stars of this study.

CHAPTER 5

STELLAR PROPER MOTION

The search for low mass stars has traditionally been confined to the immediate Solar vicinity as a consequence of the intrinsically low luminosities of these objects. Astronomers have identified numerous nearby stars, the majority being M dwarfs, by measuring the proper motions of stars photographed via large scale surveys (for example the Lick and Palomar Observatory surveys). Indeed, proper motion surveys are a powerful tool for separating both nearby stars and high velocity stars from the multitude of Galactic field stars that populate the astronomer's line of sight. It is easily seen that the angular shift in position, $\Delta\theta$, a star exhibits over time ΔT is constrained by its tangential velocity, σ_T, and distance, D, from the Sun, according to

$$\frac{\Delta\theta}{\Delta T} \propto \frac{\sigma_T}{D} \quad . \tag{5.1}$$

This is the essential definition of stellar proper motion.

In this study we hope to supplement the photometry and color-color results of Chapter 4 with proper motion measurements of the candidate foreground stars; if these are truly foreground objects, their maximum distances are delimited by the Taurus and Ophiuchus molecular clouds. Our motivation is augmented by the fact that we have deep photometric data extending over relatively long baselines. Along with our photographic data of Taurus (epoch 1986.8) and Ophiuchus (epoch 1982.4), and CCD data of Taurus (epoch 1989.9) and Ophiuchus (epoch 1990.4), epoch 1950 Palomar Sky Survey (POSS)

plates of these two fields are also available. In the following sections we describe our technique for computing proper motions, and present our results for the Taurus and Ophiuchus samples. In the next chapter we assemble the most likely foreground candidates based on the photometry, and, with an appropriately lower weight, the proper motions. We begin this chapter with a brief introduction to the kinematic properties of the Galaxy's stellar constituents, concentrating on the motions of the nearby stars and the Sun itself.

5.1 Galactic Stellar Kinematics

The fundamental observational parameters of the stellar kinematics of the Galaxy are the radial and tangential components of the space motions of the stars. These velocities are, of course, measured with respect to the Sun, and, as such, do not reflect the motions of the stars with respect to the Galactic center. In order to understand the kinematic properties of the nearby stars, we must therefore also understand the Galactic motion of the Sun/Earth system.

When astronomers allude to the motions of stars within the Milky Way, they are usually referring to stellar *peculiar velocities* measured with respect to the local standard of rest (LSR). The so-called "kinematic" LSR is an idealized reference frame in the Galactic disk whose mean motion is defined to be a circular orbit around the Galactic center, and accordingly, whose radial and z (direction perpendicular to the Galactic disk) velocity components are zero. Any given star (including the Sun) will have small departures from a perfectly circular orbit, and thus, will possess a peculiar motion with respect to the LSR. If we want to infer the space motions of a star based on tangential and radial velocity measurements, we must then consider the peculiar velocity of the Sun as well as the peculiar velocity of the star itself. For the case where an observed star is located far from the Solar neighborhood ($D >> 100$ pc), an additional component due to differential Galactic

rotation must also be considered. In this study, we are primarily concerned with nearby stars and as such, ignore the contribution due to differential rotation (the reader is referred to Mihalas and Binney 1981, chapter 8, for further discussion of this effect).

The space velocity of a star with respect to the Sun is related to the peculiar velocity of the star and Sun according to

$$\begin{aligned} U_* &= u_* - u_\odot \\ V_* &= v_* - v_\odot \\ W_* &= w_* - w_\odot \end{aligned} \tag{5.2}$$

where the * subscript refers to the stellar component and ⊙ to the solar component, and the velocity components follow the usual convention: u is the peculiar radial component as measured from the Galactic center, v is the peculiar tangential component in the plane of the Galactic disk, and w is the peculiar component perpendicular to the disk. We now consider the separate terms of Equation 5.2, the peculiar velocities of Galactic disk and spheroid stars, and the Solar motion with respect to the LSR.

5.1.1 Kinematics of Galactic Disk and Spheroid Stars

Through empirical and theoretical considerations, it has become apparent that the peculiar velocities of stars are correlated with age. The older the star, the more likely that it has dynamically interacted with another star, or more significantly, encountered a molecular cloud in the Galactic disk. The result of such a 'collision' is an exchange in energy. For example, a star passing near a giant molecular cloud (GMC) will receive an energy boost from the cloud because of the latter's vastly greater mass (~5 - 6 orders of magnitude) and gravitational potential energy; the result is an increase in the kinetic energy and hence, the space velocity, of the star. The 'gravity assist' that the star receives from the GMC is also governed by the relative encounter velocity between the two objects. This

star-cloud dynamical interaction was first theoretically described by Spitzer and Schwarzschild (1951); the reader is also referred to Mihalas and Binney 1981, chapter 7, for further discussion of other kinematic 'diffusion' effects.

The stellar age-velocity effect is clear in various spectral and luminosity classes (*cf.* Wielen 1974). M dwarfs, for example, have on average a higher peculiar velocity than stars of earlier spectral types, and super-giants have small velocities compared to those of the dwarf or giant luminosity classes since such stars have high masses (and thus young precursors). In general, the later the spectral type of a main sequence star, the higher its peculiar velocity. The kinematics of stars belonging to the Galactic spheroid/halo population are also influenced by star-star and star-cloud interactions; however, very few GMCs reside far from the plane of the disk and thus spheroid stars rarely encounter these objects.

It is conventional to describe the observed space velocities of stars in terms of gaussian dispersions; the stellar peculiar velocity components are thus associated with root mean square velocities $\langle u^2 \rangle^{1/2}$, $\langle v^2 \rangle^{1/2}$, and $\langle w^2 \rangle^{1/2}$. In Table 5.1, we list the mean peculiar velocities of disk dwarfs and giants, as well as spheroid subdwarfs (adapted from Mihalas and Binney 1981, Table 7-1).

Table 5.1

Peculiar Dispersion Velocities for Disk and Spheroid Stars*

Spectral Type	$\langle u^2 \rangle^{1/2}$ km s^{-1}	$\langle v^2 \rangle^{1/2}$ km s^{-1}	$\langle w^2 \rangle^{1/2}$ km s^{-1}
Disk Dwarfs			
F0	10	9	6
A0	15	9	9
A5	20	9	9
F0	24	13	10
F0	24	17	17
G5	26	17	20
G5	32	17	15
A0	28	16	11
K5	35	20	16
M0	32	21	19
M5	31	23	16
Disk Giants			
F	26	15	9
G	26	16	15
K0	31	28	16
K3	31	21	17
M	31	23	16
Spheroid			
Subdwarf	100	75	50

* Adapted from Mihalas and Binney 1981 (Table 7-1)

5.1.2 Solar Peculiar Motion

Due to the Sun's motion with respect to the LSR, stars located in the direction of the Solar motion (also known as the Solar apex) will appear, on average, to stream *radially* toward the Sun, and stars located opposite to the apex (the antapex) will appear to have a net motion divergent from the Sun. Stars located in between these two directions will have geometrically smaller motions depending on the angle made with the apex/antapex. This Solar anisotropy or "reflex" produces important proper motion (tangential) effects, particularly for stars located near the Sun.

As deduced from the net motions of stars, the Solar peculiar motion is found to be in the direction of Hercules ($\alpha_A = 18^h\ 4^m$, $\delta_A = +30°$; $\ell_A = 56°$, $b_A = +23°$). The speed $V_\odot$ is deduced to range from 15 - 20 Km s^{-1}, depending on the method used to compute the stellar peculiar velocities (*cf.* van de Kamp 1967); typical mean values of the peculiar velocity components are $(u,v,w)_\odot = (-9, 12, 7$ km $s^{-1})$. For a further discussion of these parametric values, see Mihalas and Binney (1981), chapter 6.

The effect of the solar reflex motion on the radial and tangential motions of the nearby stars is illustrated Figure 5.1. A star positioned at coordinates (α,δ) and located distance D from the sun makes an angle, λ, with the Solar apex, and its equatorial coordinates are related to those of the Solar apex by the angle ψ (see Figure 5.1a); using standard spherical trigonometry, we find

$$\cos\lambda = \sin\delta \sin\delta_A + \cos\delta \cos\delta_A \cos(\alpha - \alpha_A)$$
$$\sin\psi = \frac{\cos\delta_A \sin(\alpha - \alpha_A)}{\sin\lambda} \quad , \tag{5.3}$$

where (α_A, δ_A) are the coordinates of the Solar apex.

Let us now relocate into the reference frame centered on the star (Figure 5.1b). As observed from Earth, the star has a peculiar velocity described via radial and tangential

(a)

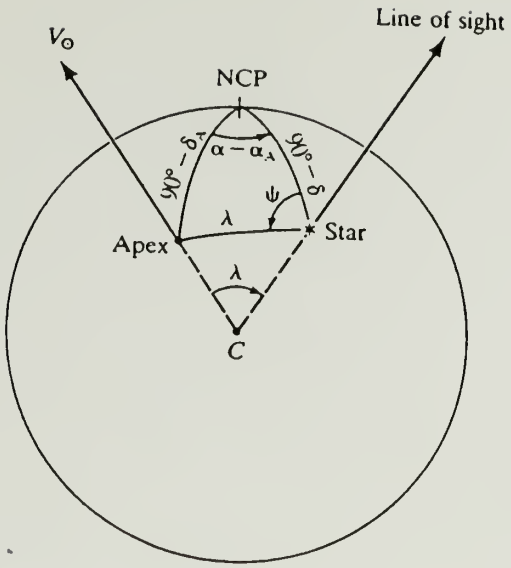

Figure 6-8. Relation of the angular distance λ and the angle ψ to the positions of the apex and a star on the celestial sphere.

(b)

Figure 6-9. The proper motion μ of a star may be expressed in equatorial components ($\mu_\alpha \cos \delta$, μ_δ) or in components (υ, τ), measured along the great circle joining the star and the apex, and in the direction perpendicular to this circle, respectively. All vectors shown lie in the plane of the sky.

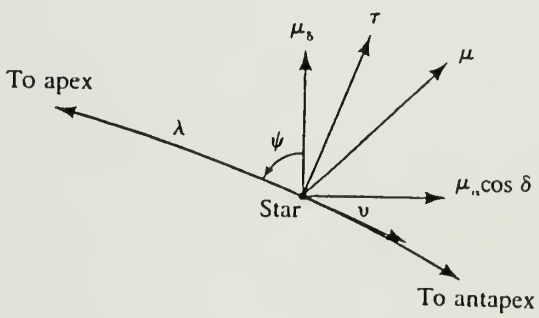

Figure 5.1 The effect of the Solar motion on the space motions of stars. In (a) we illustrate the geometry of the Solar-stellar motion in the frame of the celestial sphere. In (b) we consider the affect of Solar reflex as seen in the reference frame of the star. The figures are reproduced from Mihalas and Binney (1981).

components v_r and v_t, respectively. The radial velocity exhibited by the star will have, along with its true peculiar radial velocity, an added component due to the Solar motion toward the apex, of

$$v_r(true) = v_r + V_\odot \cos\lambda \tag{5.4}$$

The tangential motion is more complicated. Here we make use of the stellar equatorial proper motion, $\mu_\alpha\cos\delta$ and μ_δ, which are related to the apex-antapex direction via the so called "upsilon" and "tau" components, respectively υ and τ, in Figure 5.1. The tau component is not affected by the Solar reflex (but does figure importantly in the method of statistical parallax; see Mihalas and Binney 1981 for further discussion of this technique) and is given by

$$\tau = \mu_\alpha \cos\delta \cos\psi + \mu_\delta \sin\psi \quad , \tag{5.5}$$

The upsilon component, on the other hand, is affected by the Solar motion. The velocity along the upsilon axis is given by

$$v_\upsilon(true) = v_\upsilon + V_\odot \sin\lambda \quad , \tag{5.6}$$

where the observed upsilon peculiar velocity, v_υ, is a function of the tangential velocity, or in more practical terms, by the proper motions, according to

$$\upsilon = \mu_\alpha \cos\delta \sin\psi - \mu_\delta \cos\psi \quad . \tag{5.7}$$

Thus, the total motion in the upsilon direction is given by Equation 5.7, along with the Solar reflex contribution, $V_\odot\sin\lambda$; expressed in terms of angular motion in seconds of arc

per year, we have

$$\upsilon[''\, yr^{-1}] = \mu_\alpha \cos\delta \sin\psi - \mu_\delta \cos\psi + \left[\frac{V_\odot \sin\lambda}{4.74\, D}\right] \qquad (5.8)$$

where the distance D is given in parsecs and υ is negative in the direction of the apex. It can be seen from Equation 5.8 that the magnitude of the shift induced by the Solar reflex, similar to proper motion (see Equation 5.1), is inversely proportional to the distance from the Sun.

We illustrate in Figure 5.2 the magnitude of the Solar reflex as a function of distance for a variety of Solar-Stellar-apex orientations (specified in terms of angle λ). Here we adopt a Solar peculiar velocity of 18 km s^{-1}, and show solutions for λ = 90°, 70°, 50°, 30° and 10°, as well as the solution for the direction toward the Ophiuchus field, λ = 59°. The solution for the direction toward the Taurus field, using λ = 121°, is nearly identical to that of Ophiuchus. It can be seen that the largest magnitude of reflex occurs at λ = 90°, while at small angles, the reflex approaches zero. At distances beyond 300 pc or so, the Solar reflex at all orientations is less than ~1″ $cent^{-1}$, which is about the minimum measurable angular motion for most proper motion surveys. In this next section, we will discuss the implications of the Taurus and Ophiuchus reflex motions in our proper motion calibrations.

5.2 Results

In this section we present the results of the proper motion analysis for the Ophiuchus and Taurus stellar samples. The general technique that we use to determine the proper motions is to compare the 4-m photographic data and red POSS plates with the corresponding CCD data. Nearby stars, as measured from the photograph or CCD image will have angular offsets from their corresponding positions on the POSS plates, which

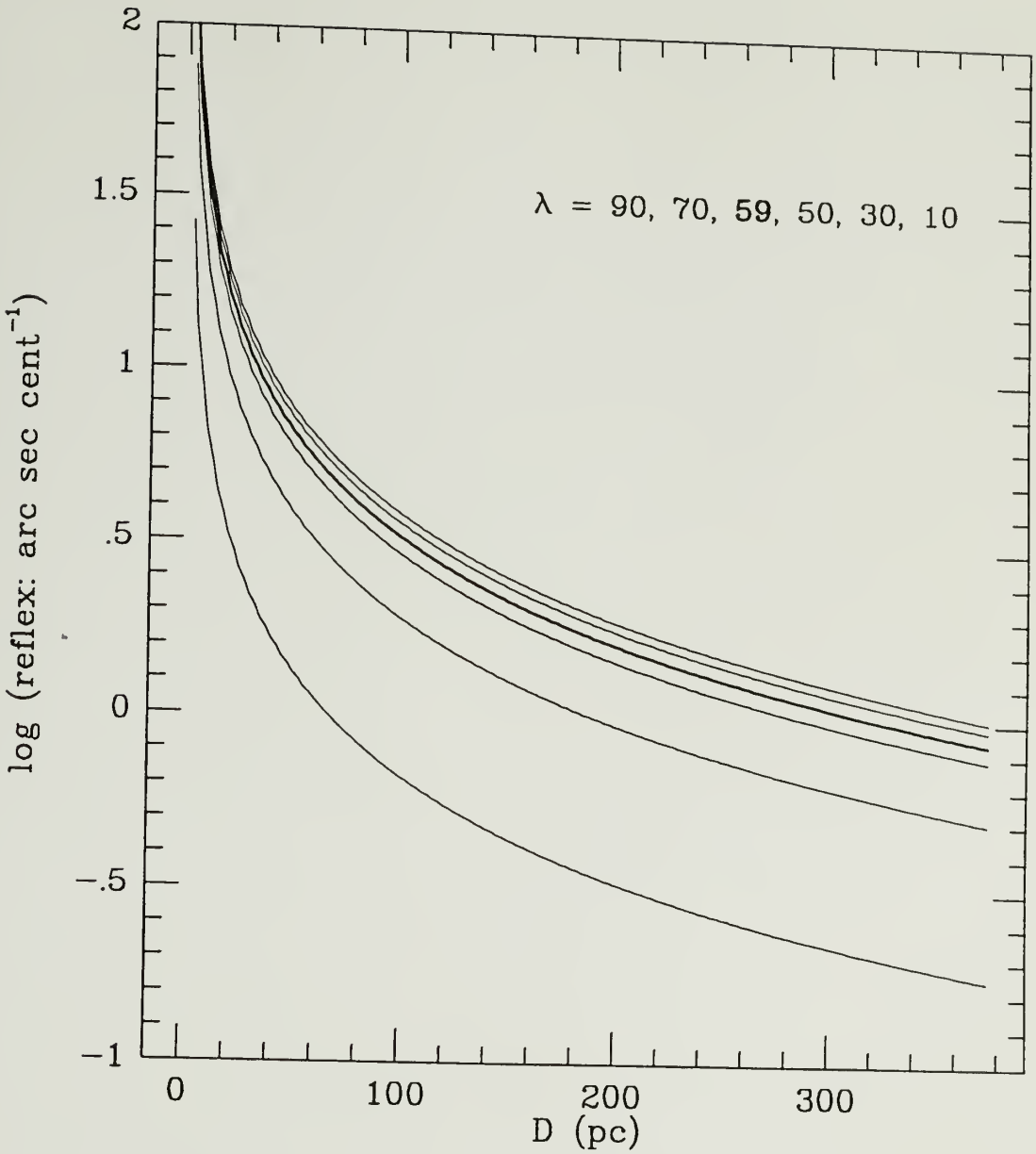

Figure 5.2 The Solar reflex to distance relation for a star located at a set of positional angles from the Sun - apex, given by $\lambda = 90°$, 70°, 59°, 50°, 30° and 10°. The solution corresponding to the directions toward the Taurus and Ophiuchus fields ($\lambda = 121°$ and 59°, respectively), is represented by the single dark solid line.

were exposed around 1950. The amount of angular shift a star will exhibit depends on its tangential velocity, σ_t, and distance, D, from the Earth, and the baseline (difference in epoch) ΔT between the respective data bases; a convenient form of this relation is reproduced here from Equation D.2 (see Appendix D):

$$\Delta\theta'' \cong \frac{0.211\ \sigma_t[km\,s^{-1}]\ \Delta T[yrs]}{D[pc]} \tag{5.9}$$

where the angular change is in seconds of arc. We adopt the conventional notation for the equatorial proper motion; accordingly,

$$\mu_\alpha \cos\delta \equiv \frac{-\Delta\theta_x}{\Delta T}\ ;\ \ \mu_\delta \equiv \frac{\Delta\theta_y}{\Delta T} \tag{5.10}$$

where the CCD rectangular coordinates (x,y) correspond to the respective equatorial coordinates (α,δ).

In appendix D we describe a method for computing the angular shifts for stars common to photographic or CCD and POSS data. The basic idea is to use a set of reference stars to define a positional mapping between the two data sets. The functional form of the mapping is a cubic polynomial, which we fit, via the reference stars, with the aid of a least squares analysis. The reference stars are chosen according to the following criteria: they must exhibit negligible angular shift (consequently, most of these stars will be field stars located far from the Sun), and they must as far as possible be uniformly distributed relative to each other (otherwise, the cubic polynomial will be biased for those stars closely grouped together). Note that stars with immeasurably small true proper motions will, in all likelihood, exhibit some spurious proper motion because of intrinsic uncertainties in the stellar source positions and goodness of the polynomial fits.

We expect the positional accuracy of the CCD data to be *at least* as good as the size of the pixels, ~0.77″. In fact, given that the source central positions are determined

using a centroid-type algorithm, the positional accuracies are typically closer to ~0.3″; however, the accuracy decreases for fainter stars because of the S/N uncertainty belonging to each pixel used in the computation of the positional centroid. For the faintest stars in this study, we expect the positional uncertainties to be in the range of 0.4 - 0.6″. The photographic data has correspondingly greater positional accuracy because the centroid computations are limited by only the size of the emulsion grain itself (grain size ~ several microns).

The errors associated with the least squares fit between field pairs is less easily characterized. The accuracy of the fit depends on the number of reference stars used, how the stars are distributed relative to each other, and the location of the fit; that is to say, due to the unequal distortions of the photographic and CCD data, the accuracy of the fit varies over the plate. The cubic polynomial is used for the explicit purpose of correcting for the non-linear distortions typical of Schmidt photographs; nevertheless, the distortions at the extreme edges of the plates and CCDs are very difficult (if not impossible) to correct with high precision.

The procedure to identify useful reference stars for a plate/CCD pair follows a number of steps and iterations: (1) identify several bright stars common to both the POSS plate and CCD image (here the human eye is an effective tool); (2) for these stars determine the relation between the POSS machine magnitudes and the CCD R or I magnitudes; (3) determine the cubic polynomial mapping for the plate to CCD using the reference stars found from step 1; (4) apply the mapping coefficients found from the previous step to the positions of all stars detected on the CCD, and determine stellar matches with the POSS stars (also check to see that the magnitude relation of step 2 holds); (5) from the pairs found in the previous step, select out those with small angular shifts (and such that they are uniformly distributed) and use these as new reference stars, and; (6)

repeat the cycle beginning at step 2. After several iterations, the fit converges in a least squares sense and the iteration process is terminated.

Once a satisfactory number of reference stars is identified such that the root sum dispersion in the relative angular shifts between the stellar pairs is minimized, the angular shifts for the remaining stars can be computed using the resultant set of polynomial coefficients.

The Taurus and Ophiuchus candidate foreground stars are next investigated for measurable proper motions. Their relative positions are further refined by fitting a polynomial (linear, quadratic, or cubic, depending on the available number of reference stars) to the *local* group of stars immediately surrounding each star. The local set of reference stars is, as far as possible, confined to a rectangular area typically ~5 - 10 arc minutes in diameter. The use of local mappings in the vicinity of each candidate star maximizes the accuracy of any corresponding angular shifts. The local fitting procedure also has the added feature of being an interactive process.

5.2.1 Proper Motions of the Ophiuchus Sample

The field pairs that we use in the calculation of the Ophiuchus stellar proper motions are:

CCD R-image vs. POSS E-plate; baseline = 35.9 years,
CCD I-image vs. 4m N-band photographic plate; baseline = 8.0 years.

The total number of reference stars used for the polynomial mappings consisted of ~150 CCD-POSS stars, and ~550 CCD-4m stars. There was a vastly greater number of CCD-4m reference stars because both of the latter data sets have similar limiting brightness: $I_c \approx I_N \sim$ 21 mag. In the first case, the R limiting magnitude of the POSS plate is about 20 mag, or ~2 mag brighter than the CCD limiting R magnitude, which reduces the number of pairs. The magnitude relations between the data bases are shown in Figures 5.3 and 5.4, where

we plot the CCD-POSS and CCD-4m reference star magnitudes. One can see in Figure 5.3 that the accuracy of the POSS machine magnitude (denoted by T mag) begins to break down at ~12.6 (corresponding to $R_c \sim 20$ mag); furthermore, the relationship between it and R_c is non-linear. In contrast, the CCD-4m magnitude relation, Figure 5.4, is linear (with a slope ~ 1), and is maintained well up to the limiting magnitude, I ~ 20 - 21. From these two plots alone, we may surmise that derived CCD-4m stellar angular shifts will have greater accuracy than those of CCD-POSS stellar pairs; however, the baseline of CCD-POSS pair is 4.5 times longer, and consequently, this measure will be more useful for identifying stars with small intrinsic proper motions.

We show the relative (x,y) locations of the reference stars within the Oph field, along with the angular shifts associated with the mapping transformation (represented in the Z-direction) using 3-D surface plots; Figure 5.5 represents the CCD-POSS stars, and Figure 5.6 the CCD-4m stars. Most of the Oph area is devoid of stars (recall that the molecular cloud is very opaque), and consequently, it is difficult to collect a set of reference stars that are distributed relatively uniformly over the CCD field. To minimize fitting errors due to these field inhomogeneities we subdivide the Oph field into 4 smaller areas, each with roughly the same number of reference stars.

The fits are not as good for the CCD-POSS stars as they are for the CCD-4m stars. We may evaluate the errors associated with the fitting procedure (described in Appendix D) for the two plate pairs by plotting histograms of the angular shifts derived for the reference stellar pairs. In Figure 5.7, we plot the histogram for the CCD-POSS pair total angular shifts, expressed in terms of Δr^2, where $\Delta r^2 = \Delta x^2 + \Delta y^2$. It is important to note that the values are not symmetrically distributed about $\Delta r^2 = 0$, but rather can be characterized by a distribution centered at some mean value, $\overline{\Delta r^2}$, with a mean variance, $\sigma^2 = \langle \Delta r^4 \rangle$.

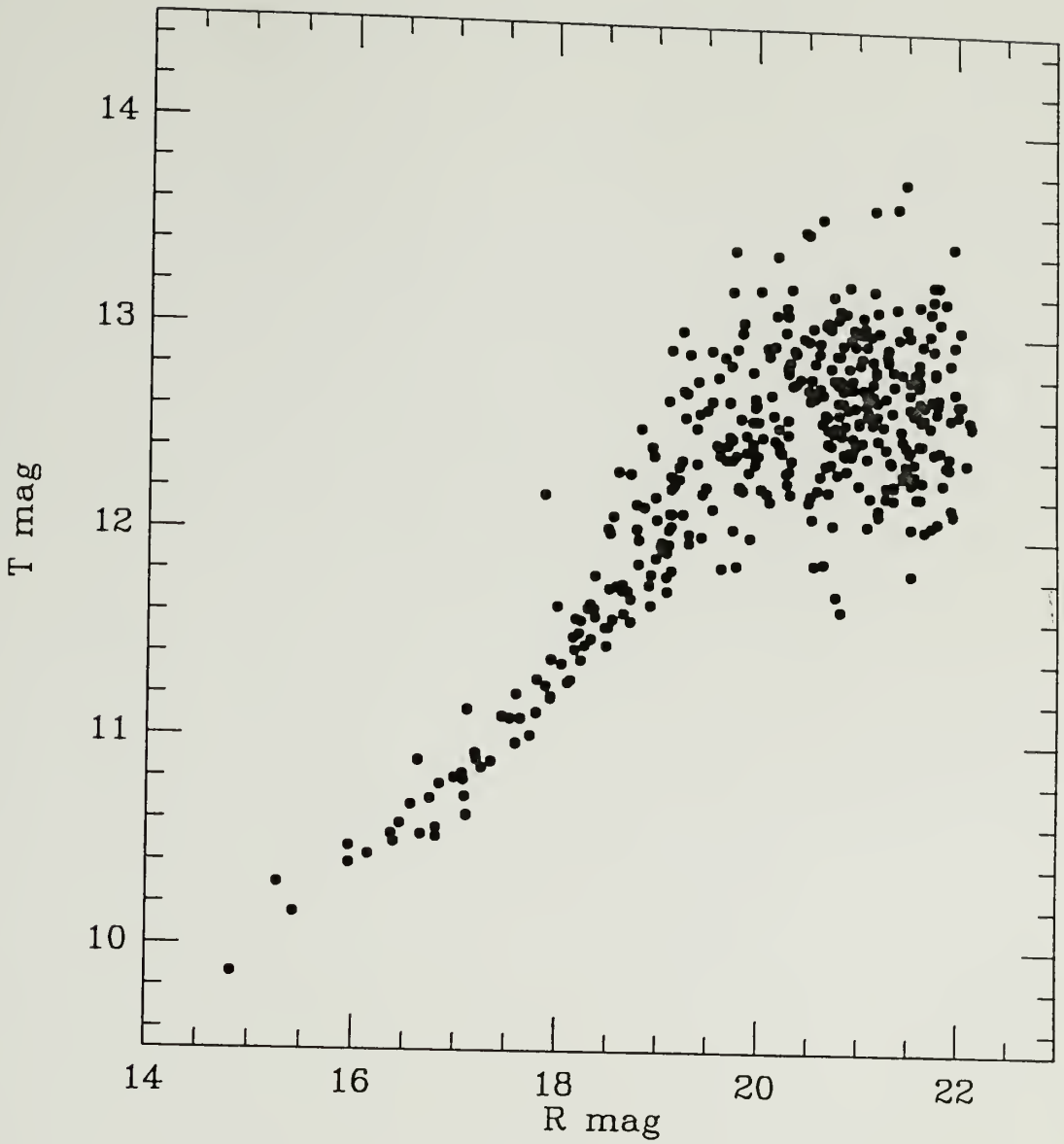

Figure 5.3 Magnitude relation for the Oph CCD-POSS stellar reference pairs. The machine magnitudes of the POSS stars are denoted by T mag, and the CCD stars by R mag.

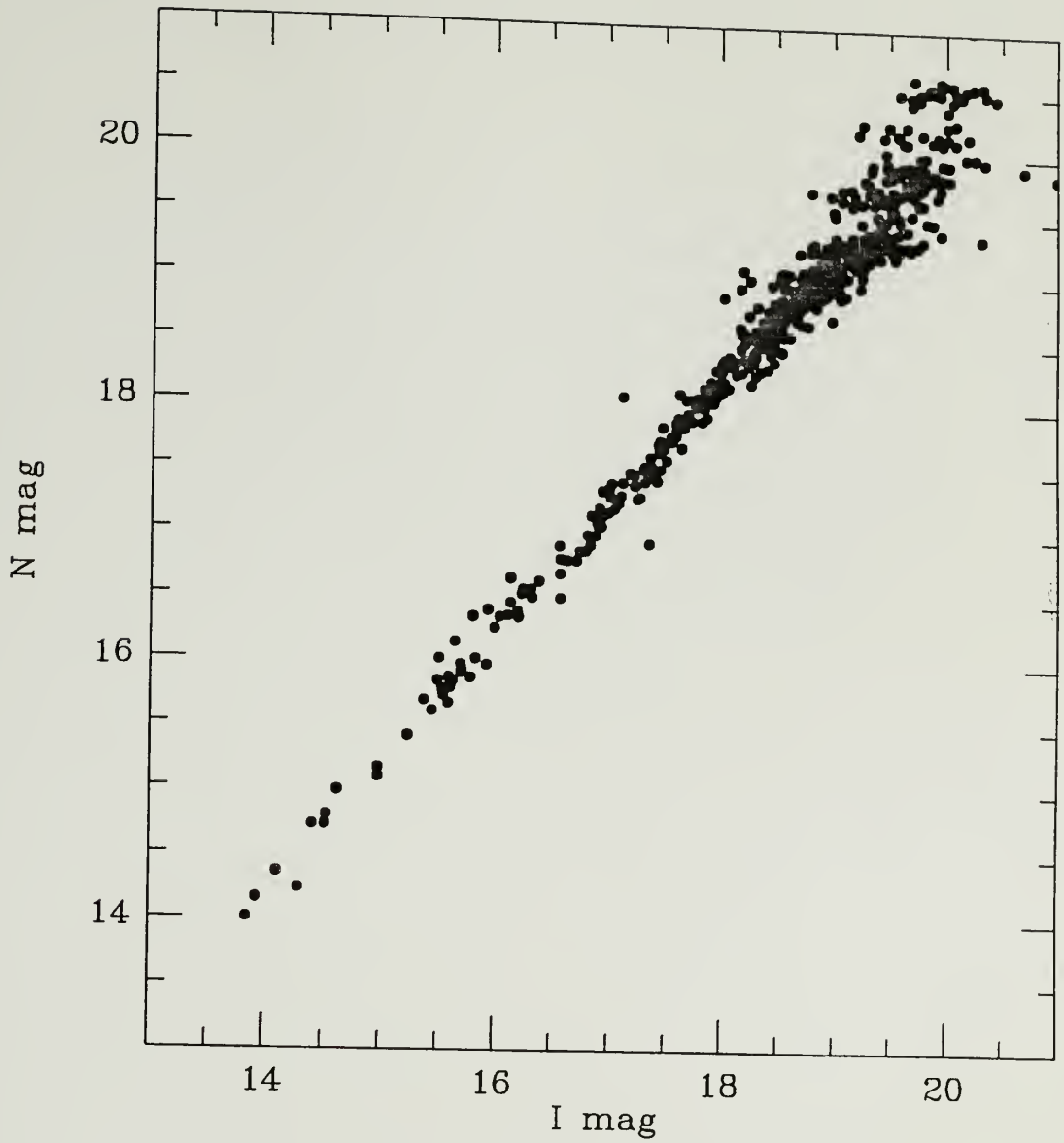

Figure 5.4 Magnitude relation for the Oph CCD-4m stellar reference pairs. The 4-m data is at Kron N band, and the CCD data at I_c mag.

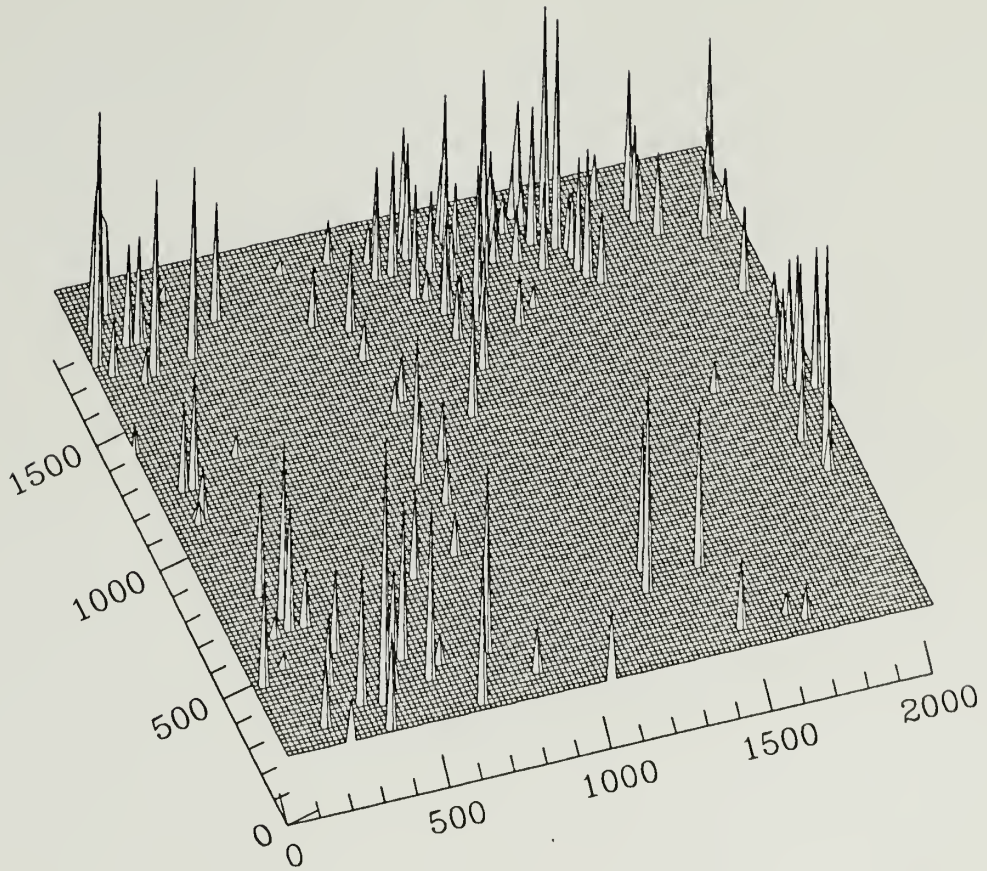

Figure 5.5 Locations and angular shifts of the Oph CCD-POSS stellar reference pairs. The x,y positional coordinates are those of the CCD. The third dimension represents the total angular shift, $\Delta r = (\Delta x^2 + \Delta y^2)^{1/2}$. The maximum angular shift is ~2″. The orientation altitude and azimuth are 45° and 20°, respectively.

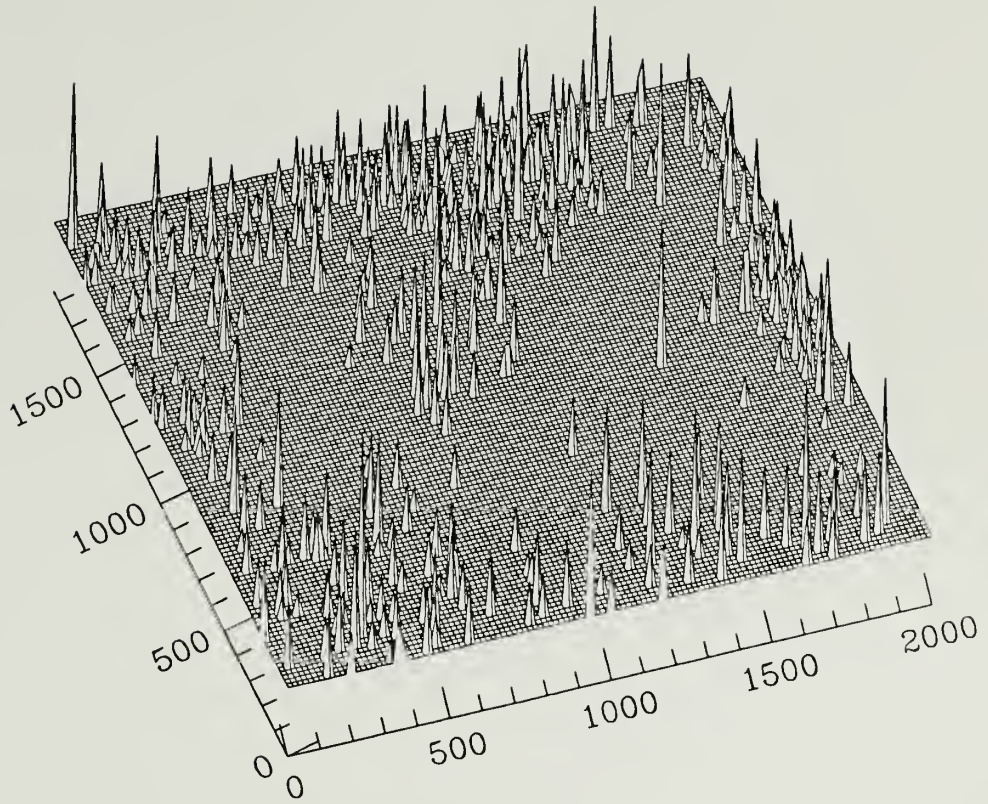

Figure 5.6 Locations and angular shifts of the Oph CCD-4m stellar reference pairs. The x,y positional coordinates are those of the CCD. The third dimension represents the total angular shift, $\Delta r = (\Delta x^2 + \Delta y^2)^{1/2}$. The maximum angular shift is ~1″. The orientation altitude and azimuth are 45° and 20°, respectively.

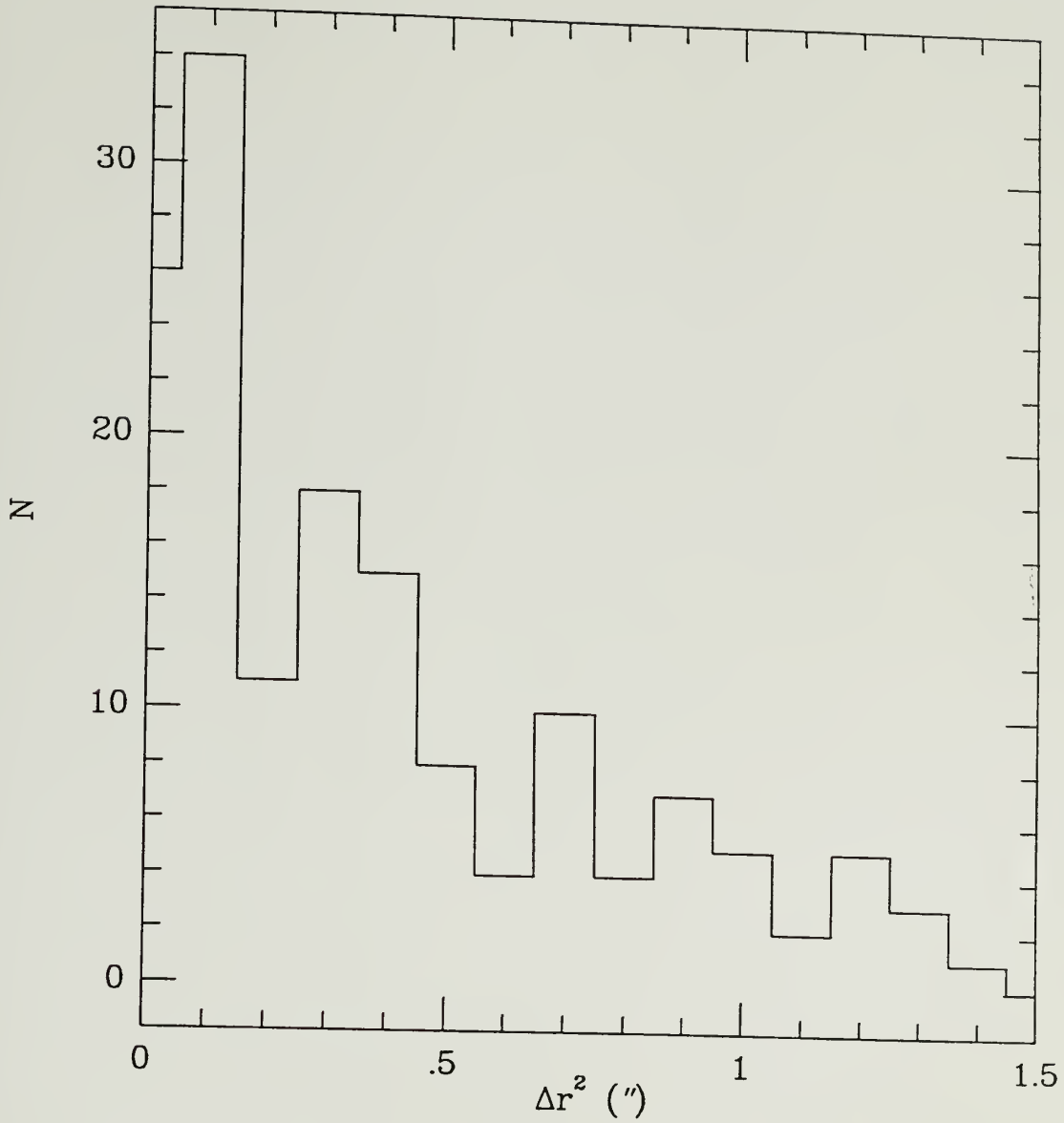

Figure 5.7 Histogram of the square of the total angular shifts of the Oph CCD-POSS stellar reference pairs.

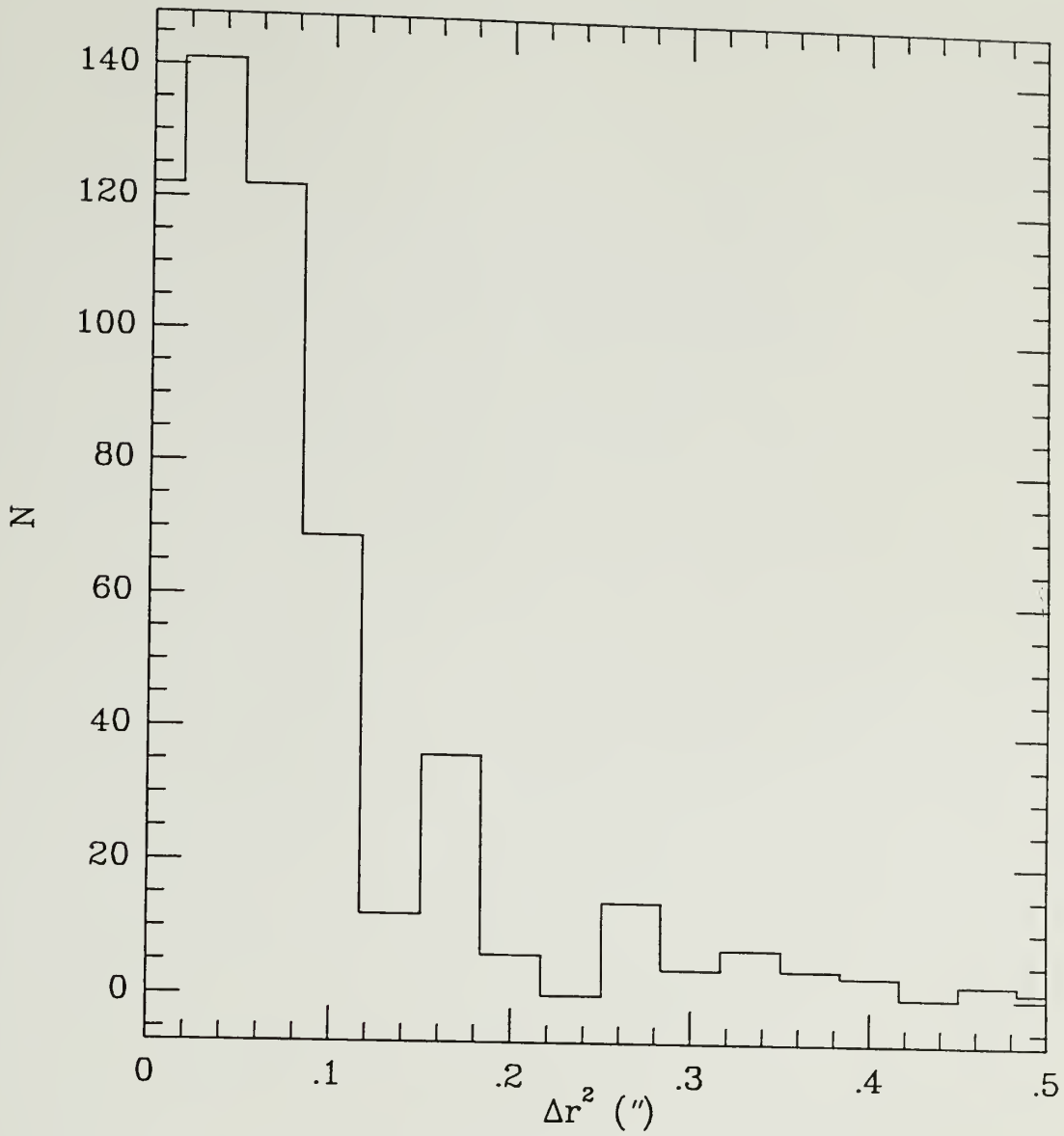

Figure 5.8 Histogram of the square of the total angular shifts of the Oph CCD-4m stellar reference pairs.

The offset arises from the fact that the background stars are not located at infinity and are subject to both proper motion and Solar reflex displacements.

We demonstrated in section 4.2 (see Figure 4.4) that the background field star population is dominated by G and K dwarfs. Let us estimate their expected proper motion. These stars have typical absolute visual magnitudes between 5 and 6. According to the observed stellar densities, their apparent brightness peaks around V ~ 21 - 22. If we assume that the mean visual extinction of the ρ Oph cloud is about 8 mag (see the Ophiuchus visual extinction map, Figure 3.2), then the adjusted distances of these objects are between 250 and 630 pc. If we assume a typical velocity dispersion of 25 km s^{-1} for these stars (see Table 5.1), the typical proper motion of field G and K dwarfs is between 0.8 and 2.1″ $cent^{-1}$. These values translate to an angular shift (over a 35.9 year baseline) between 0.3 and 0.8″; while an ensemble average of the proper motions of these field stars should cancel, that is, $\langle \Delta x \rangle = \langle \Delta y \rangle = 0$, they do contribute to the statistics of Δr^2 as described below.

We now estimate the contribution from the Solar reflex motion in the direction of the Oph field. Using the spherical geometry relations, Equation 5.3, we find that $\lambda = 59°$ for Ophiuchus. Assuming a heliocentric velocity of 18 km s^{-1}, the typical Solar reflex motion expected from G and K field dwarfs in that direction then ranges between 0.5 to 1.3″ $cent^{-1}$, which translates to an angular shift (over a 35.9 year baseline) between 0.2 to 0.5″.

Our concern here is to determine the minimum detectable threshold of any proper motions measured with the CCD-POSS and CCD-4m materials. To do so, we must understand how the motions of the reference stars and their uncertainties enter into the Δr^2 distributions.

The squared angular shift of the i^{th} reference star is given by

$$\Delta r_i^2 = \Delta x_i^2 + \Delta y_i^2 \qquad (5.11)$$

where Δx_i and Δy_i are the x and y components of the shift. We assume that these can be written

$$\begin{aligned} \Delta x_i &= \delta x_i + \bar{x} \\ \Delta y_i &= \delta y_i + \bar{y} \end{aligned} \qquad (5.12)$$

where $\bar{x}$ and $\bar{y}$ are the mean offsets due to the Solar reflex motion, and δx and δy are normally distributed uncertainties in the stellar positions (which include proper motions) and which have zero mean. For simplicity, we assume that the uncertainties are symmetric about the x-y plane; accordingly,

$$\sigma^2 = \delta x^2 = \delta y^2 \quad . \qquad (5.13)$$

It follows that the mean expectation value of Δr^2 is

$$\langle \Delta r^2 \rangle = 2\sigma^2 + \bar{r}^2 \quad , \qquad (5.14)$$

where $\bar{r}^2$ is defined to be

$$\bar{r}^2 = \bar{x}^2 + \bar{y}^2 \quad . \qquad (5.15)$$

The second moment of the Δr^2 distribution is

$$\langle \Delta r^4 \rangle = 8\sigma^4 + 8\sigma^2\bar{r}^2 + \bar{r}^4 \quad . \qquad (5.16)$$

The expected mean and variance are in fact related, and thus we may solve for $\bar{r}$, according to

$$\bar{r}^4 = 2\langle \Delta r^2 \rangle^2 - \langle \Delta r^4 \rangle \quad . \tag{5.17}$$

Finally, the dispersion can be solved for using Equations 5.14 and 5.17.

The mean expectation values corresponding to the Ophiuchus CCD-POSS and CCD-4m distributions, Figures 5.7 and 5.8, are

$$\begin{aligned} \langle \Delta r^2 \rangle &\approx 0.38 \ , \quad CCD\text{-}POSS \\ \langle \Delta r^2 \rangle &\approx 0.06 \ , \quad CCD\text{-}4m \end{aligned} \tag{5.18}$$

where the units are in arc seconds squared. We adopt the square roots of these values, 0.6″ and 0.2″, respectively, as the minimum detectable thresholds of any resultant proper motions measured with the CCD-POSS and CCD-4m material. We may also check these values for consistency with the expected Solar reflex motion and position uncertainties by applying Equation 5.17. The second moment of the mean expectation value, $\langle r^4 \rangle$, was found to be 0.2 and 0.0 arc seconds to the fourth power for the CCD-POSS and CCD-4m data, respectively. Solving for $\bar{r}$ using Equation 5.17 indicates that the resultant estimate for the Solar reflex motion is 0.5″ over 36 years (CCD-POSS) and 0.2″ over 8 years (CCD-4m). These values are consistent with the expected reflex motion a field G or K dwarf would exhibit. Finally, the dispersion, σ, obtained from the data is 0.3″ for the CCD-POSS distribution and 0.1″ for the CCD-4m distribution.

Note that the difference between the Δr offsets of the CCD-POSS and CCD-4m distributions are consistent with our interpretation that the offset is due, in part, to the baseline difference, and to the accuracy of the polynomial mapping — as mentioned earlier, the CCD-4m plate fit has the luxury of having almost 4 times as many reference stars available than the CCD-POSS mapping. All normalized proper motions, in seconds of arc

per century, will reflect the accuracy of the measured angular shifts, as well as the length of the field pair baseline.

For example, consider the typical angular shift a nearby M-dwarf would exhibit over the baselines of the Oph fields. Given a mean dispersion velocity of ~28 km s^{-1} for these stars (see Table 5.1), the angular shifts across the observer's line of sight for a number of distances from the Sun are the following (Table 5.2):

Table 5.2

Expected Angular Shift for an M-dwarf Star*

D (pc)	CCD vs. POSS $\Delta\theta''$	CCD vs. 4m $\Delta\theta''$
5	42	9.5
10	21	4.7
25	8.5	1.9
50	4.2	0.9
75	2.8	0.6
100	2.1	0.5
160	1.3	0.3

* Assuming a dispersion velocity of 28 km s^{-1}.

It can be seen that the CCD-POSS analysis should be able to discern the angular shift of a typical M dwarf out to distances ~ 125 pc, and that the CCD-4m data permit the detection of M dwarf stars located within 25 pc of the Sun. The CCD-4m shifts are not too useful for our purposes, since we want to be complete to the distance of the Oph cloud, ~160 pc (note that several foreground candidates appear to be located near the cloud). However, foreground candidate stars that possess a high apparent proper motion (detected using the CCD-POSS pairs) should also be detectable with the CCD-4m pairs. The CCD-

4m data is, therefore, used as a confirming eheck of the CCD-POSS data, whose measured angular shifts are less aeeurate, partieularly at the edges of the field.

5.2.1.1 Photometric Foreground Candidates

In Table 5.3, we show the proper motion results for the photometrie foreground candidates described in Chapter 4 (see Table 4.2). Ineluded in the table are the equatorial proper motions (Equation 5.10), the estimated error and the dedueed tangential velocity, where we have made use of Equation 5.9 and the dedueed distances from Table 4.2. The aecuraey of the angular shifts estimated for these stars was maximized by performing a final, local fit between the two fields. The smaller the area of the fit, the more aecurate the mapping, sinee the scale of the plate distortions is relatively large. However, the size of the local area whieh could be fit depended upon the number of referenee stars near the candidate star. Generally, the smallest possible reetangular area eontaining enough stars for the final mapping fit was chosen. These are shown in Figures B.1(a-u), in whieh we show the loeal fit areas for eaeh photometric foreground eandidate in the 4m, CCD, and POSS data sets; these figures also serve as coarse finding charts for these stars. The photometric candidates are the large eirele in each box. The reference stars used in the polynomial mappings are represented by filled cireles; the other stars are represented by crosses. The angular shifts obtained for the two baselines are also shown in each figure.

A few of the CCD-POSS proper motion measurements listed in Table 5.3 are undoubtedly in error. Candidates #19 and #74 have deduced tangential velocities that are unphysical, whieh strongly suggests that the stellar pairs are mismatehed; in any case, the proper motions computed using the CCD-4m pairs eorresponding to the two stars are not consistent with longer-baseline values. Indeed, one can see from Figures B.1c and B.1n that a fair amount of eonfusion is associated with the areas around these stars.

Table 5.3

Proper Motions of the Ophiuchus Photometric Candidates

ID #	CCD vs. POSS[a]				CCD vs. 4m[b]			
	$\mu_\alpha \cos\delta$ ″ cent^{-1}	μ_δ ″ cent^{-1}	$\delta\mu$[c] ″ cent^{-1}	V_t km s^{-1}	$\mu_\alpha \cos\delta$ ″ cent^{-1}	μ_δ ″ cent^{-1}	$\delta\mu$[c] ″ cent^{-1}	V_t km s^{-1}
13	-12.3	10.0	3.1	39 ± 15	6.3	6.3	1.8	22 ± 8
18	2.2	0.3	1.2	18 ± 16	2.5	-1.3	1.8	23 ± 10
19	-73	-31	3	670 ± 90	1.3	-5.0	1.8	44 ± 26
25	-4.7	2.8	2.1	4 ± 4	3.8	2.5	3.9	5 ± 6
26	-1.7	0.8	1.2	11 ± 11	2.5	-1.3	1.8	18 ± 17
26	-72	42	3	203 ± 23	3.8	-5.0	3.9	15 ± 12
33	2.2	-0.3	2.1	3 ± 3	0.0	-1.3	1.8	1 ± 2
34	-0.6	1.9	1.6	3 ± 3	0.0	-2.5	1.8	3 ± 4
37	-4.7	0.8	1.9	30 ± 19	3.8	-1.3	1.8	25 ± 17
42	-	-	-	-	1.3	-8.8	3.5	19 ± 13
33	-3.1	-0.3	1.2	12 ± 7	1.3	3.8	1.8	16 ± 11
48	-	-	-	-	-	-	-	-
59	0.6	-0.3	1.2	1 ± 1	3.8	1.3	1.8	3 ± 3
74	-34	55	3	374 ± 50	1.3	2.5	1.8	16 ± 16
76	5.8	-1.9	1.9	28 ± 11	6.3	1.3	1.8	29 ± 13
80	-0.3	-1.9	1.4	7 ± 8	1.3	3.8	2.0	14 ± 10
183	-0.3	-1.1	1.2	-	8.8	8.8	1.8	-
183	-20	51	2	55 ± 4	2.5	0.0	1.8	3 ± 3
223	30	34	3	173 ± 16	-5.0	1.3	1.8	20 ± 11
908	2.8	-1.7	1.2	11 ± 7	1.3	0.0	1.8	4 ± 7
909	-0.3	-11	1.2	44 ± 9	-2.5	-11	2.5	46 ± 20

[a] 35.9 year baseline.
[b] 8.0 year baseline.
[c] the standard error in one coordinate.

Both source confusion, and the relatively bright limiting magnitude of the POSS contribute to such mismatches. Recall that the POSS E-plate limiting magnitude is about 20; in some cases, for example near the edges of the POSS plate and in confused regions, this limiting magnitude may be ~1 magnitude brighter.

Other foreground candidates stars that have very high CCD-POSS proper motions include #28, 183 and 223. The proper motions of these stars are probably in error since the corresponding CCD-4m proper motions do not reveal anything unusual.

Several of the stars from Table 5.3 do not have measurable proper motions (that is, their angular shifts fall within the expected minimum detection threshold); these include #18, 25, 26, 33, 34, 59, and 80. Star #48 does not have a proper motion estimate because of source confusion. Of course, nearby stars that exhibit only small proper motions may, in fact, have intrinsically small tangential velocities, or may even have space motions that are along the direction of the Solar motion (in which case the tangential velocity is canceled or diminished by the Solar motion). This is the major problem of proper motion surveys: they are kinematically biased towards stars with large tangential velocities. Small proper motions are expected for candidates 18 and 26 based on their deduced distances (see Table 4.2), and in that sense the proper motions of #10, 18, 26, 37, 42, 43, 76, 908 and 909 are clearly consistent with their being foreground stars. The white dwarf candidate, #113, has a measurable proper motion according to the CCD-4m pair of $\mu_r \approx 12''$ cent^{-1} (it is less clear what is happening with the CCD-POSS pair, since confusion is a problem for the POSS local area). If we use the mean dispersion velocity of 40 km s^{-1} typical of white dwarfs, then the deduced distance of the star from the Sun would be ~70 pc, and its corresponding absolute magnitude $M_V \approx 13.1$. This is consistent with typical intrinsic values for these evolved degenerate stars.

As we discussed early in this chapter, the Solar apex motion will tend to cause reflex angular shifts for nearby stars. Let us consider the reflex in the direction of the Ophiuchus field. Using the spherical trigonometry relations, Equation 5.3, we find that λ = 59° and ψ = -24° for Ophiuchus. The magnitude of the reflex depends on the distance (see Equation 5.8 and Figure 5.2), and for a distance of 160 pc and a heliocentric velocity of 18 km s^{-1}, the reflex is ~ 0.02″ yr^{-1}, or equivalently, 2″ $cent^{-1}$. Thus, a star associated with the Ophiuchus molecular cloud should have a total proper motion of ~2″ $cent^{-1}$ toward the southwestern part of the cloud (*i.e.*, 24° west of the declination axis).

In Figure 5.9, we plot the equatorial proper motions of the candidate stars listed in Table 5.3. We also indicate the direction and magnitude of the expected Solar reflex in the plot. It is interesting to note that the protostellar candidate #42 (IRS15a,b) has a proper motion higher than expected for a star with the space velocity typical of a young star at the distance of the Oph cloud. However, the offset of the star is less than 2σ (as can be seen from the error bars); the fit for the CCD-4m pair is quite poor, predominantly due to the lack of nearby reference stars (see Figure B.1j). This double star system is located in the densest region of L1689, consequently, no background stars are able to leak through the cloud within a radial distance of about 7 - 10′ from this object. We were left with little choice but to use the global fit in order to estimate the shifts for this star. The other stars suspected to be associated with the Oph cloud, namely #59, 25 and 33, in any case have proper motions (or the lack thereof) consistent with their being at a distance of at least as far as the Oph cloud.

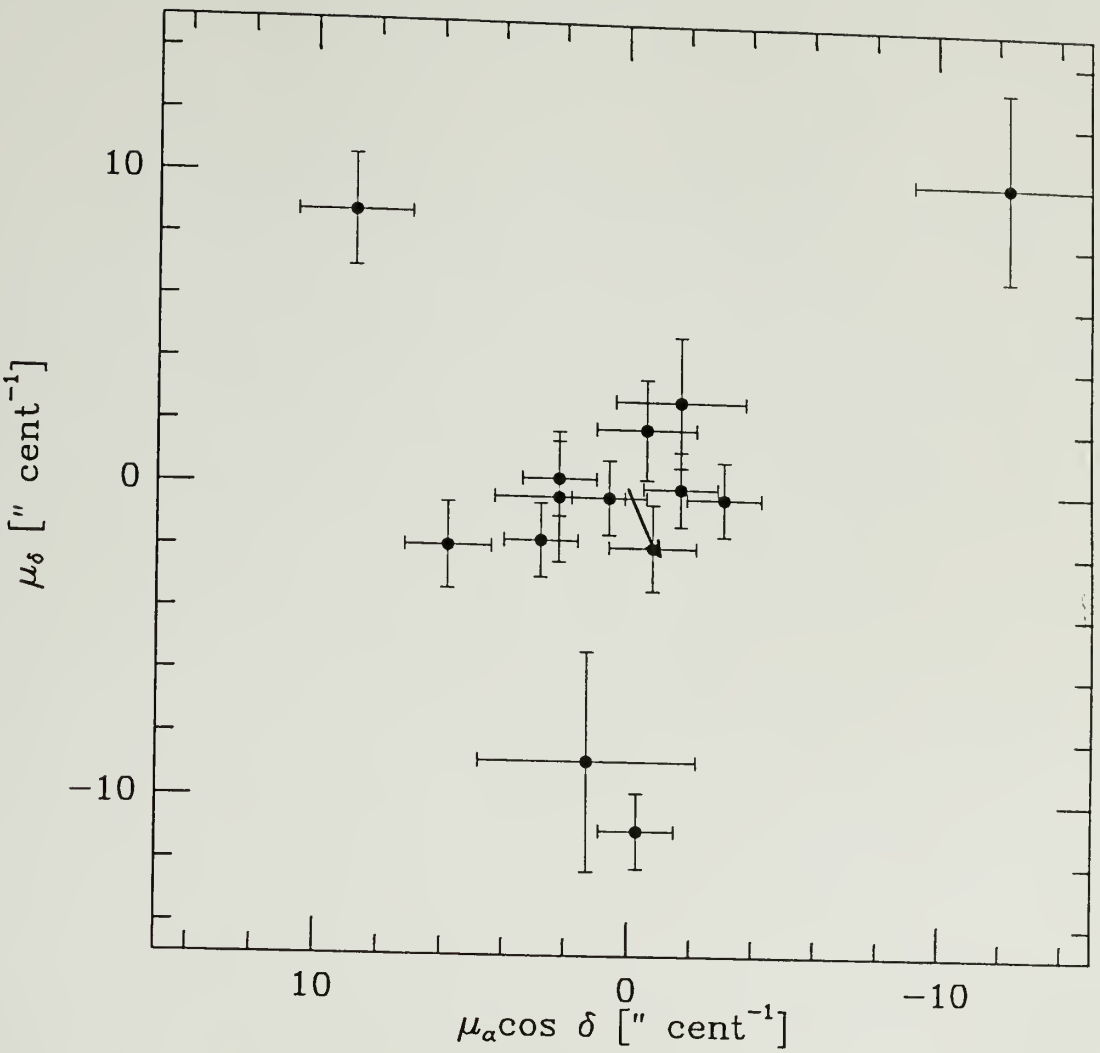

Figure 5.9 Equatorial proper motions of the Oph photometric foreground candidates. The arrow shows the direction of the Solar reflex, and the length of the arrow represents the expected reflex motion at a distance of 160 pc.

5.2.1.2 Proper Motions of R, I Foreground Candidates

We have computed the proper motions of the R,I candidates of Table 4.4 using the CCD-4m angular shifts. (The CCD-POSS stellar pairs were not sufficiently deep enough to include these very faint, red stars.) In Table 5.4 we present the results of this analysis.

Table 5.4

Proper Motions of R, I Foreground Candidates

ID #	CCD vs. 4m			
	$\mu_\alpha \cos\delta$ $''$ cent^{-1}	μ_δ $''$ cent^{-1}	$\delta\mu$ $''$ cent^{-1}	V_t km s^{-1}
397	-1.3	-1.3	1.8	10 ± 12
398	1.3	1.3	1.8	9 ± 11
450	2.5	2.5	2.0	18 ± 15
465	2.5	2.5	1.8	21 ± 14
466	-3.8	0.0	1.8	23 ± 14

The proper motions of all 5 stars are small, comparable to the minimum detection threshold. However, since the deduced distances for these stars are relatively large, ranging from 90 to 145 pc (see Table 4.4), the proper motions are nonetheless consistent with what would be expected for these objects. There is little else that can be concluded from these results.

5.2.1.3 Proper Motions of the Optical/Infrared Sources

A list of the equatorial proper motions for the Optical/Infrared sources are shown below in Table 5.5. Most of these stars do not have proper motions that exceed the minimum angular shift that is measurable for the CCD-4m stellar pairs. This result is 'consistent' with the optical/infrared stars being associated with the Oph molecular cloud,

as evident in Figure 5.10. There are three notable exceptions for this set of objects. Two of the stars are photometric candidates, IRS06 (#909) and IRS15a,b (#42a,b), which were discussed in section 5.2.1.1. The third star, IRS21 (#29), clearly has a proper motion along the right ascension axis, accordingly, $\mu_\alpha \cos\delta = 7.5 \pm 1.7$ " cent^{-1}. The magnitude of this motion is beyond any that an Oph cloud member should posses, even if we include the added reflex motion of the Solar motion. The optical colors of this star, V-R = 2.69 ± 0.09 and R-I = 2.36 ± 0.05, and to a lesser extent, the infrared colors, J-H = 1.88 and H - K = 0.70, clearly indicate that the colors are reddened by a significant amount of interstellar extinction (presumably due to the cloud).

One possible solution to this apparent inconsistency of a high proper motion coupled with a deduced distance near (though behind) the cloud (>160 pc), is that IRS21 is a high proper motion object (belonging to the intermediate or 'thick' disk population) passing near the Solar neighborhood. We may test this hypothesis by de-reddening the colors according to the amount of visual extinction along the line of sight of IRS21, and, with the use of the spectral reddening curves (see Appendix C) estimate the spectral type (assuming the main-sequence and old/subdwarf color tracks are similar). According to our extinction estimates for the L1689 filament of Ophiuchus (Figure 3.2), the amount of visual extinction blocking the light from IRS21 is about 10.1 mag. If we de-redden the colors by an amount corresponding to $A_V \sim 10$ mag using the reddening curves of Figures C.1 and C.2, the resultant spectral type ranges from A3 to F8, and the corresponding absolute visual magnitude ranges from ~ 1 to 3.5 mag. The apparent visual magnitude of IRS21 is 20.61 ± 0.05, and thus, the de-reddened apparent magnitude becomes, V ~ 10.6. Using the distance modulus, we therefore find that the deduced distance of IRS21 ranges from 250 to 800 pc. Finally, using Equation 5.9 in conjunction with the deduced distance and total proper motion, ~7.5" cent^{-1}, we estimate the tangential velocity of this star to be from 90 to

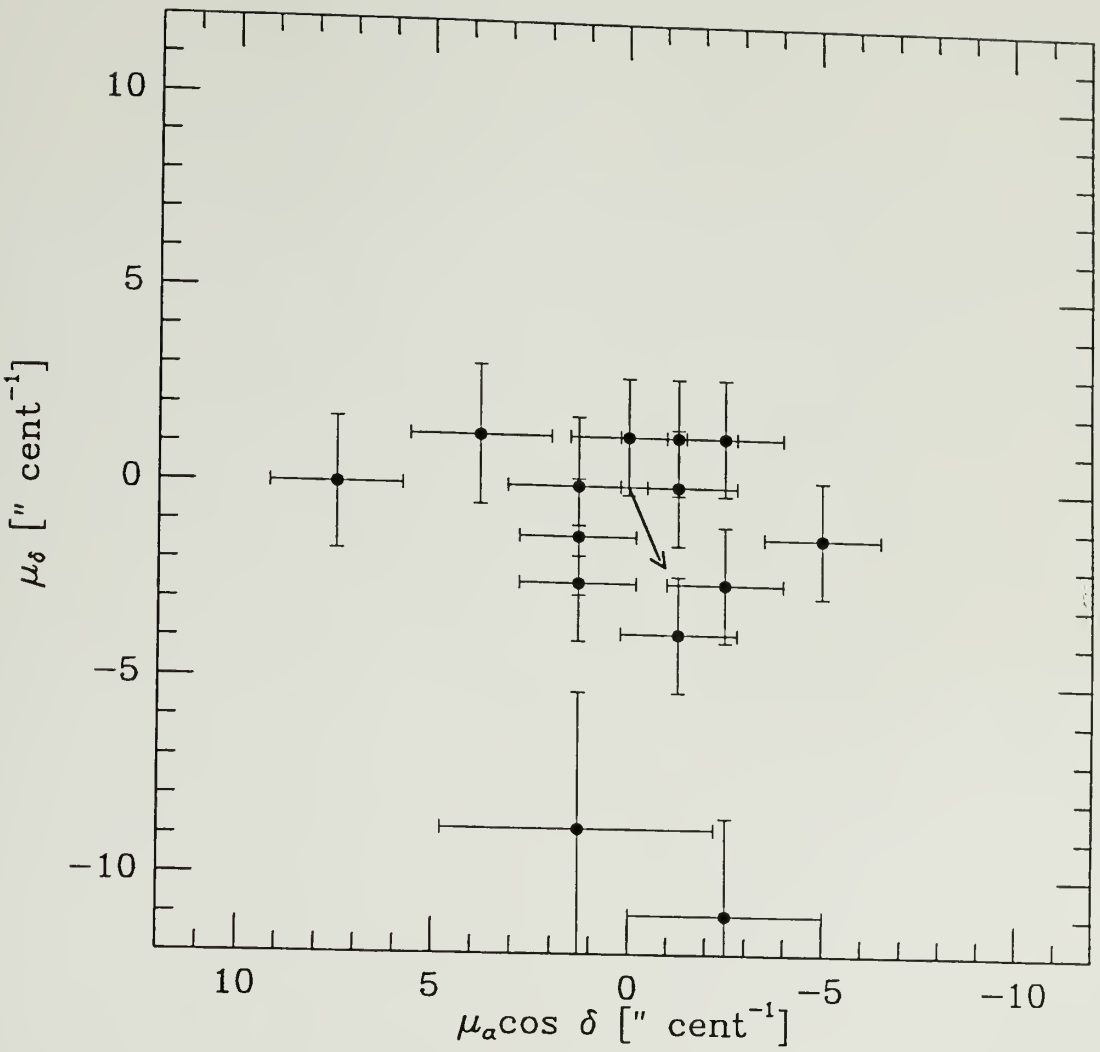

Figure 5.10 Equatorial proper motions of the Oph optical/infrared sources of Table 4.5. The arrow shows the direction of the Solar reflex, and the length of the arrow represents the expected reflex motion at a distance of 160 pc.

280 km s^{-1}. The upper limit slightly exceeds the standard value attributed to the Galactic rotation; nevertheless, the estimated mean ~150 km s^{-1} is well within the range of the observed dispersion velocities characterizing subdwarfs and other population II stars. However, the deduced spectral type is clearly too early to be population II; therefore, this object must either be a high velocity star belonging to an intermediate or thick disk population, or its proper motion is overestimated.

Table 5.5

Proper Motions of the Optical/Infrared Sources

IRS Name	Optical ID #	CCD vs. 4m		
		$\mu_\alpha \cos\delta$ ″ $cent^{-1}$	μ_δ ″ $cent^{-1}$	$\delta\mu$ ″ $cent^{-1}$
IRS01a	556	-2.5	1.3	1.5
IRS01b	538	-0.0	-1.3	1.5
IRS03	514	-0.0	1.3	1.5
IRS05b	443	-1.3	1.3	1.5
IRS06	909	-2.5	-11	2.5
IRS07a	59	3.8	1.3	1.5
IRS08b	494	1.3	-1.3	1.5
IRS08b	443	-1.3	1.3	1.5
IRS15b	42a	1.3	-0.0	3.5
IRS15b	42b	-	-	-
IRS16	119	-1.3	0.0	1.5
IRS16	98	1.3	-2.5	1.5
IRS21	29	7.5	0.0	1.8
IRS22	908	1.3	0.0	1.8
IRS24a	598	-	-	-
IRS24b	600	-	-	-
IRS27	439	-2.5	-2.5	1.5
IRS028b	498	-1.3	-3.8	1.5

5.2.2 Proper Motions of the Taurus Sample

The field pairs that we use in the calculation of the Taurus stellar proper motions are:

CCD R-image vs. POSS E-plate; baseline = 39.0 years, and
CCD I-image vs. 4-m N-plate photographic plate; baseline = 3.1 years.

Since the Taurus field consists of three CCD grids, there are considerably more reference stars for the plate pair mappings than there were in the case of Ophiuchus; consequently, the Taurus mappings will reflect a greater accuracy than those of Ophiuchus. The magnitude relation between the POSS machine magnitudes (denoted by T mag) and the CCD R magnitudes is also better defined in this case than that of Oph, as can be seen in Figure 5.11. As with the Ophiuchus reference stars, the CCD-POSS magnitude relation breaks down for stars with R magnitudes fainter than ~20. The Taurus CCD-4m magnitude relation is similar to that found for the Ophiuchus reference stars.

In Figures 5.12 and 5.13 we show the relative locations of the Taurus CCD-POSS and CCD-4m reference stars, respectively; the total angular shifts (in arc seconds) are represented along the z-axis. It is clear that the reference stars are not uniformly distributed, but rather are clumped in groups because of the presence of the molecular cloud. It was therefore necessary to divide the field into 4 subfields, each having a comparable number of reference stars whose relative distribution was generally uniform.

We may evaluate the errors associated with the fitting procedure for the four subfields of the two plate pairs by again plotting histograms of the angular shifts derived for the reference stellar pairs. In Figures 5.14 and 5.15, we plot the histograms for the CCD-POSS and CCD-4m pair total angular shifts, expressed in terms of Δr^2.

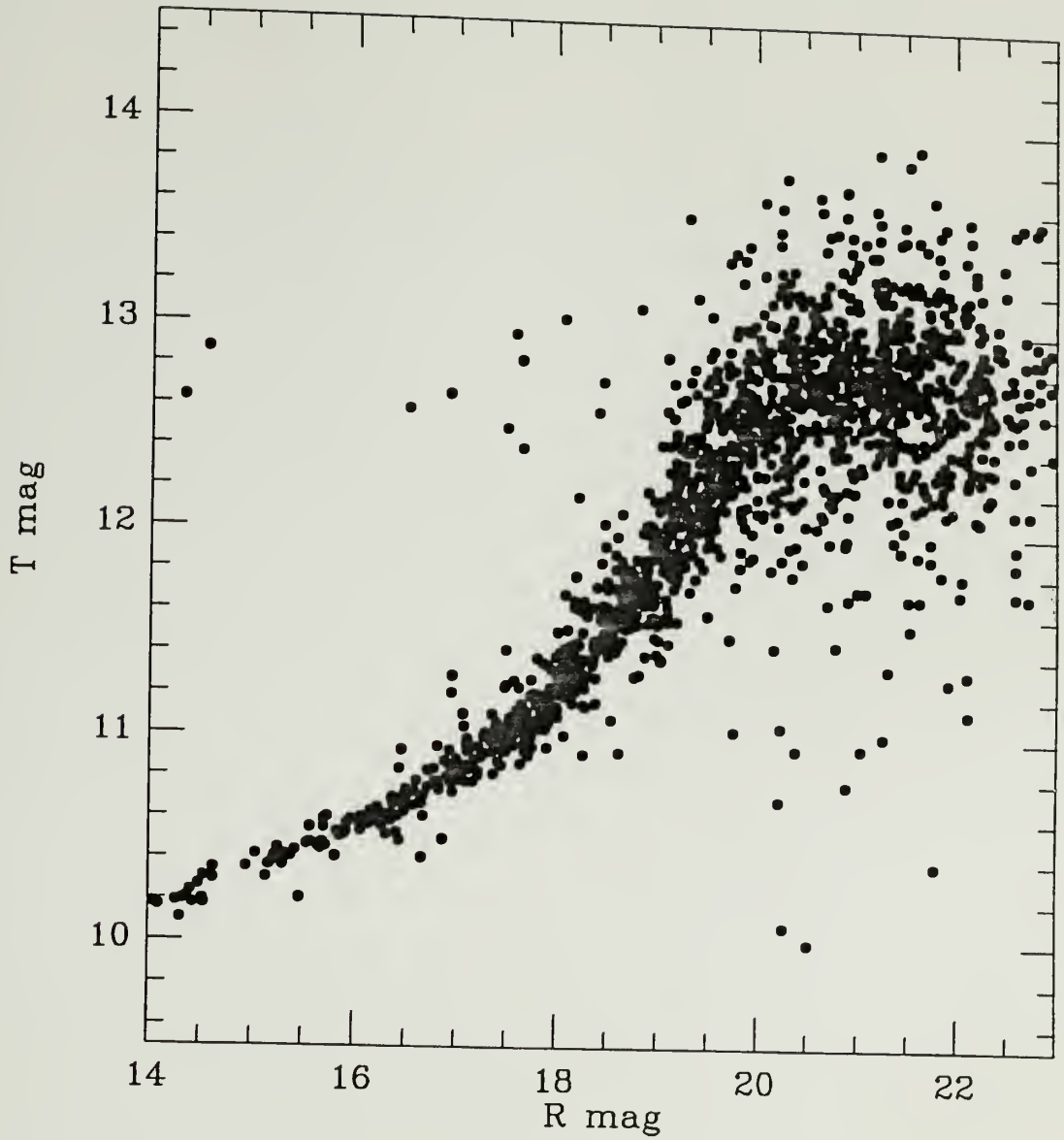

Figure 5.11 Magnitude relation for the Taurus CCD-POSS stellar reference pairs. The machine magnitudes of the POSS stars are denoted by T mag, and the CCD data by R mag.

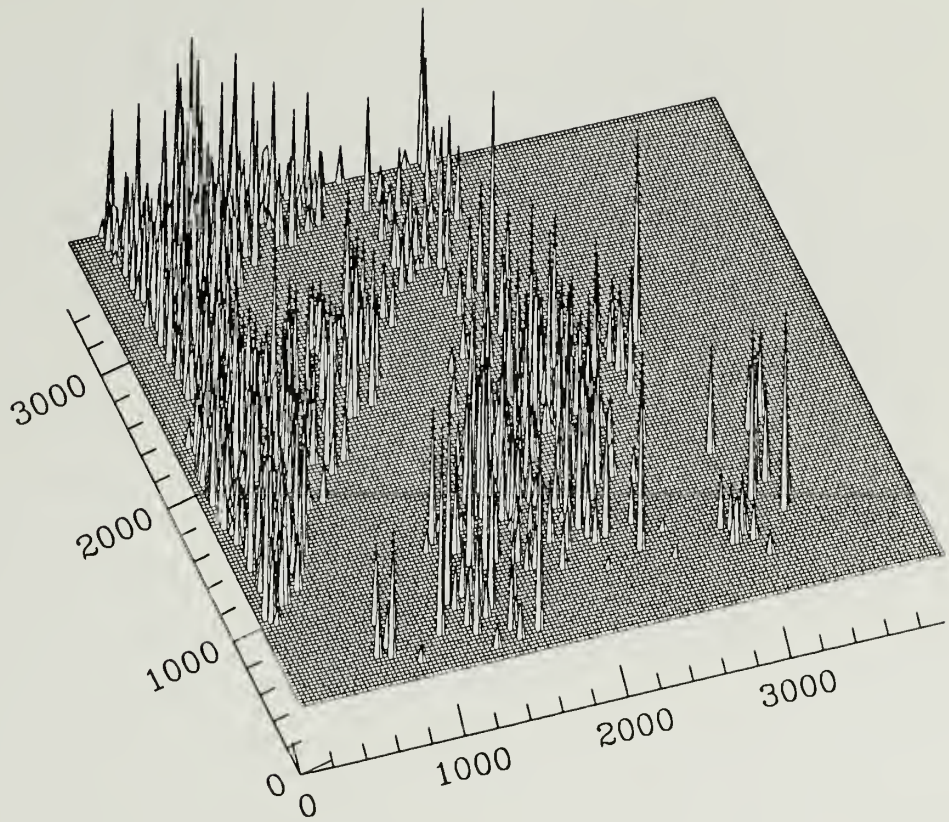

Figure 5.12 Locations and angular shifts of the Taurus CCD-POSS stellar reference pairs. The x,y positional coordinates are those of the CCD. The third dimension represents the total angular shift, $\Delta r = (\Delta x^2 + \Delta y^2)^{1/2}$. The maximum angular shift is ~2″. The orientation altitude and azimuth are 45° and 20°, respectively.

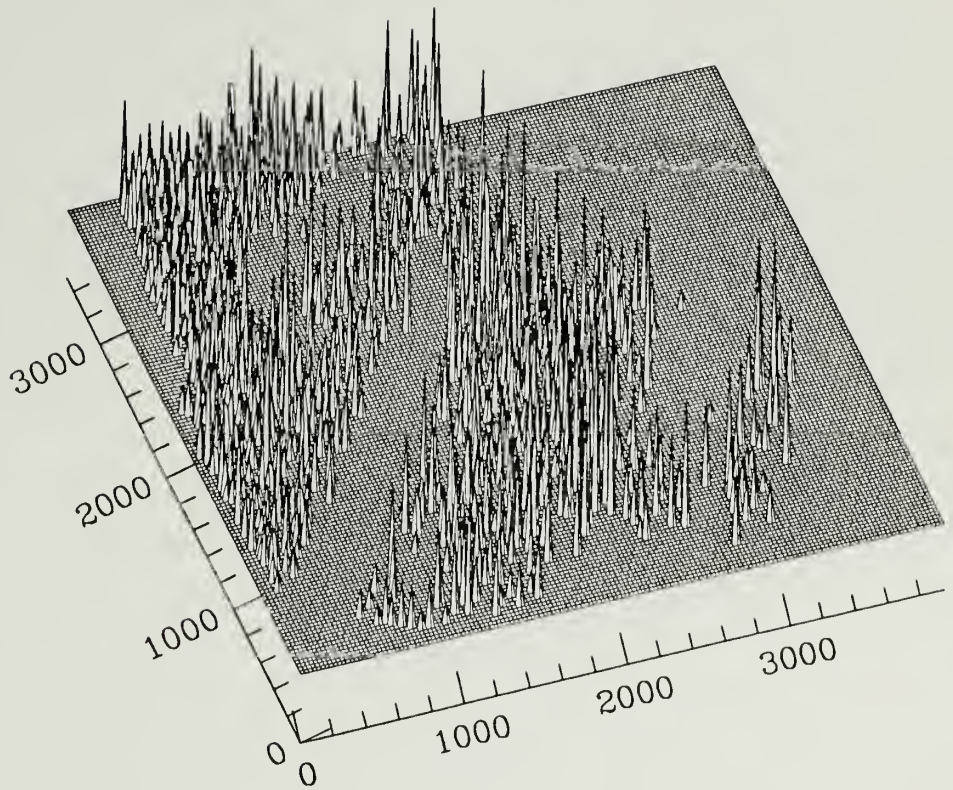

Figure 5.13 Locations and angular shifts of the Taurus CCD-4m stellar reference pairs. The x,y positional coordinates are those of the CCD. The third dimension represents the total angular shift, $\Delta r = (\Delta x^2 + \Delta y^2)^{1/2}$. The maximum angular shift is ~1″. The orientation altitude and azimuth are 45° and 20°, respectively.

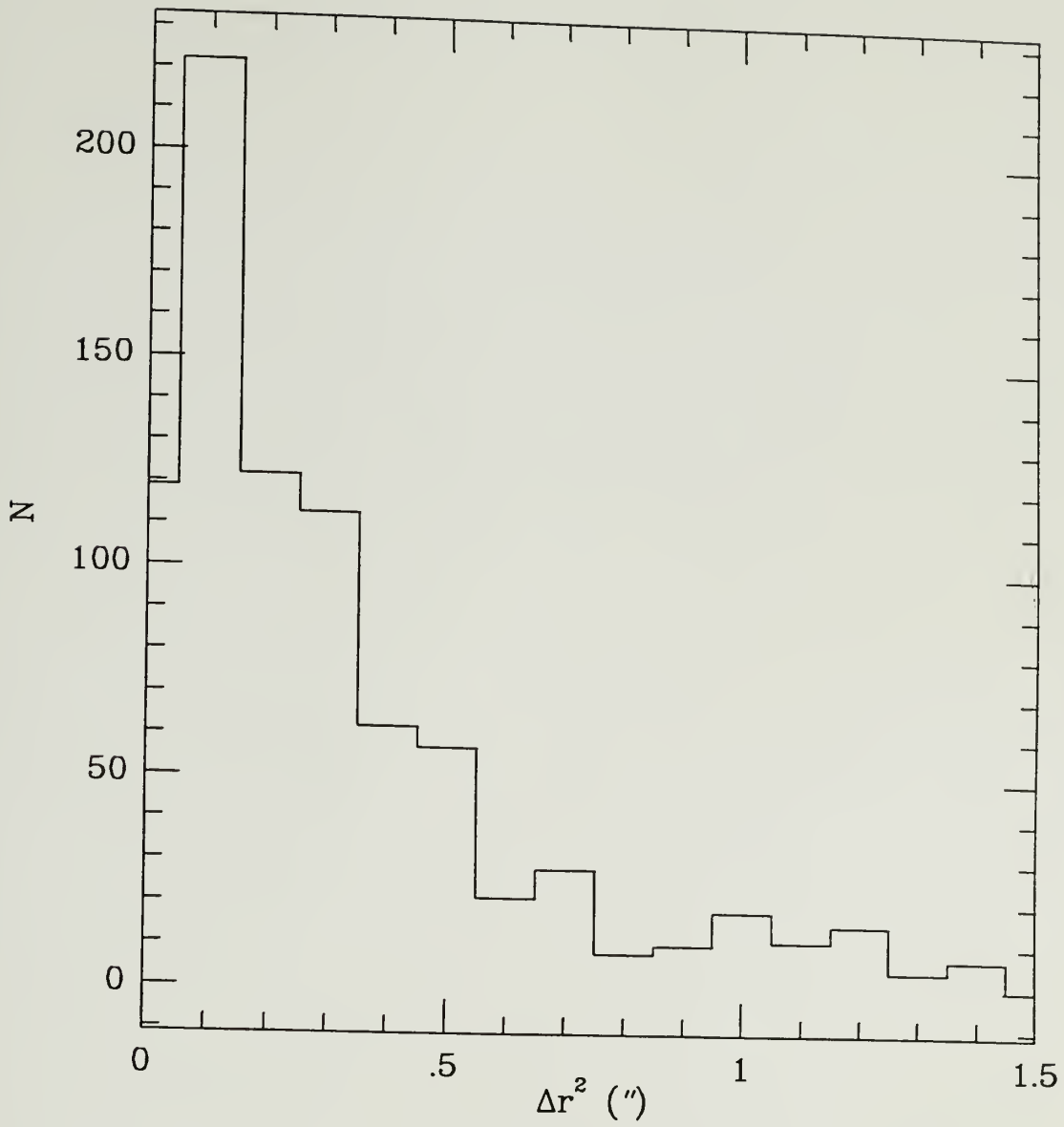

Figure 5.14 Histogram of the square of the total angular shifts of the Taurus CCD-POSS stellar reference pairs.

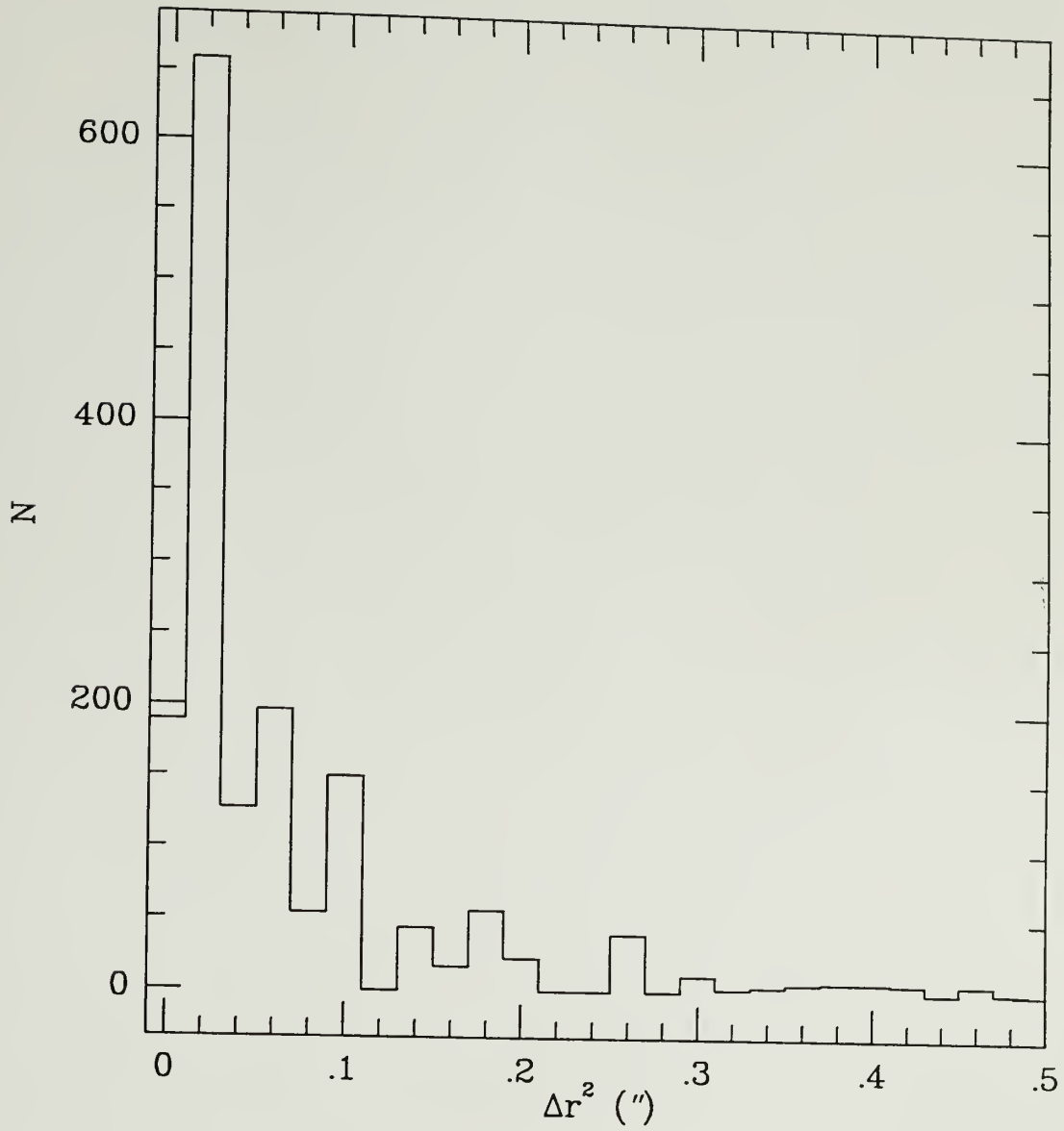

Figure 5.15 Histogram of the square of the total angular shifts of the Taurus CCD-4m stellar reference pairs.

As in the case with Ophiuchus, the Δr^2 values are not symmetrically distributed about $\Delta r^2 = 0$, but rather can be characterized by a distribution centered at some mean value, $\overline{\Delta r}^2$, with a mean variance, $\sigma^2 = \langle \Delta r^4 \rangle$. For the same reasons described in section 5.2.1, the offset arises from the fact that the background stars are not located at infinity and are subject to both proper motion and Solar reflex displacements.

We follow the same procedure in the case of Oph to determine the minimum detectable threshold of any proper motions measured with the CCD-POSS and CCD-4m materials. The square roots of the mean expectation values corresponding to the CCD-POSS and CCD-4m distributions are defined as the minimum detectable thresholds; the mean expectation values determined from the histograms, Figures 5.14 and 5.15, are

$$\begin{aligned} \langle \Delta r^2 \rangle &\approx 0.30 \ , \quad CCD\text{-}POSS \\ \langle \Delta r^2 \rangle &\approx 0.02 \ , \quad CCD\text{-}4m \end{aligned} \tag{5.19}$$

where the units are in arc seconds squared.

We check these values for consistency with the expected Solar reflex motion and position uncertainties by applying Equation 5.17. The second moment of the mean expectation value, $\langle r^4 \rangle$, was found to be 0.1 and 0.0 arc seconds to the fourth power for the CCD-POSS and CCD-4m data, respectively. Solving for $\overline{r}$ using Equation 5.17 indicates that the resultant estimate for the Solar reflex motion is 0.5″ over 39 years (CCD-POSS) and 0.1″ over 3 years (CCD-4m). These values are consistent with the expected reflex motion a field G or K dwarf would exhibit. Finally, the dispersion, σ, obtained from the data is 0.2″ for the CCD-POSS distribution and 0.1″ for the CCD-4m distribution.

In terms of proper motion, the expected minimum detection threshold for the proper motion using the CCD-POSS data is ~1.4″ cent^{-1}. The baseline of the CCD-4m pair is quite short, only 3.1 years, and the resulting angular shifts reflect this shortcoming. The estimated minimum threshold of the CCD-4m reference star distribution is only 4.5″ cent^{-1}.

Therefore, the proper motions estimated using the CCD-4m data will not be very useful for our purposes. We can demonstrate this shortcoming by again considering the expected angular shift an M-dwarf would exhibit over the baselines of the Taurus fields. Similar to Table 5.2, we list the angular shifts an M-dwarf would exhibit assuming a tangential dispersion velocity of 28 km s^{-1}, and baselines of 3.1 and 39 years.

Table 5.6

Expected Angular Shift for an M-dwarf Star[a]

D (pc)	CCD vs. POSS[b] $\Delta\theta''$	CCD vs. 4m[c] $\Delta\theta''$
5	46	3.7
10	23	1.8
25	9.2	0.7
50	4.6	0.4
75	3.1	0.2
100	2.3	0.2
140	1.6	0.1

[a] Assuming a dispersion velocity of 28 km s^{-1}.
[b] 39.0 year baseline.
[c] 3.1 year baseline.

Clearly, the transverse motion of an M dwarf located at *any* distance from the Sun cannot be detected using the CCD-4m stellar pairs, but can be measured using the CCD-POSS data for distances approaching that of the Taurus molecular cloud, ~140 pc. We will thus use the CCD-4m data only for cases in which the proper motion appears to be unusually high, > 10″ $cent^{-1}$.

An important test of the validity and accuracy of the methods used in this study to determine proper motions *via* plate/image fields can be made by comparing our results with

those of the Jones and Herbig (1979) proper motion survey. Their survey data base consisted of Lick astrograph plates and Palomar Schmidt plates (including POSS), with estimated accuracies of 0.7 - 1.0″ cent^{-1} in one coordinate. Thus, the accuracy of their proper motion measurements is similar to those of this study (they are, in fact, about 20 - 40% more accurate). In Table 5.7 we list the equatorial proper motions of stars common to both surveys.

Table 5.7

Proper Motions of Stars from Jones and Herbig (1979)

Jones and Herbig			this study			
Star ID#	$\mu_\alpha \cos\delta$ ″ cent^{-1}	μ_δ ″ cent^{-1}	Star ID#	$\mu_\alpha \cos\delta$ ″ cent^{-1}	μ_δ ″ cent^{-1}	$\delta\mu$ ″ cent^{-1}
GN Tau	0.2	-2.5	5556	0.0	-1.5	1.4
Haro 6-32	0.3	-3.0	5556	1.0	-3.3	1.0
218	-0.4	-5.1	144	-0.3	-2.8	1.0
220	2.5	-7.6	9997	2.3	-7.4	1.0
220	1.6	-1.5	926	1.3	-1.3	1.2
220	10.2	-6.3	8001	9.5	-6.4	1.3
223	0.3	-2.0	535	1.3	-1.3	1.4

In general the proper motion estimates from Jones and Herbig agree with those of this study to better than ~10%, particularly for the high proper motions stars, J&H #220 and 222. Where there is significant difference (*e.g.*, J&H #223), the expected error bars adequately cover the apparent discrepancy. We conclude that the method used in this study is adequate for estimating proper motions measurements with accuracy of 1-1.4″ cent^{-1}.

5.2.2.1 Photometric Foreground Candidates

The results of the proper motion analysis for the Taurus photometric foreground candidates are shown in Table 5.8. As with the Ophiuchus analysis, the tangential velocity is estimated using the deduced distances from Table 4.8, the total proper motion, and Equation 5.9. For each star in Table 5.8 we have performed a fit between the CCD and POSS stars located in the immediate vicinity of the star in order to best estimate the rectangular angular shifts. In Figures B.2(a-p), we show the local areas for each Taurus photometric candidate in the 4-m, CCD, and POSS data sets.

Only one star, #1173, appears to have a proper motion that is clearly in error. The proper motion for this star, determined using the CCD-POSS data, is in excess of 16″ cent^{-1}, which is substantially greater than the value deduced from the CCD-4m fields, <10″ cent^{-1}. This object is quite faint at R ~20.1 mag, which is about the limiting magnitude of the POSS survey. Thus, the most logical explanation of its anomalous proper motion is that the CCD-POSS stellar pair is a mismatch. Star #847 does not have a clear POSS match, but as one can see from Figure B.2i, there is a POSS star in close proximity (~2″) of the expected location of the match to CCD star #847. We believe the mismatch is due to a discrepant apparent magnitude for the POSS star; possibly, the star is variable. On the other hand, a large proper motion is consistent with the results found using the CCD-4m data, where the total proper motion was found to be 10 ± 3 ″ cent^{-1}.

Two stars, #32 and 535, do not have measurable proper motions, and thus, little conclusion can be made about the nature of these stars. The remaining foreground candidates appear to have proper motions consistent with their being located in front of the Taurus molecular cloud. All have deduced distances relatively far from the Sun, ranging from 65 to 140 pc, and thus, the effect of the Solar reflex motion is partially minimized. We may illustrate this by once again considering Equations 5.3 and 5.8.

Table 5.8

Proper Motions of the Taurus Photometric Candidates

ID #	CCD vs. POSS[a]			
	$\mu_\alpha \cos\delta$ $''$ cent^{-1}	μ_δ $''$ cent^{-1}	$\delta\mu$[b] $''$ cent^{-1}	V_t km s^{-1}
18	4.6	-1.0	0.9	22 ± 7
29	-1.5	-6.7	1.3	37 ± 10
32	-0.3	-2.1	1.4	4 ± 5
41	1.3	-1.0	1.1	10 ± 9
535	-2.6	-1.3	1.4	5 ± 3
604	-5.4	-6.2	1.3	50 ± 15
794	4.6	-2.6	0.9	31 ± 11
823	1.3	3.8	1.3	18 ± 9
847	-[c]	-[c]	-[c]	-[c]
926	2.1	-1.8	0.9	19 ± 10
951	2.8	-3.6	0.9	22 ± 9
994	4.6	-6.2	0.9	23 ± 5
1173	16.4	-36	1.4	185 ± 30
1235	6.2	-5.4	1.4	33 ± 9
1372	2.8	0.5	1.4	22 ± 18
1552	-1.5	0.3	1.1	12 ± 13

[a] 39.0 year baseline.
[b] The standard error in one coordinate.
[c] No data was available

For a direction given by the center of our CCD field, the angles corresponding to the Solar-antapex-Taurus orientation are: $\lambda = 120.5°$ and $\psi = 21.7°$. The direction of the reflex in the equatorial plane is therefore about 22° east of the $-\delta$ axis. The amount of reflex a star is subjected to if it lies in the direction of Taurus at a distance of 140 pc is ~2.3″ cent^{-1}. In Figure 5.16, we show the equatorial proper motions of the foreground candidates of Table 5.8, and the direction and magnitude of the reflex at a distance of 140 pc. It is seen that several stars cluster within 2σ of the tip of the arrow, suggesting their possible association with the cloud, or more likely, their locations relatively near the cloud. More importantly, most of the stars in Table 5.8 have equatorial proper motions that generally group *along* the direction of the Solar reflex, which strengthens their case as being foreground to the molecular cloud.

5.2.2.2 Proper Motions of the Known and Candidate T-Tauri Stars

In Table 5.9 we list the equatorial proper motions of the known and candidate T-Tauri stars of Table 4.9. In Figure 5.17 we illustrate the proper motions in the equatorial plane. The known protostellar or T-Tauri type stars, namely Haro 6-31, 6-32, and 6-33, all have equatorial proper motions that cluster near the tip of Solar reflex arrow, and thus are consistent with their association with the Taurus molecular cloud. Most of the candidate PMS stars also possess equatorial proper motions expected of association stars. The exceptions are stars #111 and 121, both of which have proper motions in excess of the typical values characteristic of those stars recently formed in Heiles' Cloud 2 (Jones and Herbig 1979). Either the measurements are in gross error ($>3\sigma$), or the stars are not in fact associated with the cloud. In the latter case, it is difficult to understand the true nature of these stars given that their optical colors are anomalously blue.

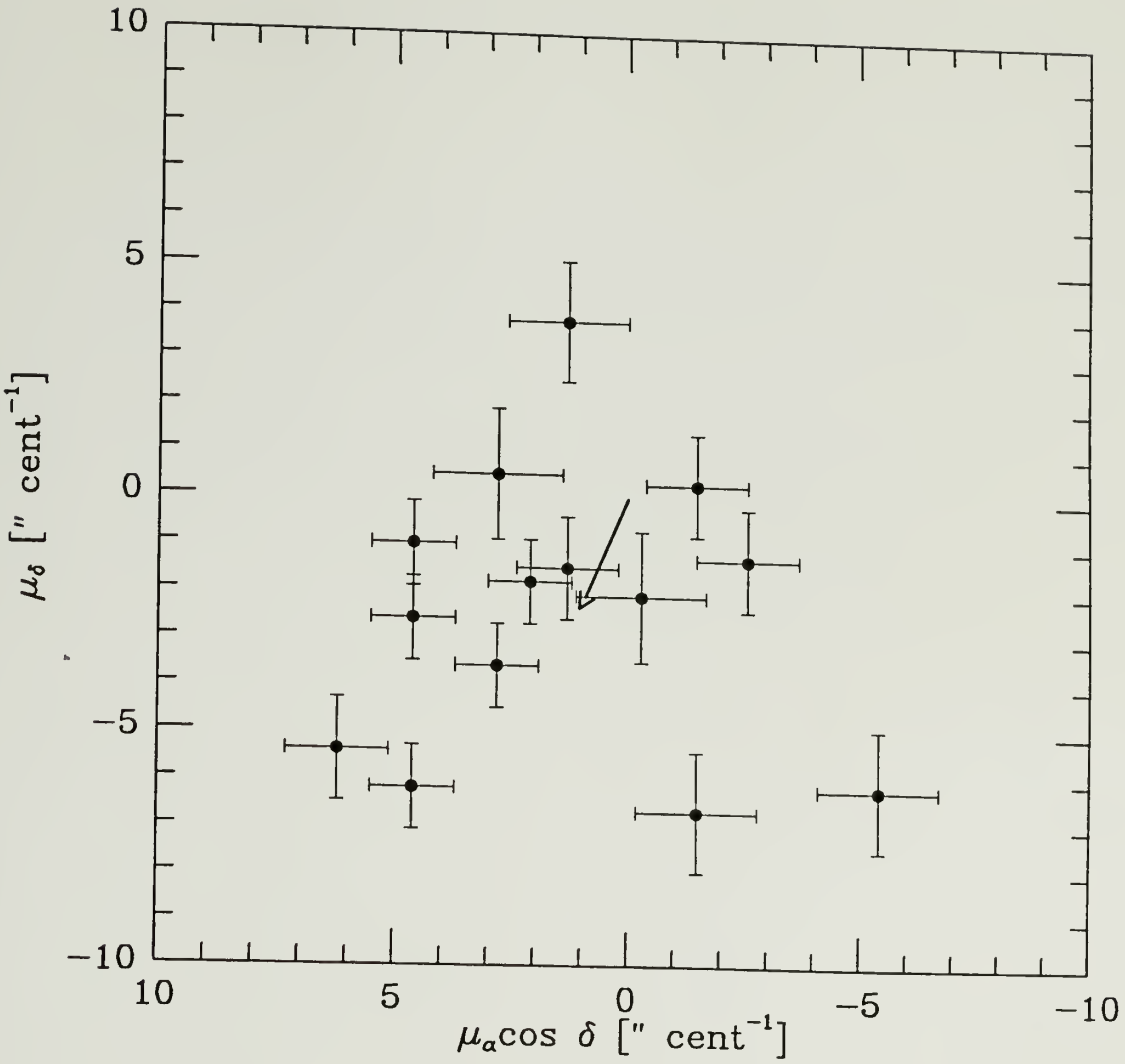

Figure 5.16 Equatorial proper motions of the Taurus photometric foreground candidates. The arrow shows the direction of the Solar reflex, and the length of the arrow represents the expected reflex motion at a distance of 140 pc.

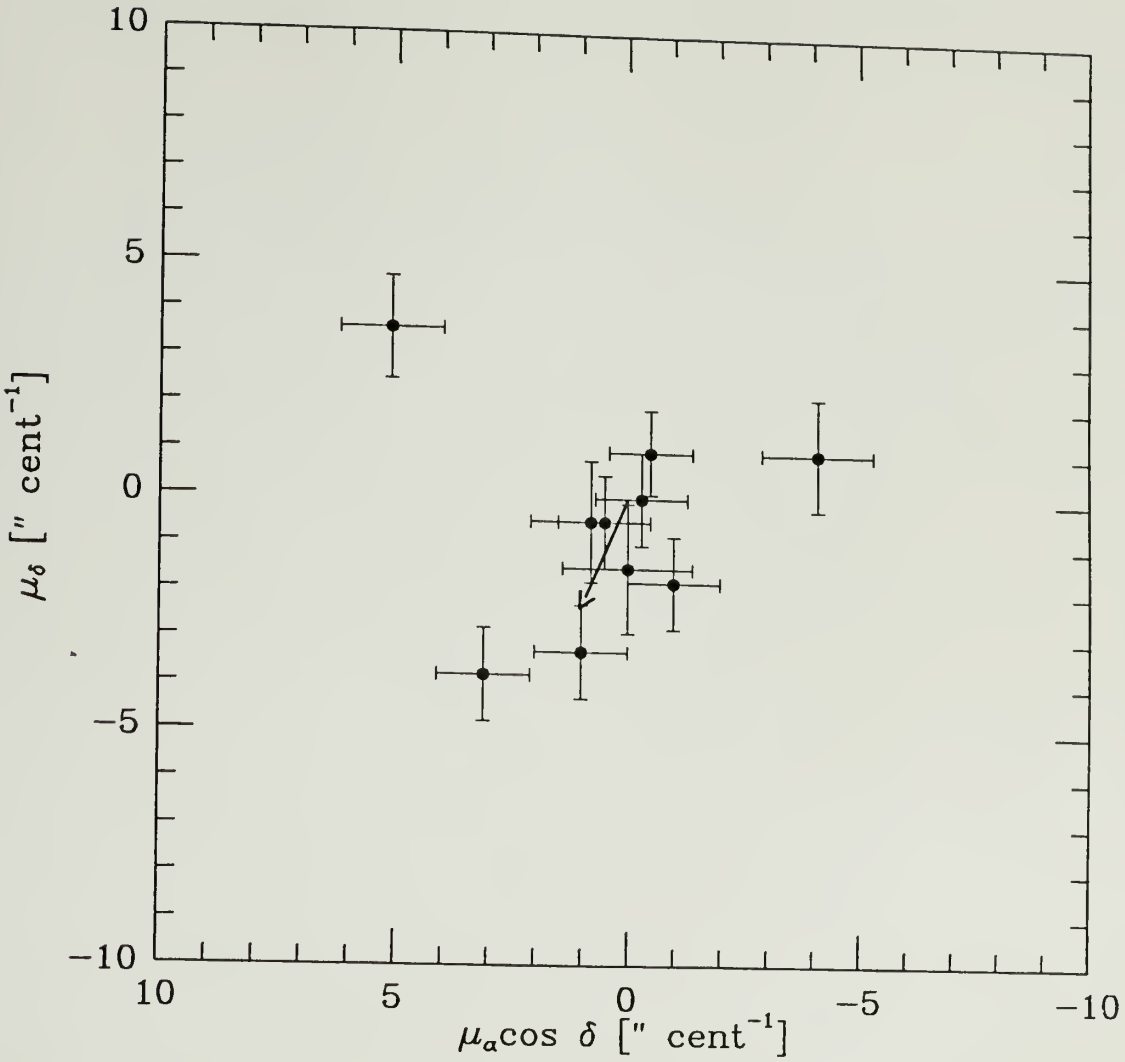

Figure 5.17 Equatorial proper motions of the Taurus optical/infrared sources of Table 4.8. The arrow shows the direction of the Solar reflex, and the length of the arrow represents the expected reflex motion at a distance of 140 pc.

Table 5.9

Proper Motions of the Taurus T-Tauri Candidates

ID #	CCD vs. POSS		
	$\mu_\alpha \cos\delta$ $''$ cent^{-1}	μ_δ $''$ cent^{-1}	$\delta\mu$ $''$ cent^{-1}
111	-4.1	1.0	1.2
121	5.1	3.6	1.1
893	-	-	-
1012	-	-	-
1029[a]	0.8	-0.5	1.3
1041[b]	-1.0	-1.8	1.2
1046	-0.3	0.0	1.0
1147	-0.5	1.0	0.9
1338	3.1	-3.8	1.0
1382	0.5	-0.5	1.0
1467	-	-	-
5555[c]	1.0	-3.3	1.0
5556[d]	0.0	-1.5	1.4

[a] Double I-band Source.
[b] Haro 6-33.
[c] Haro 6-32.
[d] Haro 6-31; GN Tau.

In summary, we find that more than 90% of the Taurus and Ophiuchus candidate foreground stars have proper motions consistent with their being located in front of the molecular clouds. As a check to the methods presented in this chapter and the previous chapter, we obtained redband spectra of three Taurus foreground candidate objects. The results of this effort are illustrated in the following chapter.

CHAPTER 6

CANDIDATE FOREGROUND STARS

In this chapter we summarize the results of the previous two chapters, and present optical spectra for three of the Taurus candidate foreground stars. The optical spectra are discussed in the following section.

The candidate foreground stars of the Ophiuchus and Taurus samples are listed in Tables 6.1 and 6.2, respectively, and represent probable luminosity class V stellar objects located in front of the Taurus and Ophiuchus molecular clouds. Along with most of the photometric candidate foreground stars of Chapter 4, the tables also include the R,I candidate stars (Tables 4.4 and 4.9) that have *only* a foreground solution. Finally, those photometric candidates (discussed in Chapters 4 and 5) that are suspected to be associated with the molecular clouds are excluded from the tables.

Included in Tables 6.1 and 6.2 are the coordinates, photometry, absolute magnitude, effective temperature and spectral type of each candidate stars. The absolute magnitude, M_V, is estimated from the photometry and the parameter M_I^0 found in Tables 4.2, 4.4, 4.8 and 4.9, and the spectral type corresponding to M_V is taken from Table 4.1. The effective temperature is calculated using the $(R\text{-}I_c)$ color and Equation 4.3, except when $R\text{-}I > 2.1$, in which case we interpolate the T_{eff} values found in Table 4.1.

Table 6.1

Ophiuchus Foreground Candidates

ID#	RA[a] (hh:mm:ss)	DEC[a] (° ′ ″)	V	V-R	R-I_c	M_V	T_{eff}	Spectral Type
10	16:28:56.0	-24:33:28	19.94	1.90 ± 0.07	2.06 ± 0.04	16.5	2850	M5
18	16:30:30.2	-24:32:37	20.77	1.57 ± 0.08	1.81 ± 0.04	14.7	3050	M5
19	16:30:08.3	-24:32:10	21.23	1.59 ± 0.09	1.90 ± 0.05	15.0	3000	M5
28	16:29:32.4	-24:30:11	21.23	2.14 ± 0.13	2.63 ± 0.06	18.5	2600	M7
34	16:30:00.0	-24:27:53	21.25	2.60 ± 0.10	2.44 ± 0.05	19.1	2450	>M7
37	16:28:55.3	-24:26:59	20.76	1.69 ± 0.08	1.87 ± 0.04	15.4	3000	M6.5
43	16:30:00.0	-24:23:05	17.45	1.33 ± 0.05	1.61 ± 0.03	13.0	3200	M4
48	16:28:54.7	-24:23:05	20.86	1.94 ± 0.08	2.13 ± 0.04	16.8	2850	M6
74	16:30:01.9	-24:21:26	21.81	1.74 ± 0.13	2.24 ± 0.06	18.5	2600	M6
76	16:29:41.0	-24:20:42	19.09	1.55 ± 0.05	1.71 ± 0.03	14.1	3100	M4 - M5
80	16:29:58.1	-24:20:09	21.84	2.13 ± 0.14	2.23 ± 0.05	17.6	2700	M6.5
183	16:29:28.9	-24:13:30	19.09	1.88 ± 0.07	2.51 ± 0.05	17.4	2700	M6.5
223	16:30:22.2	-24:16:53	21.53	1.91 ± 0.10	2.32 ± 0.05	17.2	2750	M6.5
908	16:29:33.6	-24:17:32	16.60	1.13 ± 0.02	1.60 ± 0.02	12.3	3200	M4
909	16:29:07.8	-24:16:40	11.99	0.62 ± 0.02	0.54 ± 0.02	7.3	4500	K5

ID#	RA[a] (hh:mm:ss)	DEC[a] (° ′ ″)	I	R-I_c	M_V	T_{eff}	Spectral Type
397	16:28:56.2	-24:30:57	18.63	2.30 ± 0.07	18.6	2600	M7
398	16:29:00.0	-24:30:54	18.70	2.39 ± 0.08	17.7	2700	M6.5
450	16:30:13.2	-24:26:29	18.70	2.39 ± 0.08	17.7	2700	M6.5
465	16:29:58.6	-24:24:53	18.55	2.29 ± 0.06	16.6	2800	M6
466	16:30:29.2	-24:24:48	18.43	2.25 ± 0.06	18.6	2600	M7

[a] Epoch 1950.

Table 6.2

Taurus Foreground Candidates

ID#	RA[a]	DEC[a]	V	V-R	R-I_c	M_V	T_{eff}	Spectral Type
18	4:38:24.9	25:26:37	18.88	1.51 ± 0.02	1.70 ± 0.02	14.0	3100	M4 - M5
29	4:38:38.2	25:28:30	17.95	1.30 ± 0.01	1.54 ± 0.01	12.6	3200	M4
32	4:38:44.0	25:28:55	21.89	2.36 ± 0.09	2.56 ± 0.04	17.3	2800	M6
41	4:37:35.9	25:29:57	21.39	1.89 ± 0.07	2.00 ± 0.04	16.3	2900	M6
535	4:37:45.5	25:45:35	15.57	1.40 ± 0.10	1.56 ± 0.10	13.1	3200	M4 - M5
604	4:38:17.1	25:47:02	20.58	1.59 ± 0.03	1.94 ± 0.02	15.3	2950	M5
794	4:36:20.4	25:33:54	21.31	1.74 ± 0.06	2.02 ± 0.03	15.8	2950	M5.5
823	4:36:32.1	25:36:54	21.14	1.85 ± 0.04	2.10 ± 0.04	15.5	2950	M6
847	4:36:00.2	25:38:47	20.34	2.31 ± 0.05	2.46 ± 0.05	18.5	2600	M7
926	4:37:15.4	25:45:14	15.61	1.07 ± 0.05	1.08 ± 0.05	9.6	3650	M1
951	4:36:54.6	25:46:34	15.57	1.33 ± 0.05	1.30 ± 0.05	12.5	3400	M3 - M4
994[b]	4:37:33.8	25:49:12	19.69	1.81 ± 0.03	1.88 ± 0.04	15.7	3000	M5.5
1173	4:37:53.1	25:55:38	22.13	2.01 ± 0.11	2.21 ± 0.04	17.2	2900	M6
1235	4:38:37.5	25:58:06	15.37	1.07 ± 0.05	1.31 ± 0.04	10.8	3400	M4
1372	4:37:14.5	26:02:13	20.90	1.65 ± 0.04	1.79 ± 0.03	14.7	3100	M5
1552	4:37:36.0	26:05:35	20.98	1.63 ± 0.06	1.83 ± 0.07	15.0	3050	M5

ID#	RA[a] (hh:mm:ss)	DEC[a] (° ′ ″)	I	R-I_c	M_V	T_{eff}	Spectral Type
1252	4:37:27.1	25:58:33	18.10	2.37 ± 0.06	17.7	2700	M6.5
2430	4:36:34.6	25:46:37	18.57	2.31 ± 0.07	18.6	2600	M7

[a] Epoch 1950.

[b] Probable background field star; see section 6.1.3.

6.1 Spectra of Three Taurus Candidates — A Check on Methods

During December 22 and 23 of 1990, three of the Taurus foreground candidate stars[1], #604, 823 and 994, were observed at the author's request by Terry Herter of Cornell University using the spectrograph mounted to the 4-Shooter CCD camera on the 5.1-m Hale Telescope located atop Palomar Mountain in California. The spectrograph covers a wavelength range from 6000 Å to 9000 Å and was a 300 line/mm grating, which yields a spectroscopic resolution of ~15 Å. A slit width of 2′ × 1.5″ was employed. The data reductions were carried out by the author of this study; the images of the spectra were flat-fielded, bias-subtracted, sky-subtracted and converted to one-dimensional spectra using the appropriate routines in the IRAF (NOAO) software/analysis package. The spectra were wavelength calibrated using a He-Ne-Ar reference spectrum. Finally, the spectra were flux calibrated using IIDS standard stars and various IRAF routines. Strong absorption features attributed to terrestrial O_2 at ~6800 Å and ~7600 Å, and H_2O at ~7200 Å were not removed from the spectra.

Since our goal was to confirm that these stars are late-type M dwarfs, we must review the techniques used to classify and differentiate M dwarfs from early type stars and late-type giants. As discussed by Wing and Dean (1983) the temperature scale corresponding to K and M stars can be determined according to the strengths of various molecular TiO bands, particularly the band at 7120 Å, in the sense that the equivalent widths of the TiO features strengthen as the stellar surface temperature decreases. For the late M stars Bessell (1991) points out that the molecular VO bands near 7500 Å, 7900 Å and 8700 Å are a better discriminator of temperature than those given by the TiO bands.

---

[1] Two of the stars, #604 and 823, were selected from the sample based on their "good" colors and high proper motions; whereas candidate #994, whose colors indicate marginal foreground candidacy, was selected primarily due to its very high proper motion.

The relative strengths of the molecular features in spectra of late-type M giants can be seen in Figure 6.1 (taken from Bessell 1991, Fig. 5). From this spectral sequence it is clear that as one progresses from an M6 to an M10 star, the TiO feature at 7100 Å saturates, while the VO features strengthen. This same effect can be seen in the spectral sequence of M dwarfs, Figure 6.2 (taken from Bessell 1991, Fig. 6). Indeed, the spectra of late-type giants and dwarfs are much the same. In order to distinguish between dwarfs and giants, we must consider atomic and molecular species sensitive to atmospheric pressure (as discussed in Chapter 4, section 4.1). Several high-gravity features are prominent in the red-band spectra of dwarf stars, including CaOH at 6230 Å, CaH at 6385 Å and 6910 - 6950 Å, K I at 7665 Å and 7699 Å, Na I at 8193 Å and 8195 Å, Ca II at 8500 Å, and FeH at 9900 - 10100 Å (*cf.* Turnshek *et al.* 1985). For illustrative purposes, we show in Figure 6.3 the spectrum of GL 406 (LHS 36), a nearby M6 dwarf (V-R = 1.86, R-I = 2.18). In the figure we have identified most of the high gravity features, as well as the TiO and VO bands. Based the strength of the gravity-sensitive features, in particular the sodium doublet at ~8200 Å and the prominent VO absorption at 7500 Å and 7900 Å, it is clear that GL 406 is a very cool dwarf star. Also, the strong Hα emission feature at 6563 Å is indicative of chromospheric activity (a common property of M dwarfs; see section 4.1). We can compare and contrast this spectrum with that of an M giant, Figure 6.4, which is a spectrum of HR6495, an M5 III star. Notice that the spectrum of HR6495 contains prominent TiO bands at 7200 Å, 7800 Å and 8500 Å, but is lacking the high gravity features, particularly the CaH, Na I and K I absorption lines.

The spectra of stars #604, 823 and 994 can be seen in Figures 6.5, 6.6 and 6.7, respectively. For our purposes and given the difficulty of measuring the TiO and VO band equivalent widths because of contamination from the telluric absorption features, we favor spectral classification of these stars *via* a qualitative comparison between the

temperature and gravity-sensitive features exhibited in the spectra of these stars with those of the Bessell M dwarf spectral sequence, Figure 6.2, and with those of the spectrum of the late M dwarf, Gl 406, Figure 6.3. The results are summarized in the following sections.

6.1.1 Spectrum of Candidate #604

The most striking properties exhibited in the spectrum of #604, Figure 6.5, are the rising flux continuum toward red wavelengths, and the numerous absorption features blanketing the continuum. Specifically, the major TiO features discussed previously, including the TiO bands at 7200 Å, 8300 Å and 8500 Å, are present in the spectrum; the spectrum strongly suggests that this star is very cool. In fact, the strengths of these bands are comparable to those in stars with a spectral type later than M4. Furthermore, there does appear to be a hint of molecular VO at 7500 Å and particularly, at 7900 Å, but longward of 8500 Å it is impossible to distinguish between absorption features because of the poor signal to noise; nevertheless, the spectrum suggests a temperature class corresponding to that of an M5 star, but probably no later than this.

More importantly, the spectrum undoubtedly corresponds to that of a dwarf because of the many tell-tale gravity-sensitive features prominent in the spectrum, including CaOH at 6250 Å, possibly CaH at 6400 Å, K I at 7700 Å, and the prominent Na I feature at 8200 Å. The strength of the sodium feature itself suggests that this star is at least as late as M4 V and is probably an M5 dwarf. Finally, the Hα emission feature is prominent in the spectrum of #604, hinting at considerable chromospheric activity, and thus, is also consistent with this star being a late-type M dwarf.

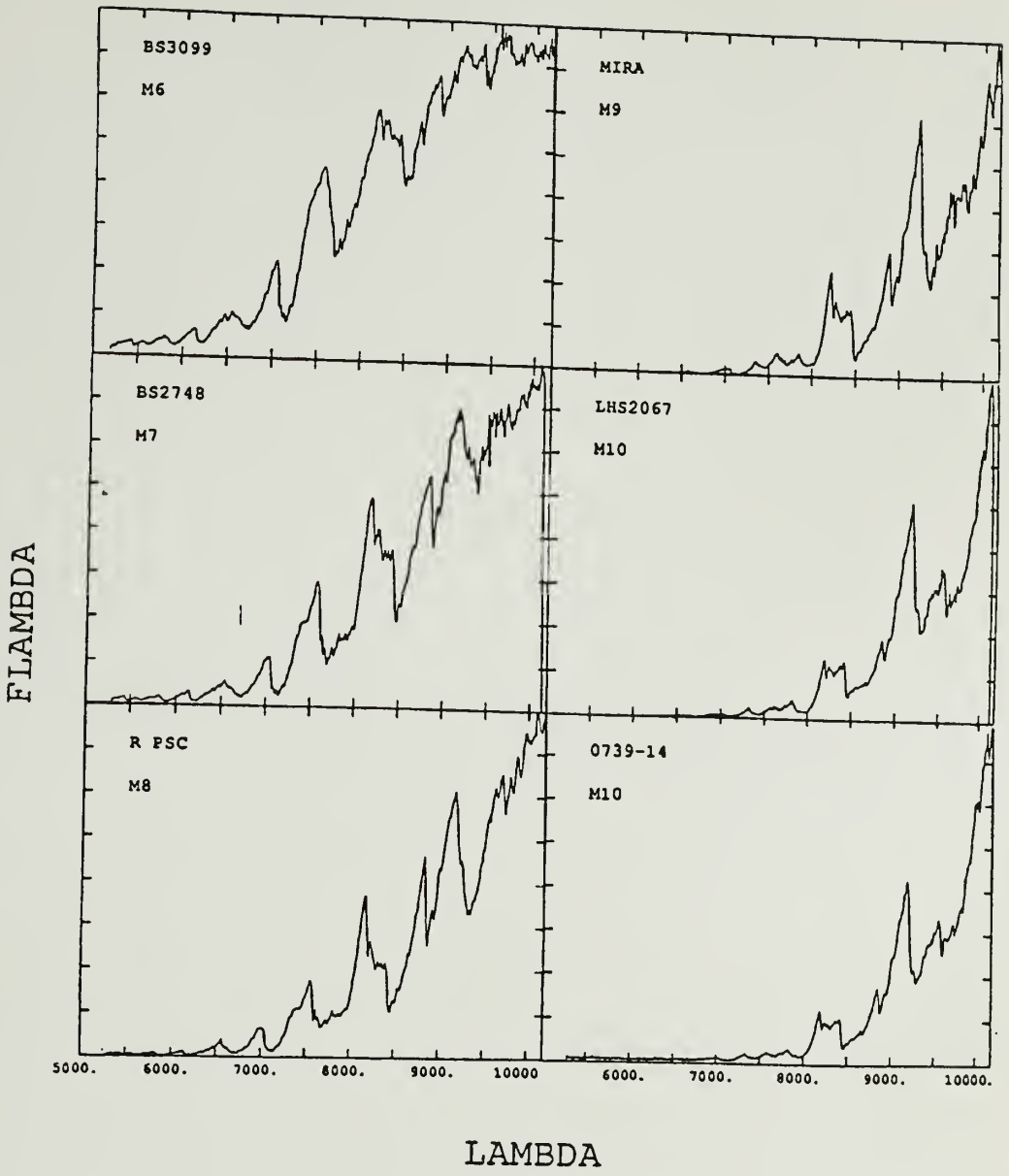

FIG. 5. Spectra of some M giants to illustrate the Wing spectral types.

Figure 6.1 Spectral sequence of some late-type M giants. The figure is taken from Bessell (1991).

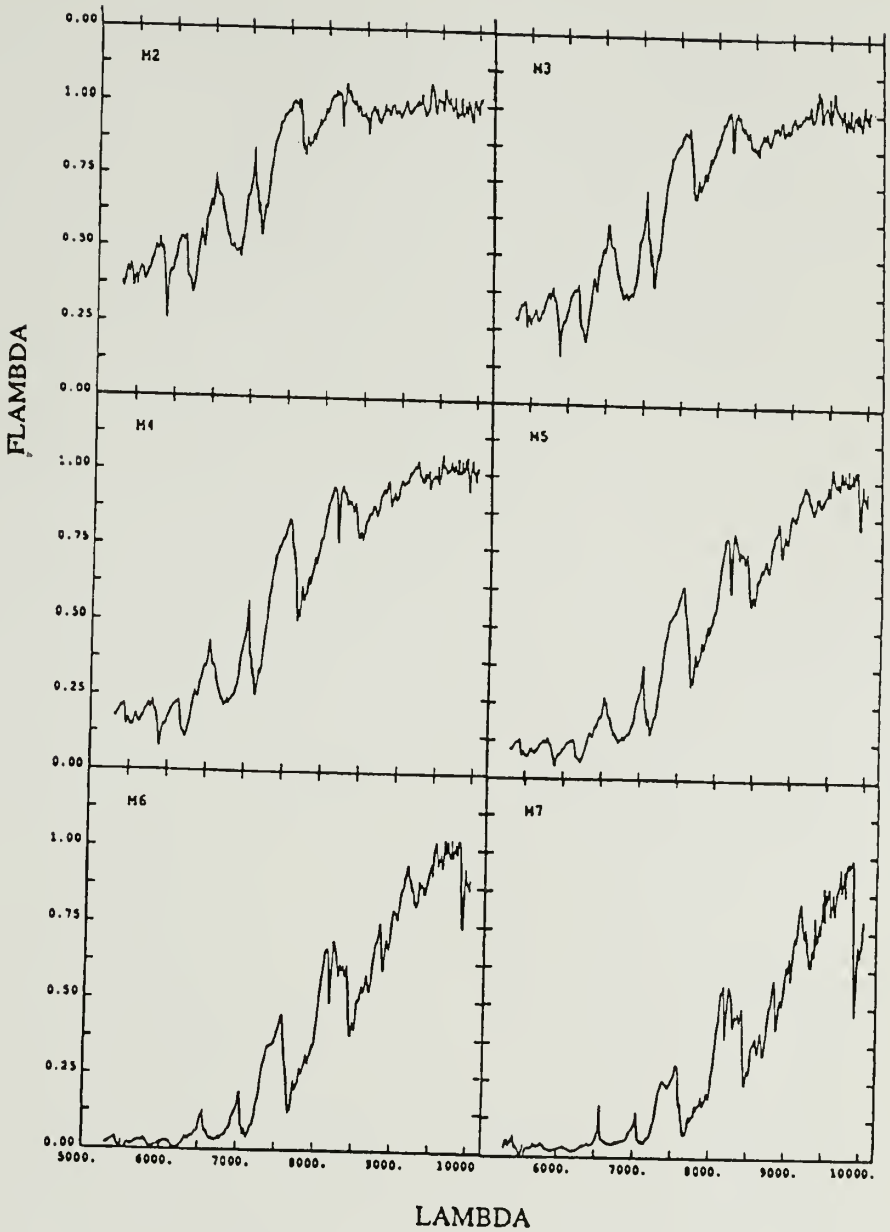

Figure 6.2 Spectral sequence of M dwarfs. The figure is taken from Bessell (1991).

Figure 6.3 Spectrum of GL 406. This dwarf star is of spectral type M6 V.

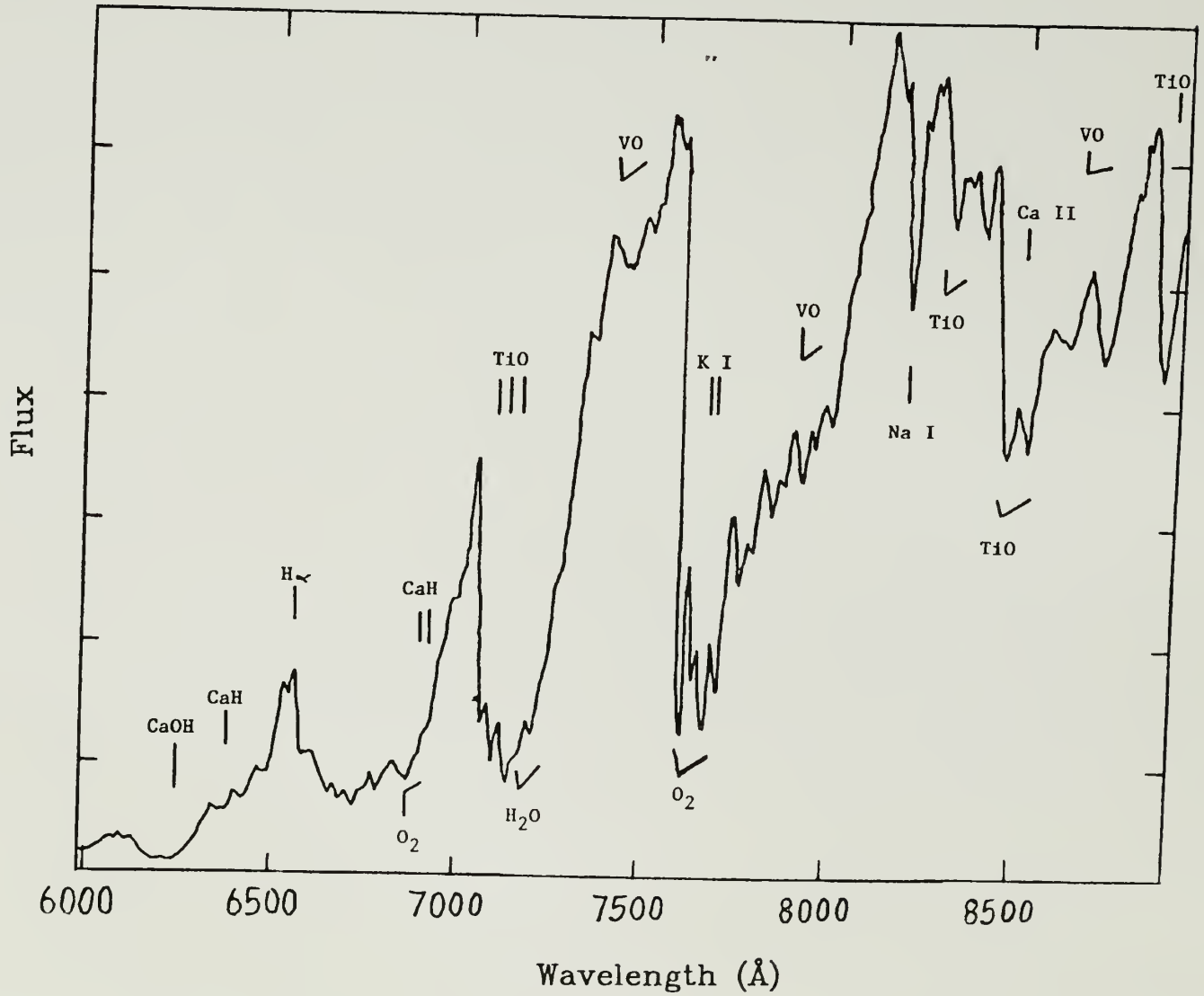
Flux
6000
6500
7000
7500
8000
8500
Wavelength (Å)
CaOH
CaH
H
CaH
TiO
VO
K I
VO
TiO
Na I
Ca II
VO
TiO
TiO
O_2
H_2O
O_2

Figure 6.4 Spectrum of HR6495. This evolved star is of spectral type M4.5 III.

Flux (10^{-12} erg cm^{-2} sec^{-1} Å^{-1})
60
40
20
7000
7500
8000
8500
Wavelength (Å)

Based on the spectral evidence outlined above, we favor the classification of candidate star #604 as an M5 V or M6 V, where the spectral type M5 V is probably the better estimate. From Table 4.1, we see that an M5 dwarf has the following properties:

$$M_V = 14.7 \text{ and } M_I = 11.3 ,$$

$$V\text{-}R_c = 1.5 \text{ and } R_c\text{-}I_c = 1.9 .$$

These values are consistent (within ~10%) with the observed broad band colors and deduced luminosities for foreground candidate #604; see Table 6.2.

6.1.2 Spectrum of Candidate #823

The spectrum of foreground candidate #823, Figure 6.6, is similar to that of #604, in that it is clearly a cool star. Fortunately, the flux S/N is considerably better for this star, and thus, it is easier to identify molecular and atomic features. Comparing this spectrum with that of #604, we see that the TiO features at 8500 Å and 8900 Å are equally prominent (and better-defined), and, more significantly, there is a hint of the VO bands at 7500 Å and 7900 Å for #823. Indeed, the molecular features in the spectrum of star #823 are similar to those seen in the spectrum of GL 406 (Figure 6.3), which as we mentioned before is an M6 dwarf. Moreover, several gravity-sensitive features are present in this spectrum of #823, including CaOH at 6250 Å, CaH at 6900 Å (though there is contamination from the O_2 telluric band), K I at 7700 Å, Ca II at 8500 Å (note however, there is contamination from the nearby TiO band), and finally, a prominent Na I feature at 8200 Å. As in the case of #604, there is a significant Hα emission line.

Figure 6.5 Spectrum of candidate foreground star #604. The flux levels are in units of 10^{-16} ergs cm^{-2} sec^{-1} $Å^{-1}$.

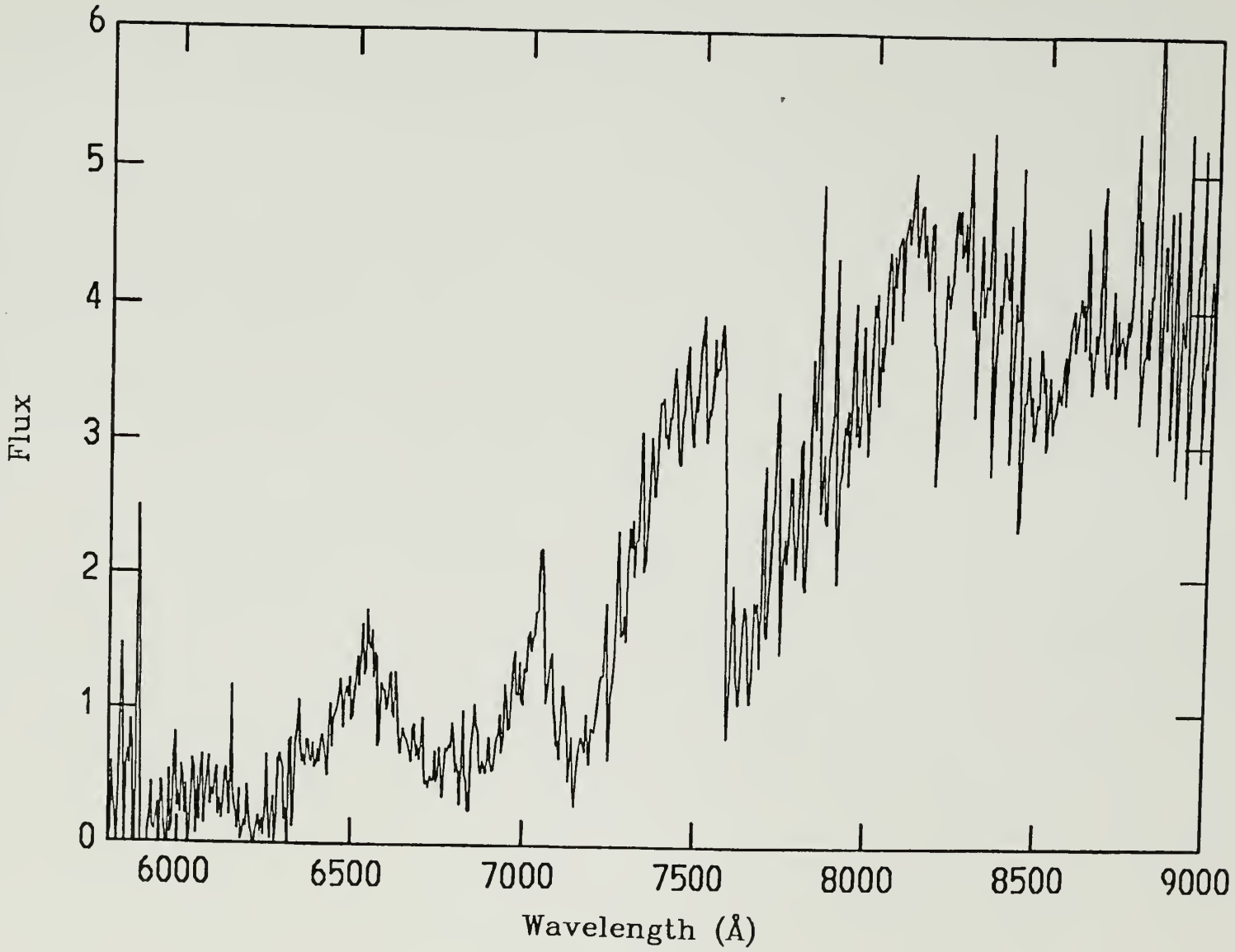
Flux
0
1
2
3
4
5
6
6000
6500
7000
7500
8000
8500
9000
Wavelength (Å)

Based on the gravity features and the strengths of the TiO and VO bands, we favor the classification of this star as a dwarf of spectral type between M5.5 and M6. From Table 4.1, we see that an M6 dwarf has the following mean properties:

$$M_V = 16.6 \text{ and } M_I = 12.5 ,$$

$$V\text{-}R_c = 1.9 \text{ and } R_c\text{-}I_c = 2.2 .$$

These values are consistent (within ~10%) with the observed broad band colors and deduced luminosities for foreground candidate #823, listed in Table 6.2.

6.1.3 Spectrum of Candidate #994

The spectrum of foreground candidate #994, Figure 6.3, is markedly different from those of the previous two candidates. In particular, the spectrum is noticeably lacking in molecular features. The features that are identified at 6900 Å, 7300 Å and 7600 Å are probably due to terrestrial oxygen and water absorption; however, there is a hint of the TiO bands at 7200 Å and 8500 Å. Furthermore, it is difficult to identify any of the gravity-sensitive features. There may, however, be some Hα emission at 6563 Å, though it is difficult to tell. Based simply on the relatively weak molecular bands, this star probably is not very late-type. On the other hand, the continuum flux is clearly rising beyond 9000 Å (of course, this is expected based on the red broad band colors observed for this star), which is inconsistent with the interpretation that #994 is an early type star. This apparent paradox can be resolved if we consider a scenario in which this star lies behind the cloud. In this case its flux is subject to interstellar reddening from the intervening cloud.

Figure 6.6 Spectrum of candidate foreground star #823. The flux levels are in units of 10^{-16} ergs cm^{-2} sec^{-1} $Å^{-1}$.

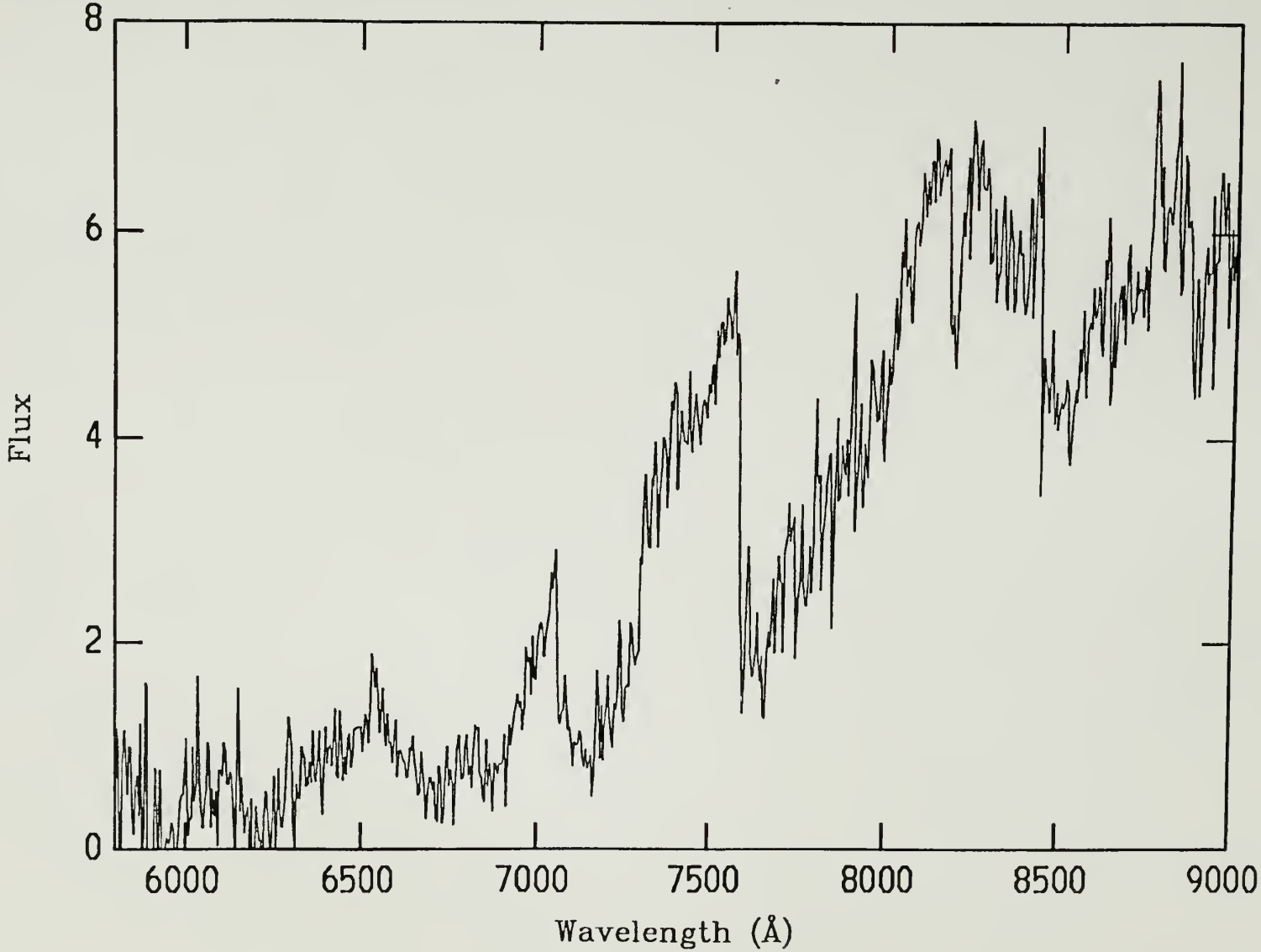
8
6
4
2
0
Flux
6000
6500
7000
7500
8000
8500
9000
Wavelength (Å)

The unreddened flux, $F_{\lambda 0}$, is degraded by an amount given by the factor

$$\frac{F_{\lambda 0}}{F_{\lambda}} = 10^{A_{\lambda}/2.5} \tag{6.1}$$

where F_{λ} is the observed flux and A_{λ} is the extinction. In our case, a flux reddening ratio can be computed from the visual (~5600 Å) and far-red wavelengths (~9000 Å), and is given by the factor

$$\sim 10^{(A_V - A_I)/2.5} \tag{6.2}$$

The projected location of the star #994 on the Taurus molecular cloud corresponds to a visual extinction of about 5 mag and $A_I \sim 3$ mag. Thus, the flux at 9000 Å is differentially *elevated* with respect to the flux at 6000 Å by a factor of ~6. If we account for this then the spectral continuum of #994 becomes more or less flat, which is consistent with its being a K5 or M0 star.

Let us further consider this hypothesis in conjunction with the observed photometric properties. If the star is a K5 dwarf, then the intrinsic visual magnitude must be ~7.6. The apparent visual magnitude (extinction-corrected with $A_V \sim 5$) is ~14.7, and thus, the deduced distance from the Sun is about 260 pc, which is a reasonable location for a Galactic disk dwarf. Even if the star is an M0 dwarf, its intrinsic magnitude is ~8.8, and the resultant distance is ~150 pc, still beyond the cloud (though the close proximity of the star and cloud raises the possibility of some kind of association).

The dereddened colors of star #994 are consistent with the two cases described here (the dereddened colors lie somewhere between those of a K5 V and those of an M0 dwarf). However, if the star is a K5 III giant, then the intrinsic magnitude is ~0.3, and the deduced distance is ~7.6 kpc, which is considerably beyond the Galactic plane (recall the Galactic coordinates for Taurus are $\ell \sim 175°$, $b \sim -15°$). Even if we take into account the general

interstellar absorption, ~1 mag per kpc, the deduced distance is beyond 4 kpc. Therefore, we consider the field dwarf explanation as the more likely scenario.

As discussed in Chapter 5, candidate #994 has a significant proper motion of ~7.7″ $cent^{-1}$ (see Table 5.8). If our interpretation that this star is a field dwarf located at a distance between 150 and 260 pc from the Sun is correct, then the deduced tangential velocity must be in the range from 55 to 95 km s^{-1}! Since a dispersion velocity of this magnitude is almost certainly beyond what could be expected for old disk K and M dwarfs, the possibility arises that this star is, in fact, a high velocity subdwarf belonging to an intermediate or spheroid population.

It is clear from the spectral analysis of the three Taurus candidate stars that two of the stars, #604 and 823, are undoubtedly late-type M dwarfs, which is consistent with the results found in the previous two chapters using photometric and proper motion analysis. Star #994, however, appears to be a background, reddened field star, possibly belonging to the spheroid population. The photometric and proper motion analysis techniques of this study are, therefore, not immune to background field stars contaminating the foreground sample. Indeed, it should be noted that the colors of #994 are not *clearly* consistent with its being a foreground M4 dwarf, but rather, are slightly offset from the expected values of this type of star (but within the 2σ criterion limits adopted by this study); furthermore, the color offset is in the area of the color-color plane where the reddening curves align, making it difficult to differentiate between very late foreground stars, and reddened background objects.

Figure 6.7 Spectrum of candidate foreground star #994. The flux levels are in units of 10^{-15} ergs cm^{-2} sec^{-1} $Å^{-1}$.

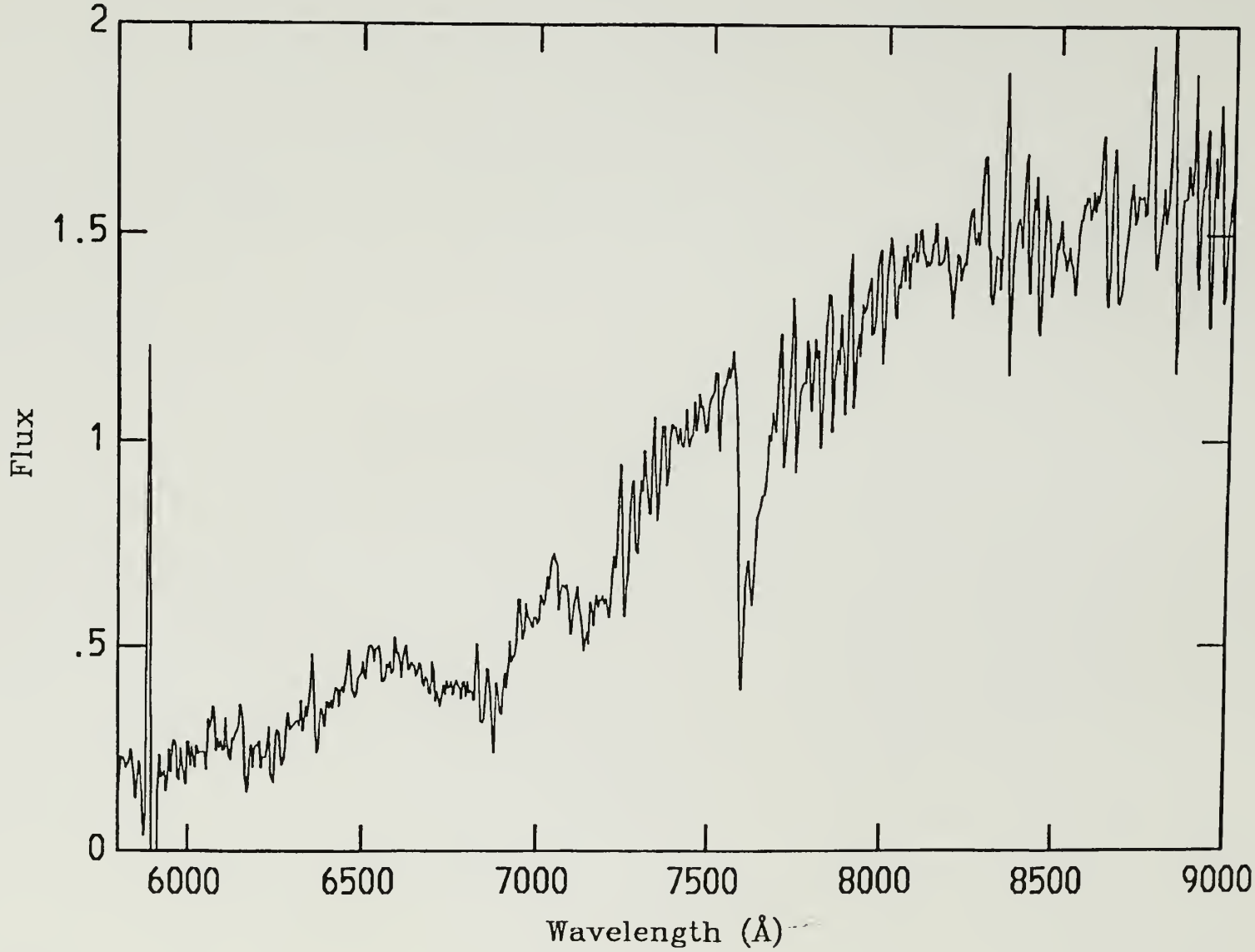
2
1.5
1
.5
0
Flux
6000
6500
7000
7500
8000
8500
9000
Wavelength (Å)

CHAPTER 7

THE LUMINOSITY FUNCTION

In this chapter we constrain the faint end of the field star luminosity function using the foreground candidates found in the preceding chapters, and compare our results with previous determinations of the luminosity function. We discuss the problems and uncertainties that are endemic to surveys of this kind, including issues of completeness and duplicity, and we outline future work that should significantly improve the poor statistics that affect our results. Finally, in the last section we discuss some of the broader implications of our results with regard to the initial mass function.

7.1 The Faint End of the Stellar Luminosity Function

The stellar luminosity function, $\phi(M)$, is defined as the number of stars per unit magnitude per unit volume; in this sense, apart from its normalization, ϕ may be considered a probability density (Scalo 1986). The luminosity function is traditionally expressed in terms of either the absolute visual magnitude, M_V, or the absolute bolometric magnitude, m_{bol}. We shall use the former approach throughout this chapter since it avoids the additional uncertainties associated with bolometric corrections. In order to successfully estimate the luminosity function, one must observe a complete sample of stars that are within a well-determined volume. There are two major approaches to this problem.

The most accurate estimate of the luminosity function comes from samples of nearby stars. In this case, the distances of the stars are accurately determined *via*

trigonometric parallaxes and proper motions. Though the volume is well-determined for the nearby stars, it is unfortunately quite limited in size since parallaxes can be measured for distances extending to only 30 pc or so. As a result, there are appreciable statistical uncertainties associated with studies of ϕ based in the nearby stars, particularly at the bright end, and at the faint end, there are potential problems associated with the completeness of the kinematically - selected samples.

The other major approach used to characterize the luminosity function is the so-called photometric parallax method. In this case, the distances of the stars are estimated using a magnitude-color constraint. The advantage of this method is that it is not kinematically biased or limited by trigonometric parallax: using photometric parallax, observers can survey much larger volumes to distances limited by only the depth of the photometry. However, an obvious disadvantage of the photometric parallax approach is that deduced distances have a built-in uncertainty that depends on the accuracy of the photometry and the magnitude-color relation. In a related problem, the fact that the photometric samples are inevitably magnitude-limited introduces completeness complications at the faint magnitude end of the estimated luminosity function. These limitations are usually treated as Malmquist effects, and as such, are corrected using familiar (and subtle) methods. We will shortly return to these issues.

The opaque-screen method implemented in this study can be best described as a photometric parallax approach, but with one important difference from the traditional method described above. With the opaque-screen method, the complete sample of stars located in front of the molecular cloud is isolated from background field stars. Thus, the sample is in principle distance limited, and *not* magnitude limited. In practice however, the faintest magnitude bins of the luminosity function may be magnitude limited if the

photometry is not sufficiently deep enough to observe the faintest stars out to the distance of the molecular cloud. We shall discuss this problem below.

7.1.1 The Ophiuchus/Taurus Luminosity Function

We construct the luminosity function using the Ophiuchus and Taurus foreground candidates shown in Tables 6.1 and 6.2. The two data sets are combined rather than treated separately because the volume corresponding to the Ophiuchus field, ~71 pc^3, is too small to yield a statistically meaningful estimate of the number density of stars. The total volume of the survey is ~198 pc^3. The luminosity function corresponding to some magnitude interval, $M_V \pm 0.5$, is given by

$$\phi(M_V) = \frac{N(M_V)}{V}, \quad -0.5 + M_V \leq M_V \leq M_V + 0.5 \tag{7.1}$$

where $N(M_V)$ is the total number of stars with absolute visual magnitude within the magnitude interval and V is the total volume of the survey, 198 pc^3. The expected uncertainty due to counting statistics is

$$\Delta\phi_N(M_V) = \frac{\sqrt{N(M_V)}}{V} \tag{7.2}$$

There is also a degree of uncertainty belonging to the volume, predominantly due to uncertainties in the estimated distances to the molecular clouds. Propagating the estimated distance error, ΔD, in the luminosity function, we find that the uncertainty due to ΔD is

$$\Delta\phi_D(M_V) = 3\left(\frac{\Delta D}{D}\right)\phi(M_V) \tag{7.3}$$

where D is the distance to the cloud. Thus, a 10% error in the distance to the cloud translates to a 30% error in the resultant luminosity function. Since $\Delta\phi_N$ and $\Delta\phi_D$ are

statistically independent, the total uncertainty, $\Delta\phi$, is

$$\Delta\phi = \sqrt{\Delta\phi_N^2 + \Delta\phi_D^2} \quad . \tag{7.4}$$

It should be emphasized that $\Delta\phi$ represents only the internal, random uncertainties associated with the estimated luminosity function. Potentially more serious (and unquantifiable) systematic errors, most already discussed, are not included.

Note that the composite Taurus + Ophiuchus luminosity function will consist of stars from two very different regions of the Galaxy; recall that the Galactic coordinates of the two fields are ℓ = 353°, b = 17° (Ophiuchus) and ℓ = 173°, b = -15° (Taurus). An additional complication associated with mixing the two stellar samples arises from the fact that they are incomplete to different depths. As discussed in Chapter 4, the Ophiuchus data go to m_V ~22 mag, and the Taurus data to m_V ~ 22.5. Since the distance modulus corresponding to the Ophiuchus cloud is ~6 mag, and the value corresponding to the Taurus cloud ~5.7, the two samples are therefore complete to only M_V = 16.0 and 16.8, respectively. While fainter stars can be detected in both samples, they must lie closer than the molecular cloud and the volume over which such objects can be detected in our survey is correspondingly reduced. Consequently, the luminosity function for these stars must be adjusted for its lack of completeness, as described below. The maximum distance out to which the faintest M dwarfs can be detected toward each cloud field is given in Table 7.1.

The usual method to correct for incompleteness is to apply the V_{max} method (*cf.* Schmidt 1975). The basic idea behind the method is simple. Suppose N′ stars are detected in a luminosity function survey within the absolute magnitude bin ($M_V \pm 0.5$), and suppose that the survey is complete only to a distance d′. If the luminosity function is complete for

Table 7.1

Completeness Limits of the Taurus and Ophiuchus Samples

Spectral Type	M_V	Ophiuchus D(pc)	Taurus D(pc)
M5.5	15.75	>160	>140
M6	16.63	120	>140
M6.5	17.70	72	90
M7	18.60	48	60
M7.5	>19	<40	<50

brighter stars to a distance of d (>d′), the least biased estimate for the stellar population of the bin within the full survey volume is clearly

$$N = N' \left(\frac{d}{d'} \right)^3 \quad . \tag{7.5}$$

Notice that, unavoidably, the counting uncertainty associated with the corrected bin population is not $\sqrt{N}$, but $\sqrt{N'(d/d')^3}$.

The V_{max} method is implemented by deducing for each star in some magnitude interval the maximum volume in which it can be located and still be detected in the survey. For example, the maximum volume, V^i_{max}, corresponding to the i^{th} star of a bin sample is obtained from:

$$m_V^{lim} - M_V^i = 5\log(D^i_{max}) - 5 \tag{7.6}$$

where m_V^{lim} is the limiting magnitude of the survey, and M^i_V and D^i_{max} the associated absolute magnitude and distance limit. V_{max} is defined by

$$V^i_{max} = \Omega \left(D^i_{max} \right)^3 \tag{7.7}$$

where Ω is the survey solid angle. Hence, the space density corresponding to the magnitude interval is simply

$$\phi = \sum_{i=1}^{N} \frac{1}{V^{i}_{max}} \tag{7.8}$$

where N is the total number of stars within the magnitude bin. The expected uncertainty is inferred from the variance,

$$var(\phi) = \sum_{i=1}^{N} \left(\frac{1}{V^{i}_{max}} \right)^2 \tag{7.9}$$

Magnitude-limited photometric studies of the luminosity function are usually subject to Malmquist-type bias in their estimates of the stellar luminosities. This bias arises from the fact that any given spectral type has an intrinsic scatter in luminosity. That is to say, stars classified as being of a particular spectral type will have in fact a range in absolute magnitude that can be characterized by a mean value, M_0, and a gaussian dispersion, σ. In a photometric survey, the intrinsically brighter members of a spectral type will be sampled to greater distances than the fainter members. Consequently, the *deduced* absolute magnitude, $\bar{M}$, of a given spectral type will typically be brighter than the characteristic mean of the spectral type, *i.e.*, $\bar{M} < M_0$. The correction for Malmquist bias is rather straightforward (the reader is referred to a nice discussion in Mihalas and Binney, 1981).

There is yet another systematic bias that plagues photometric parallax surveys sometimes referred to as the Malmquist *effect* (*cf.* Stobie *et al.* 1989). It arises from the fact that the magnitude-color relation used to derive luminosities and deduce distances itself is fraught with uncertainty (both of an inherent and empirical nature). Consequently the

intrinsically brighter stars are observed at greater distances and, because of the solid-angle effect, there are more of these stars to "scatter" into adjacent faint magnitude bins. Thus, the net effect is to boost the total number of stars within an absolute magnitude interval. The correction for the Malmquist effect is not particularly straight forward (for an excellent discussion, see Stobie *et al.* 1989, and Leggett and Hawkins 1988).

We do not attempt to correct our data for Malmquist-type systematic effects since only those magnitude bins with $M_V > 16$ are affected, and since the effects are most likely small compared to the large poisson uncertainties that poison our data. Indeed, it is worth pointing out that one advantage of a (sufficiently) opaque screen luminosity survey is its freedom from Malmquist effects.

As discussed in Chapter 4, the Oph and Taurus surveys are complete to the distance of the clouds for even the lowest mass stars *if* we use only the R and I data. Unfortunately, with only one color it is very difficult to separate unreddened foreground dwarfs from reddened background field stars. Owing to this shortcoming we must regard the R,I foreground candidates, listed in Tables 6.1 and 6.2, as very weak candidates. Their inclusion in the number density estimates are flagged accordingly in the plots and tables.

In addition to the problems of completeness that affect the faintest magnitude bins of our composite sample, there may be a significant degree of contamination from reddened field stars and/or associated cloud members. We showed in the last chapter that 1 of 3 Taurus foreground candidates observed spectroscopically is in fact a reddened star, probably of spectral type earlier than M1. Of course, there is the possibility that this star is very unusual, perhaps belonging to the spheroid population, given that it appears to have a high proper motion; in that case, we were simply unfortunate to choose it for spectroscopic observation. Nevertheless, we must consider the possibility that the contamination rate for our composite sample may be ~33%. This value is of course very crude given that only 3

stars are involved in its determination, but it represents the least biased estimate of the integrity of the sample. On the other hand, we do not expect significant contamination from stars with brighter magnitudes because of two important factors: first, the bright stars have accurate photometric measurements, and second, the molecular clouds effectively screen out all of the intrinsically bright background stars. As discussed in Chapters 4 and 5, the greatest source of background star contamination arises from field G and K dwarfs located some 300 - 500 pc from the Sun. Given the mean extinctions of the clouds and the limiting magnitudes of the surveys, the absolute magnitude bins affected most are those with $M_V > 14$ mag. We therefore shall apply the 33% contamination correction factor only to those magnitude intervals with $M_V > 14$.

A final consideration that must be addressed for this study (and all other photometric parallax surveys) is the problem of duplicity. It is an empirical certainty that most field stars reside in binary and multiple stellar systems. Amongst the nearby stars, the binary fraction[1] is reported to be between 30 and 50% (*cf.* Henry and McCarthy 1990; Reid 1991). Of the nearby stars, the range in projected separations between the two components of binary systems vary from ~10 to 1200 au (the numbers of stars per log separation interval is roughly constant over this range). Generally astronomers working in this field regard separations less than 10 au as "near" binaries and separations greater than 10 au as "wide" or "far" binaries.

As discussed in previous chapters, the seeing conditions for our observing runs varied from 1 to 2″. Taking the 2″ value as our limiting angular resolution (corresponding to ~3 CCD pixels), we list the limiting separation between two stars of a binary system as a function of distance in Table 7.2.

---

[1] The binary fraction is defined to be the ratio of binary stellar systems to the total number of systems (including single stars). Occasionally the binary fraction is understood to be the ratio of all multiple stellar systems to the total number of systems.

Table 7.2

Angular Separation

D(pc)	sep. (au)
5	10
10	20
20	40
50	100
75	150
100	200
150	300

It can be seen from Table 7.2 that our survey should be sensitive to "wide" binaries (>300 au), but is quite incomplete beyond 50 pc for "near" binaries. We therefore expect perhaps a few binary systems within our sample to be misidentified as single star systems. The composite luminosity of a binary or multiple system is of course greater than the true luminosity that characterizes the primary component of the system, and the composite color will also be different from the color of the primary (for example, an early type M dwarf with a late-type companion will have a composite color that is redder than the color of the early-type star). In any case, the net result is that the total number density — and more importantly the total mass density — will be under-represented in our survey. In this spirit, our estimate of the stellar luminosity function more accurately measures the number density corresponding to stellar systems, *i.e.*, the *system* luminosity function. It should be noted that there is a fair amount of controversy as to the role of binary systems in the stellar luminosity function, and it has been suggested that binaries systems do not in fact significantly alter the empirical luminosity function (*cf.* Reid 1987 and 1991; Stobie *et al.* 1989). We will return to this issue in the next section when we outline previous work done

on the luminosity function. With the cautions outlined above, we now present the faint end of the stellar luminosity function corresponding to the Taurus and Oph stellar samples. In Table 7.3 we show the results of the binning of the stars from Tables 6.1 and 6.2. The total volume surveyed here is 198 pc^{-3}. The column denoted ϕ^* is the luminosity function based on the sample with 33% less stars for magnitude bins with $M_V > 14$ mag. The number densities corresponding to the magnitude bins $M_V \geq 17$ have in both cases been corrected using the V_{max} technique; the numbers appearing in parenthesis are the *uncorrected* densities, and since our survey suffers from incompleteness at the very faint end, $M_V \geq 17$, these values are to be regarded as lower limits only (they are also lower limits in so far as the V_{max} corrected densities suffer from Malmquist effects; and thus, the number densities corresponding to $M_V > 17$ are *over*estimated).

Table 7.3

The Luminosity Function Based on Counts Within 140 and 160 pc

M_V	N		$\phi(M_V)$	$\phi^*(M_V)$
(± 0.5)	Oph	Taurus	(100 × stars mag^{-1} pc^{-3})	(100 × stars mag^{-1} pc^{-3})
10	0	1	0.51	0.51
11	0	1	0.51	0.51
12	1	1	1.01	1.01
13	1	2	1.52	1.52
14	1	1	1.01	1.01
15	3	3	3.03	2.02
16	0	2	1.01	0.51
17	4	3	8.13 (3.54)	6.03 (2.53)
18	1	0	4.79 (0.51)	3.16 (0.51)

The composite luminosity function, ϕ_V, is shown in Figure 7.1, where the data points (denoted by filled circles) are plotted along with their total estimated errors given by Equation 7.4. The densities that have been corrected using the V_{max} method are denoted by open circles, while the uncorrected values — which we regard as lower limits to the densities — are denoted by filled squares. We also plot the same function with 1.5 magnitude intervals in Figure 7.1b. By increasing the size of the magnitude bins we decrease the rather large uncertainties due to statistical noise. In Figure 7.2 we show the same function except that only the lower limits to the densities corresponding to the faint magnitude bins are shown (denoted by the filled squares), as are the densities corresponding to the addition of stars determined from the R,I one-color constraint (denoted by the open squares). As noted previously, the candidate sample determined from the one-color criterion is in principle complete to the distance of the molecular clouds. Thus, the addition of the R-I stars to the estimated number densities represents a further constraint on the true density values. However, since the sample of R,I candidates is probably incomplete due to other factors (*e.g.*, the extreme difficulty in distinguishing intrinsically red stars from reddened background stars), the densities estimated from the addition of these stars are more likely to be lower limits to the true density values.

In Figure 7.3 we plot the composite luminosity function, ϕ^*_V, determined using a 33% contamination correction applied to the bins with $M_V > 14$. The symbols are same as used in Figure 7.1. ϕ^*_V is also shown in Figure 7.4, except as with Figure 7.3, only the lower limits to the densities in the faint magnitude bins are shown, along with the densities based on adding the R-I stars.

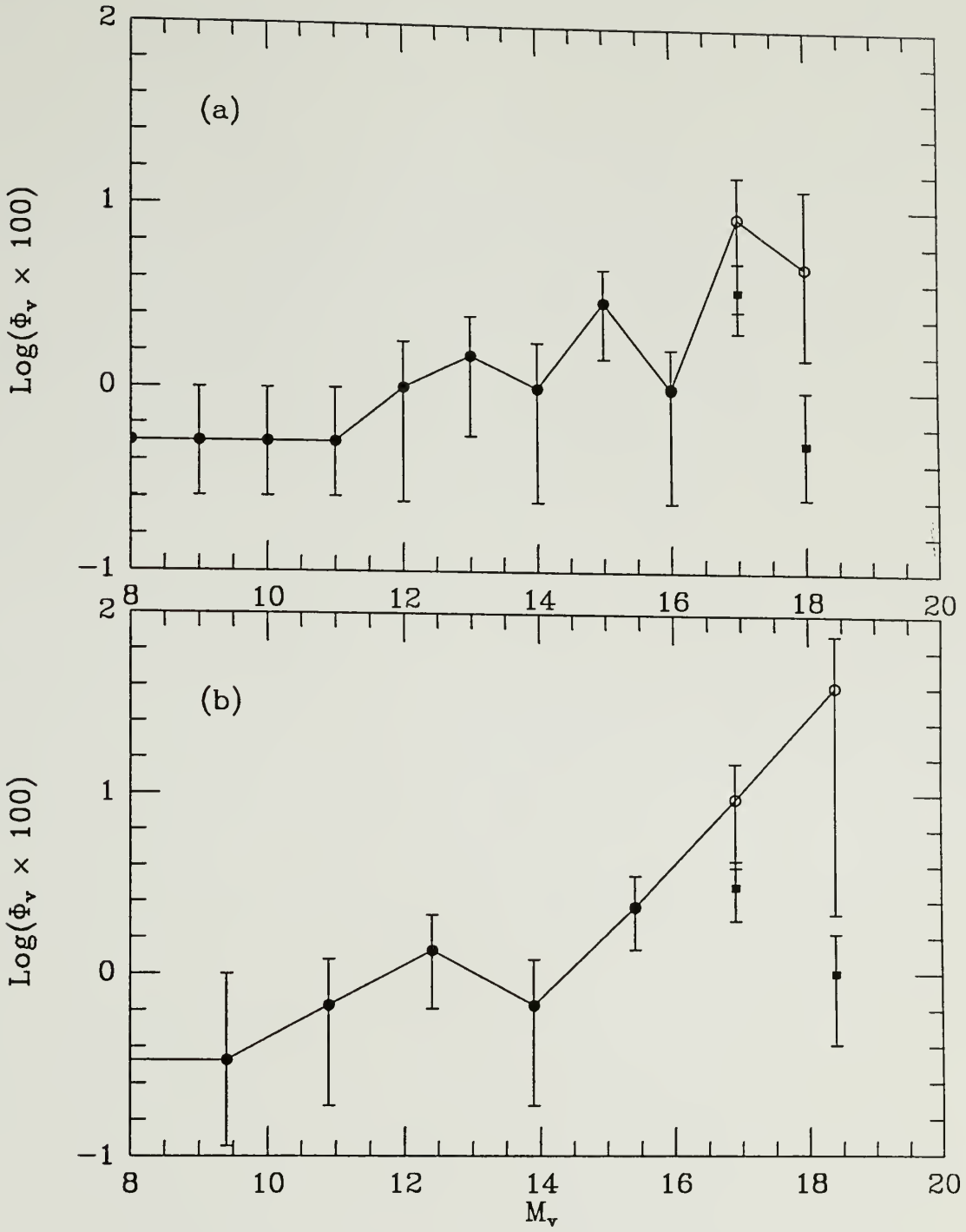

Figure 7.1 The observed visual luminosity function corresponding to the Taurus and Ophiuchus fields. ϕ_V is the numbers of stars pc^{-3} visual mag^{-1}. The data is plotted in (a) ±0.5 magnitude bins and (b) ± 0.75 magnitude bins. The filled circles correspond to the number density of stars found using a two-color constraint, and the open circles represent the V_{max} corrected number density of stars. Due to completeness problems the number density shown for bins with $M_V > 17$ (filled squares) represents a lower limit to the true density. The error bars represent the total estimated uncertainty, given by Equation 7.4.

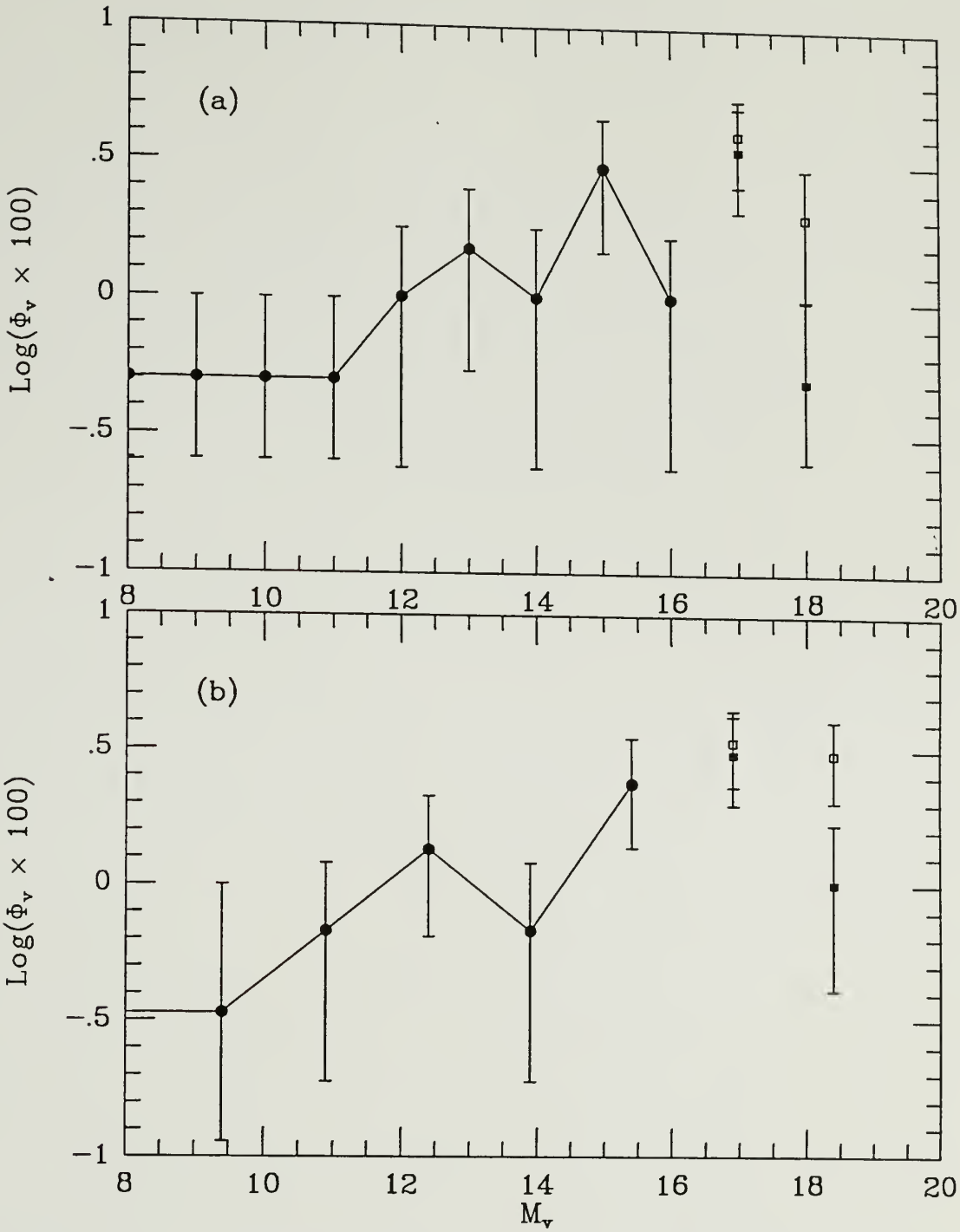

Figure 7.2 The observed visual luminosity function corresponding to the Taurus and Ophiuchus fields. ϕ_V is the numbers of stars pc^{-3} visual mag^{-1}. The data is plotted in (a) ± 0.5 magnitude bins and (b) ± 0.75 magnitude bins. The filled circles correspond to the number density of stars found using a two-color constraint, and the open squares represent the number density of stars found using both a two-color and a one-color constraint. Due to completeness problems the number density shown for bins with $M_V > 17$ (filled squares) represents a lower limit to the true density. The error bars are given by Equation 7.4.

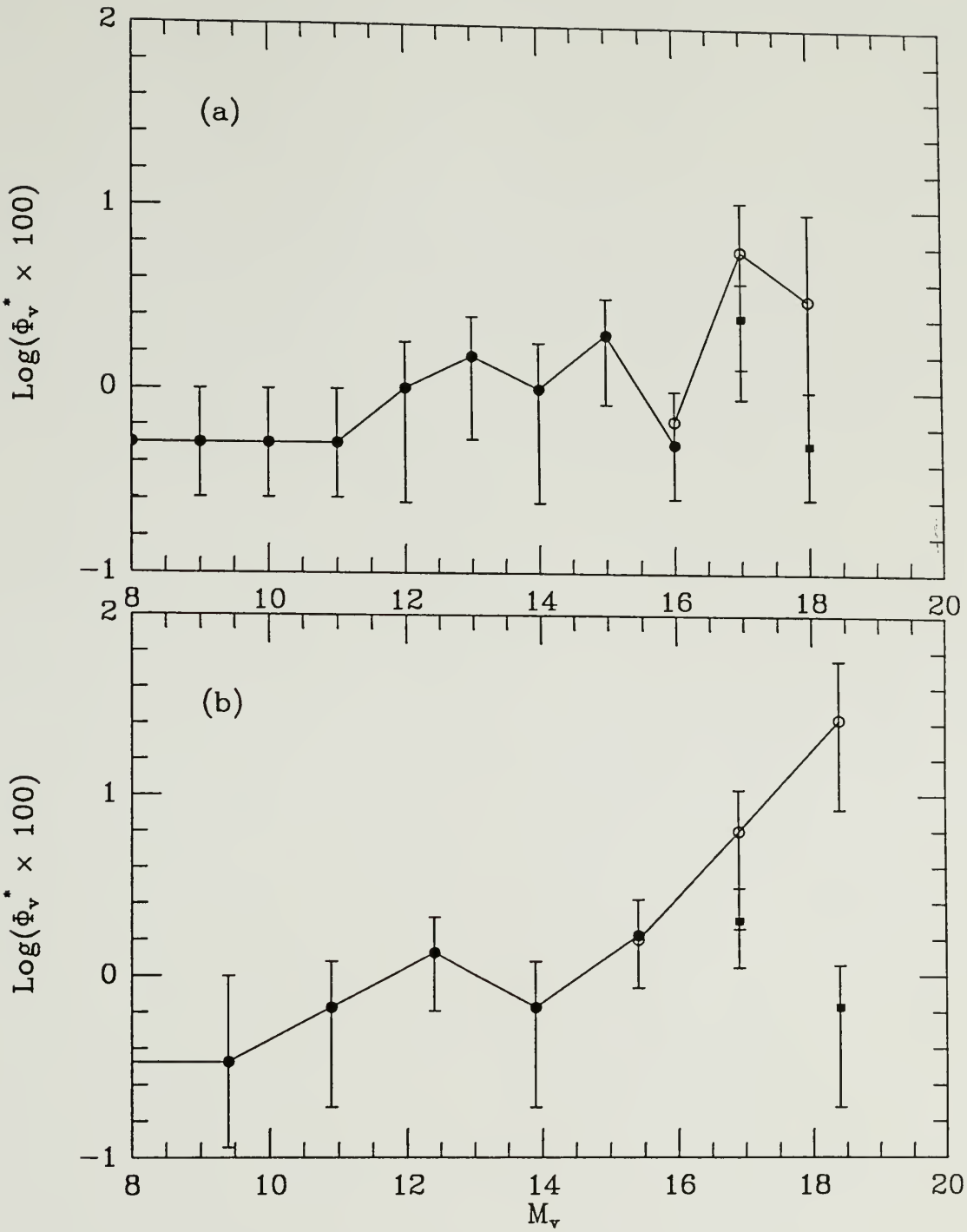

Figure 7.3 The corrected visual luminosity function corresponding to the Taurus and Ophiuchus fields. ϕ_{V^*} is the numbers of stars pc^{-3} visual mag^{-1}, where 33% of the objects have been subtracted from each magnitude bin satisfying $M_V > 14$. The data is plotted in (a) ±0.5 magnitude bins and (b) ± 0.75 magnitude bins. The open circles represent the V_{max} corrected number density of stars. Due to completeness problems the number density shown for bins with $M_V > 17$ (denoted by filled squares) represents a lower limit to the true density. The error bars represent the total estimated uncertainty, given by Equation 7.4.

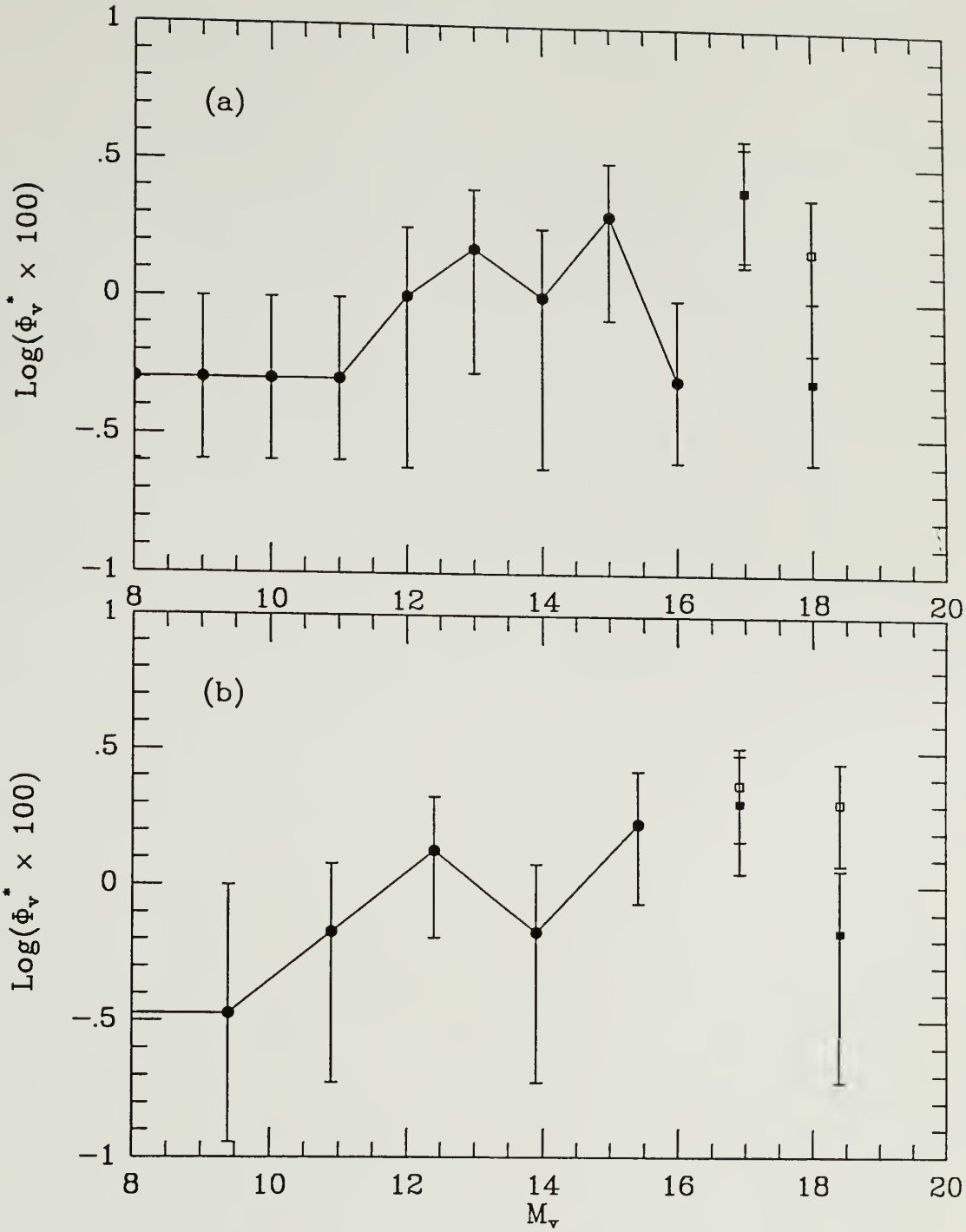

Figure 7.4 The corrected visual luminosity function corresponding to the Taurus and Ophiuchus fields. ϕ_{V^*} is the numbers of stars pc^{-3} visual mag^{-1}, where 33% of the objects have been subtracted from each magnitude bin satisfying $M_V > 14$. The data is plotted in (a) ±0.5 mag bins and (b) ± 0.75 mag bins. The open squares represent the number density of stars found using both a two-color and a one-color constraint. Due to completeness problems the number density shown for bins with $M_V > 17$ (denoted by filled squares) represents a lower limit to the true density. The error bars are given by Equation 7.4.

In spite of the dreadful statistical noise associated with these results, the faint end of the stellar luminosity function appears to rise (as suggested by Figures 7.1 and 7.3) or at least remains flat beyond $M_V \sim 14$ or 15 (as suggested by Figures 7.2 and 7.4). In order to shed more light on these results we next turn to previously determined luminosity functions and compare our results with them.

7.2 Comparison with other Work

The luminosity function determined from the sample of nearby stars is generally considered the standard benchmark for comparison with other work in this field. In particular, the work of Wielen, Jahreiss and Kruegger (1983; hereafter referred as WJK) is usually cited as the best determined luminosity function for absolute magnitudes extending to $M_V \sim 13$ - 14. The WJK luminosity function is based on the sample of stars within ~20 pc of the Sun (parallax $\pi \sim 0.05''$) listed in the Gliese catalogue. Other surveys of the nearby stars which count stars within 5.2 pc of the Sun are generally complete to absolute magnitudes much fainter than that of WJK. One of these, by Dahn, Liebert and Harrington(1986; hereafter referred as DLH) comes from the Luyten (LHS) catalogue, a kinematic study of high proper motions stars, and from further astrometric, photometric, and spectroscopic observations. Another noteworthy study comes from Henry and McCarthy (1990) who observed basically the same sample as DLH using infrared speckle interferometry. With this technique, Henry and McCarthy were able to detect "near" binary/multiple companions to many of these stars (with separations as small as ≤10 au). Though the DLH luminosity function is complete to $M_V \sim 17$ mag, and the Henry and McCarthy K-band luminosity function is complete to the limit of the hydrogen-burning main sequence, they suffer from statistical noise since the 5 pc limited volume is considerably smaller than that of the WJK study (though, about double the size of the

volume surveyed in this study) and there is also some concern that their samples are incomplete because of kinematic bias toward high proper motion stars. In any event, a major advantage that the WJK, DLH, and particularly the Henry and McCarthy determinations possess is that they are sensitive to closely separated stellar systems ("near" binaries); thus, these luminosity functions represent *true* stellar density distributions.

The luminosity functions of WJK and DLH are plotted in Figure 7.5. Both are characterized by increasing stellar densities toward the faint luminosities, where an apparent maximum occurs at $M_V \sim 12 - 13$. Thereafter, there is a decline toward $M_V \sim 14$, and a general flattening of the number density at the faintest luminosities. Whereas the K-band luminosity function determined by Henry and McCarthy (not shown here) exhibits a significant *rising* trend that extends to the limit corresponding to the lowest mass stars, but immediately thereafter declines. It is interesting to note that the luminosity function of DLH compares quite closely with the most conservative estimate of this study, Figure 7.4, up to $M_V \sim 17$, while the Henry and McCarthy result is consistent with the V_{max} corrected faint end of the luminosity function from this study. The simplest interpretation of these results is that the stellar *system* luminosity function determined in this study sufficiently represents the true *stellar* luminosity function at least for magnitudes extending to $M_V \sim 17$. In this interpretation, the contribution from faint companions in binary systems to the total population of nearby stars is small. This story however, does not end on this note, as discussed below.

The other major approach used to determine the stellar luminosity function is *via* photometric parallax. As discussed earlier, this method uses magnitude-color constraints to estimate the distance and spectral type of the observed stars. For reasons which are still unclear, the faint end of the luminosity function determined by the method of photometric parallax differs significantly from that associated with the nearby stars. Photometric studies

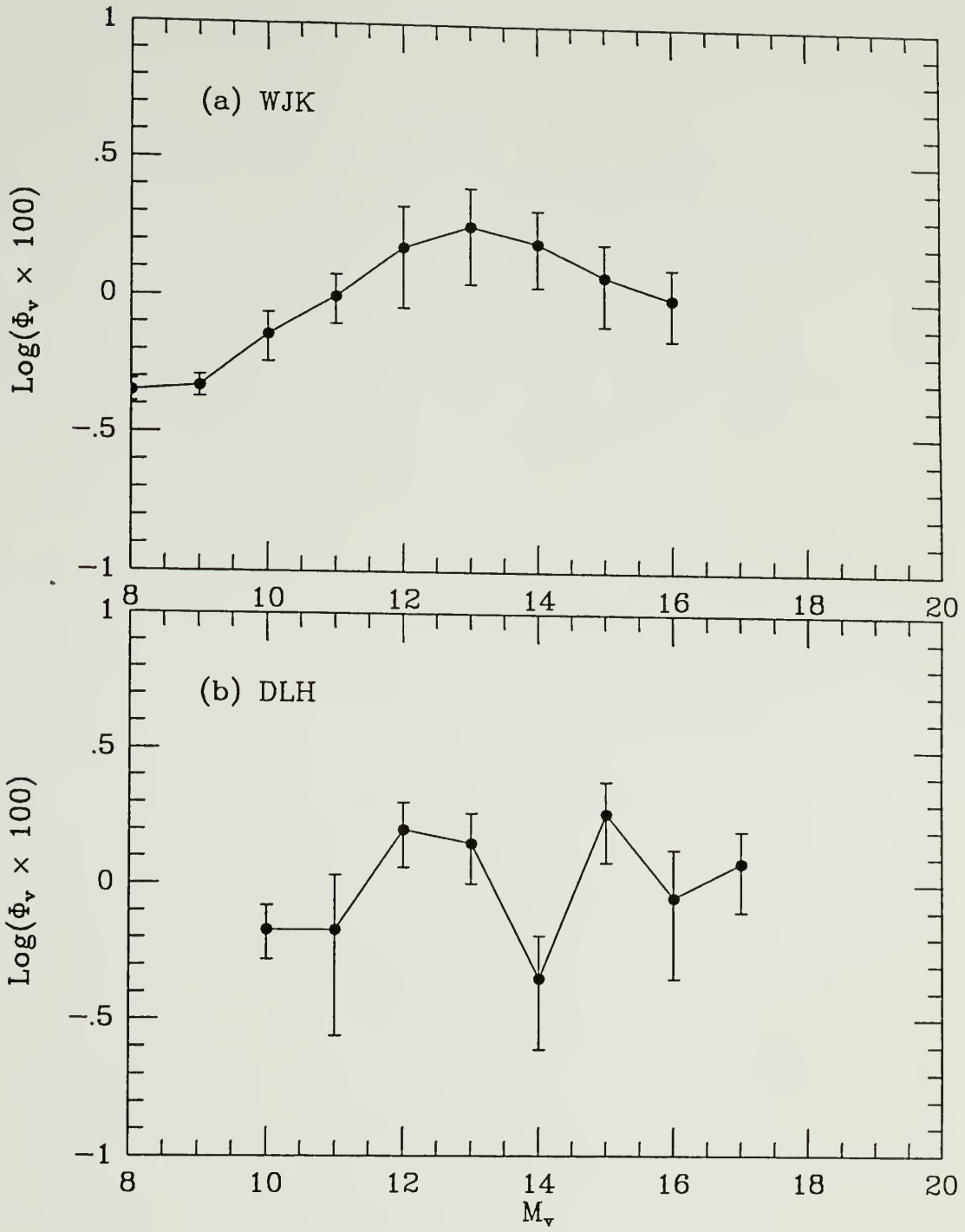

Figure 7.5 The observed visual luminosity function corresponding to the nearby stars. In (a) we plot the luminosity function of Wielen, Jahreiss and Kruegger (1983), and in (b) the luminosity function of Dahn, Liebert and Harrington (1986). ϕ_V is the numbers of stars pc^{-3} mag^{-1}. The error bars represent the $\sqrt{N}$ uncertainty in each bin.

by Reid and Gilmore (1982; hereafter referred as RG) and Hawkins and Bessell (1988; hereafter referred as HB) show that a number density peak at $M_V \sim 12$ (agreeing with WJK and DLH), but thereafter rapidly decreasing at fainter luminosities. Note however, that both studies of RG and HB do suggest a rise or at least flattening of the luminosity function at $M_V > 16$. In Figure 7.6 we show the respective number densities determined by RG and HB[2]. As with the WJK and DLH functions, the number density of objects determined in this study appears to agree with those determined by RG and HB, for luminosities extending to $M_V > 12 - 14$. On the other hand, there is a large disparity for the faint magnitude bins — although the statistical errors are admittedly large, we find more stars than these surveys do.

The large statistical errors associated with the relatively small numbers of stars in our sample can be reduced somewhat by comparing *cumulative* number densities. In Table 7.4 we show the cumulative number of stars as a function of absolute magnitude for various luminosity functions. All the data has been normalized to the volume of this study, ~198 pc^3, and the number densities have been summed from $M_V = 9.5$. Also shown in the table (in parenthesis) are the expected $\sqrt{N}$ errors.

It can be seen in Table 7.4 that the cumulative number of objects found in this study agrees quite well with those deduced from other surveys, for limiting magnitudes brighter than $M_V \sim 15 - 16$. There appears to be complete agreement between our results and those of DLH for magnitudes extending to $M_V \sim 17$. This result is illustrated in Figure 7.7a. On the hand, for the photometric parallax surveys, the differences become striking at

---

[2] It should be noted that these authors have corrected their data for Malmquist bias. However, there remains some question as to the accuracy of these corrections (see Stobie *et. al.* 1989). In any case, the corrected or uncorrected number densities do not significantly alter the discussion in this chapter.

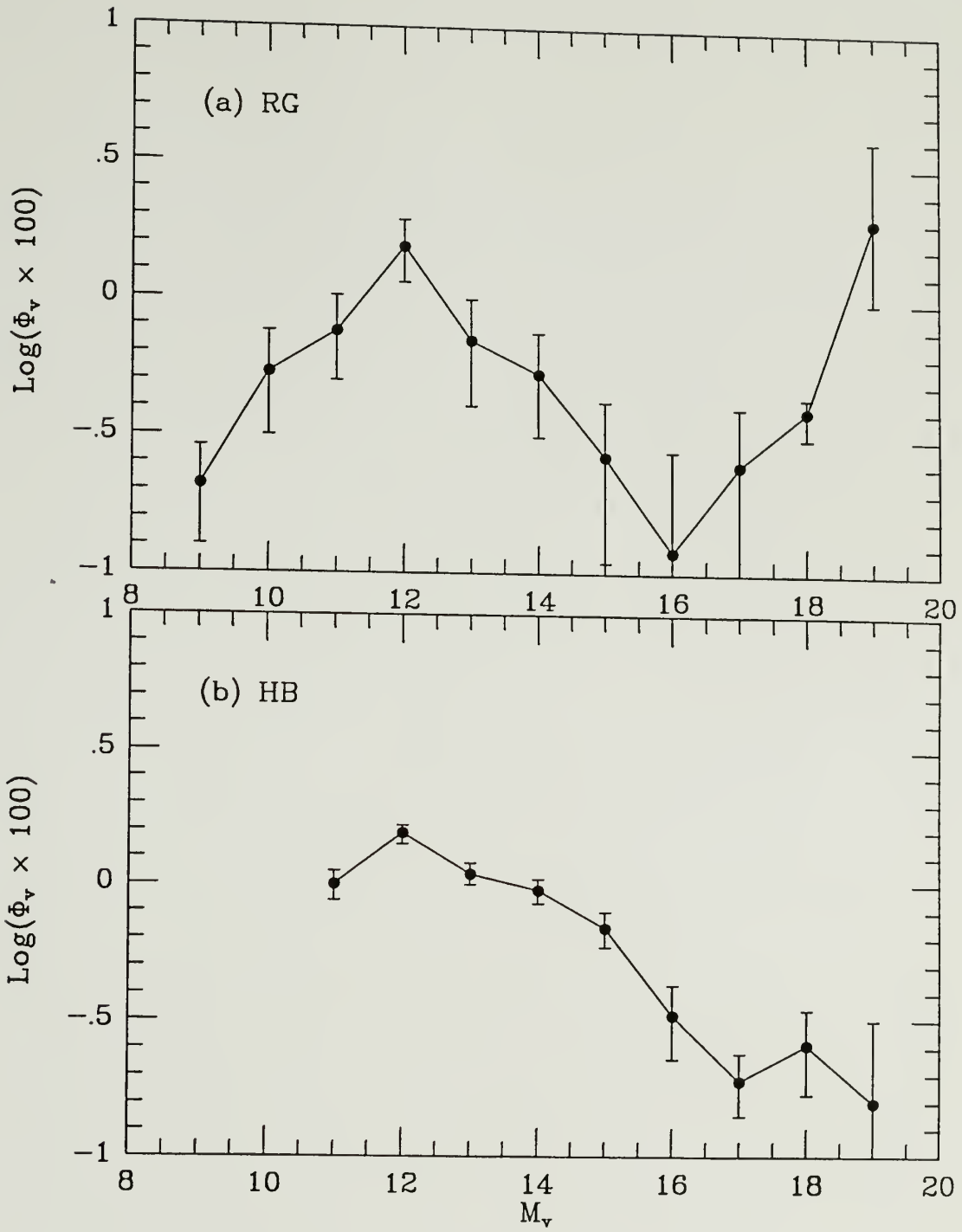

Figure 7.6 The observed visual luminosity function corresponding to the SGP and other southern hemisphere fields. In (a) we plot the luminosity function of Reid and Gilmore (1982), and in (b) the luminosity function of Hawkins and Bessell (1988). ϕ_V is the numbers of stars pc^{-3} mag^{-1}. The error bars represent the $\sqrt{N}$ uncertainty in each bin.

Table 7.4

Cumulative Number of Objects from Various Surveys

M_V^{lim}	N_V^{lim}						
	this study[a]		WJK	DLH	RG	HB	NGP[b]
10.5	1 (1)		1 (1)	1 (1)	1 (1)	1 (1)	1 (1)
11.5	2 (1)		3 (2)	2 (1)	3 (2)	3 (2)	3 (2)
12.5	4 (2)		6 (2)	5 (2)	6 (2)	6 (2)	5 (2)
13.5	7 (3)		10 (3)	8 (3)	7 (3)	8 (3)	7 (3)
14.5	9 (3)			9 (3)	9 (3)	9 (3)	8 (3)
15.5	13 (4)			13 (4)	9 (3)	10 (3)	9 (3)
16.5	14 (4)			15 (4)	9 (3)	10 (3)	9 (3)
17.5	>19 (4)	26 (5)		17 (4)	10 (3)	11 (3)	10 (3)
18.5	>20 (4)	32 (6)			11 (3)	11 (3)	

[a] Computed from ϕ^*; see Figures 7.3 and 7.4. The values corresponding to M_V = 17.5 and 18.5 represent lower limits in the left hand boxes; the right hand boxes contain values corrected by the V_{max} technique.
[b] Determined for stars toward the NGP (Stobie *et al.* 1989).

the fainter magnitudes. Even if we ignore the completeness corrections, it can be seen from Figure 7.7b that our study contains ~30% *more* stars at the faint end where both photometric studies are presumed to be complete — we find roughly 2σ more objects at the faintest luminosities ($M_V > 17$) than do Hawkins and Bessell or Reid and Gilmore. The disparity is much larger if our corrected number densities are used. Other than statistical aberration, it is not clear what the cause of this apparent discrepancy is. However, two contributing factors may be the Galactic density distribution and duplicity. We consider these problems below.

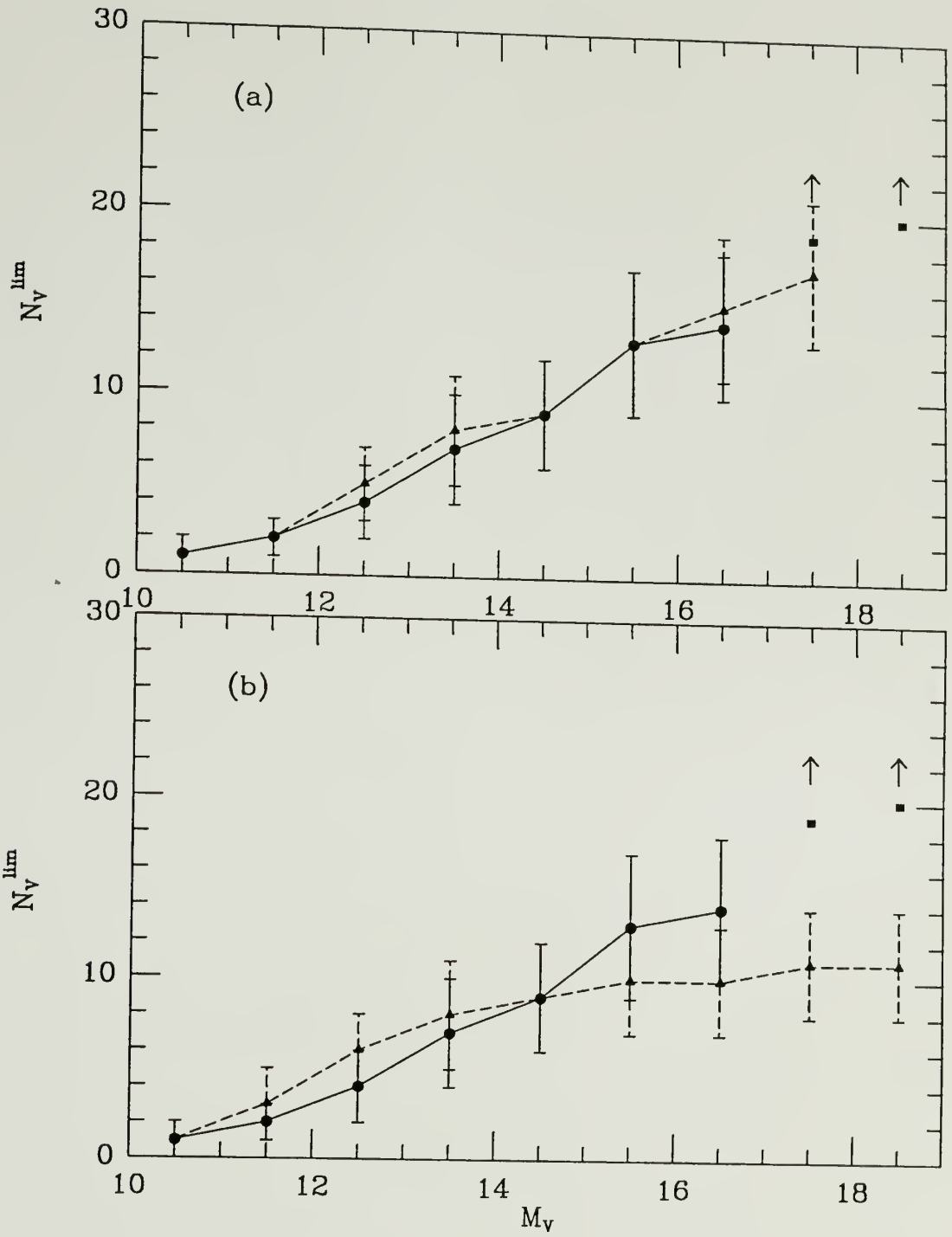

Figure 7.7 The cumulative number of objects as a function of limiting absolute magnitude. The data is normalized to a volume of 198 pc^3. In (a) we show the cumulative number of objects found from this study (filled circles and a solid line) and from the nearby stellar sample of DLH (filled squares and dashed lines). In (b) we compare the cumulative number of objects found from this study with that estimated from the study of HB (filled squares and dashed lines). The filled squares (with arrows) denote lower limits to the true values. The error bars represent the $\sqrt{N}$ uncertainty in the cumulative counts.

As we discussed previously, studies using photometric parallax have the distinct advantage of surveying large volumes of space. Reid and Gilmore surveyed more than 18 square degrees toward the south Galactic pole with a limiting magnitude of I ~ 17, while HB surveyed some 85 square degrees of southern hemisphere fields with similar magnitude limits. Thus, not only are these studies complete to the faintest stellar magnitudes (within distances from 50 to 100 pc) but their statistics are rather good as well. The differences between these luminosity functions and those determined for the nearby stars are a source of continuing debate and puzzlement, and the issues of the Galactic density distribution and stellar duplicity have been suggested as possible origins in this case as well.

Consider the stellar density distribution first. The deep photometric surveys of RG and HB are principally focused towards the southern Galactic pole, whereas Stobie *et al.* (1989) concentrated their efforts toward the northern Galactic pole[3]. These surveys contain stars predominantly located far from the Sun (~100 pc) in directions of decreasing number density, whereas the studies by WJK, DLH, and Henry and McCarthy were limited to the nearby stars (~5 - 20 pc; north of $\delta = -30°$) whose distribution is for the most part uniform over the sky. In this study we isolated stars located in the directions of Taurus and Ophiuchus. If we ignore for now the radial component of the Galactic stellar distribution and consider only the z component (*i.e.*, the direction perpendicular to the disk), we may roughly estimate the expected number density contrast between directions toward the poles and the Taurus and Oph fields.

[3] Stobie *et. al.* (1989) did apply a density correction to their NGP data using a similar technique described here.

If we characterize the stellar distribution according to (see Appendix F),

$$\rho(z) \rightarrow \rho_0 \exp\left(-\frac{z}{\beta}\right) \tag{7.10}$$

where ρ_0 is the local number density, β is the disk scale height and z is the distance from Sun along the z-axis. For a given distance from the Sun, D, the ratio between the density toward the SGP and the density in the direction of Taurus follows:

$$\exp\left[\frac{D}{\beta}(\sin b - 1)\right] \tag{7.11}$$

where b is the Galactic latitude of Taurus, ~ -15°. Let us consider the number density of late-type stars, whose scale height is ~400 pc (Appendix F). Then, for example, at a distance of 50 pc, the density of stars between the two directions differs by ~10% (in the sense that at a distance of 50 pc the SGP has 10% less stars than those lying in direction of Taurus). At yet greater distances the disparity widens; at 100 pc the ratio difference is ~17%, and at 150 pc the difference is ~24%. If we integrate Equation 7.10 over some volume, we arrive at the total number of stars within the volume. We find that for a volume extending 150 pc from the Sun, the number of objects located in the volume toward b = -15° is about 20% larger than the number of objects located in an equivalent volume toward b = 90° (*i.e.*, towards the poles). Note that this result does not affect the *shape* of the luminosity function, only the absolute value.

We may estimate more accurately the number density ratios between the various fields mentioned here by including the radial component of the Galactic stellar distribution. In this more complicated case, we make use of the model described in Appendix F. Here we compute the total number of stars in a volume whose extent is delimited at a number of distances from the Sun. Only those stars with magnitudes satisfying $9.5 \leq M_V \leq 18.0$ are counted. Further, the local stellar density is assumed to be represented by the luminosity

functions of WJK ($M_V \leq 13$) and DLH ($M_V > 13$). The results are shown in Figure 7.8, where we have plotted the expected number ratio as a function of distance between stars lying toward the Taurus and Ophiuchus clouds (denoted by filled circles and solid line), and the expected number ratio between stars lying toward the Galactic pole and the Ophiuchus cloud (denoted by open circles and dashed line). It can be seen that for a volume extending beyond 100 pc, there are about 5% more stars located in the Ophiuchus volume than in the Taurus volume. This difference nicely illustrates the radial dependence of the Galactic distribution. Ophiuchus lies in a direction that is within 10° of the Galactic center, whereas the Taurus cloud is located in the direction of the anticenter. More importantly, there are about 10 - 15% less stars located within 100 pc along the direction of the Galactic poles than toward the Ophiuchus or Taurus clouds. This contrast contributes perhaps 50% toward the disparity between the *uncorrected* luminosity function of this study and those of RG and HB. There still remains a minimum of another 15% or so disparity between the two luminosity functions.

It has been suggested by DLH that the differences at the faint end of the various luminosity functions arise from unresolved binary companions. Recall that photometric parallax surveys are not sensitive to these objects. And yet simple models which factor in the contribution from various binary systems (*e.g.*, equal and unequal mass systems) imply that unresolved binaries probably cannot account for the large apparent differences between the two types of luminosity functions (Stobie *et al.* 1989). For example, Reid (1987; 1991) finds that the *system* number density determined from a photometric parallax study underestimates at most ~ 25 - 30% of the true stellar number density. Reid (1991) in fact concludes that the inherent systematic uncertainties of photometric parallax compensate for the loss of unresolved (unequal mass) companions of binary and multiple systems. In any

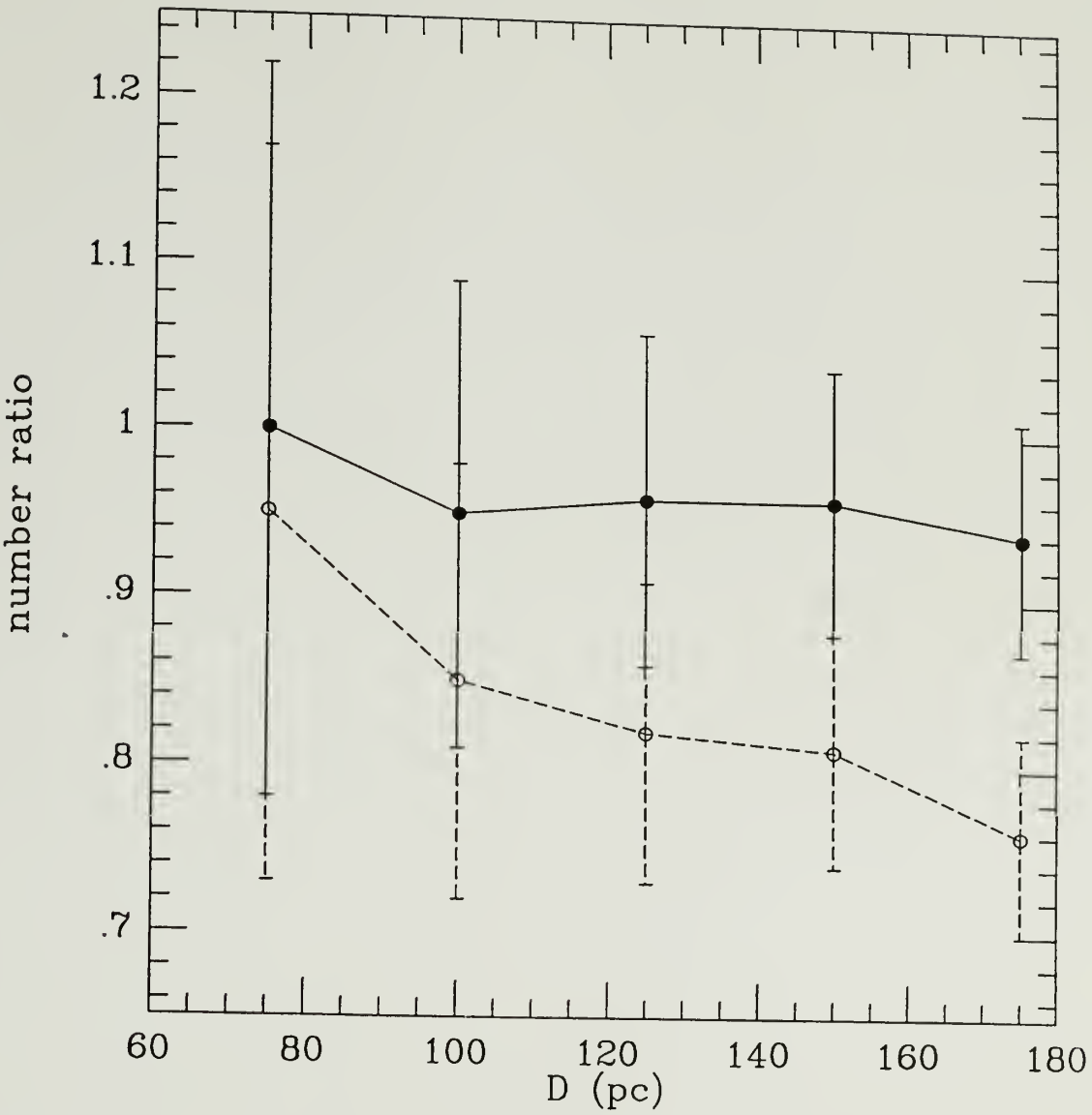

Figure 7.8 The expected number ratio between stars lying toward the Taurus and Ophiuchus clouds (denoted by filled circles and solid line), and the expected number ratio between stars lying toward the Galactic pole and the Ophiuchus cloud (denoted by open circles and dashed line). The values are estimated using the Galactic distribution model described in Appendix F, where we have computed the total number of stars in a volume whose extent is delimited at various distances from the Sun. Only those stars with magnitudes satisfying $9.5 \leq M_V \leq 18.0$ are counted. The local stellar density is assumed to be represented by the luminosity functions of WJK ($M_V \leq 13$) and DLH ($M_V > 13$). The error bars represent the $\sqrt{n}$ uncertainties in the ratio.

case, while our survey undoubtedly contains a few unresolved binary systems, apparently they cannot resolve the discrepancy between our results and the others given in Table 7.4.

In summary, the faint end of the stellar luminosity function determined in this work resembles the local number density determined by WJK and DLH up to $M_V \sim 16$. At still fainter absolute magnitudes, we find the shape of our visual luminosity function to be consistent with that exhibited by the K-band luminosity function determined by Henry and McCarthy for very low mass stars; furthermore, we find at least ~15% more stars than do photometric parallax studies of the polar regions. This difference widens dramatically if even the simplest correction for incompleteness is applied to our data. While statistical noise due to our small sample, systematic effects, the Galactic density distribution, and multiplicity may all contribute to the disparity, it nonetheless seems real and substantial. We therefore tentatively conclude that the luminosity function rises beyond $M_V = 16$; even if we discard our attempts to correct for incompleteness in the faintest magnitude bins, there appears to be little doubt that the luminosity function at least remains flat for the lowest mass stars.

7.3 Future Work

As was discussed in Chapter 2, the molecular cloud B5 was originally targeted as the third field to be observed for this study. Unfortunately, this observing run was weathered out in 1990 December. A future KPNO date has been rescheduled (mid-December of 1991) in order to observe toward this cloud using the 4-m telescope and a large format CCD.

Barnard 5, $\alpha[1950] = 3^h\ 44^m\ 29^s$, $\delta[1950] = 32°\ 44'\ 30''$, $\ell = 161°$, $b = -16.8°$, is endowed with an extended, very high extinction core, and lies ~2 times further from the Sun than the Taurus or Oph clouds. A relatively large volume of space lies between the

Sun and cloud, and thus, this cloud offers superb potential to sample the faint end of the luminosity function.

Our observations will consist of deep V, R and I imaging of an area equivalent to one CCD field. Using a large format CCD mounted at prime focus, we will be able to survey an area ~324 square arc minutes. The estimated distance to B5 is 350 pc (Langer *et al.* 1989). Thus, the effective survey volume is ~392 pc^3. We hope to achieve visual limiting magnitudes of ~24 with 5-10% photometric accuracy, so that our sample will be complete to the distance of the cloud for stars brighter than $M_V \sim 16$. Moreover at this limiting magnitude enough stars fainter than $M_V = 16$ will be detected to resolve definitely the question of the luminosity function's rise.

To illustrate this, we may estimate the total number of stars expected in our B5 sample. Once again employing the Galactic distribution model described in Appendix F, where we assume a local number density given by WJK and DLH, we find that a total of 35 or so stars with magnitudes satisfying $10 \leq M_V \leq 18$ should be visible in our survey. Thus, the addition of the B5 sample to our Taurus and Ophiuchus samples will *effectively double* the total sample size. In Figure 7.9 we illustrate the results of this simulation, where we have plotted the cumulative number of stars, N_V^{lim}, representing the Taurus and Ophiuchus samples (solid line) and the combined Taurus, Ophiuchus and B5 samples (dashed line). For the combined samples, we expect a total of *at least* 50 stars. With the addition of the B5 stars, the luminosity function determined in this study should be sufficiently refined that a firm conclusion can be made regarding the rising or flat nature of the faint end of the stellar luminosity function.

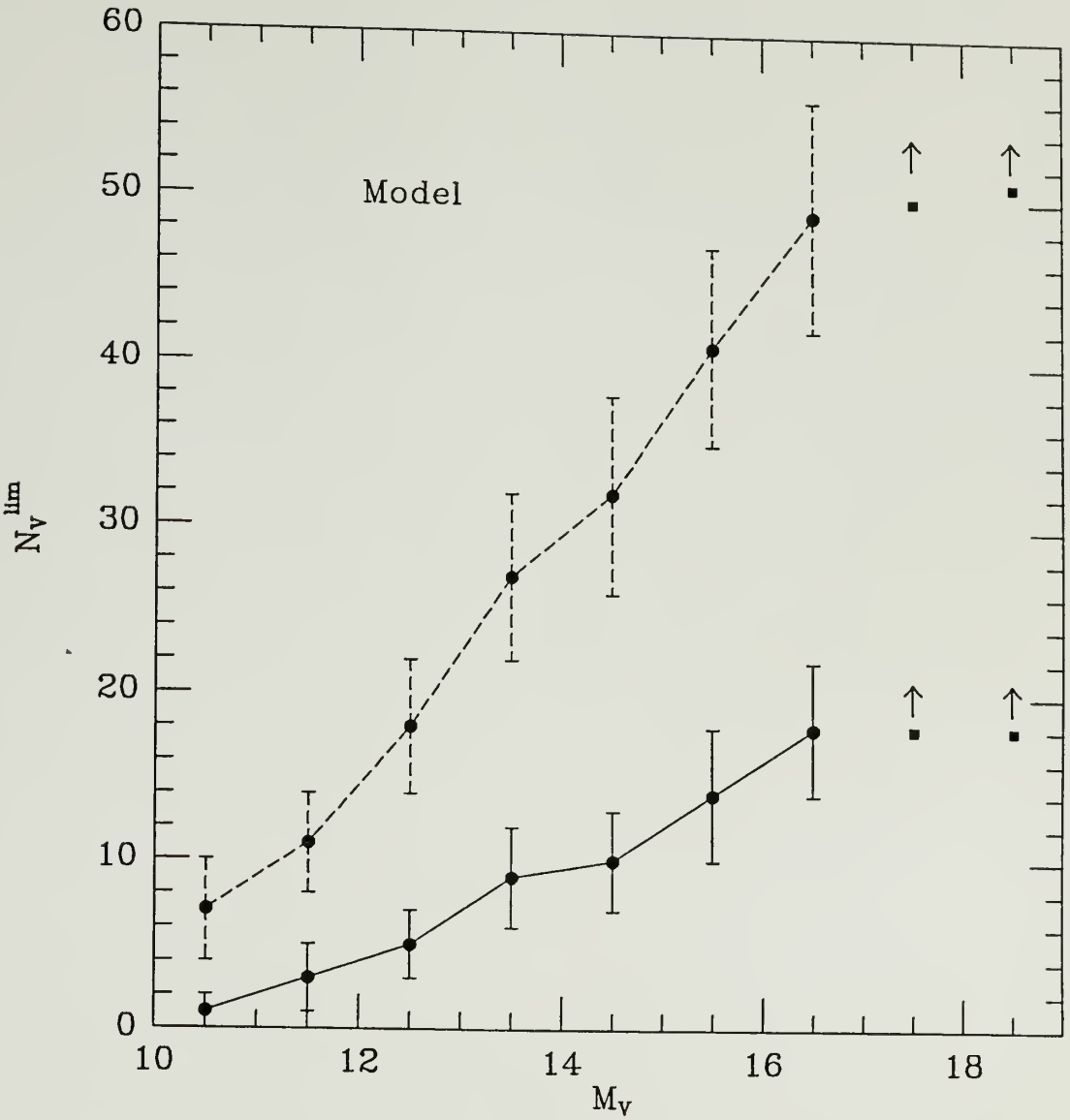

Figure 7.9 The expected cumulative number of stars representing the Taurus and Ophiuchus samples (solid line) and the combined Taurus, Ophiuchus and B5 samples (dashed line). The values are estimated using the Galactic distribution model described in Appendix F, where we assume a local number density given by WJK and DLH, and restrict the counts to those stars with magnitudes satisfying $10 \leq M_V \leq 18$. The error bars represent the $\sqrt{N}$ uncertainty in the cumulative counts.

7.4 Implications — the Initial Mass Function

In this study we have been primarily interested in constraining the faint end of the stellar luminosity function. This information must, however, be related to some sort of mass spectrum if we are to properly address the issues of the Galactic disk's local mass density and the frequency of the lowest mass stars and "brown dwarfs" (see Chapter 1). The transformation of the luminosity function into a stellar mass spectrum is a formidable task, given the uncertainties in the various conversion factors and the luminosity function itself. Notwithstanding these obstacles, we forge ahead.

Our aim is derive the mass frequency that describes the relative number of stars born within a given region of space, the so-called initial mass function. The standard approach (*cf.* Miller and Scalo 1979) is first to define the present day mass function, $\Psi(M)$, which represents the accumulated number density[4] of stars *born* with mass M. It should be emphasized that Ψ includes only those stars that have yet to evolve away from the main sequence. However, a sizeable fraction of the Galactic constituents are evolved objects, including giants and supergiants, white dwarfs and other degenerate remnants; at the other end of the age spectrum there are pre-main sequence stars. In order to include all of these objects, a second form of the mass spectrum is defined, namely, the aggregate initial mass function, $\xi(M)$, which represents the accumulated number of stars born of mass M. The two mass functions are related by the stellar birth rate, B(t). However, for our purposes the two mass functions are equivalent since the lowest mass stars have characteristic main-sequence lifetimes of order of the age of the Galactic disk (Scalo 1986). Henceforth, we shall refer to only the initial mass function (IMF). Moreover, since the lowest mass stars

[4] The mass function is generally expressed as a surface density, but may also be normalized as a volume density.

(*i.e.*, the M dwarfs) all have roughly the same Galactic disk scale height, we shall express the initial mass function as a volume density.

The IMF is related to the luminosity function according to (*e.g.*, Scalo 1986),

$$\xi(M) = \phi(M_V) \times \frac{dM_V}{dL} \times \frac{dL}{dM} \qquad (7.12)$$

where ξ is the number of stars per cubic parsec per unit mass, (dM_V / dL) is the bolometric correction and (dL / dM) is the mass-luminosity (M-L) function. The luminosity function, $\phi(M_V)$, is the fundamental observational quantity of Equation 7.12.

The mass-luminosity relation is very uncertain for low mass stars ($M < 1\ M_\odot$). In fact, for the lowest mass main sequence stars ($M \sim 0.08\ M_\odot$) and brown dwarf degenerates, we must rely exclusively on numerical models in order to estimate the M-L relation. These models (*cf.* D'Antona and Mazzitelli 1985; Dorman *et al.* 1989) are very sensitive to the boundary conditions and input parameters, including radiative opacities and the equation of state for the interior and atmosphere; these quantities are very uncertain for the lowest mass stars and degenerate objects.

In Figure 7.10, we show the M-L relation corresponding to the low mass stars. The figure is taken from Dorman *et al.* 1989 and is based on observational data (shown with error bars) and numerical simulations (two versions are shown). The M-L relation follows roughly a power law for stars with $M > 0.5\ M_\odot$, and a general "flattening" occurs between $0.2 < M < 0.5\ M_\odot$, followed by a steep decline for the lowest masses. Given this result and the fact that there are no data for masses smaller than $\sim 0.1\ M_\odot$, an alarming uncertainty for the lowest mass stars and degenerates is introduced into the IMF through the M-L relation. It is not difficult to recognize that the IMF may actually *rise* due to the steepness of the M-L relation, even for a luminosity function that is slightly decreasing at

the faint end of the spectrum; moreover, the IMF will almost surely rise toward the low mass end given a luminosity function that rises or at least remains flat for faint luminosities. For further discussion of the M-L relation, the reader is referred to the review by Reid 1987.

As a matter of convenience, we combine the bolometric correction with the M-L relation and rewrite the IMF similar to the convention adopted by Rana (1987), namely,

$$\xi(\log M) = \phi(M_V) \times \left| \frac{dM_V}{d\log M} \right| , \qquad (7.13)$$

where ξ is the number of stars per cubic parsec per unit logarithmic mass, and the (dM_V / d log M) relation is shown in Figure 7.11 (taken from Rana 1987). Using the M-L relation of Rana (1987) and the luminosity function, ϕ_V^*, determined from this study (see Table 7.3), we have computed the IMF for low mass stars, and also estimated the local disk mass density for this range in mass. The results are shown in Table 7.5, where for comparison we have also tabulated the values determined by Rana (1987). The values for ϕ^* at M_V = 17, 18 in the Table have been corrected for incompleteness using the V_{max} method; the values appearing in parenthesis correspond to lower limits (see Table 7.3 for further information). No attempt was made to estimate the uncertainty for ξ, since the uncertainties associated with the M-L relation are both large and for the most part unknown. The mass function results are plotted in Figure 7.12, where the results of Rana (1987) and Scalo (1986) are also shown.

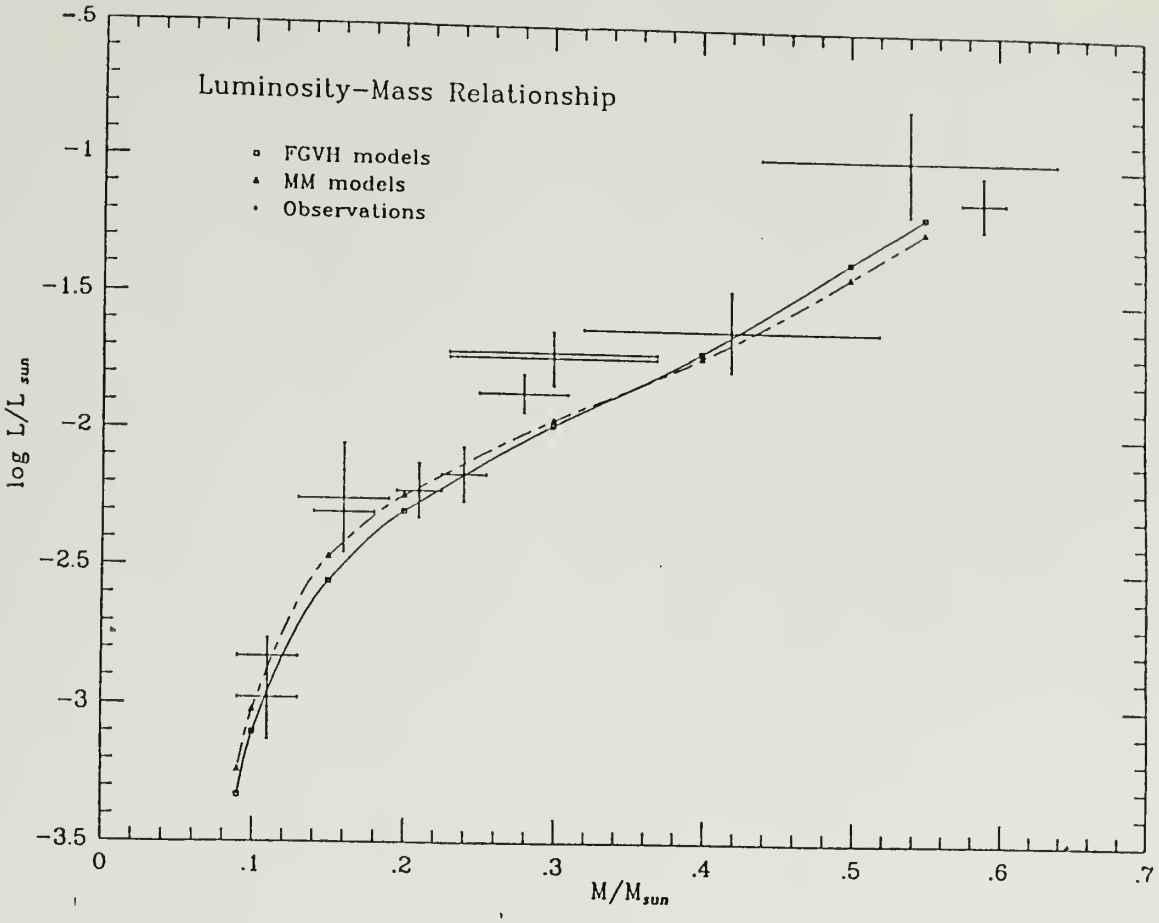

Figure 7.10 The mass-luminosity relation for low mass stars. Values determined from observations are plotted with error bars. Results from numerical models are represented by the solid and dashed lines. The figure is taken from Dorman *et al.* (1989), fig. 2.

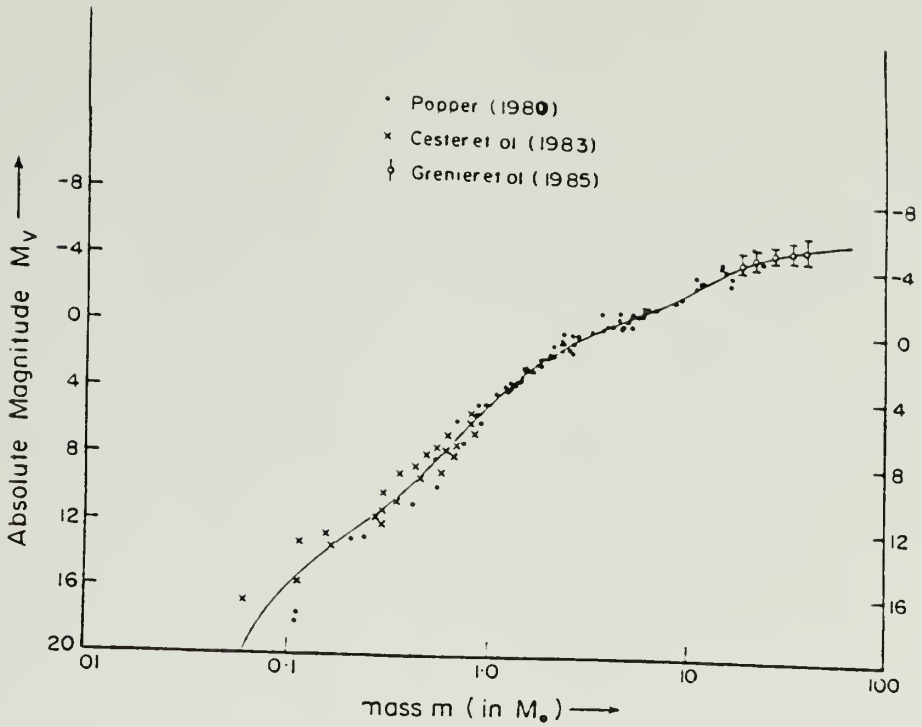

Fig. 2. Empirical calibration of the $m - M_V$ relation for the main sequence stars. Reliable estimates of both mass and luminosity are available only for the nearby binaries. The adopted relation is shown by the solid curve. It significantly deviates from both Miller and Scalo (1979) and Scalo (1986), particularly for points below $M_V = 4$

Figure 7.11 The stellar mass-absolute magnitude relation. Observational data are plotted with point symbols. The relation adopted by Rana (1987) is shown with a solid line. The figure is taken from Rana (1987), fig. 2.

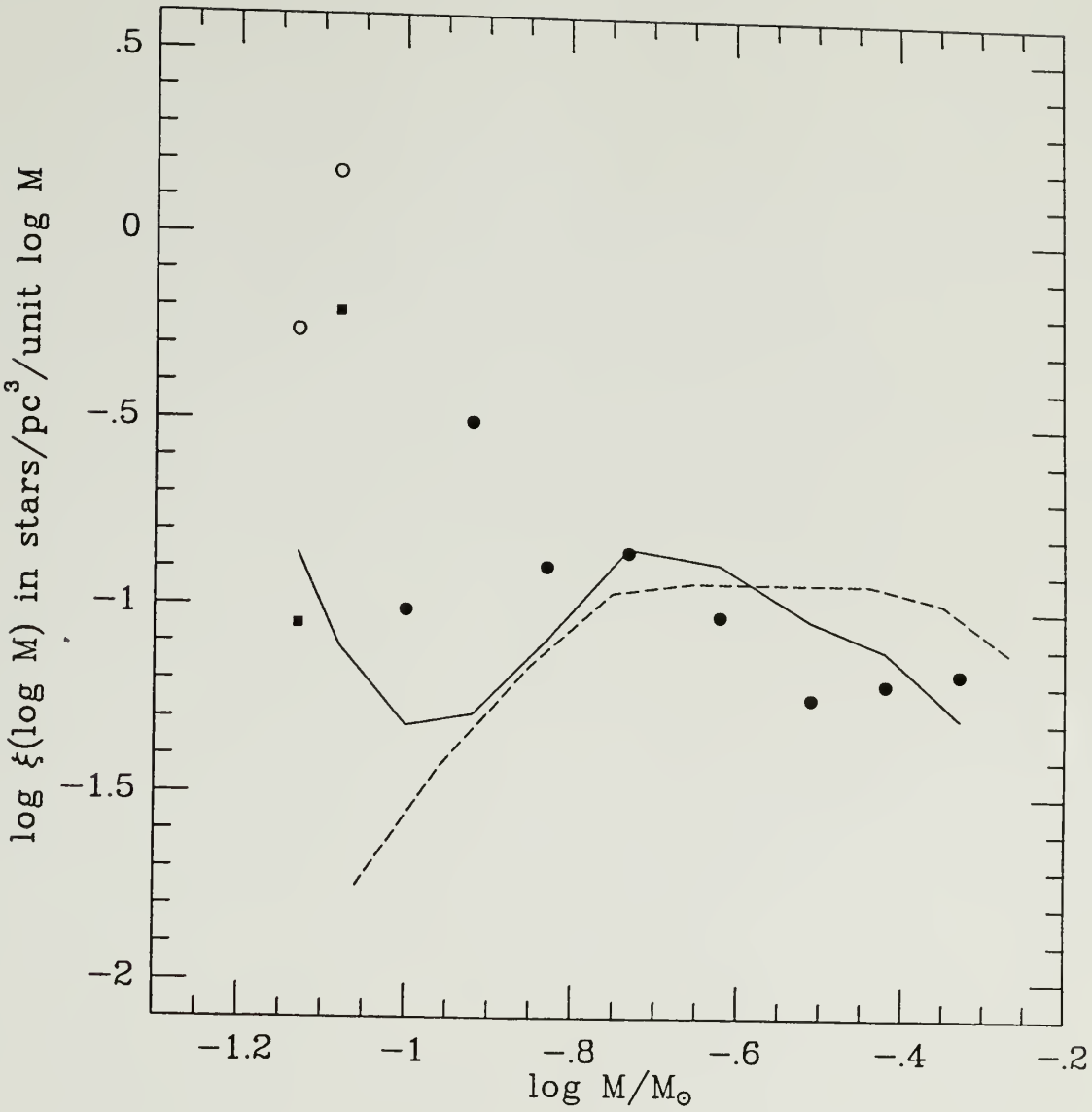

Figure 7.12 The initial mass function for low mass stars. The points denote results from this study: the open circles denote values determined from the V_{max} corrected luminosity function, and the filled squares denote values determined from the luminosity function corrected for incompleteness. The IMF determined by Rana (1987) is shown with a solid line, and the IMF determined by Scalo (1986) is shown with a dashed line.

Table 7.5

The Initial Mass Function

M_V	log $\phi^*(M_V)$	$\lvert dM_V / d\log M \rvert$	log $M/M_\odot$	log ξ(log M)		mass
				this study	Rana (1987)	log $M_\odot$ pc^{-3}
9	-2.29	13.3	-0.33	-1.17	-1.29	-2.62
10	-2.29	12.3	-0.42	-1.24	-1.11	-2.71
11	-2.29	11.3	-0.51	-1.24	-1.03	-2.80
12	-2.00	9.5	-0.62	-1.02	-0.88	-2.62
13	-1.82	9.4	-0.73	-0.85	-0.84	-2.55
14	-2.00	13.0	-0.83	-0.89	-1.09	-2.83
15	-1.70	16.2	-0.92	-0.89	-1.09	-2.62
16	-2.29	18.9	-1.00	-1.01	-1.32	-3.29
17	-1.22 (-1.60)	24.3	-1.08	0.17 (-0.21)	-1.11	-2.30 (-2.68)
18	-1.50 (-2.29)	17.2?	-1.13	-0.26 (-1.05)	-0.86?	-2.63 (-3.42)

Table notes: the values for ϕ^* at M_V = 17, 18 have been corrected for incompleteness using the V_{max} method; the values appearing in parenthesis correspond to lower limits (see Table 7.3 for further information); no attempt was made to estimate the uncertainty for ξ, since the uncertainties associated with the M-L relation are both large and for the most part unknown.

Both the systematic uncertainties associated with the M-L relation and the bolometric correction, as well as the statistical errors which stem from the small size of our stellar sample render the IMF plotted in Figure 7.12 highly uncertain. Nevertheless, several of its basic features are apparent. First, in the mass range $0.18 < M/M_\odot < 0.5$, the IMF derived here appears to be consistent with the results of both Rana and Scalo (the solid and dotted lines, respectively, in Figure 7.12). The peak in both these estimates for the IMF, which corresponds to the luminosity function peak at $M_V \sim 12 - 13$, and which Scalo refers to as the turnover point, has no clear counterpart in our result; however, our results are not statistically inconsistent with the presence of such a peak. The monotonic decline in Scalo's IMF beyond the turnover point originates in his adoption of both a flatter mass-

luminosity relation than used here and a declining luminosity function beyond the peak at $M_V \sim 12 - 13$. Although our statistical errors are clearly large, our provisional finding that the luminosity function again rises beyond this peak implies that *the IMF probably also rises beyond the turnover point.* This trend is clear from the data points associated with our volume-corrected luminosity function (the open circles in Figure 7.12); even if our most conservative estimate for the faint end of the luminosity function is used — in which no corrections whatsoever are made for incompleteness (the closed squares in Figure 7.12) — we are forced to conclude that *the IMF is at least flat down to the edge of the hydrogen-burning main sequence.*

A rising IMF suggests the existence of an alternative formation mode for very low mass stars. This may be consistent with Larson's (1986) 'bimodal' star formation mechanism, in which a second class of low mass stars forms, possibly in a burst very early in the existence of the Galaxy. Rana (1987) has even suggested that there may be hierarchical star formation, or multimodal bursts, each of which triggers or induces further episodes of star formation. A rising IMF that extends beyond the limit of the minimum mass required to sustain hydrogen-burning, ~0.08 $M_\odot$, would also suggest that there may be profuse numbers of degenerate "brown dwarf" objects in the Galactic disk. Given the absence of any confirmed brown dwarf candidates, however, it is difficult to avoid the conclusion that even if the IMF continues to rise for masses <0.08 $M_\odot$, it must soon thereafter steeply decline.

We now use these results to estimate the local mass density. From Table 7.5, we find that the mass density due to low mass stars is ~0.02 $M_\odot$ pc^{-3} for $0.08 < M/M_\odot < 0.47$. Intermediate and high mass stars with, $0.5 < M/M_\odot < 100$, add a further 0.014 $M_\odot$ pc^{-3} (Scalo 1986), evolved giants contribute ~0.001 $M_\odot$ pc^{-3}, evolved degenerates 0.01 $M_\odot$ pc^{-3} (*cf.* Reid 1987). Gas and dust from H I and molecular clouds add another ~0.04 - 0.05 $M_\odot$

pc^{-3} (Hill *et al.* 1979), though this value is very uncertain and this uncertainty is a major source of ambiguity for the total local mass density. The total mass density summed from these Galactic constituents is ~0.1 $M_\odot$ pc^{-3}. This value is about a factor of two less than that inferred from dynamical arguments by some workers (Oort 1960; Bahcall 1984). This mass deficit in the Galactic disk of 0.06 - 0.09 $M_\odot$ pc^{-3} is one of the classic pieces of evidence for a (baryonic) dark matter problem. However, this conclusion has been challenged by others (Gilmore, Wyse, and Kuijken 1989) who contend that among other things, the mass inferred from dynamical studies has in the past been overestimated.

Let us now estimate the contribution from brown dwarfs (assuming that they exist), by considering two cases: (1) the IMF remains flat for masses below 0.08 $M_\odot$, and (2) the IMF continues rising through the brown dwarf regime. From Figure 7.12, it is clear that a flat IMF low mass end may have a rather large range in value. For simplicity, we adopt a constant value of ~0.32 stars per pc^{-3} per log M, and extrapolate it over the range of brown dwarf mass. According to various fragmentation models the minimum mass from which degenerate objects may form ranges from 0.007 $M_\odot$ to as high as 0.1 $M_\odot$, with 0.01 $M_\odot$ as the minimum mass typically adopted by most studies (see Liebert and Probst 1987 for further discussion). Integrating the mass function from $0.01 < M/M_\odot < 0.08$, we find that the brown dwarfs would account for ~0.02 $M_\odot$ pc^{-3}, which still falls short of the estimated missing mass.

In the second case we consider a rising mass function. Unfortunately, it is not clear what the index of the power law characterizing the mass function should be. If we adopt the Salpeter power law, $M^{-2.35}$, or even the more modest slope, $M^{-0.8}$, suggested by Henry and McCarthy (1990) in their infrared survey of nearby M dwarf stars, then the total mass density of the brown dwarfs easily accounts for the Galactic mass deficit. For example, Liebert and Probst (1987) integrate the intermediate power law given by $M^{-1.01}$

over the mass range extending to a minimum of 0.01 $M_{\odot}$, and find a brown dwarf mass density of ~0.1 $M_{\odot}$ pc^{-3}.

Whether one chooses a flat IMF or a rising IMF (with a slope that is clearly ill-determined by this work), it should be kept in mind that any extrapolation involving brown dwarfs will possess staggering uncertainties, given our ignorance of the M-L relation and luminosity function corresponding to the brown dwarfs. Furthermore, there remains doubt as to the very existence of these objects. To date, there is not one firm identification of a brown dwarf or extra-solar Jupiter object. It is especially discouraging that the results from studies specifically designed to find brown dwarfs in binary and multiple stellar systems have been negative (*cf.* Skrutskie 1987; Skrutskie, Forrest, and Shure 1989). What we can say definitively is that the lowest mass stars are the most common stars in the Galaxy, and that given the constraints established by our luminosity function, the *most numerous* stars in the Solar neighborhood appear to have masses very near the hydrogen-burning limit.

CHAPTER 8

SUMMARY

We have implemented a new method by which to study the faint end of the field star luminosity function. The method relies on deep, multicolor photometry of fields projected against highly obscured, nearby molecular clouds. The clouds act as nearly opaque screens, enabling us to delimit a well-defined survey sample volume free of the problems of distinguishing nearby, intrinsically faint dwarf stars from more distant red giants. We have demonstrated that with this technique it is possible to probe the faint end of the luminosity function down to the hydrogen-burning limit of the main sequence out to distances much further than have been previously attempted. The main points and conclusions of this work may be summarized as follows:

- We obtained deep photographic and CCD photometry at optical (V, R, I) bandpasses towards the most obscured portions of the Taurus and Ophiuchus molecular clouds. The fields comprise a total area of ~0.63 square degrees, and the total volume delimited by the cloud distances is ~198 pc^3. Within this volume, the survey is complete for all stars brighter than M_V = 16 - 17 mag; at R and I, the survey is complete down to the lowest mass stars capable of sustaining core hydrogen burning.

- Color-color criteria were applied to our optical data in order to distinguish between background, highly reddened stars and stars located in front of the clouds. To help with this task, we developed a model of the Galactic stellar distribution based on the work of Bahcall and Soneira. The method of photometric parallax was used to deduce the absolute magnitude and spectral type of those stars found to lie in front of the clouds.

- To help further resolve foreground/background ambiguities we supplemented the photometry and color-color results with proper motion measurements of the candidate foreground sample. The proper motions were obtained from our photographic and CCD data, and from the circa 1950 Palomar Sky Survey.

- As a test of our ability to distinguish foreground dwarfs from heavily reddened background stars, we obtained redband (6000 - 9000 Å) spectra of three Taurus foreground candidate stars. In each case the spectral type was deduced from various temperature-sensitive TiO and VO molecular bands, while the luminosity class was determined from gravity-sensitive atomic and molecular features including the Na I line at 8200 Å. We determined that two of the stars are undoubtedly late-type foreground M dwarfs, with spectral type from M5 to M6 V, a result consistent with the photometric parallax and proper motion criteria. The third, however, appears to be a reddened, high velocity background star, possibly belonging to the spheroid population. Although such objects are statistically expected to be quite rare in our sample, this result illustrates that the photometric and proper motion analysis techniques of this study are not completely immune to contamination from background stars. The least biased

conclusion that we can draw regarding the integrity of our foreground sample is that there is 33% contamination from reddened background stars and/or associated cloud members. The contamination is most likely confined to the faintest magnitudes, with, $M_V > 14$.

- We estimated the field star luminosity function for the composite Taurus and Ophiuchus foreground sample. We find that the faint end of the luminosity function resembles the *local* number density determined by Wielen *et al.* (1983) and Dahn *et al.* (1986) up to $M_V \sim 16$. At still fainter magnitudes, we find the shape of the luminosity function to be consistent with that exhibited by the K-band luminosity function determined by Henry and McCarthy (1990) for very low mass stars; furthermore, we find at least 15% more stars than do photometric parallax studies of the polar regions. This difference widens dramatically if even the simplest correction for incompleteness is applied to our data. While statistical noise due to our small sample, systematic effects, the Galactic density distribution, and stellar multiplicity may all contribute to this disparity, it nonetheless seems real and substantial. Furthermore, this result is consistent with the shape of the K-band luminosity function determined by Henry and McCarthy (1990) for the lowest mass nearby stars. We therefore tentatively conclude that the luminosity function rises beyond $M_V \sim 16$; even if we discard our attempts to correct for incompleteness in the faintest magnitude bins, there appears to be little doubt that the luminosity function at least remains flat for the lowest mass stars.

- We outlined future work to be conducted in December 1991 which will extend our deep optical survey toward the Barnard 5 molecular cloud. We estimate that with the addition of the B5 data we will *effectively double* the total sample size of this study. With the addition of the B5 stars, the faint end of the luminosity function determined in this study should be sufficiently refined that a firm conclusion can be made regarding its rising or flat nature.

- Although our statistical errors are large, our provisional finding that the luminosity function rises again beyond its well-known peak at $M_V \sim 12 - 13$, also implies that the IMF probably rises beyond the turnover point associated with this peak. Even if our most conservative estimate for the faint end of the luminosity function is used — in which no corrections whatsoever are made for incompleteness — we conclude that the IMF is at least flat down to the edge of the hydrogen-burning main sequence.

APPENDIX A

CCD IMAGES

This appendix consists of two sets of photographs which show the CCD images of the Taurus and Ophiuchus fields. Figures A.1a and A.1b correspond to a mosaic of the Taurus CCD images at V and I bands, respectively. The mosaic fields are roughly of angular size 57′ × 52′, centered at $\alpha[1950] = 4^h\ 38^m$, $\delta[1950] = 25°\ 46'$. Figures A.2a, A.2b and A.2c correspond to the Ophiuchus CCD images at V, R and I bands, respectively. These fields are roughly of size 26′ × 24′, centered at $\alpha[1950] = 16°\ 29^m\ 45^s$, $\delta[1950] = -24°\ 23'$.

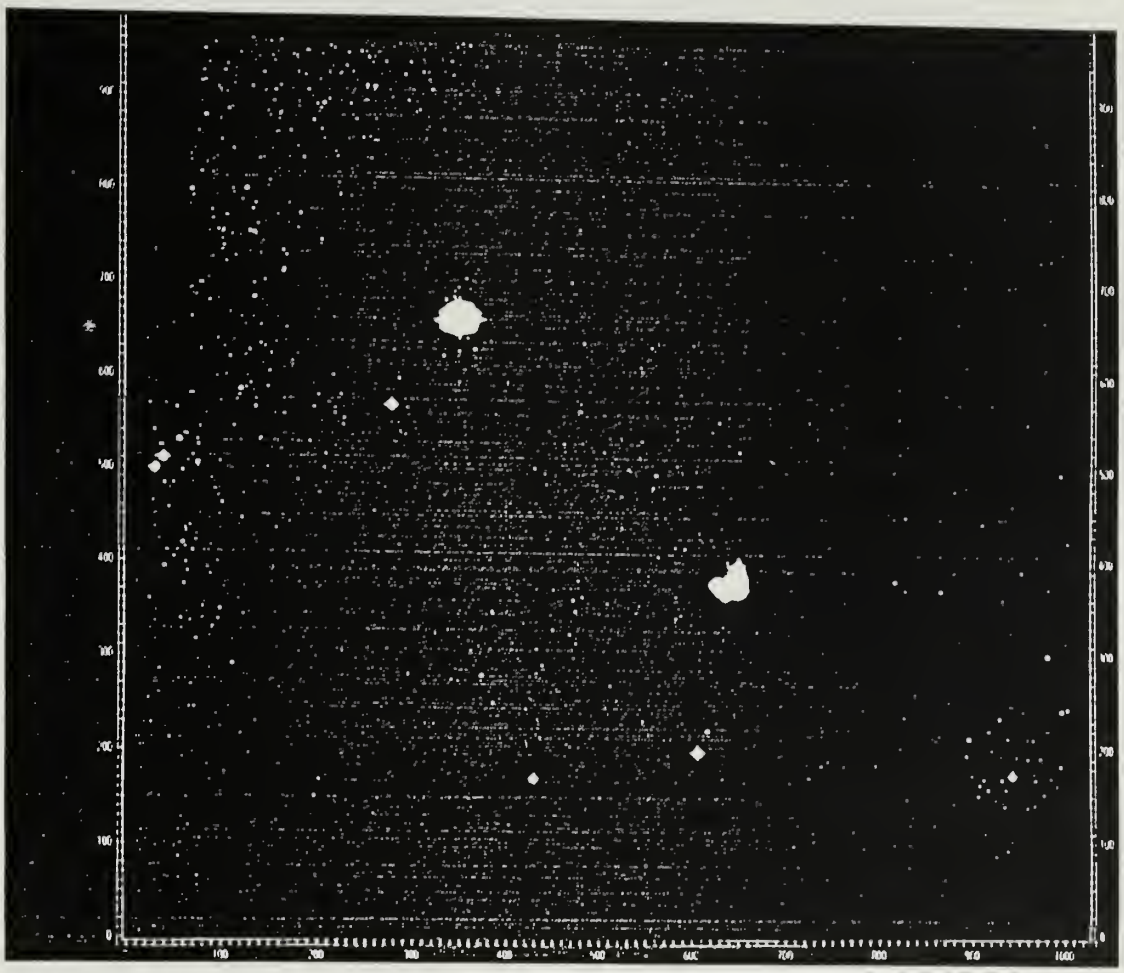

Figure A.1 V and I band mosaics of the three Taurus CCD fields. (a) The V band mosaic is of angular size ~ 57′ × 52′, centered at $\alpha[1950] = 4^h\ 38^m$, $\delta[1950] = 25°\ 46'$.

continued next page

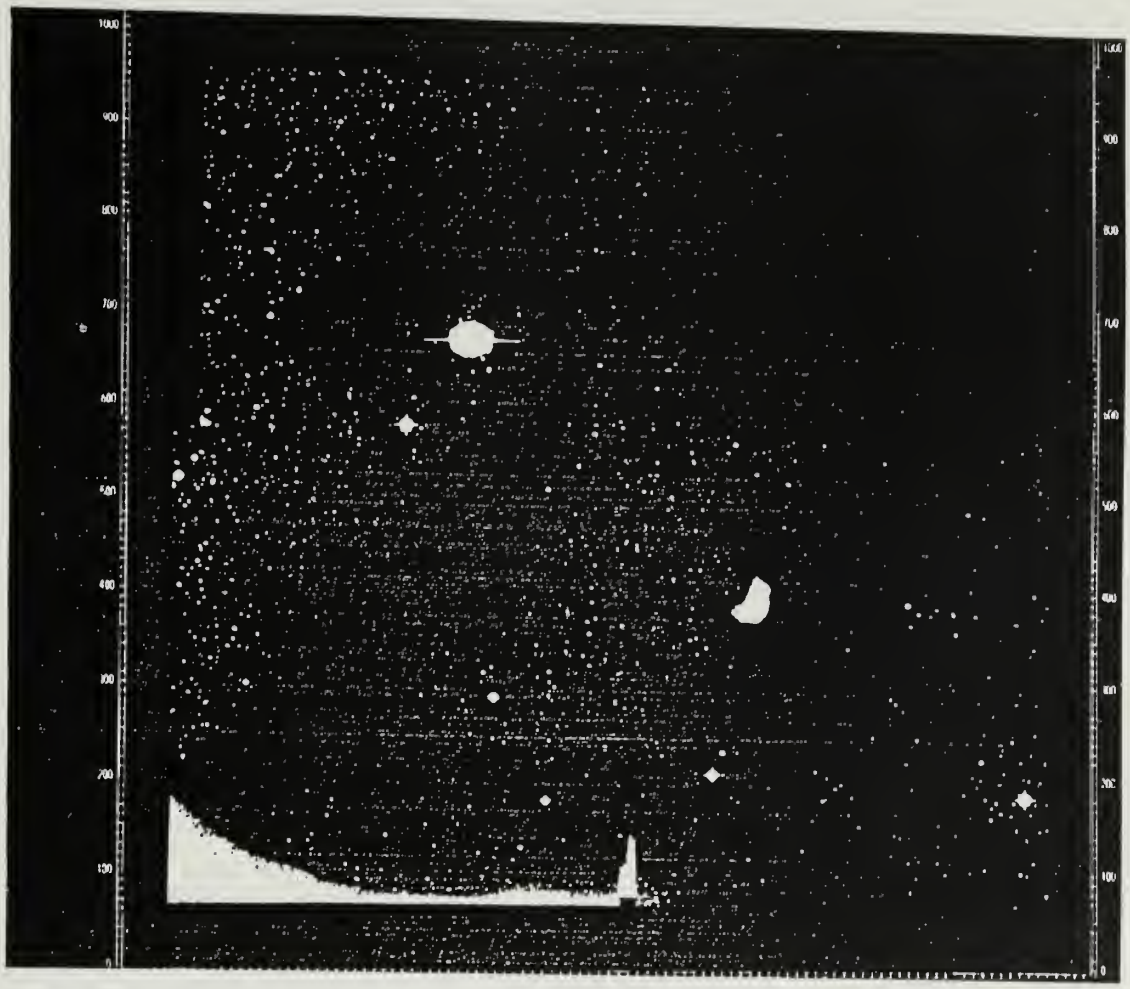

Figure A.1 continued (b) I band mosaic of the three Taurus CCD fields. The mosaic is of angular size ~ 57′ × 52′, centered at $\alpha[1950] = 4^h\ 38^m$, $\delta[1950] = 25°\ 46'$.

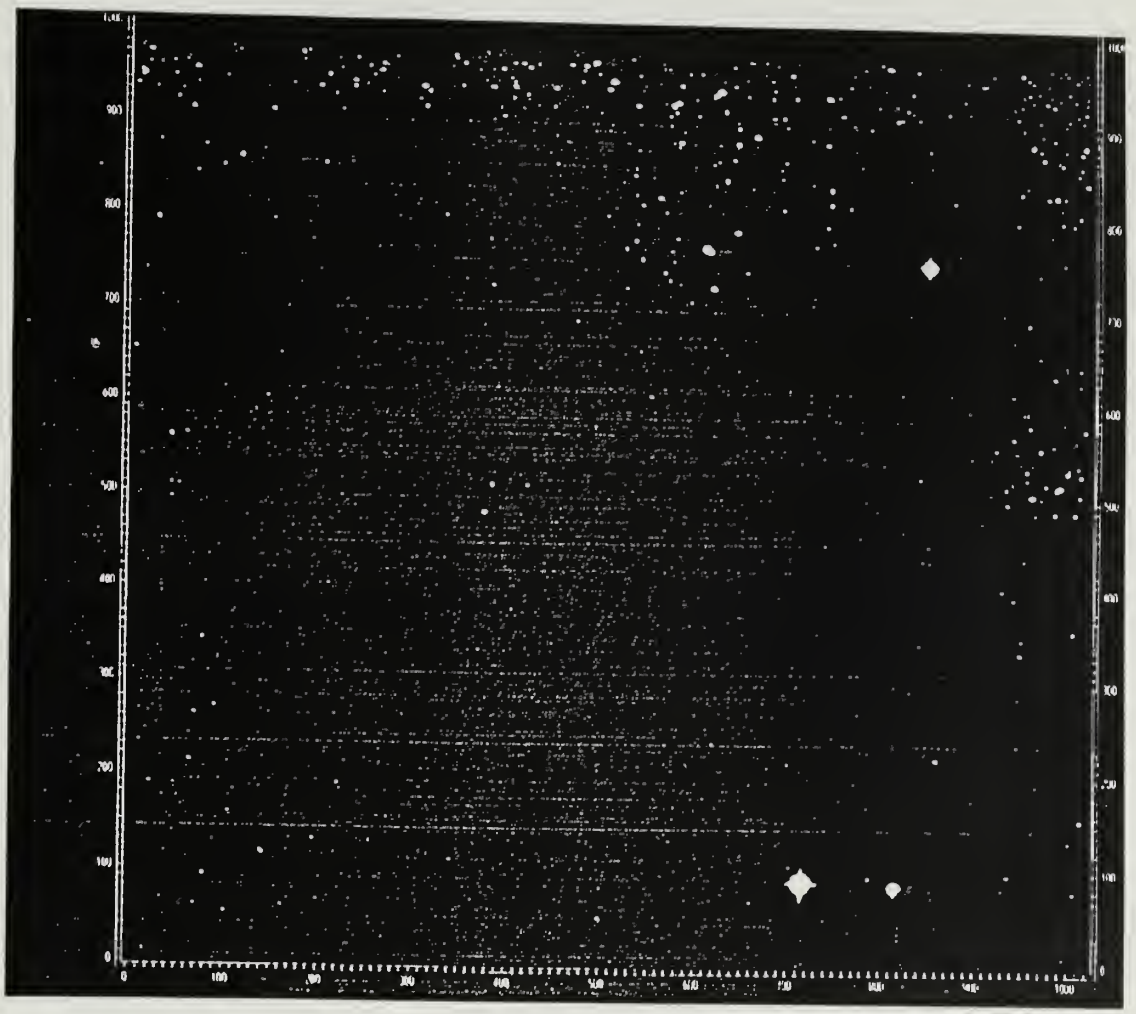

Figure A.2 Ophiuchus CCD field at V, R and I bands. (a) The V-band field is of angular size 26′ × 24′, centered at $\alpha[1950] = 16° 29^m 45^s$, $\delta[1950] = -24° 23'$.

continued next page

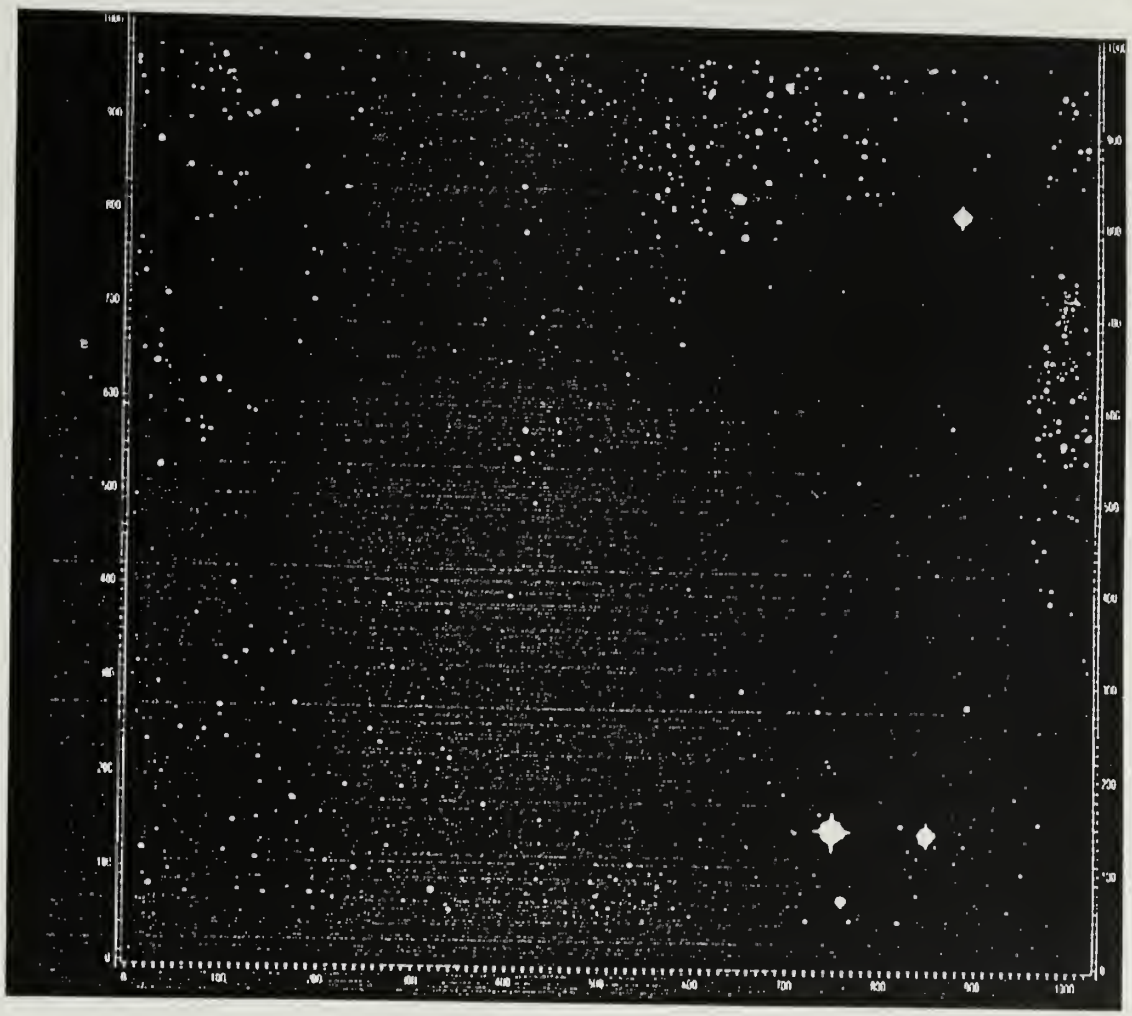

Figure A.2 continued (b) Ophiuchus CCD field at R band. The field is of angular size 26′ × 24′, centered at $\alpha[1950] = 16^{\circ}\ 29^{m}\ 45^{s}$, $\delta[1950] = -24^{\circ}\ 23'$.

continued next page

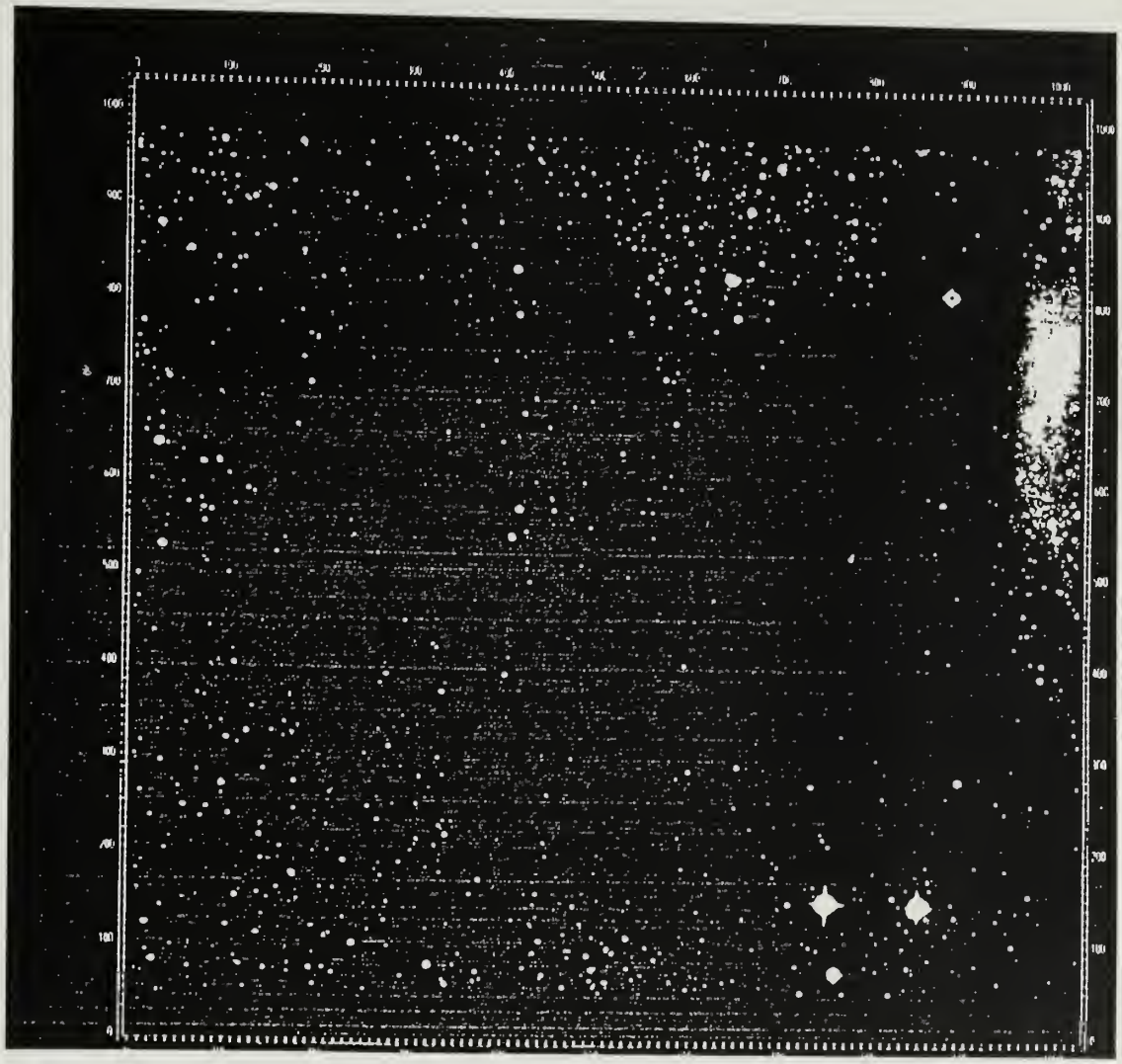

Figure A.2 continued (c) Ophiuchus CCD field at I band. The field is of angular size 26′ × 24′, centered at $\alpha[1950] = 16^{\circ}\ 29^{m}\ 45^{s}$, $\delta[1950] = -24^{\circ}\ 23'$.

APPENDIX B

FINDING CHARTS FOR THE CANDIDATE FOREGROUND STARS

This appendix consists of two sets of figures which show the local fit areas for each Taurus and Ophiuchus photometric foreground candidate in the 4m, CCD, and POSS data sets. Figures B.1(a-u) correspond to the Ophiuchus candidate stars and Figures B.2(a-p) correspond to the Taurus candidate stars.

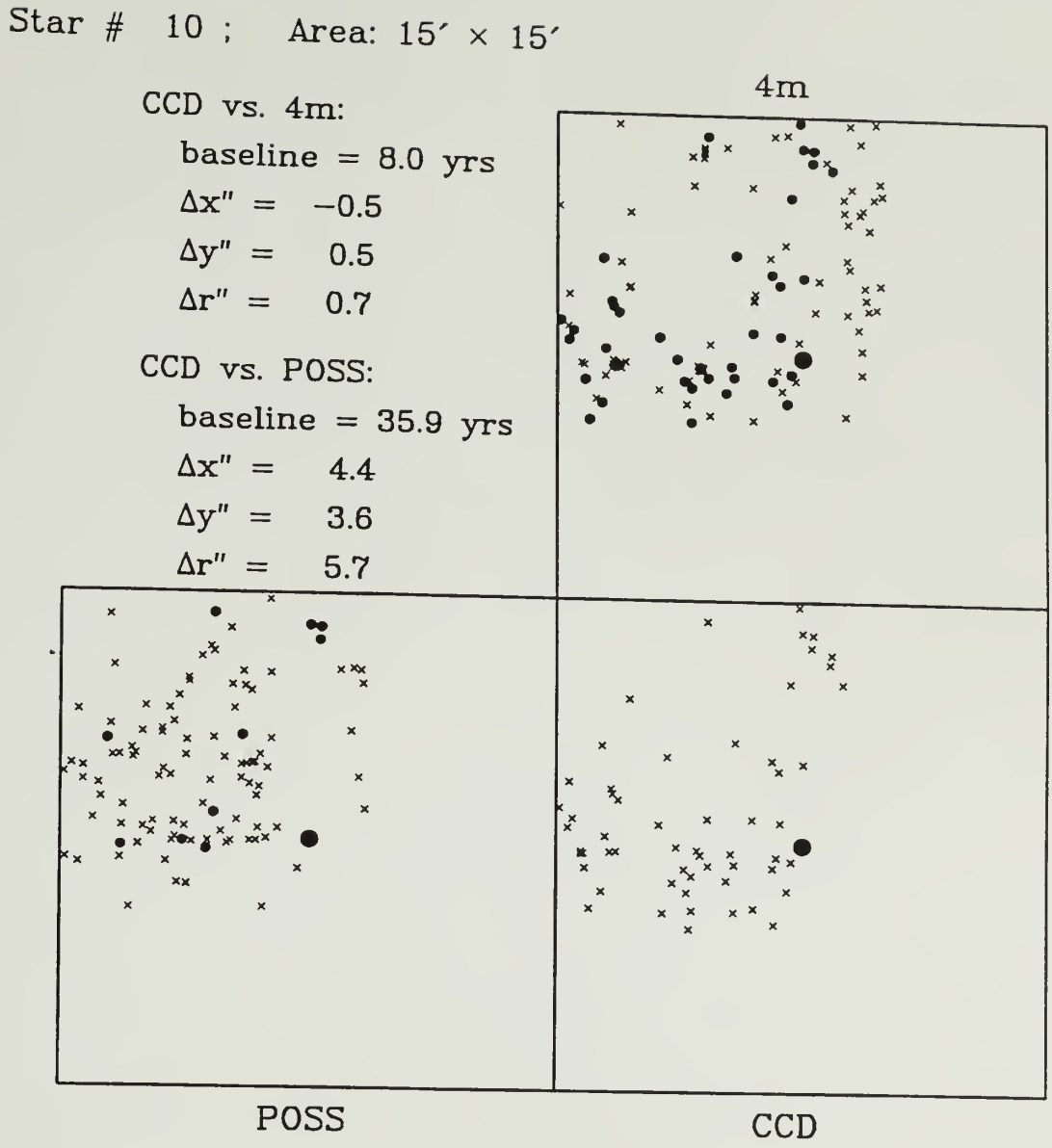

Figure B.1 Ophiuchus photometric foreground candidates. (a) The local areas for each photometric foreground candidate in the photographic 4m, CCD, and POSS E-plate data sets. The photometric candidates are the large filled circle in each box. The reference stars used in the polynomial mappings are represented by filled circles; the other stars are represented by crosses. The angular shifts obtained for the two baselines are also shown. The size of the local areas is indicated in units of arc minutes.

continued next page

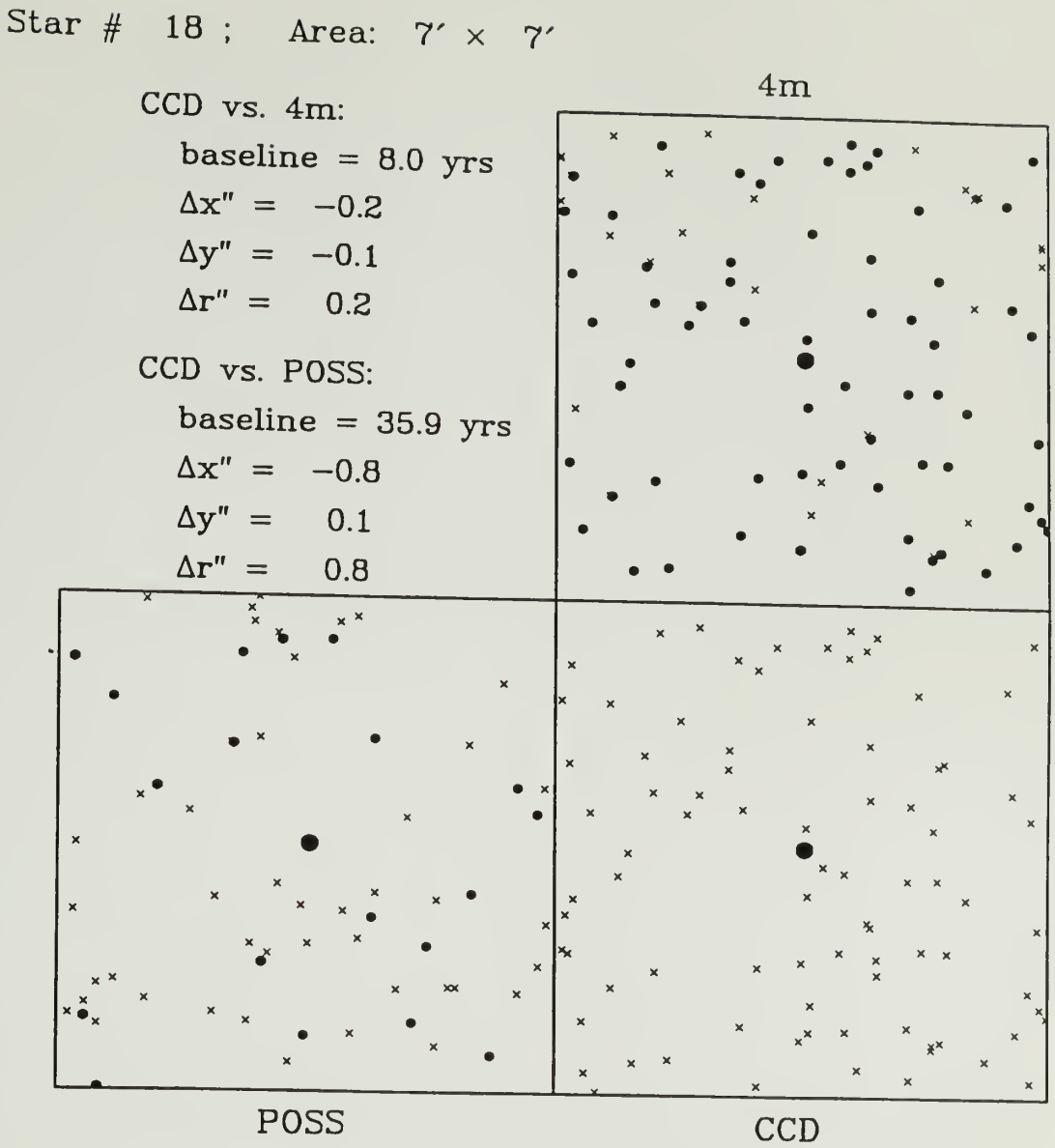

Figure B.1 continued (b)

continued next page

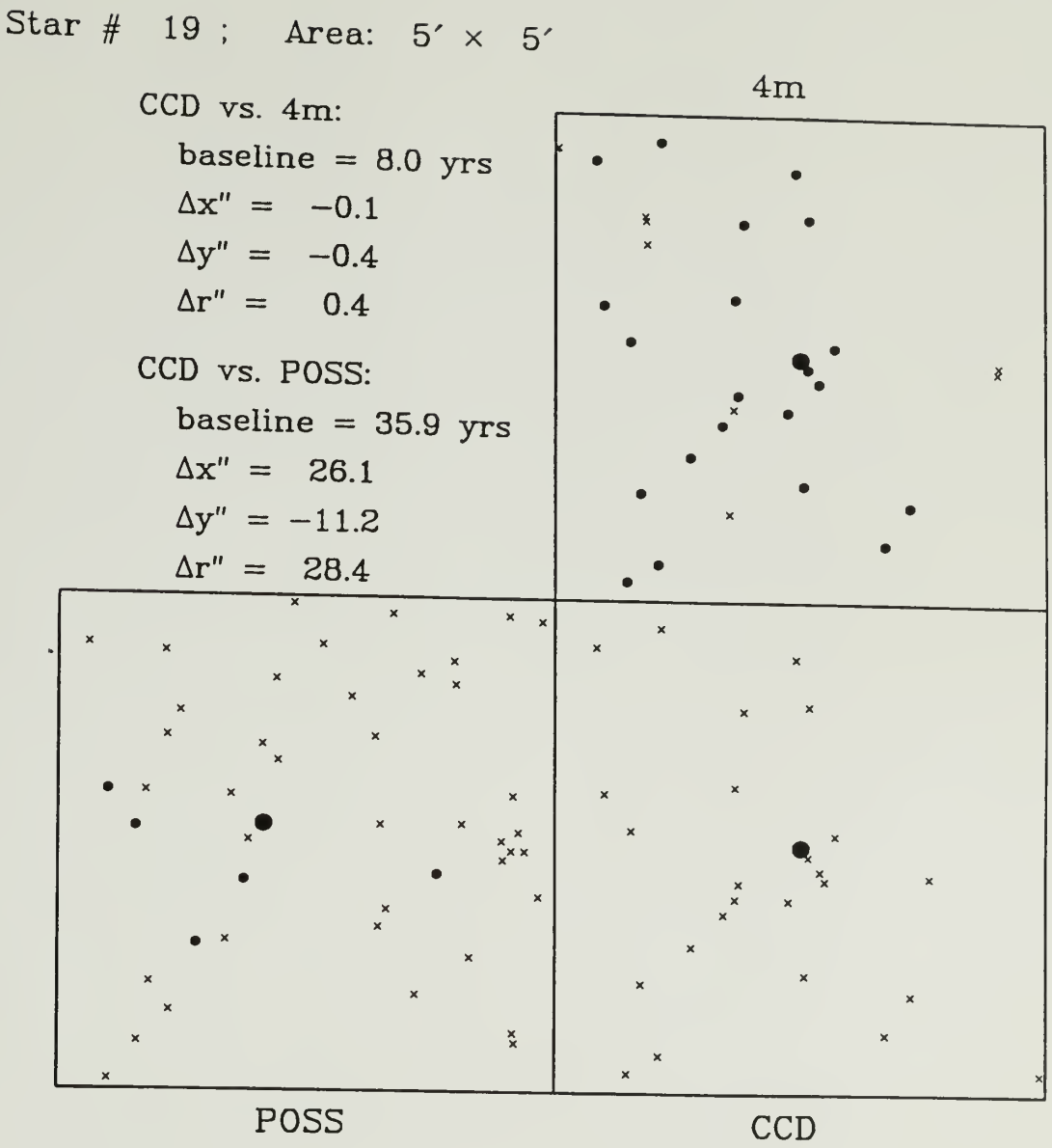

Figure B.1 continued (c)

continued next page

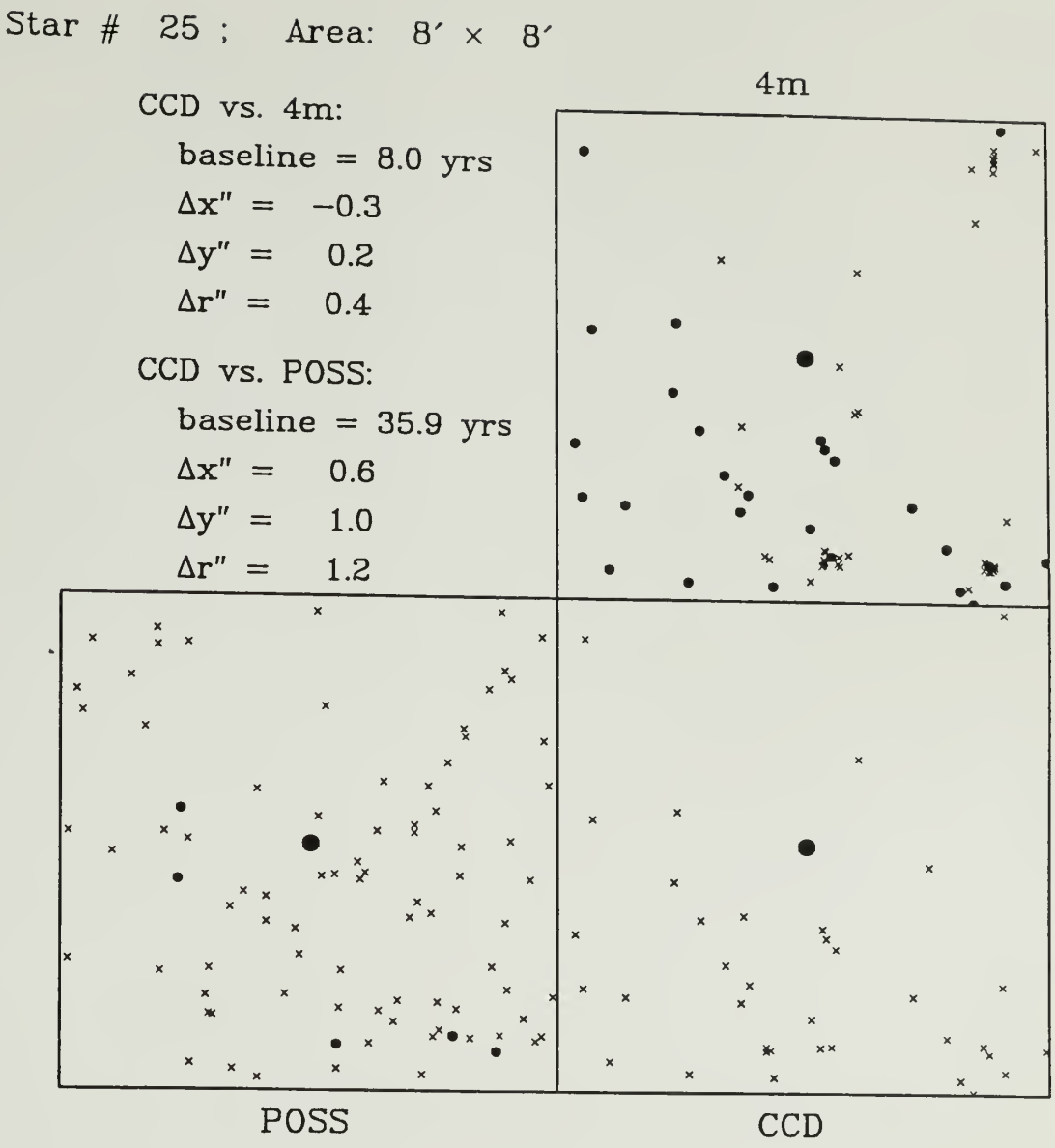

Figure B.1 continued (d)

continued next page

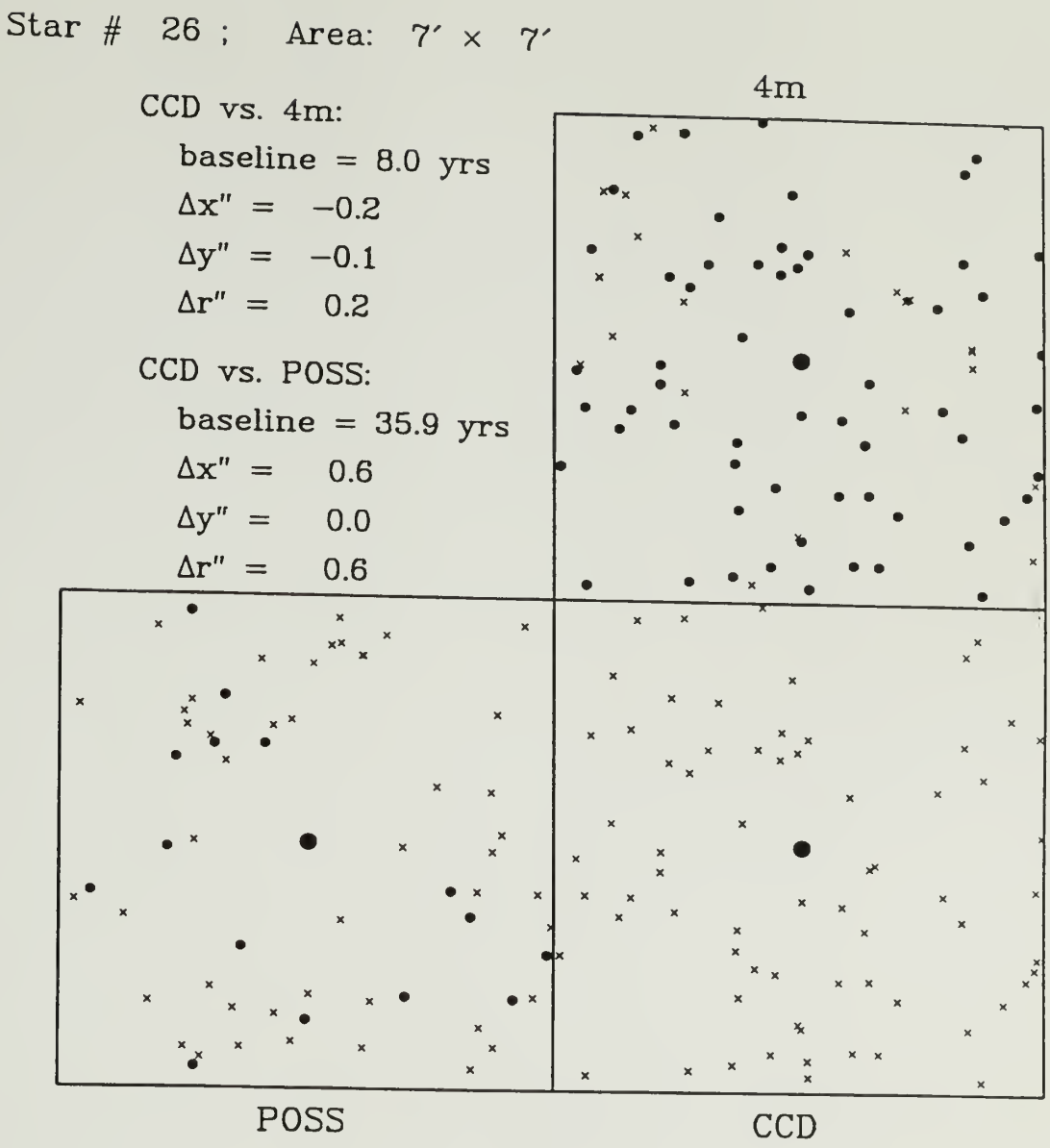

Figure B.1 continued (e)

continued next page

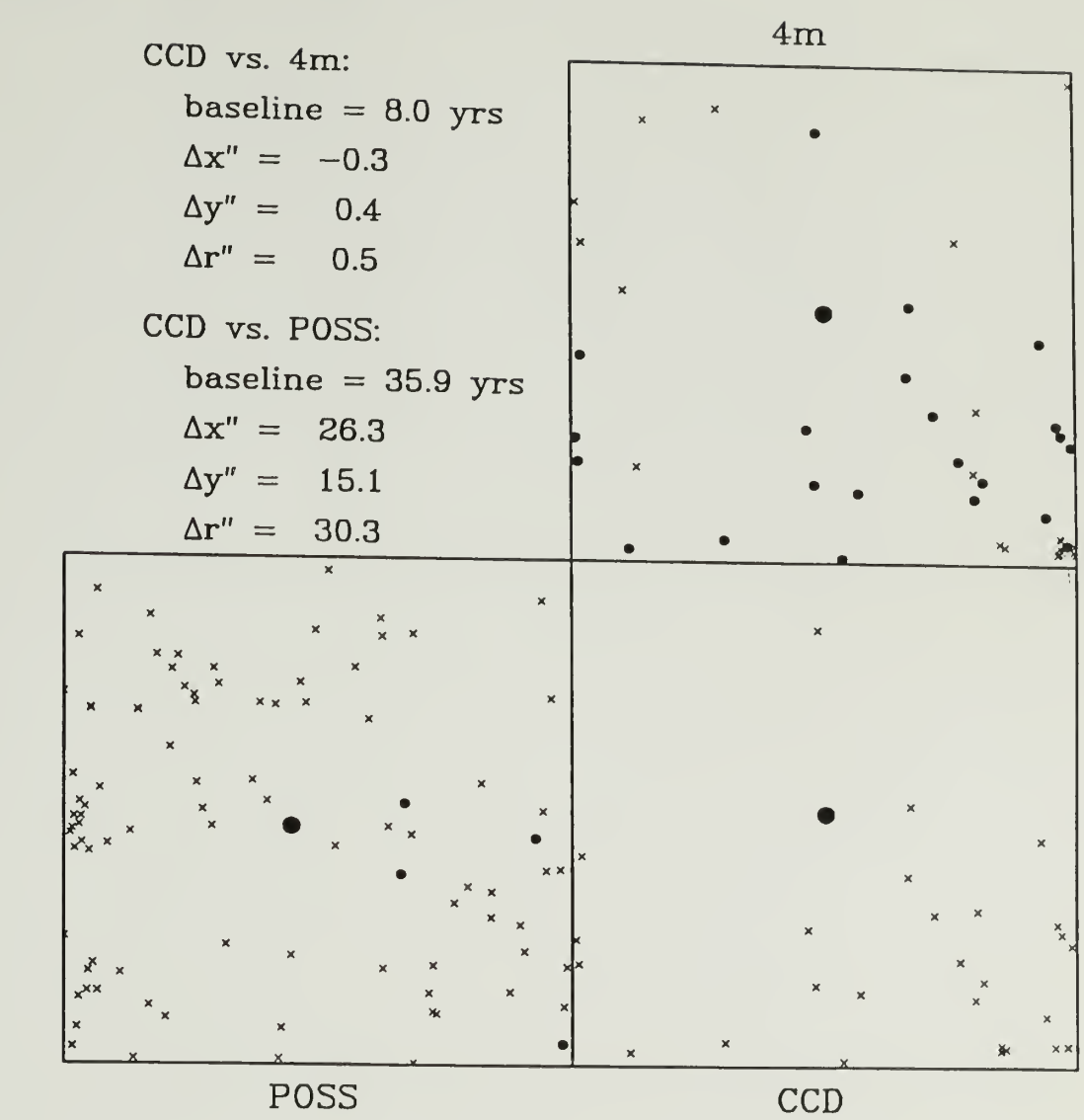

Figure B.1 continued (f)

continued next page

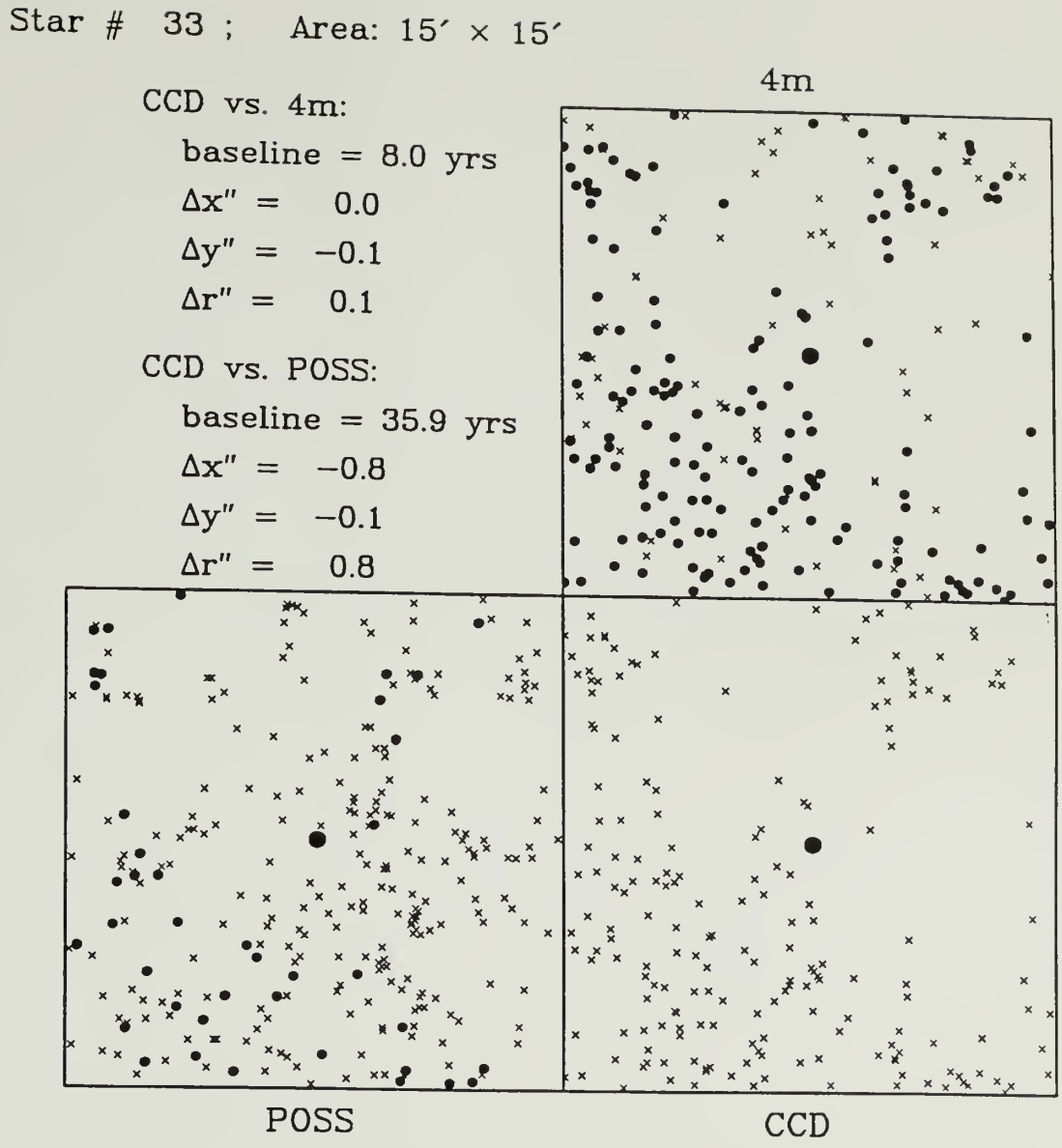

Figure B.1 continued (g)

continued next page

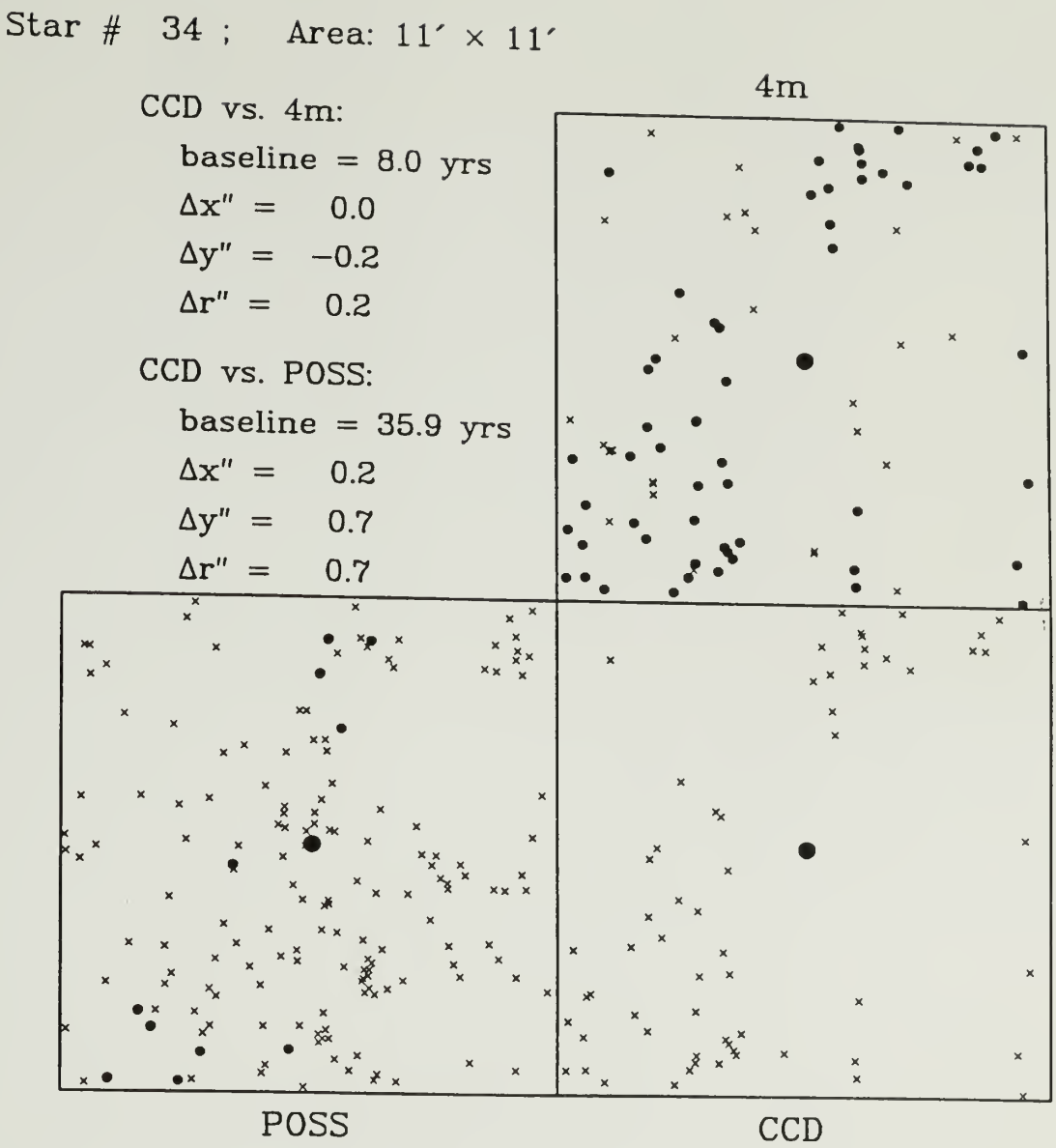

Figure B.1 continued (h)

continued next page

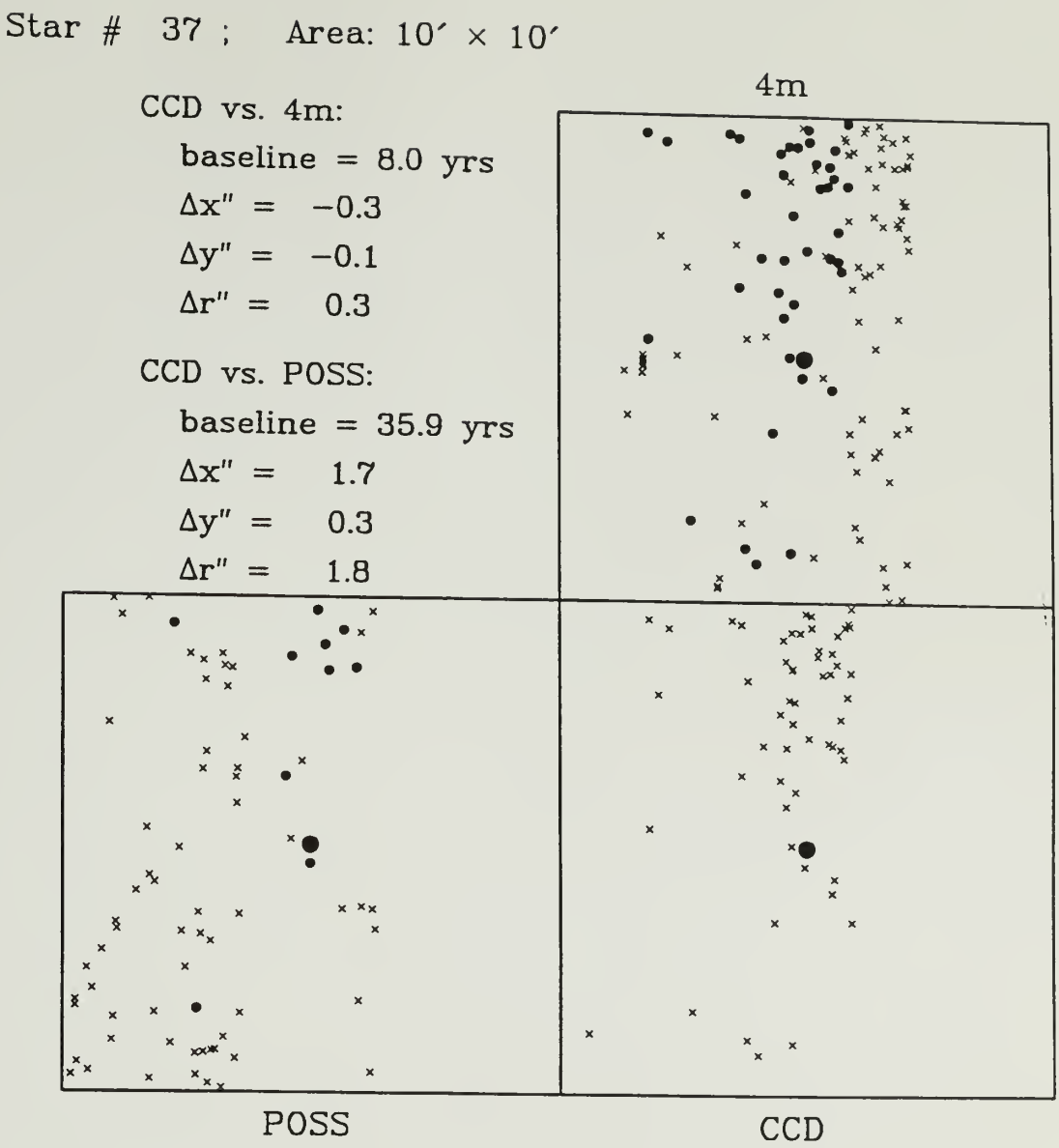

Figure B.1 continued (i)

continued next page

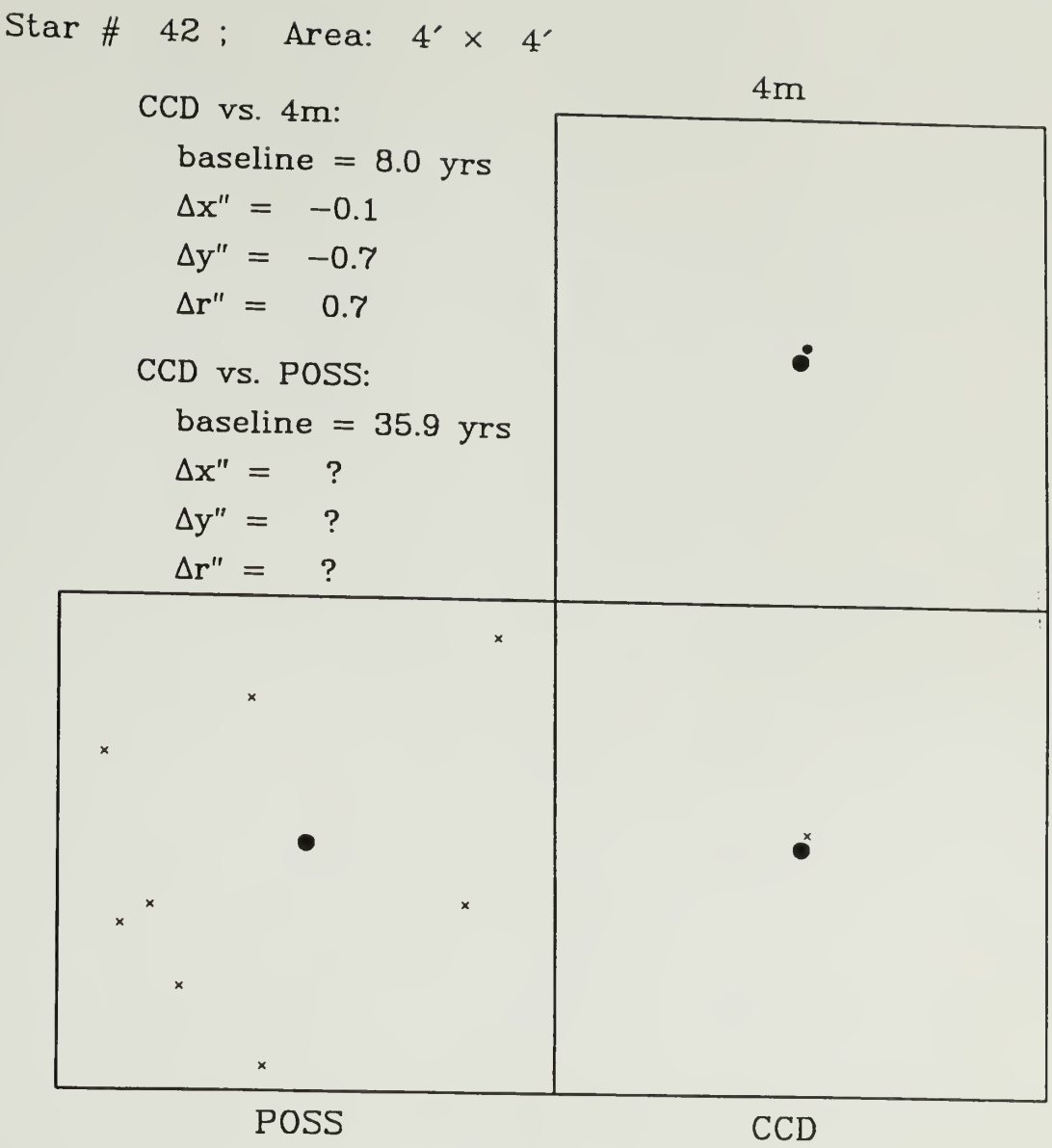

Figure B.1 continued (j)

continued next page

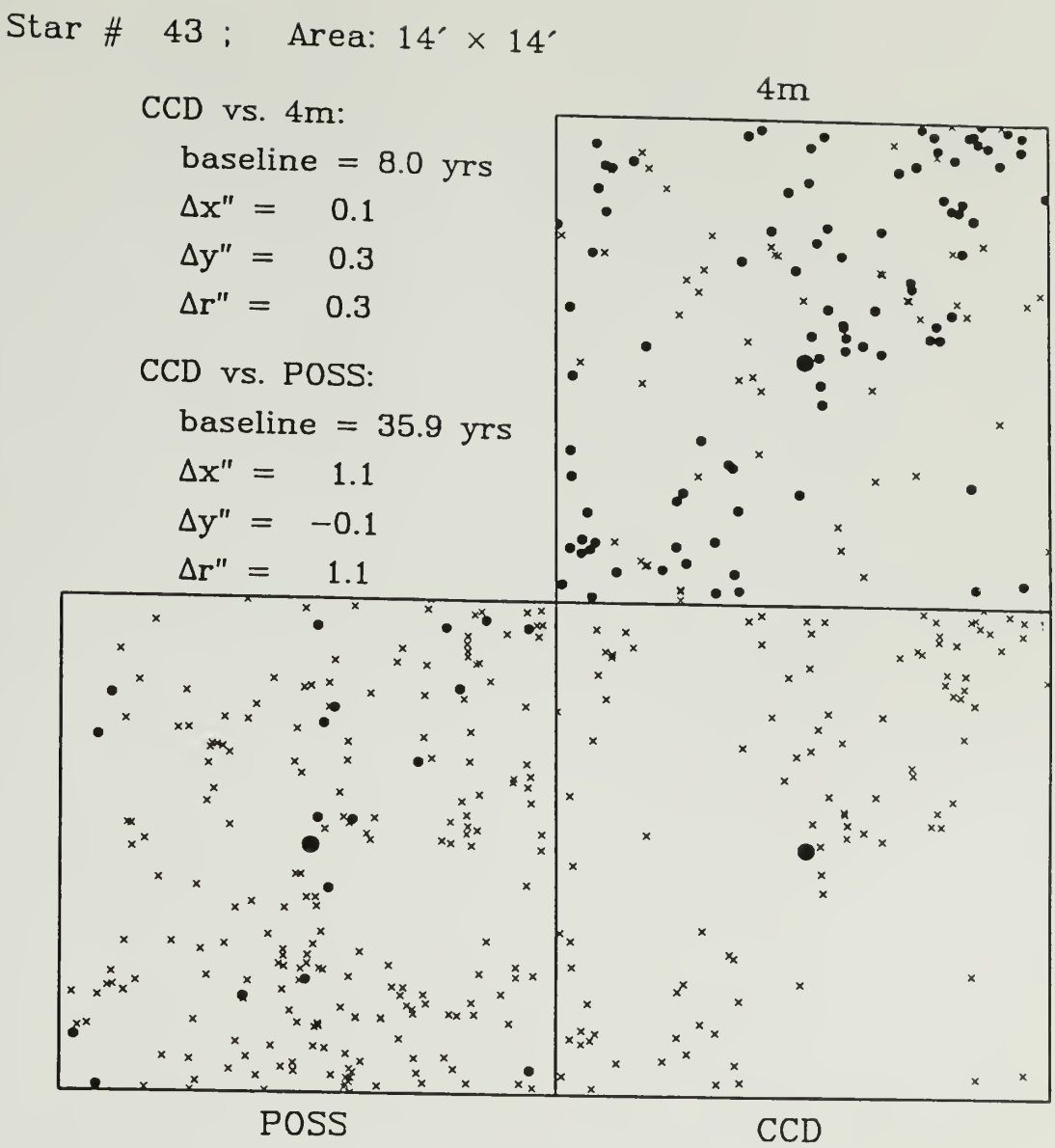

Figure B.1 continued (k)

continued next page

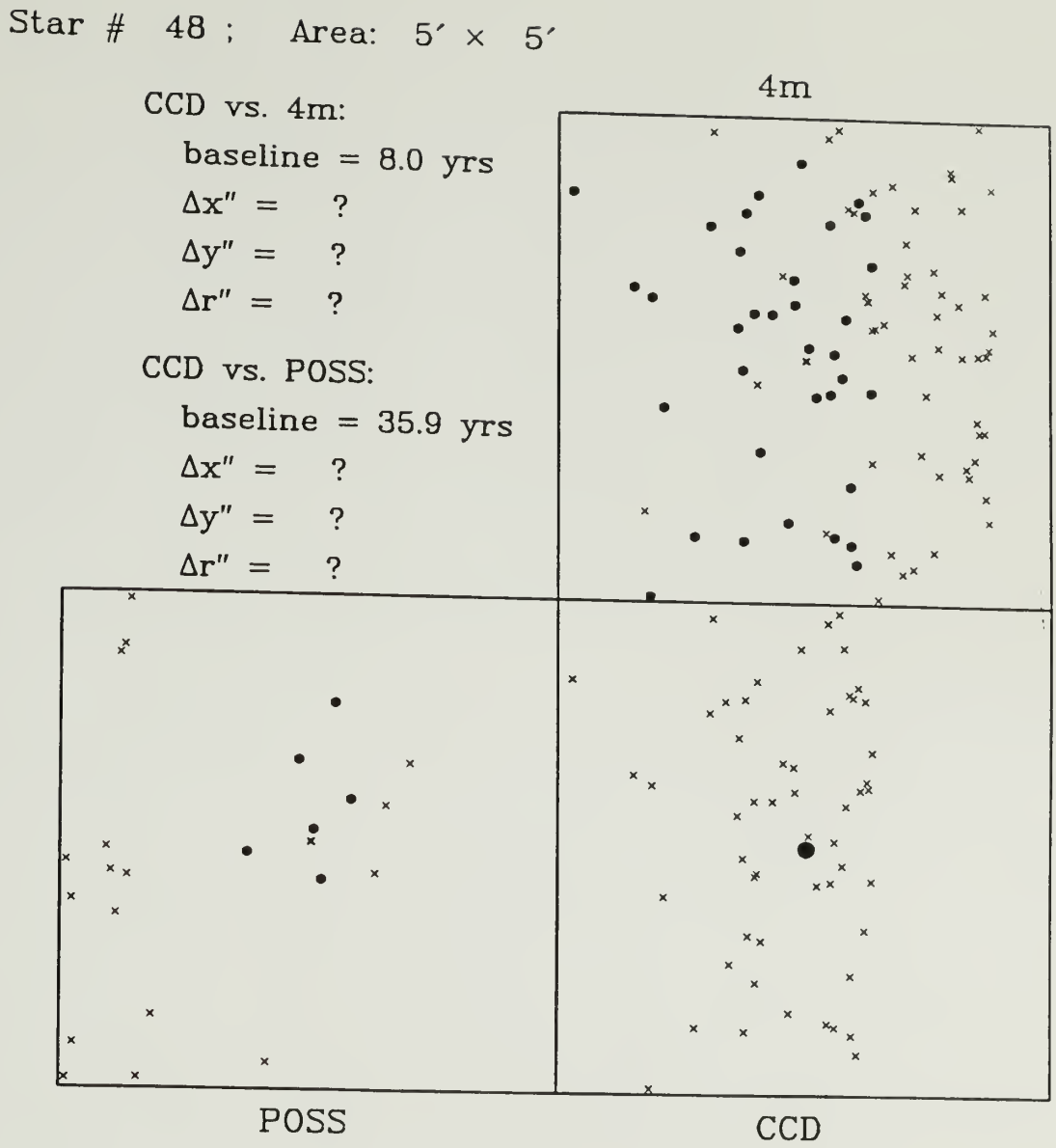

Figure B.1 continued (l)

continued next page

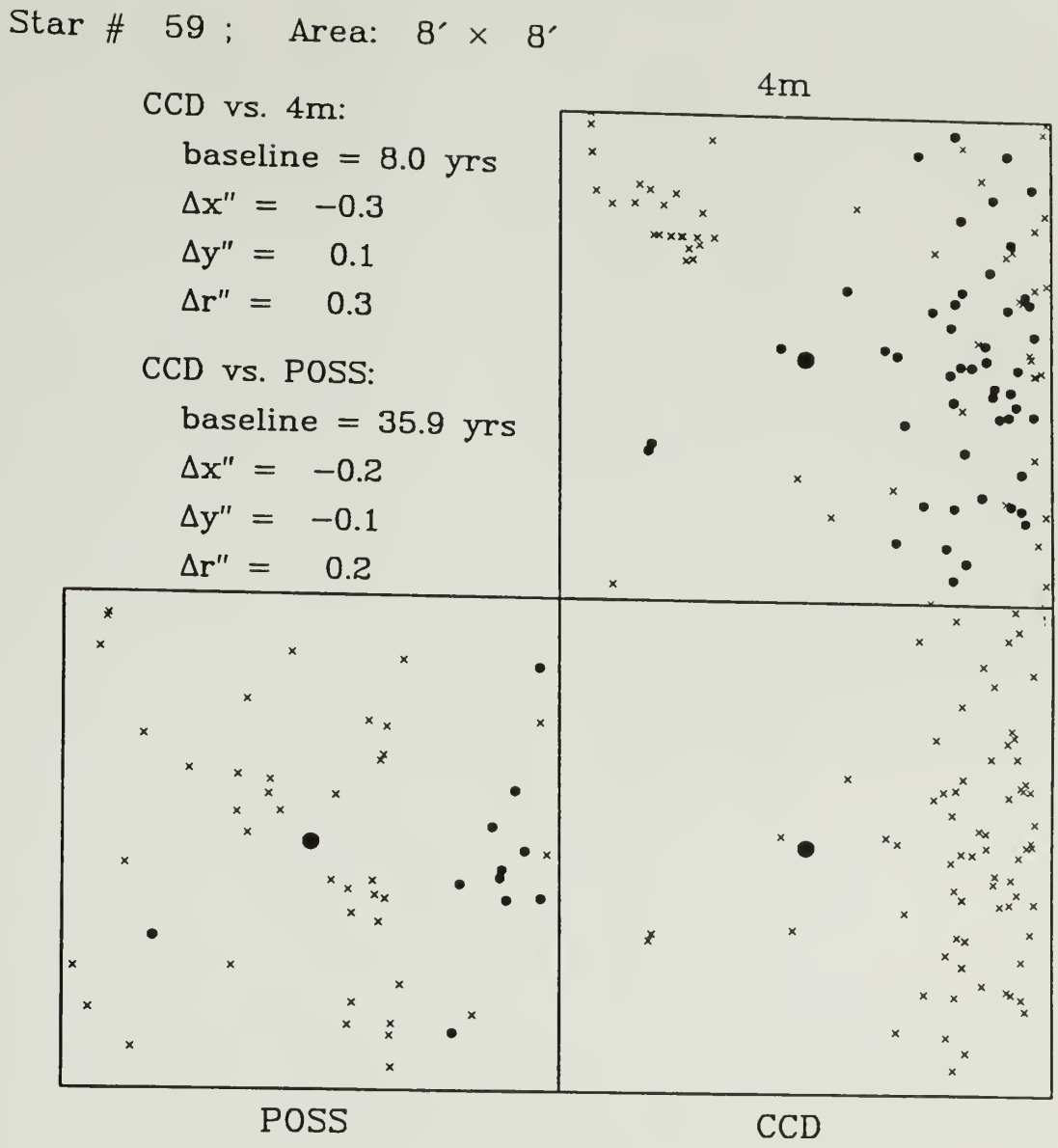

Figure B.1 continued (m)

continued next page

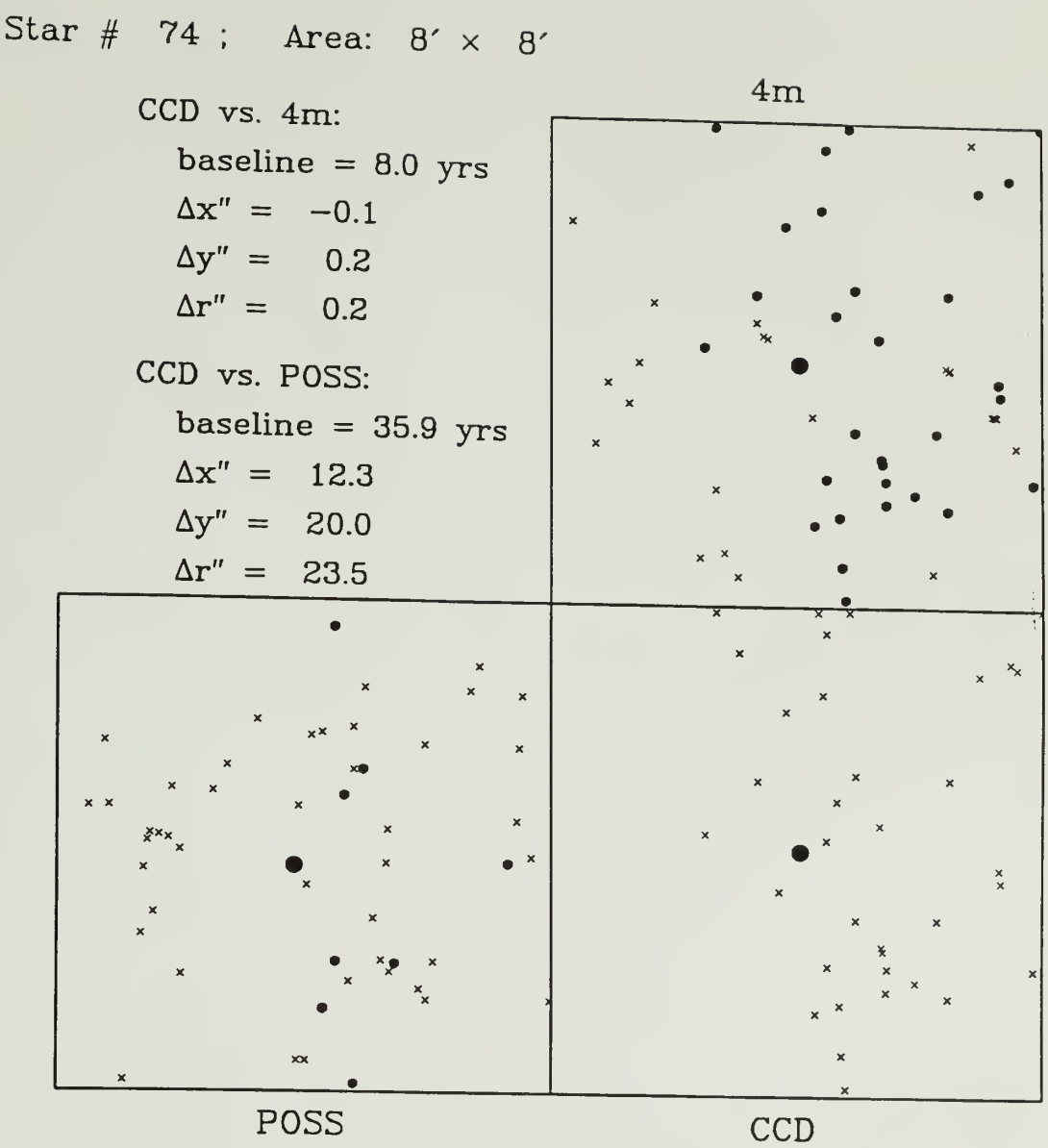

Figure B.1 continued (n)

continued next page

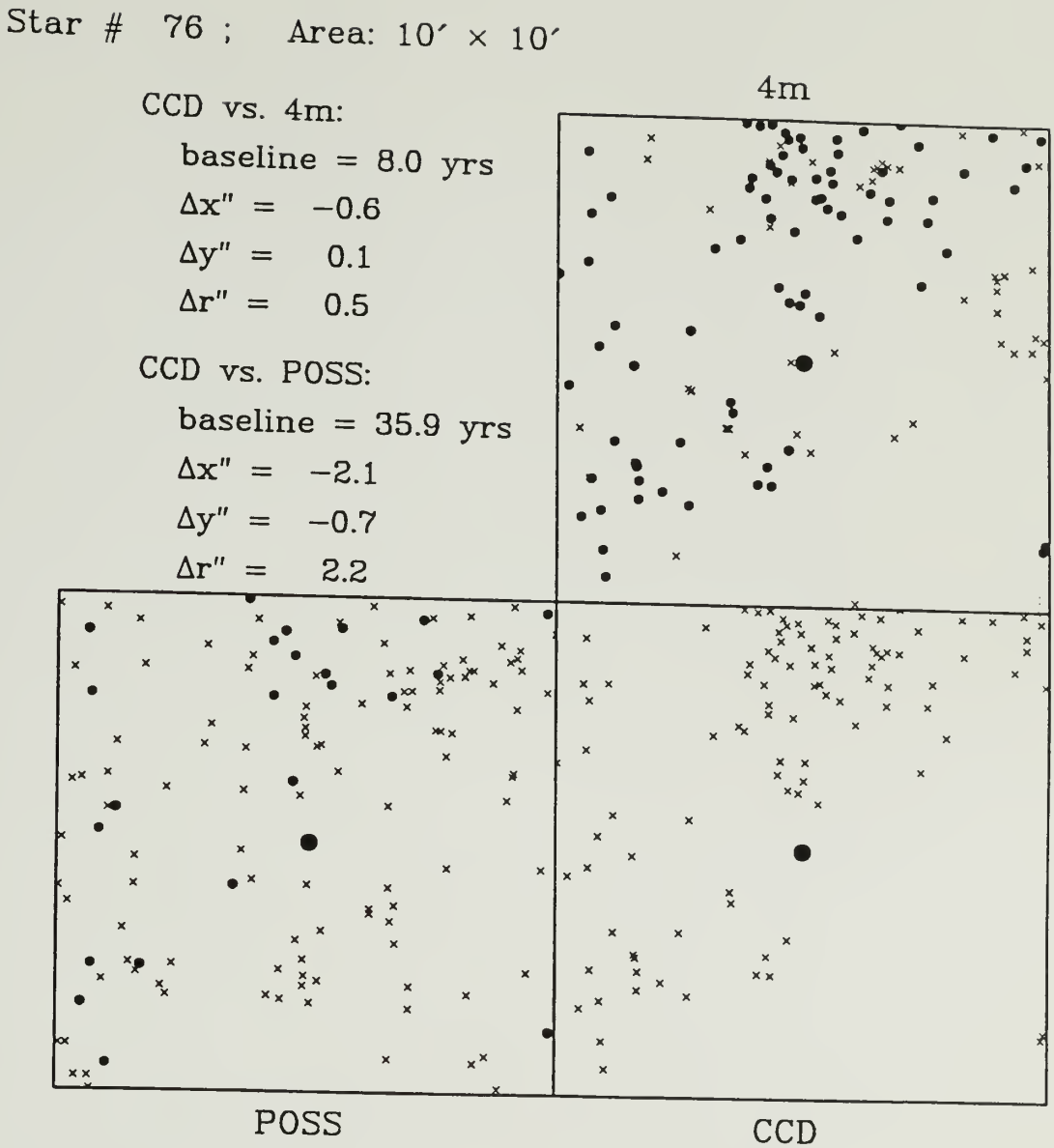

Figure B.1 continued (o)

continued next page

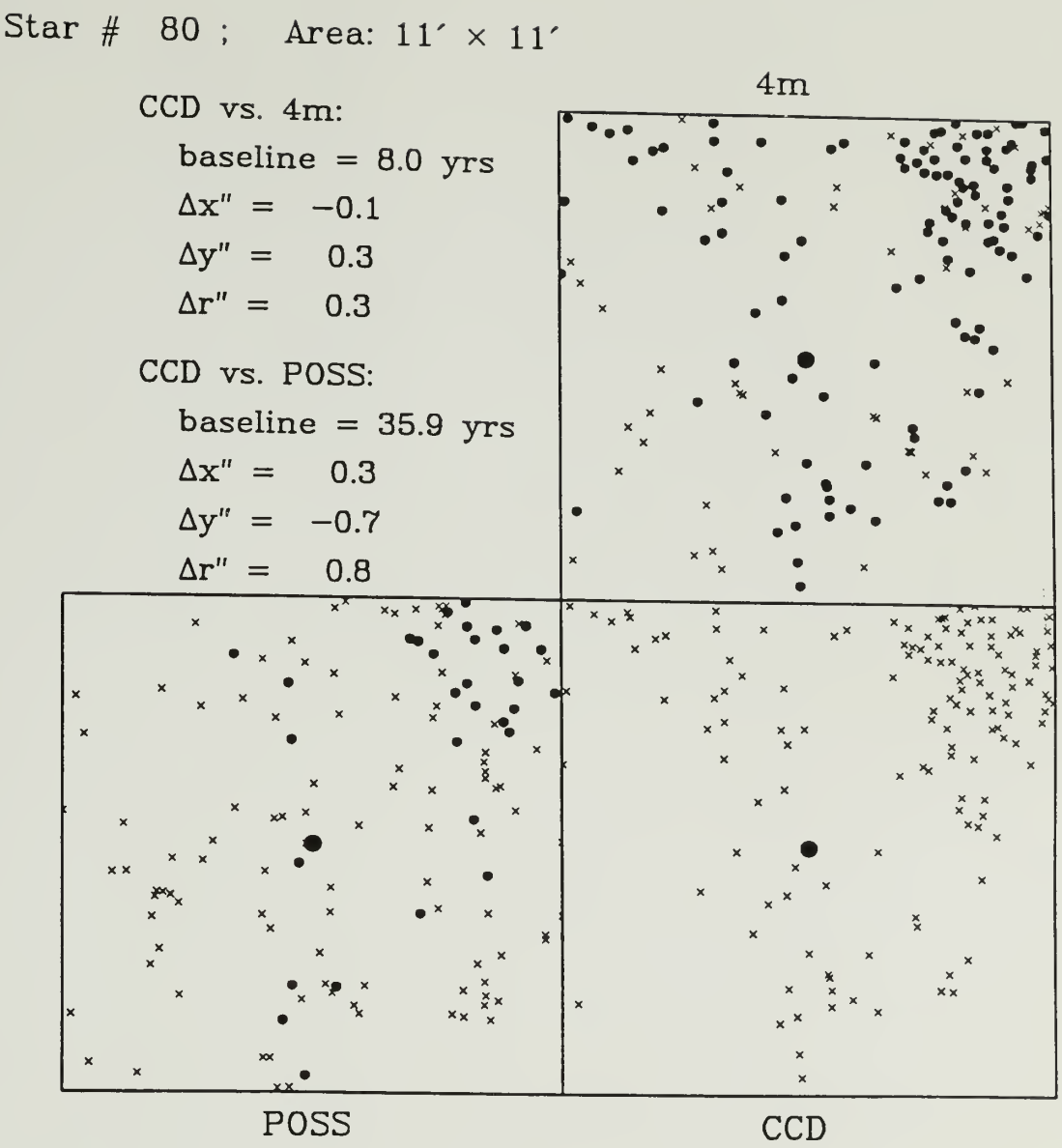

Figure B.1 continued (p)

continued next page

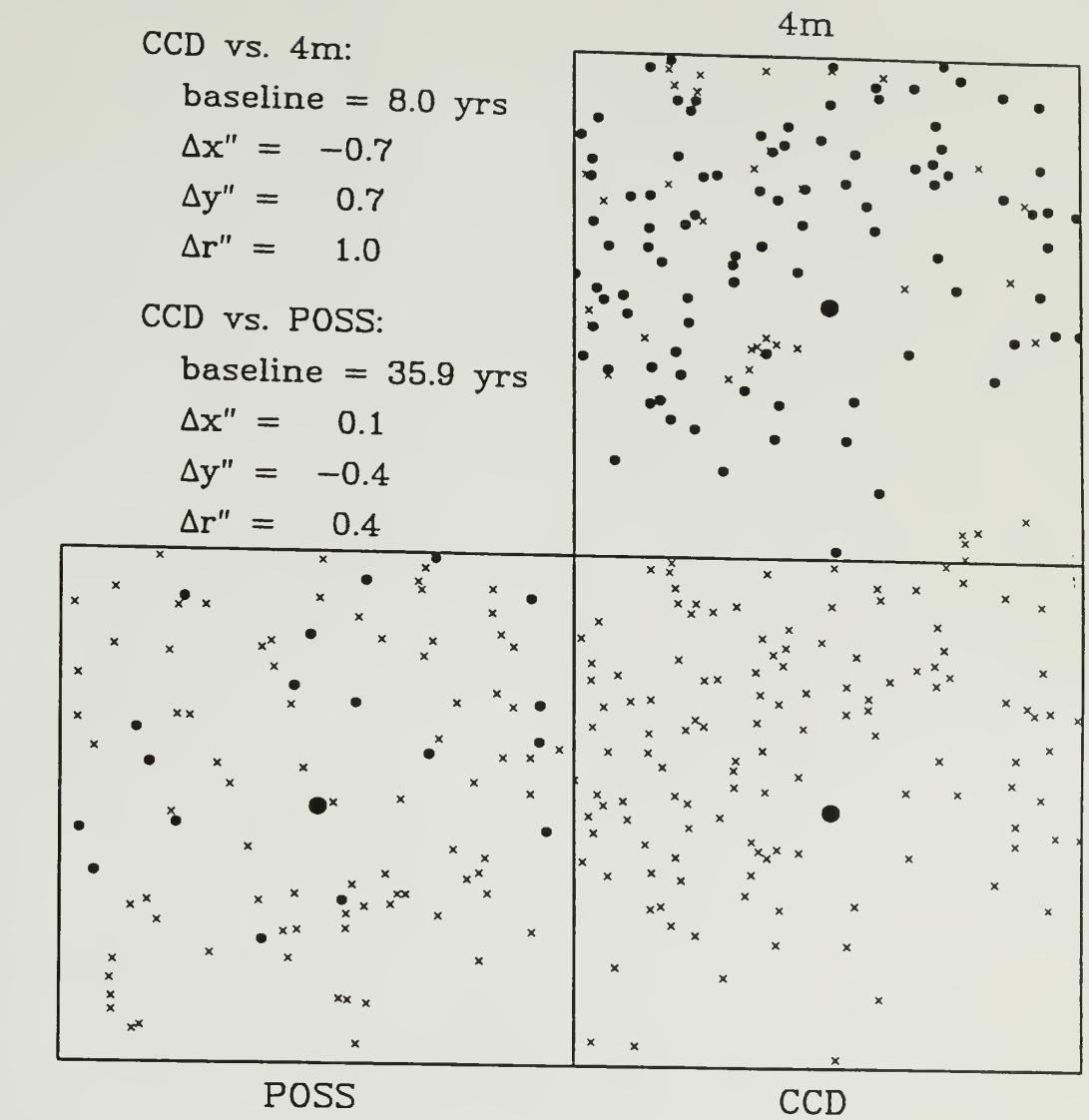

Figure B.1 continued (q)

continued next page

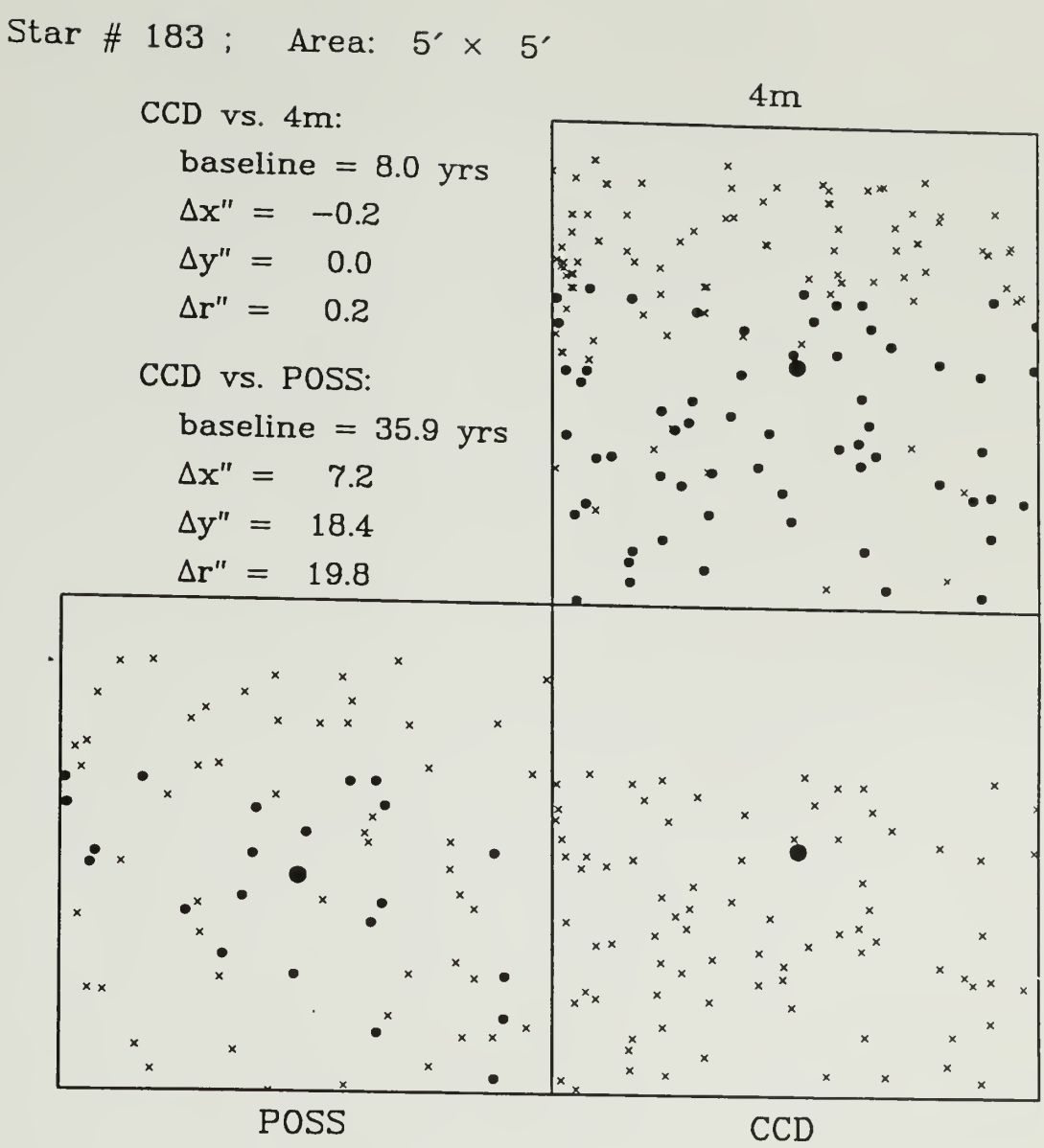

Figure B.1 continued (r)

continued next page

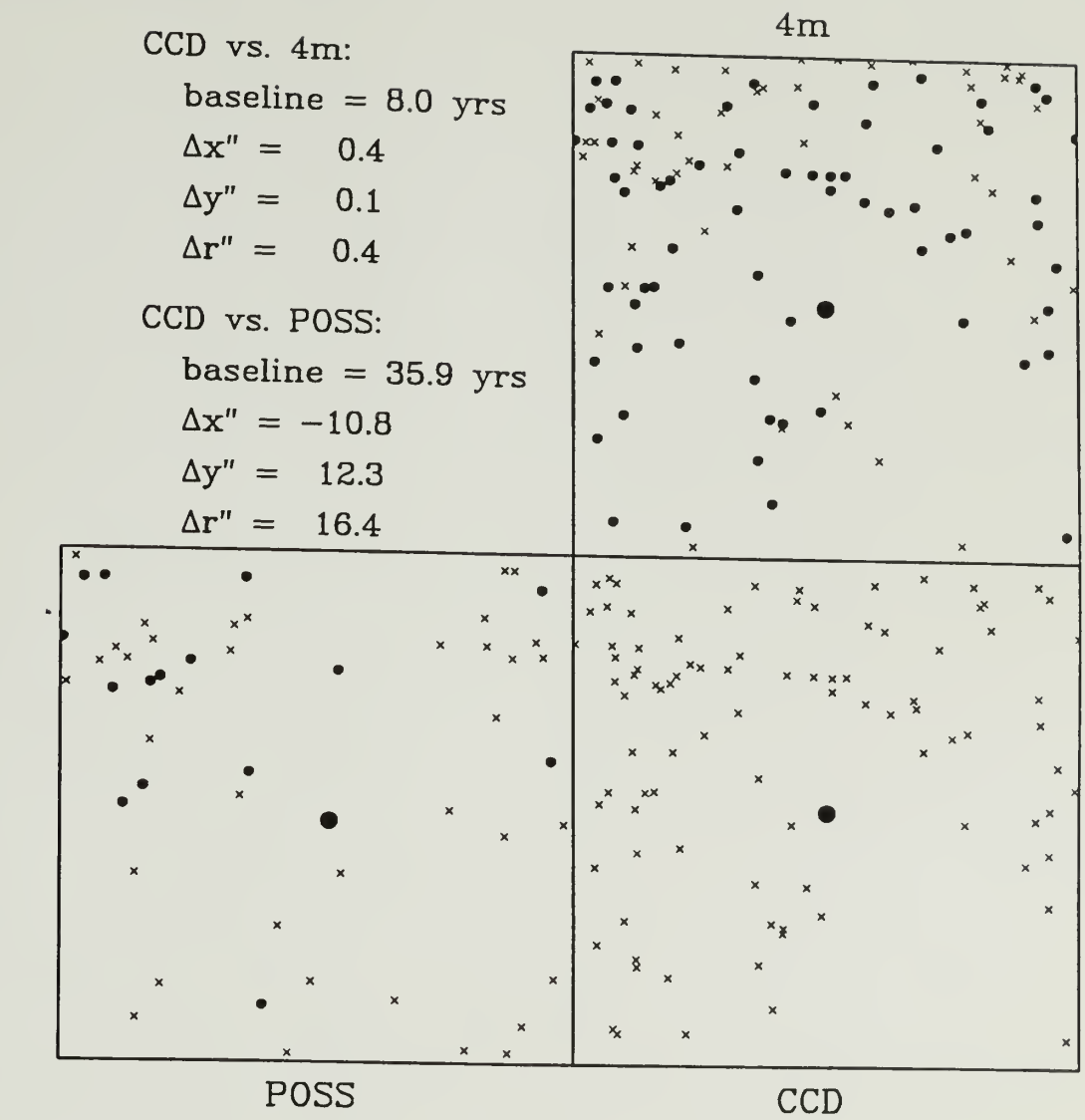

Figure B.1 continued (s)

continued next page

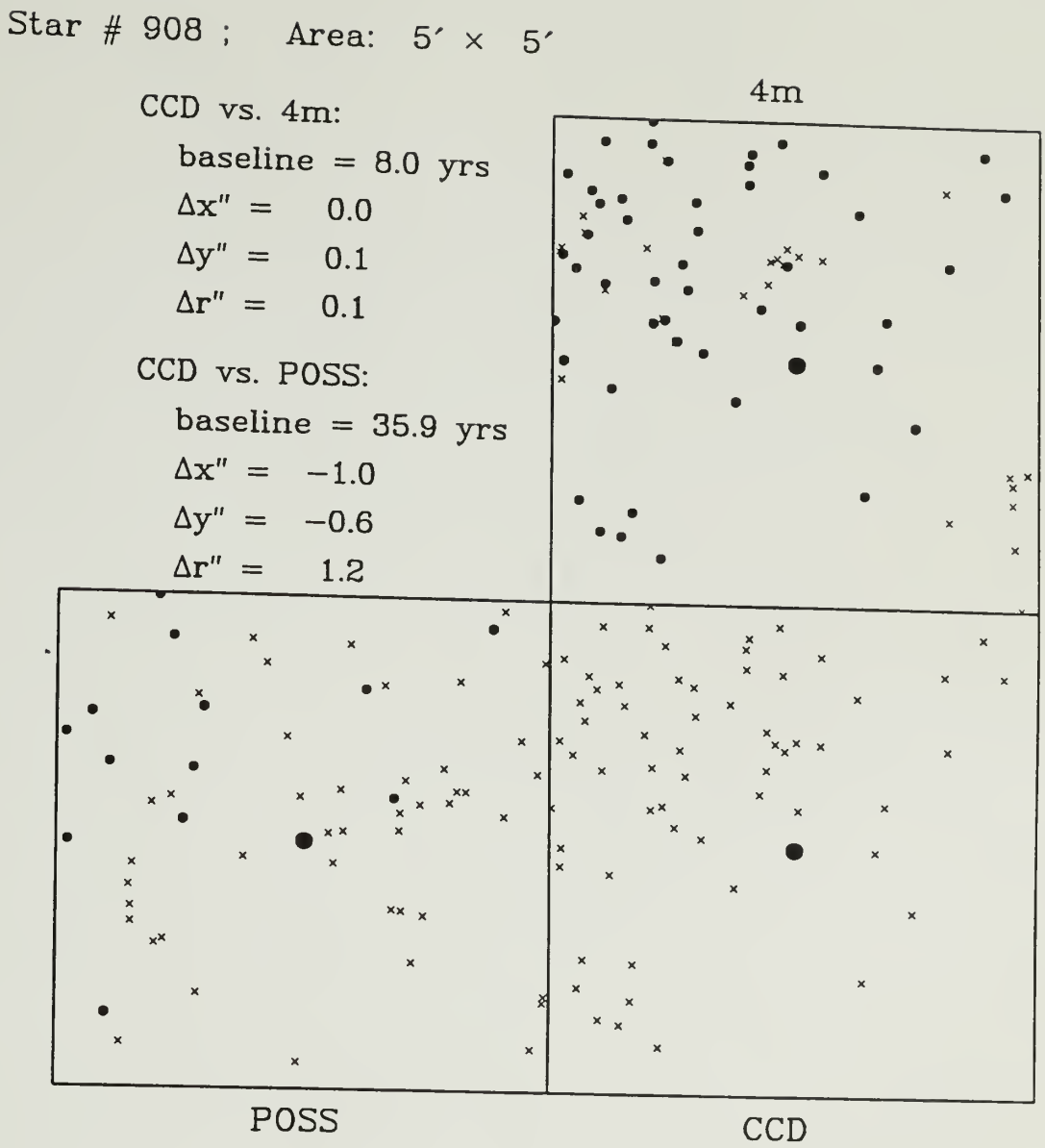

Figure B.1 continued (t)

continued next page

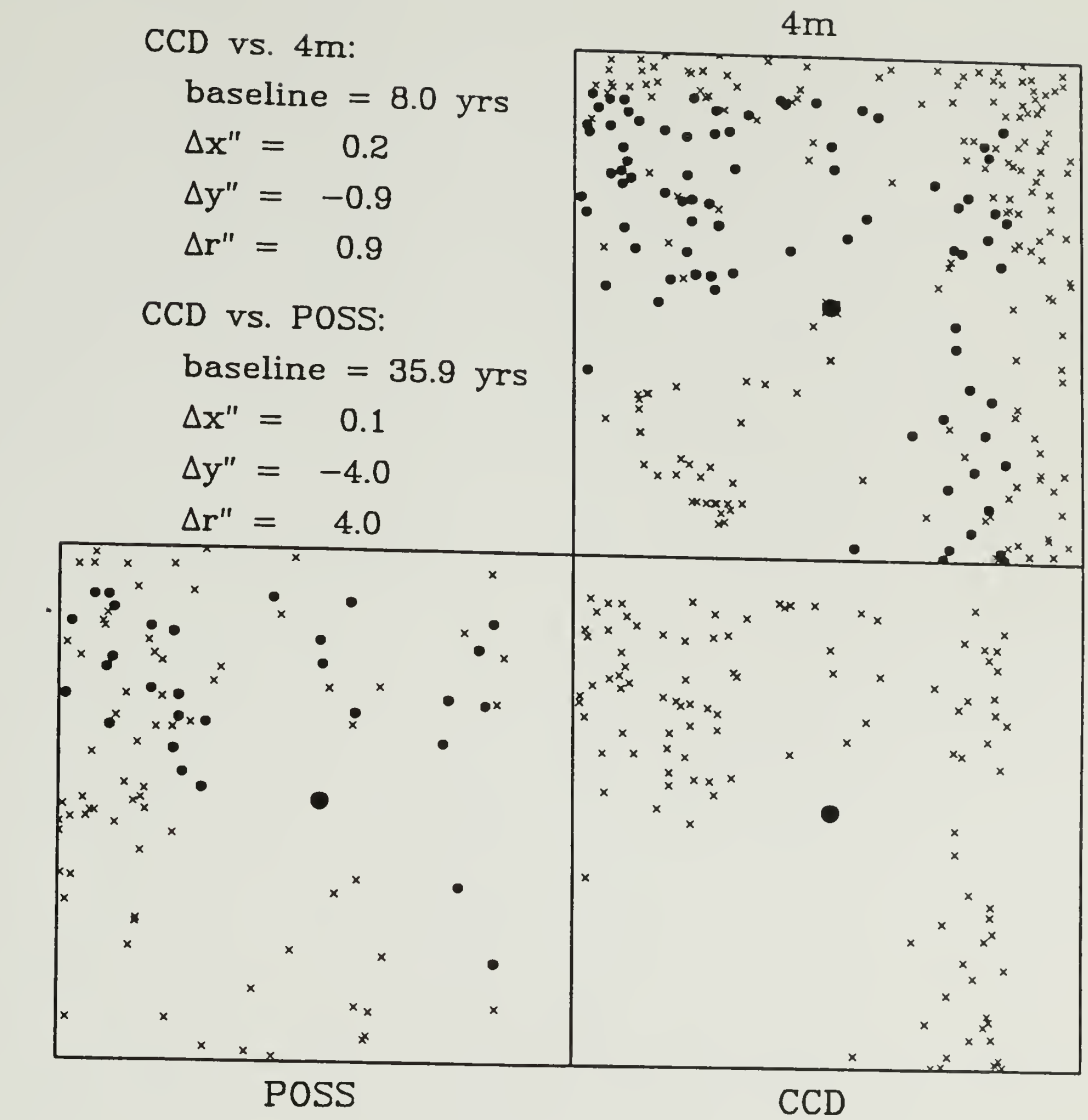

Figure B.1 continued (u)

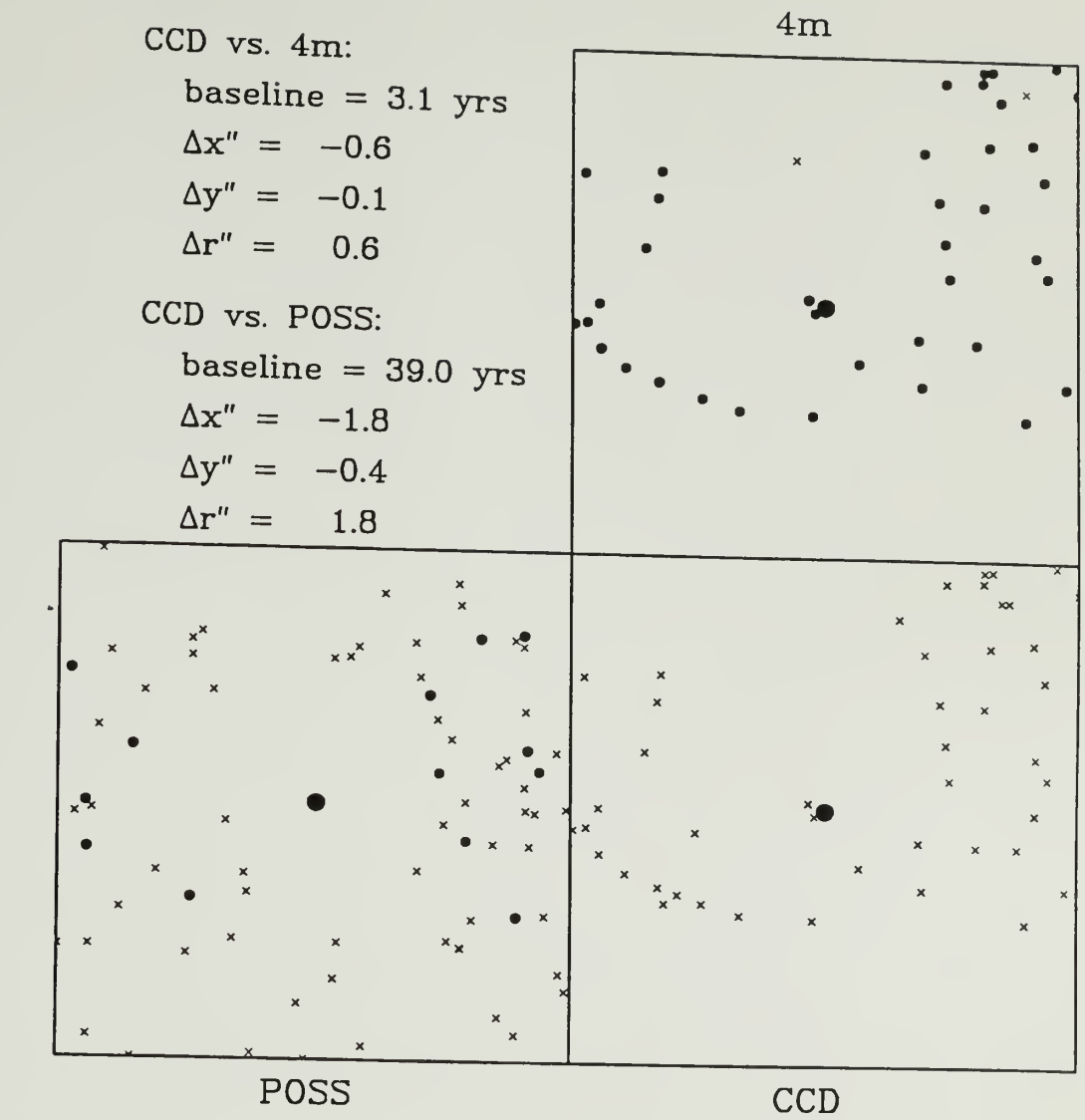

Figure B.2 Taurus photometric foreground candidates. (a) The local areas for each photometric foreground candidate in the photographic 4m, CCD, and POSS E-plate data sets. The photometric candidates are the large filled circle in each box. The reference stars used in the polynomial mappings are represented by filled circles; the other stars are represented by crosses. The angular shifts obtained for the two baselines are also shown. The size of the local areas is indicated in units of arc minutes.

continued next page

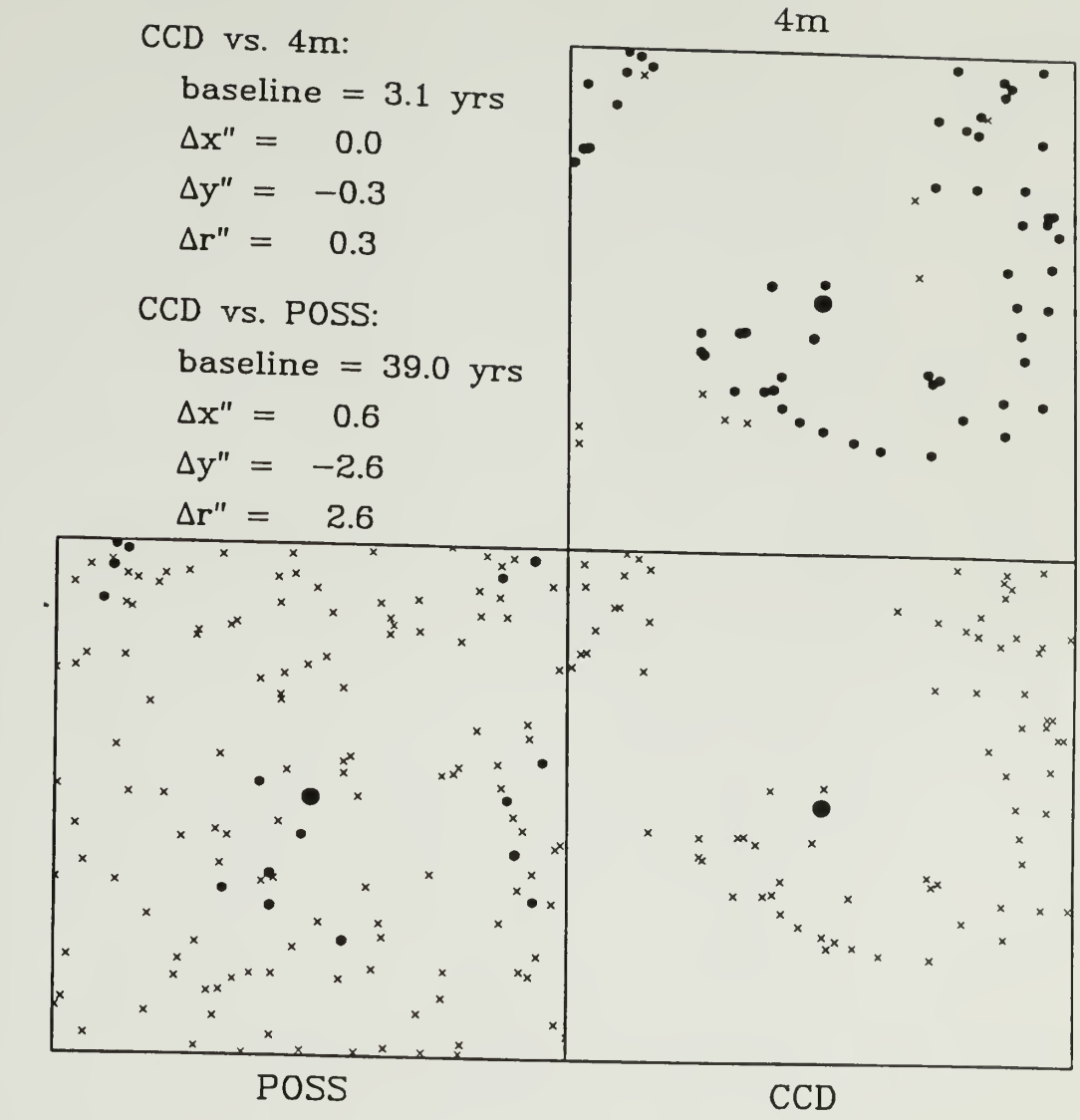

Figure B.2 continued (b)

continued next page

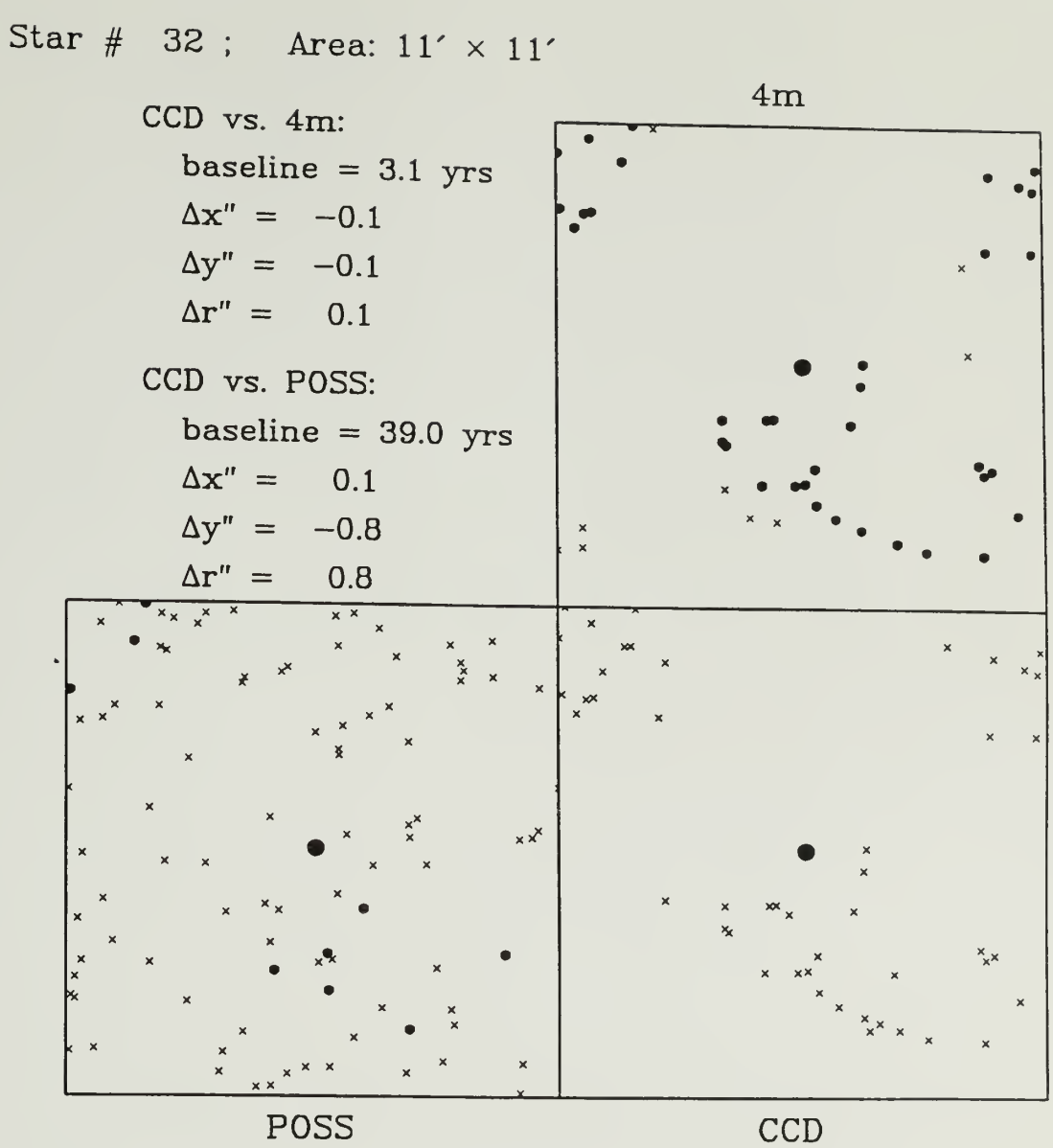

Figure B.2 continued (c)

continued next page

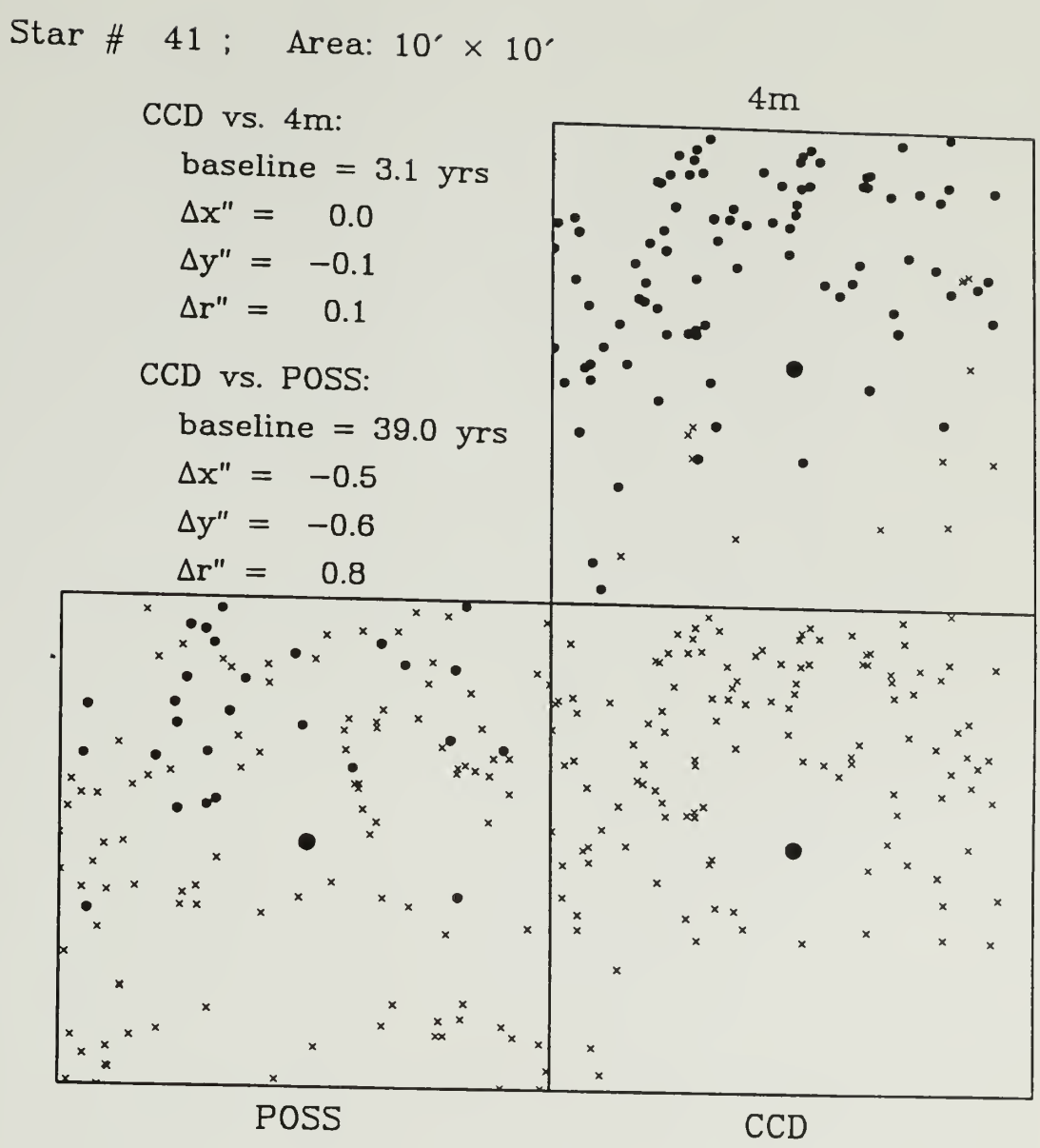

Figure B.2 continued (d)

continued next page

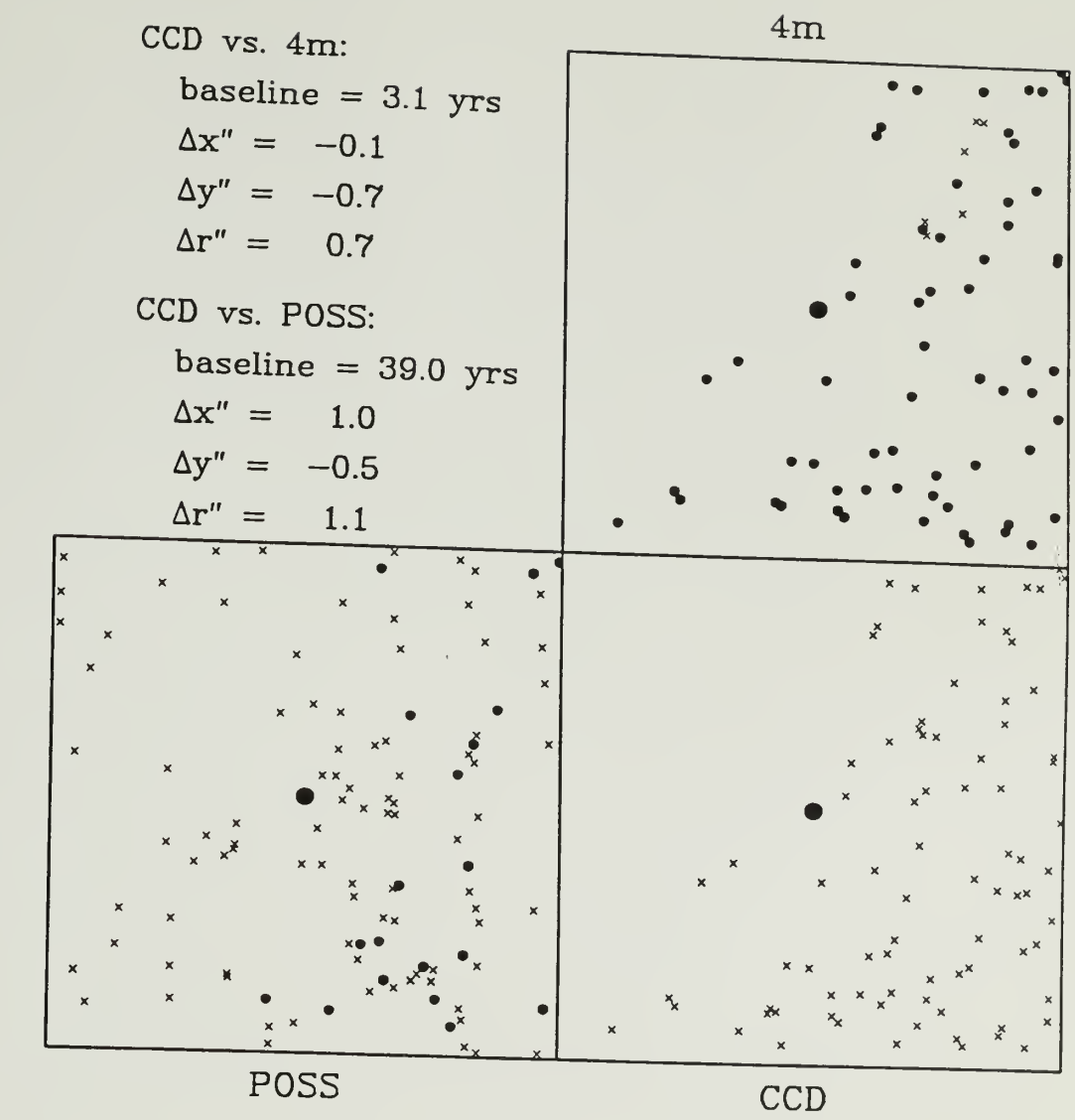

Figure B.2 continued (e)

continued next page

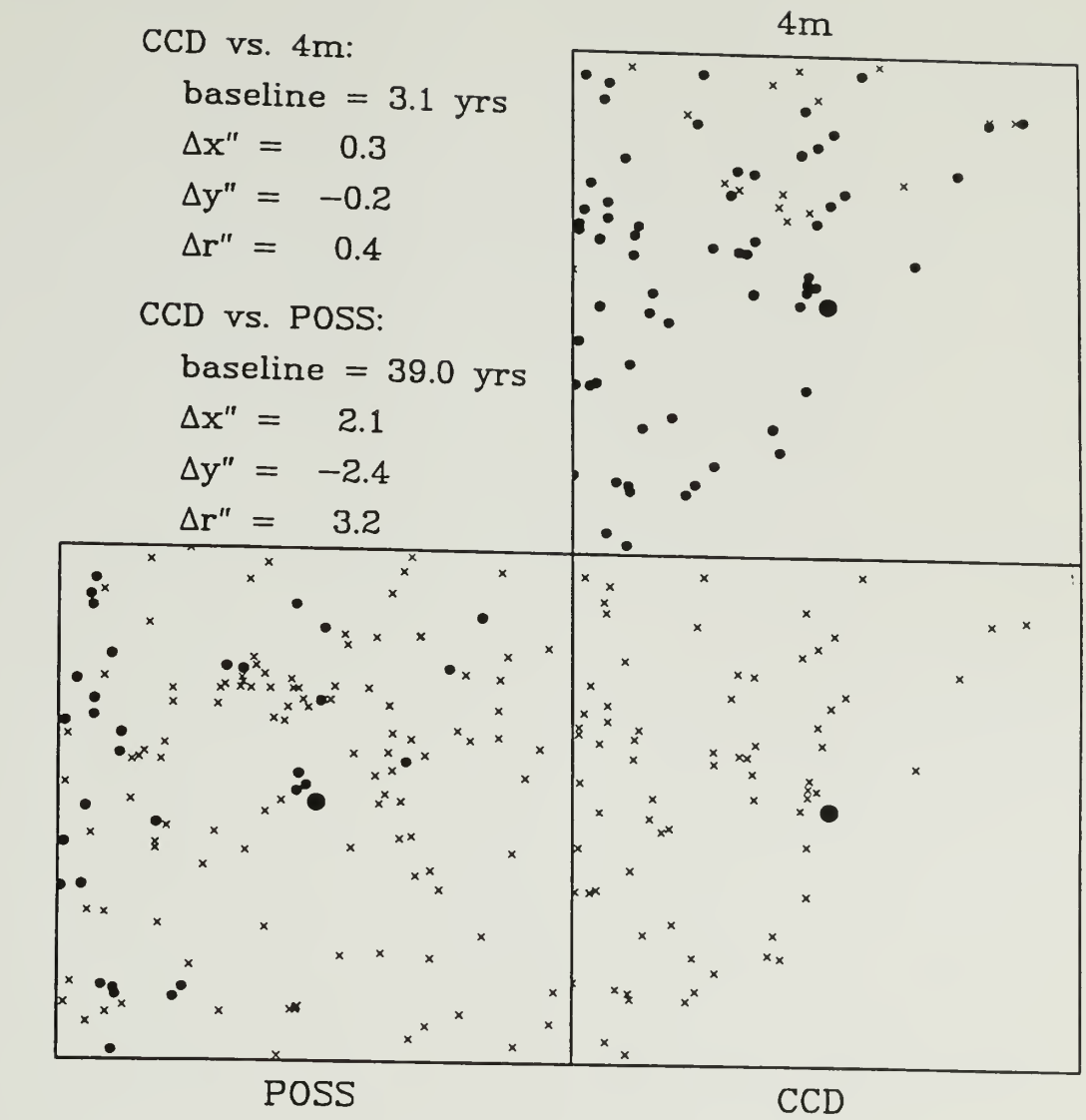

Figure B.2 continued (f)

continued next page

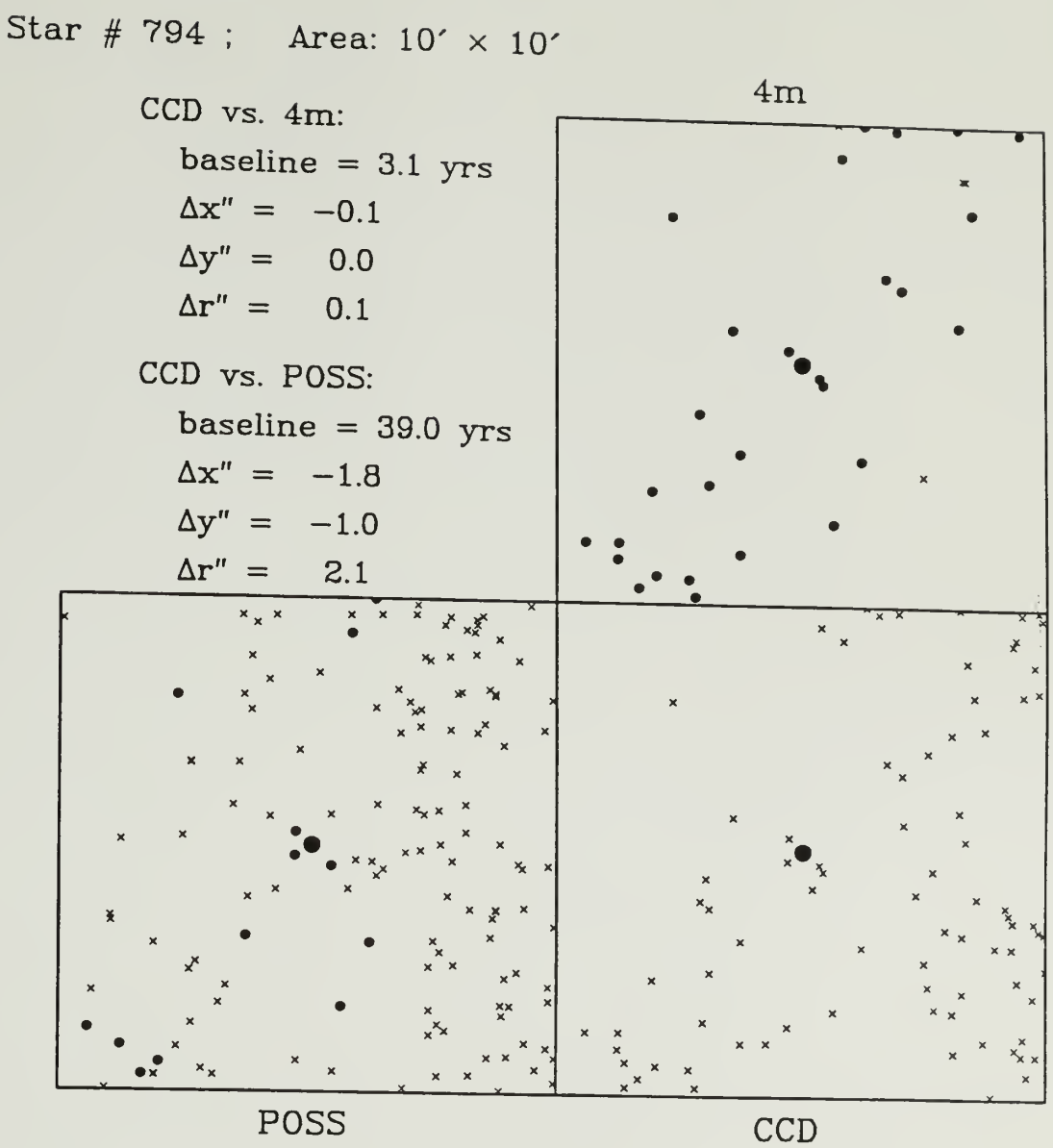

Figure B.2 continued (g)

continued next page

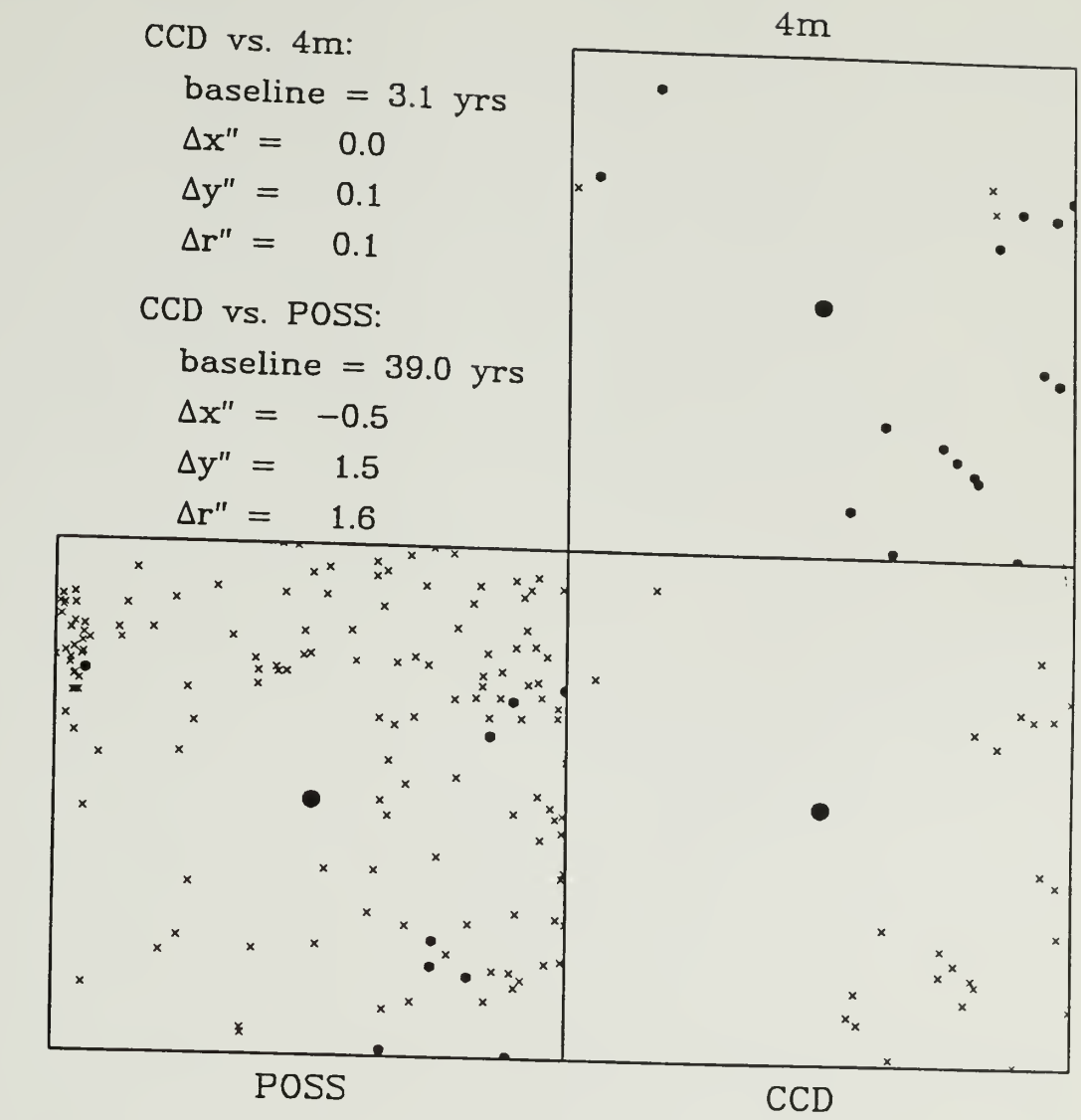

Figure B.2 continued (h)

continued next page

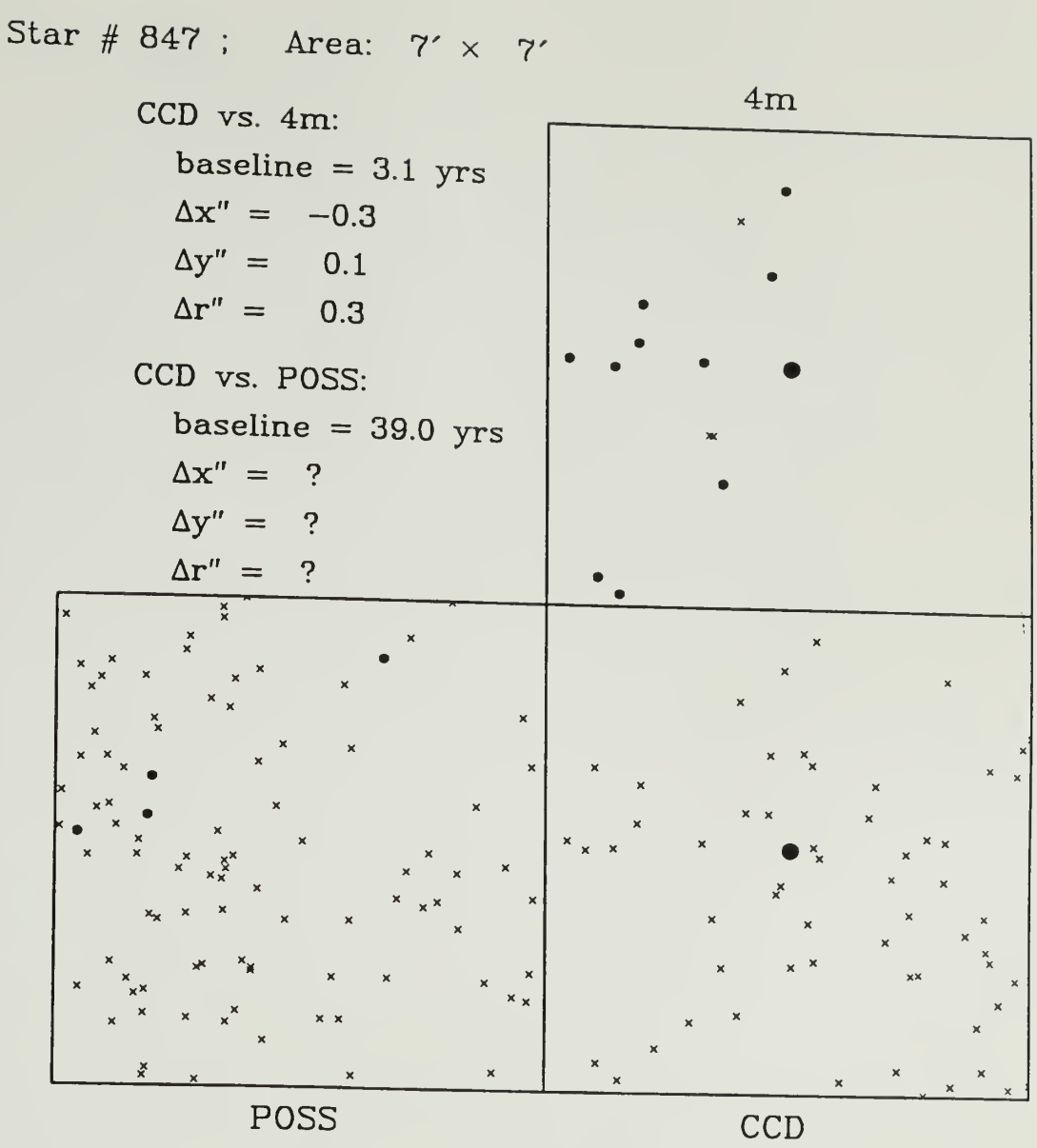

Figure B.2 continued (i)

continued next page

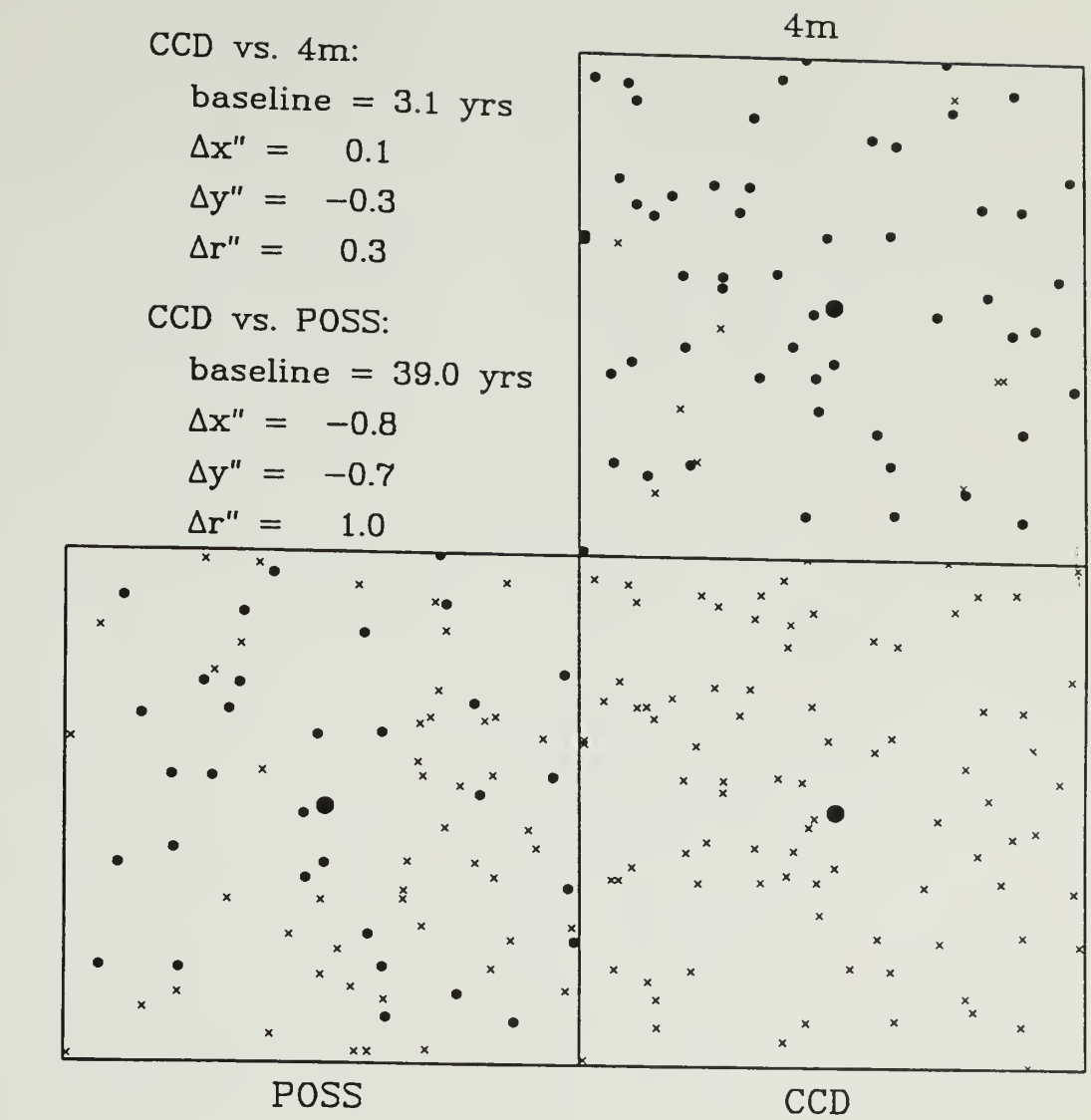

Figure B.2 continued (j)

continued next page

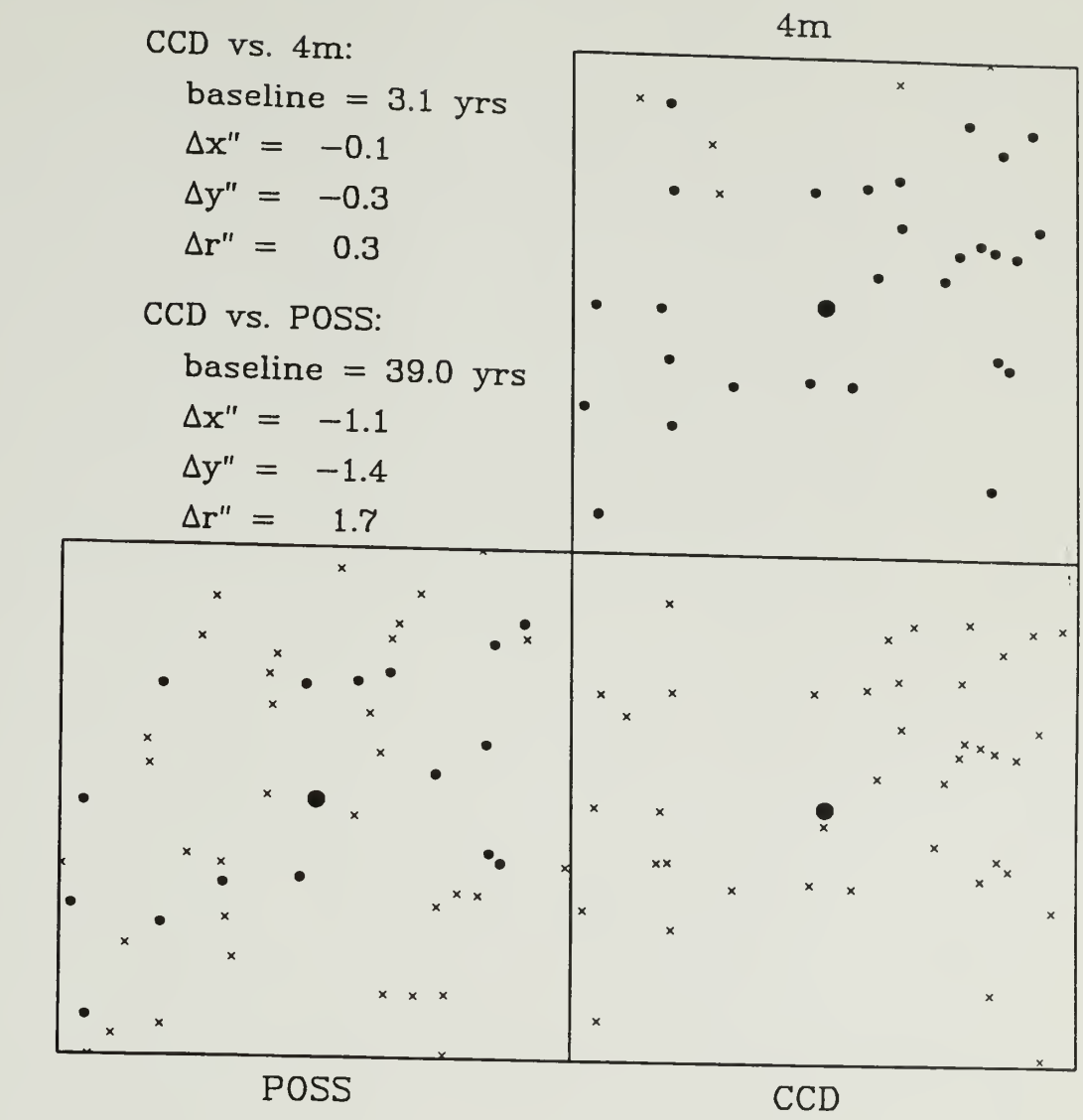

Figure B.2 continued (k)

continued next page

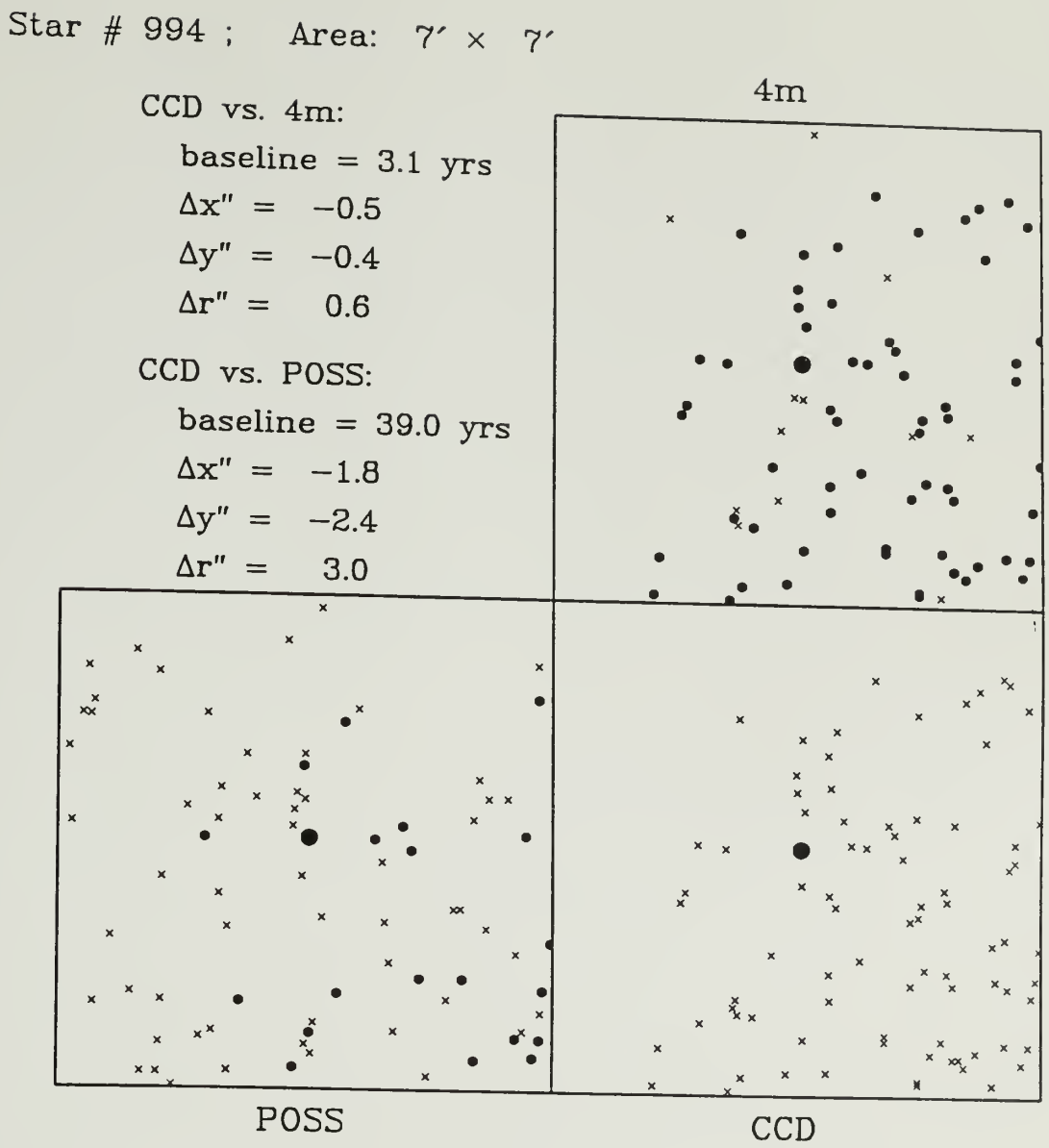

Figure B.2 continued (l)

continued next page

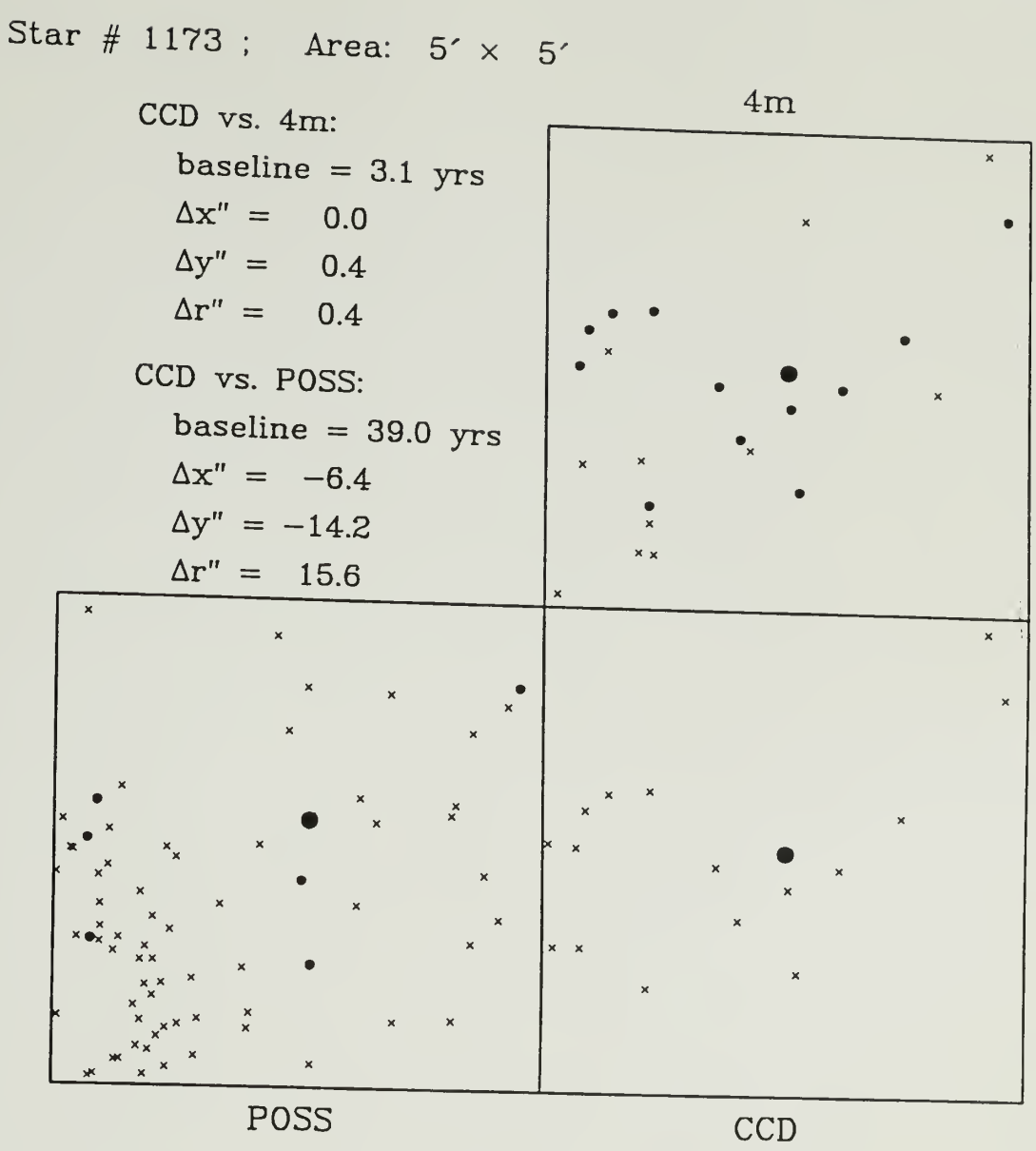

Figure B.2 continued (m)

continued next page

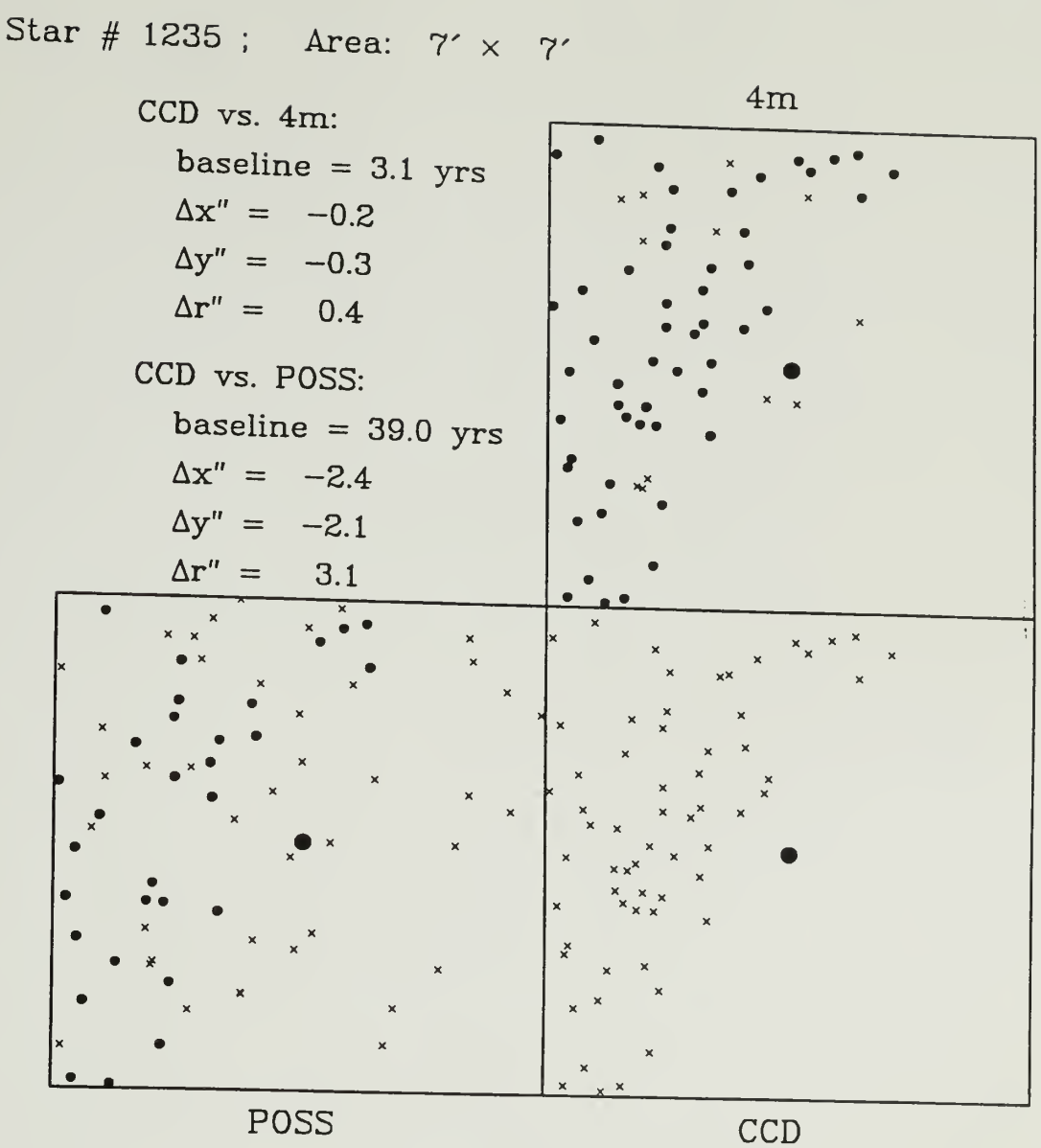

Figure B.2 continued (n)

continued next page

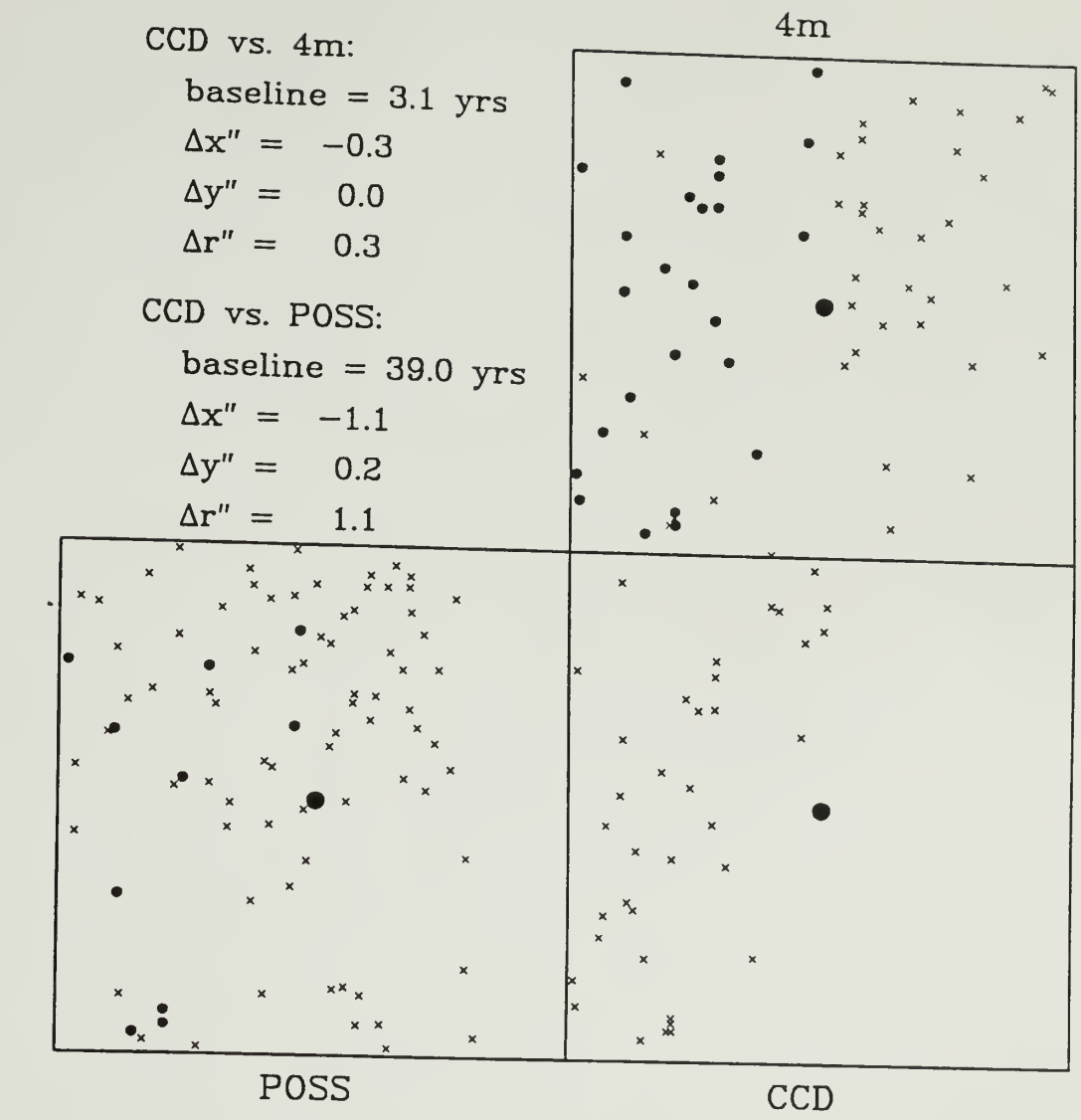

Figure B.2 continued (o)

continued next page

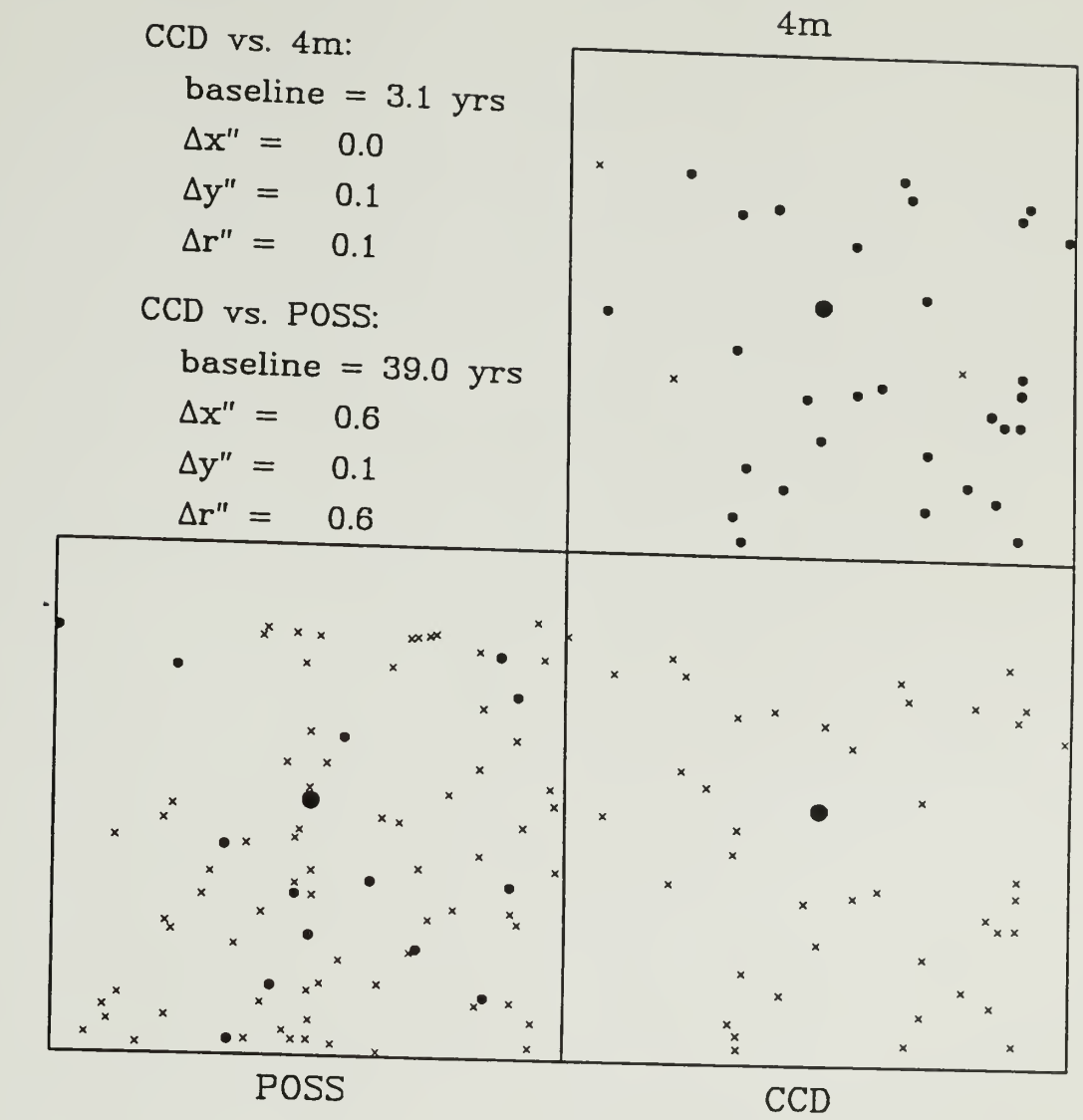

Figure B.2 continued (p)

APPENDIX C

INTERSTELLAR REDDENING

This appendix considers the problem of correcting stellar colors for the effects of interstellar extinction. To do this, we address the interaction of starlight with dust of mixed composition (*e.g.*, silicates and graphite) and calculate the transmission of the resultant reddened light through V, R and I broad band filters of a detector system. Two approaches are presented. The first is a simple model of monochromatic starlight and rectangular transmission filters. The second is a more detailed consideration of stellar flux distributions and non-rectangular filters. The first method is adequate when the interstellar extinction is small, while the second is specifically applied to cases where the extinction is appreciable.

C.1 Linear Model

Interstellar reddening is the physical process by which starlight is selectively attenuated by dust associated with star forming regions and evolved stars in the Galactic disk. The extinction is wavelength dependent, with blue starlight affected to a greater degree than red light because interstellar dust grains have sizes ~ 1000 Å. Hence, a star lying behind a molecular cloud will appear to have colors redder than what would be expected based on its spectral type. On the other hand, if we can determine the visual extinction using, for example, star count techniques, then it may be possible to *de-redden* the colors of background stars and therefore decode the corresponding spectral types.

It is conventional to write the extinction at wavelength, λ, as

$$A_\lambda = \left[\frac{f_{\lambda V}}{R} + 1\right] A_V \tag{C.1}$$

where A_v is the visual extinction, and $f_{\lambda v}$ (sometimes referred to the "reddening law") is the ratio defined as follows,

$$\begin{aligned} f_{\lambda V} = \frac{A_\lambda - A_V}{A_B - A_V} &= \frac{(\lambda - V) - (\lambda - V)_0}{(B - V) - (B - V)_0} \\ &= \frac{E(\lambda - V)}{E(B - V)} \end{aligned} \tag{C.2}$$

where the 0 subscript refers to the unreddened or intrinsic colors, and the E stands for color excess. The constant R, the ratio of total to selective extinction, has a value defined as - $f_{\lambda \to \infty}$, equivalently

$$R = \frac{A_V}{A_B - A_V} \tag{C.3}$$

The observationally measured value of R is ≈ 3.1 for the interstellar medium and 'normal' dust clouds (*cf.* Savage and Mathis 1979), but R may have anomalously large values, ≥ 5, in regions such as the Orion and ρ Ophiuchi molecular cloud complexes (Carrasco et al. 1973; Strom et al. 1975). An enhancement in the ratio of total to selective extinction is usually attributed to the formation of ice mantels on normal silicate/graphite dust grains. Evidence supporting this hypothesis comes from polarization measurements of heavily reddened stars located in the regions mentioned above. It was found that in the cases where R was measured to be anomalously large toward these stars, the parameter λ_{max}, wavelength of maximum linear polarization, was found to be similarly enhanced. Since λ_{max} is directly proportional to the mean grain diameter (Greenberg 1968), an increase

in both R and λ_{max} toward heavily reddened stars is consistent with a grain growth mechanism in dark clouds. Nevertheless, there remains inconclusive observational evidence as to the existence of an enhanced value of R in the ρ Ophiuchi molecular cloud (Elias 1978; de Geus 1988; Dickman and Herbst 1990). Since there is little incentive to employ anomalous values of R in the analysis of visual extinctions in the Taurus and Ophiuchus clouds, we adopt the standard value of 3.1 for R.

The values for $f_{\lambda v}$ are obtained from empirical interstellar reddening curves; $E(\lambda\text{-}V)/E(B\text{-}V)$ is plotted for stars of known spectral type (including main sequence dwarfs and evolved giants) against λ^{-1} (*cf.* Savage and Bless 1972; Nandy et al. 1976; Schild 1977). The reddening curves determined for stars located in Ophiuchus and Orion deviate from the mean interstellar reddening curve at the blue and ultraviolet wavelengths (particularly near the 0.2μm graphite feature) and at the longest wavelengths (where R is determined; see above). In this study, we are concerned with the red end of the spectrum (visual to near-infrared), consequently, it is sufficient to employ the mean or 'normal' interstellar extinction curve. The remaining discussion assumes this.

Tabulated in Table C.1 are $f_{\lambda v}$ values determined for wavelengths corresponding to peak transmission through optical V,R,I filters, respectively, 0.55μm, 0.67μm and 0.81μm. The data comes from Nandy *et al.* (1975), Schild (1977), Bless and Savage (1972), and van de Hulst (1949).

The ratio of E(V-R) and E(R-I) represents the reddening vector within the (V-R) versus (R-I) color-color plane. A star whose light is attenuated by visual extinction, A_v, will have colors that deviate from their intrinsic value by following a linear path with slope E(V-R)/E(R-I). As an example, consider the Savage and Mathis reddening law.

Table C.1

Optical Reddening Laws*

Source	E(B-V)	E(V-R)	E(R-I)	E(V-R)/ E(R-I)
Nandy *et al.*	1	0.75	0.62	1.22
Schild	1	0.66	0.62	1.08
Savage & Mathis	1	0.62	0.66	0.94
van de Hulst	1	0.81	0.65	1.25

* R = 3.1

Substituting the values from Table C.1 into equation C.1 gives the following relations between A_λ and A_v:

$$\begin{aligned} A_B &= 1.32 A_V \\ A_R &= 0.80 A_V \\ A_I &= 0.59 A_V \end{aligned} \qquad \text{(C.4)}$$

The visual extinction is computed by measuring the amount of reddening in the (V-R) and (R-I) plane, δ(V-R), and making use of Equation C.4, as follows:

$$\begin{aligned} A_V &= \delta(V-R) / \left(1 - \frac{A_R}{A_V}\right) \\ &\approx 5\,\delta(V-R) \end{aligned} \qquad \text{(C.5)}$$

C.2 Synthetic Photometry

The linear model presented in the preceding section is adequate when the visual extinction is not too large (Av ~ few). Non-linear effects become important when the extinction becomes appreciably greater than this. It is well known that molecular cloud cores have visual extinctions ≥ 50 (*cf.* Wilking and Lada 1984), and other regions of the

cloud may have visual extinctions ranging from 5 to 20 magnitudes. For this reason, we next consider the problem of the interstellar reddening of heavily obscured stars using the "synthetic" technique (Hayes 1974; Taylor 1986).

The *observed* flux of a star depends not only on its *intrinsic* flux, but also on the detector efficiency, filter response, and atmospheric conditions; and can be written as (*cf.* Henden and Kaichuck 1982):

$$F_\lambda = \int_0^\infty d\lambda\, \varphi_A(\lambda)\, \varphi_T(\lambda)\, \varphi_{DE}(\lambda)\, \varphi_F(\lambda)\, \varphi_{dil}(\lambda)\, F_*(\lambda) \qquad \text{(C.6)}$$

where ϕ_A is the fractional transmission of Earth's atmosphere, ϕ_T the fractional transmission of the telescope, ϕ_{DE} the detector efficiency, ϕ_F the filter response function, and F_* the flux of the star.

The factor ϕ_{dil}, represents the dilution of starlight via absorption by intervening cosmic dust. Since this is an opacity measure, we may express the dilution using an exponential function that depends on the extinction,

$$\varphi_{dil} \propto \exp(-A_\lambda) \qquad \text{(C.7)}$$

where A_λ is a function of A_V, R and $f_{\lambda V}$; see Equation C.1.

For simplicity, we assume the Earth's atmospheric transmission to be unity. Atmospheric extinction, even at 2 airmasses (typically about 0.3 magnitudes of visual extinction), is far less important than the dilution of starlight by several magnitudes of interstellar extinction. Also, we assume that the telescope transmission and detector

efficiency are both unity, as they are both linear and enter Equation C.6 as constants only. Hence, Equation C.6, the observed flux, becomes:

$$F_\lambda = \int_0^\infty d\lambda\, \varphi_F(\lambda) \exp(-A_\lambda) F_*(\lambda) \qquad \text{(C.8)}$$

Traditionally, astronomers prefer to work with logarithms, so we transform the flux into a magnitude scale. A star whose apparent flux F_λ suffers interstellar extinction has apparent magnitude:

$$m_\lambda = m_{\lambda_0} + 2.5 \log\left[\frac{F_{\lambda_0}}{F_\lambda}\right] \qquad \text{(C.9)}$$

where $\{m_\lambda, F_\lambda\}_0$ are the corresponding unreddened (*i.e.*, $A_\lambda = 0$) magnitude and flux of the star. Accordingly,

$$F_{\lambda_0} = \int_0^\infty d\lambda\, \varphi_F(\lambda)\, F_*(\lambda) \qquad \text{(C.10)}$$

Equation C.8 is solved using known stellar energy distributions and filter response functions. In practice, the integrals are not integrated over $\pm\infty$, but rather over the range of the filter response. We therefore compute F_V, F_R, F_I, and the reddened magnitudes m_v, m_R, and m_I. From these data it is then trivial to calculate reddened colors for a given spectral type. The free parameter in these calculations is the visual extinction, A_V.

We model both standard Harris filters and the Cousins (1976) broad band filter system. A description of the physical characteristics of these two systems is given in

Tables 2.5 and 2.6 (Chapter 2). The range over which the flux integrals, Equations C.8 and C.10, are solved is:

$$\begin{aligned} 0.487 \leq \lambda_V \leq 0.605\,\mu m \\ 0.573 \leq \lambda_R \leq 0.840\,\mu m \\ 0.705 \leq \lambda_I \leq 0.940\,\mu m \end{aligned} \qquad \textbf{(C.11)}$$

Spectral energy distributions were obtained from the low resolution catalogs compiled by Gunn and Stryker (1983), and Code and Bless (1970). Finally, we adopt the reddening law of Savage and Bless (1972), which is conveniently tabulated in a review by Savage and Mathis (1979; also see Table C.1), and can be satisfactorily expressed in analytic form as:

$$\begin{aligned} f_{\lambda V} &= \frac{E(\lambda - V)}{E(B-V)} \\ &\approx -2.031 + 3.585 \ln\left[\frac{1}{\lambda}\right], \qquad 0.5 \leq \lambda \leq 1\,\mu m \end{aligned} \qquad \textbf{(C.12)}$$

With this function and Equations C.1, C.8 and C.11, the form of the R-band numerical flux integral, for example, is

$$F_R = \int_{0.57}^{0.84} d\lambda\, \varphi_{F_R}(\lambda) \exp\left[-\frac{A_V}{R}\left\{R + 3.585 \ln\left(\frac{1}{\lambda}\right) - 2.031\right\}\right] F_*(\lambda) \qquad \textbf{(C.13)}$$

Several test cases were performed, including those of energy distributions belonging to cool giants of spectral type K0, K5, and M3, main sequence dwarfs of spectral type G0, G4, K5, and M2, and finally an M2 Ia supergiant, α Ori. The visual extinction was varied from 0 to 15 in 0.5 magnitude steps. Synthetic fluxes were computed along with their corresponding apparent magnitudes (Equation C.9), and, finally, reddened colors, (v-r) and (r-i). A plot of the resultant color-color reddening functions for the evolved and main sequence star sets can be seen in Figures C.1 and C.2. In addition, these curves are

compared with the linear vector[1] describing the Schild reddening law (see Table C.1), shown by the dashed curve in the figures.

At low visual extinctions, $A_v \leq 2$, the reddening follows essentially a linear vector whose slope can be predicted using the reddening laws in Table C.1. As the extinction increases, the dilution factor of Equation C.5 begins to dominate and the reddening departs significantly from the Schild reddening vector. This effect is amplified for later spectral types. Notice in Figures C.1 and C.2, for example, that the latest spectral types, M3 III and M2 V, respectively, have the greatest disparity between the synthetic and linear models. This effect can be understood by recalling from section C.1 that the shorter wavelengths of starlight are affected most strongly by intervening dust. Consequently, the blue color measure, (V-R), changes more rapidly than the red color, (R-I) extinction increases.

Additionally, the non-rectangular transmission filters of the Cousins (1976) system contribute to this effect. The R filter has a significant "leak" towards the near-infrared (*cf.* Bessell 1986), consequently the R magnitude is boosted with respect to the I band for late-type stars (whose energy distribution peaks in the far-red). Thus the color, (R-I), will change less rapidly with respect to its nominal value when the transmission filters are rectangular (as in the case described in section C.1). A third, equally important reason that blue colors change more rapidly than red for late type stars is that intrinsically cool stars have very deep absorption bands, particularly between the visual and red bandwidths. This point can be illustrated by calculating a synthetic reddening model using energy distributions which *do not* have absorption features. This can be done using blackbody functions, which adequately describe the energy distributions of stars absent line blanketing. In Figure C.3, reddening functions for four blackbodies at temperatures of 3000, 5000,

[1] Recall in the case of the linear model (section C.1), that the reddening functions are simple linear vectors (see Table C.1).

7500 and 10000 K are shown. This range of temperatures is similar to the sample shown in Figures C.1 and C.2, where late M-dwarfs have surface temperatures ~3000 K, G stars ~5000 K and A stars about 10000 K. Notice that the coolest blackbodies show the greatest departure from the linear vector of Schild, but that the disparity is not as dramatic as that for the *real* M stars.

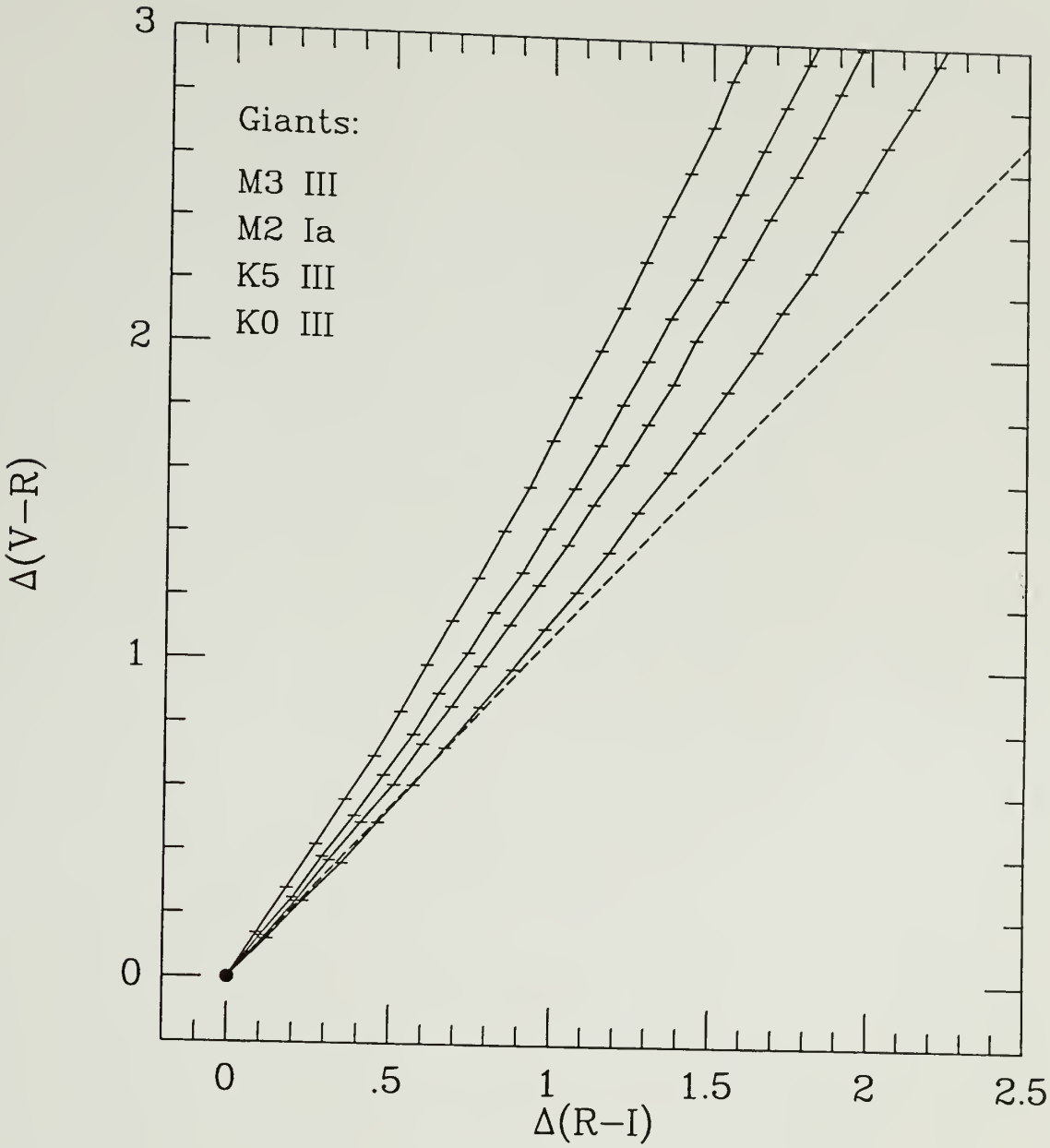

Figure C.1 Effects of interstellar reddening in the V, R, I color-color plane for evolved stars of spectral type M3 III, M2 Ia, K5 III, and K0 III. The left most curve is that of the M3 III stars; likewise, the next curve represents the M2 Ia stars, and so on. The visual extinction is varied from 0 to 15 by 0.5 magnitude intervals (represented by horizonal tick marks). $A_v = 0$ at $\delta(V\text{-}R) = \delta(R\text{-}I) = 0$. Also shown, reddening vector of Schild (1977), slope 1.08, drawn with a dashed line.

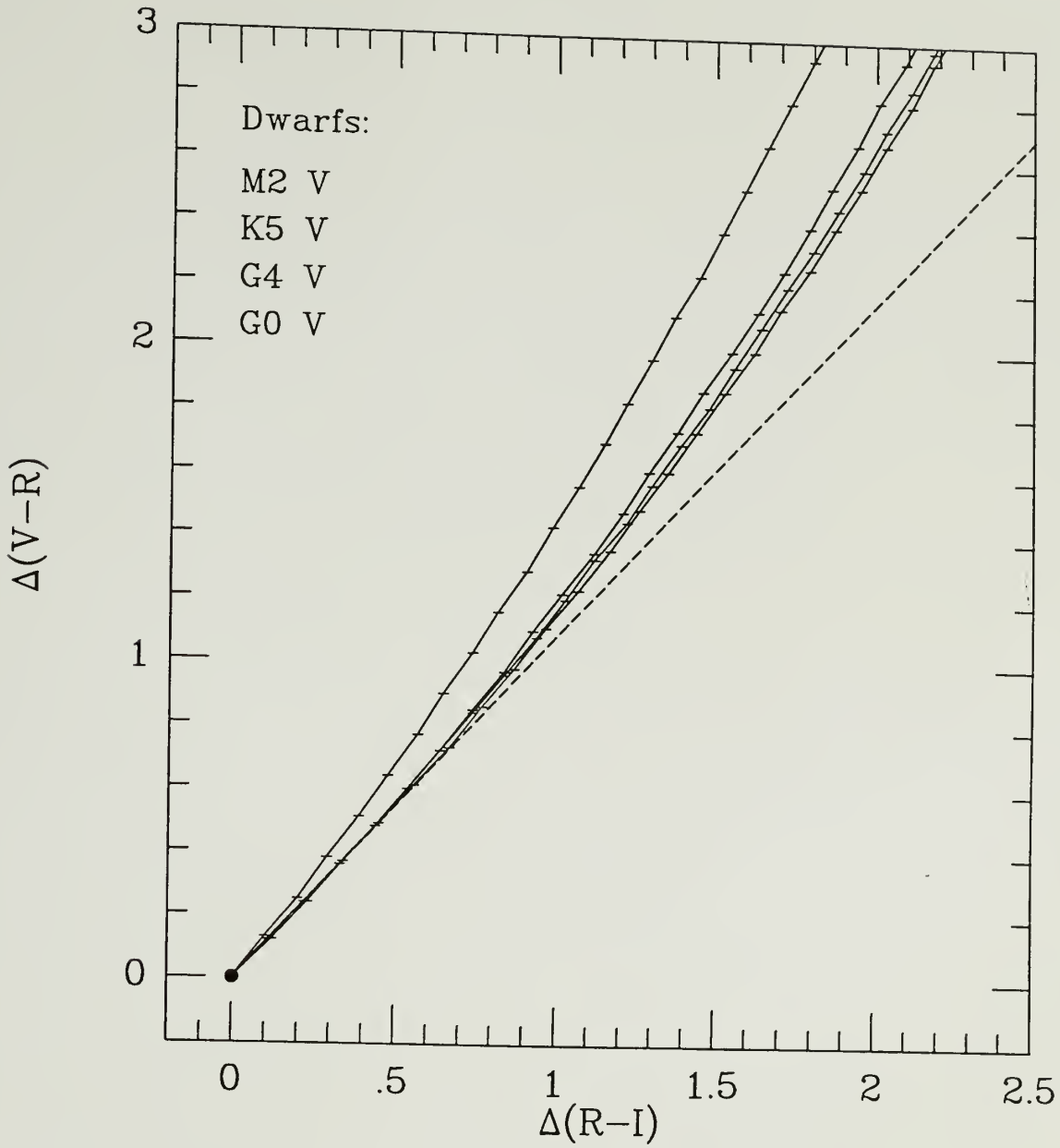

Figure C.2 Effects of interstellar reddening in the V, R, I color-color plane for main sequence stars of spectral type M2 V, K5 V, G4 V, and G0 V. The left most curve is that of the M2 V stars; likewise, the next curve represents the K5 V stars, and so on. The visual extinction is varied from 0 to 15 by 0.5 magnitude intervals (represented by horizonal tick marks). $A_V = 0$ at $\delta(V\text{-}R) = \delta(R\text{-}I) = 0$. Also shown, reddening vector of Schild (1977), slope 1.08, drawn with a dashed line.

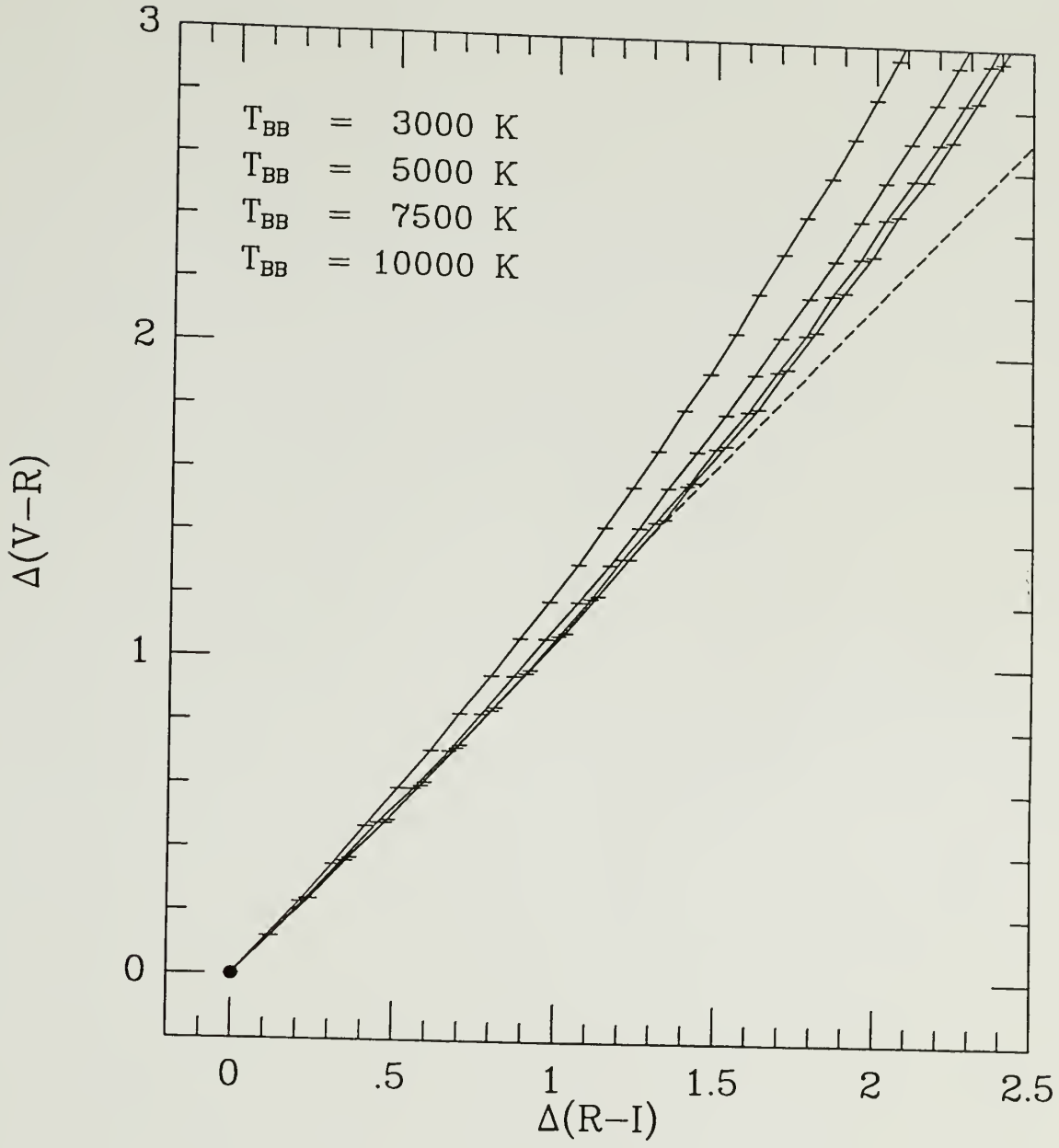

Figure C.3 Effects of interstellar reddening in the V, R, I color-color plane for blackbody functions with temperatures: 10000 K, 7500 K, 5000 K and 3000 K. The left most curve is that of the 10000 K blackbody; likewise, the next curve represents the 7500 K blackbody, and so on. The visual extinction is varied from 0 to 15 by 0.5 magnitude intervals (represented by horizonal tick marks). $A_V = 0$ at $\delta(V\text{-}R) = \delta(R\text{-}I) = 0$. Also shown, reddening vector of Schild (1977), slope 1.08, drawn with a dashed line.

APPENDIX D

DIFFERENTIAL PROPER MOTION

In this appendix we describe a technique to calculate the differential proper motions between two sets of stars taken at different epochs. Though the execution is challenging, the idea is quite simple: match a pair of photographic plates (or CCD images), each of the same field but obtained a number of years apart, by aligning the stars that have moved only minimally during the timespan between the two exposures, and thereby revealing stars which *do* have a relative shift in position in the plane of the photographs (*i.e.*, across the observer's line of sight). It is important to understand that differential proper motion, unlike absolute proper motion, simply refers to the *relative* change in tangential position between stars on plates taken at different epochs, as measured in some arbitrary coordinate system. This technique assumes two important conditions:

1. There are a sufficient number of reference stars — distant background stars with small relative proper motions — such that a reasonable match or fit between the two plates can be achieved to the order of the desired accuracy of the minimum measurable proper motions; and,

2. The pair of photographic plates or CCD images are compatible; *i.e.*, a numerical fit between the plates is possible.

The first condition depends both on the baseline (epoch difference) between the pair of plates or images, and the density of stars detected on the plates or images. A star's proper motion, or angular change in position over time, is a function of its tangential space

velocity and distance from the Earth. We may express a star's translational change in position, ΔR, thusly,

$$\Delta R \cong \sigma_t \Delta T \qquad \textbf{(D.1)}$$

where σ_t is the star's tangential velocity and ΔT is the baseline. The proper motion is customarily expressed in seconds of arc per year, and appropriately, a more handy form of Equation D.1 is:

$$\Delta\theta'' \cong \frac{0.211\ \sigma_t[km\,s^{-1}]\ \Delta T[yrs]}{D[pc]} \qquad \textbf{(D.2)}$$

where the angular change in position of a star located at distance D (pc) from the Sun is now in seconds of arc, the velocity is in units of km s^{-1}, and the epoch baseline is in years.

If we would like to measure relative stellar proper motions as small as 1″ $cent^{-1}$, then the reference stars used in the match or fit between the pair of plates must have proper motions smaller than this value. As an example, let us suppose that we are comparing photographic plates taken between 1950 and 1990, and that the mean tangential velocity dispersion for field stars is ~10 km s^{-1}. The resulting angular change in position over a 40 year baseline becomes

$$\Delta\theta'' \cong \frac{84.4}{d[pc]} \quad . \qquad \textbf{(D.3)}$$

Thus if we are to achieve an accuracy of ~1″ $cent^{-1}$, several reference stars in this example must lie at distances greater than 211 pc, which is a plausible scenario for most proper motion surveys.

The second condition stated above must be imposed because photographic plates or CCD images taken several years apart are probably also taken with different telescopes, focal ratios, fields of view, scales, etc. Photographic plates or CCD images are subject to

various kinds of distortions, depending on the factors mentioned here, and consequently starlight is not focused linearly onto the plate or image. Coma, for example, is a well-known type of distortion that appears at the edges of photographic plates taken with telescopes configured with "fast" focal ratios. Thus, when comparing a plate taken with a Schmidt camera and a CCD image taken with a telescope configured with a "slow" focal ratio, the relative scales and orientations will differ in some complicated non-linear fashion. It is thus necessary to fit a polynomial surface function to the reference stars of the field pair in order to adequately minimize the residual differences between the positions of the stars that have in reality moved very little over the time between the two successive exposures. The usual procedure is to apply a full quadratic or cubic polynomial. In the following section we discuss the procedure to map the coordinates of one plate into a second plate using a polynomial least squares fit.

D.1 Least Squares Fit of Multi-Parameter Functions

We begin by defining coordinate systems for each plate pair. Let the reference stars positioned on plate #1 be defined by rectangular coordinates (x,y), and the corresponding positions of the reference stars on plate #2 by rectangular coordinates (x′,y′). Our intention is to relate the two coordinate systems with the mapping

$$\begin{aligned} x &\mapsto x', y' \\ y &\mapsto x', y' \end{aligned} \tag{D.4}$$

An effective model that is frequently used for this mapping is the polynomial function

$$\begin{aligned} x &= a_1 + a_2 x' + a_3 y' + a_4 x' y' + a_5 x'^2 + a_6 y'^2 + \ldots \\ y &= b_1 + b_2 x' + b_3 y' + b_4 x' y' + b_5 x'_2 + b_6 y'^2 + \ldots \end{aligned} \tag{D.5}$$

where a_i and b_i are the coefficients to be solved for. Since we use as many reference stars

as possible to minimize the residuals in this mapping, we have, in fact, the problem of solving an overdetermined linear system of equations using the method of least squares. It is convenient to express the mapping of Equation D.5 with matrices. Let us consider the linear system of equations to be solved for the x coordinate mapping (the y coordinate follows in a similar fashion). Suppose we have N number of reference stars common to both plates that are to be used for the mapping, then the linear system of equations to be solved is the following:

$$\begin{bmatrix} 1 & x_1' & y_1' & x_1'y_1' & x_1'^2 & y_1'^2 & \dots & x_1'^M & y_1'^M \\ . & . & . & . & . & . & . & . & . \\ . & . & . & . & . & . & . & . & . \\ . & . & . & . & . & . & . & . & . \\ 1 & x_N' & y_N' & x_N'y_N' & x_N'^2 & y_N'^2 & \dots & x_N'^M & y_N'^M \end{bmatrix} \begin{bmatrix} a_1 \\ . \\ . \\ . \\ a_M \end{bmatrix} = \begin{bmatrix} x_1 \\ . \\ . \\ . \\ x_N \end{bmatrix} \qquad \textbf{(D.6)}$$

where the polynomials are of M^{th} order, and $M < N$. We can portray Equation D.6 more compactly by letting **M** represent the matrix of (x',y'), letting the array **a** represent the polynomial coefficients, and letting the array **x** represent the corresponding solutions. Then

$$\boldsymbol{M a} = \boldsymbol{x} \qquad \textbf{(D.7)}$$

The least squares method entails minimizing the residuals of Equations D.7, which, are given by vector

$$\boldsymbol{r} = \boldsymbol{x} - \boldsymbol{M a} \qquad \textbf{(D.8)}$$

More precisely, we aim to minimize the χ^2 of the residuals by differentiating the sum of the squares of the residuals with respect to the free parameters of Equation D.7, namely, the

polynomial coefficients. The χ^2 of the residuals can be written as

$$\begin{aligned} \chi^2 &= \boldsymbol{r}^T \boldsymbol{r} \\ &= (\boldsymbol{x} - \boldsymbol{M}\boldsymbol{a})^T (\boldsymbol{x} - \boldsymbol{M}\boldsymbol{a}) \\ &= \boldsymbol{x}^T\boldsymbol{x} - \boldsymbol{x}^T\boldsymbol{M}\boldsymbol{a} - \boldsymbol{a}^T\boldsymbol{M}^T\boldsymbol{x} + \boldsymbol{a}^T\boldsymbol{M}^T\boldsymbol{M}\boldsymbol{a} \end{aligned} \qquad \textbf{(D.9)}$$

and the differentiation of Equation D.9 follows

$$0 = \frac{d\chi^2}{d\boldsymbol{a}} = \boldsymbol{M}^T\boldsymbol{x} - \boldsymbol{M}^T\boldsymbol{M}\boldsymbol{a} \quad . \qquad \textbf{(D.10)}$$

Therefore, the least squares solution of the linear system of equations, Equation D.7, is

$$\boldsymbol{a} = (\boldsymbol{M}^T\boldsymbol{M})^{-1}\boldsymbol{M}^T\boldsymbol{x} \qquad \textbf{(D.11)}$$

and the corresponding solution for the y mapping is

$$\boldsymbol{b} = (\boldsymbol{M}^T\boldsymbol{M})^{-1}\boldsymbol{M}^T\boldsymbol{y} \qquad \textbf{(D.12)}$$

The use of quadratic or cubic polynomials in plate mappings is not without its perils. The positions of the reference stars comprising the linear system of equations, are implicitly assumed to be uniformly distributed on the photographic plates or CCD images. If, however, a majority of the reference stars are positioned in corners or in grouped clumps, then the least squares solutions of the polynomial mappings will reflect a bias toward the areas where the reference stars are clumped or primarily located. The unfortunate consequence of this condition is that areas of the plate/images where reference stars are sparsely distributed will then have large associated positional uncertainties. It is therefore important to attempt to use a set of reference stars that have a relatively uniform distribution over the fields to be matched.

APPENDIX E

A CASE STUDY OF IRS15A,B

In this appendix we attempt to decipher the nature of Wilking and Greene's infrared source IRS15a,b (optical counterpart, #42a,b, from this study), using optical and infrared photometric data. This object is in fact a double visual and infrared source, which is also associated with a 25μm IRAS point source, IRAS 16293-2424. Moreover, this source lies ~2′ south of point source IRAS 16293-2422, a source identified with an energetic high-velocity bipolar molecular outflow (Walker et al. 1986 and 1988; Mundy et al. 1986).

Bruce Wilking conducted additional photometric observations of IRS15a,b at J, H, K, L, M, N and Q wavelengths (1.25 to 22μm), using telescopes at the IRTF and CTIO during 1986 and 1989 (private communication). In Table E.1 the infrared data is reproduced for IRS15a and IRS15b.

Table E.1

Infrared Photometry of IRS15a,b (from Wilking, private communication)

Source	J (1.25μm)	H (1.6μm)	K (2.2μm)	L (3.4μm)	M (5μm)	N (10μm)	Q (22μm)
IRS15a	12.27	9.91	8.41	7.20	6.55	4.8	2.3
IRS15b	14.20	12.17	10.9	-	-	-	-

In Figure E.1 a halftone map of the 25μm IRAS emission of L1689 is shown. The IRAS sources, 16293-2424 and 16293-2422, are clearly delineated at this wavelength (the sources are marked by + symbols). In Figure E.2 a halftone map of the 100μm IRAS emission of the same region is shown. At 100μm, only the northern source, 16293-2422, is clearly present.

Combining the infrared data from Table 4.6 with the CCD data from the optical counterparts, #42a,b, in Table 4.2, we may construct the spectral energy distribution of IRS15. The conversion of stellar magnitude to flux was accomplished using the calibration method of Myers *et al.* (1987); namely, the flux of a star in janskys is given by

$$S_\nu = C_\nu 10^{-0.4 m_\lambda} \qquad \text{(E.1)}$$

where C_ν (Jy) is a constant depending on the wavelength m_λ, both found in Table 2 of Myers *et al.* (1987). The results of this analysis are shown in Figure E.3, where we have plotted the flux density λS_λ against λ for IRS15a,b. It can be seen that the energy distributions for both stars steeply rise from the optical wavelengths to the near-infrared wavelengths, peaking around K-band, 2.2μm. Even though the flux density is steeply rising toward the longer wavelengths, the V-R and R-I colors of the brighter companion are consistent with being an M7 or M8 V late-type star. Note, however, this implies that the fainter companion, assuming it is a binary companion, would have a spectral type later than M8, *i.e.*, a mass characteristic of brown dwarf objects. Fortunately, mid-infrared photometry can be used as a critical test of this hypothesis.

The flux density of IRS15a turns over beginning at ~2μm, only to rise (or at least remain flat) at the mid-infrared wavelengths (5 - 20 μm). This sort of infrared *excess* is a signature of either reradiated starlight or accretion from a circumstellar disk, a common spatial component of protostellar and T-Tauri systems (*cf.* Lada 1987; Kenyon and Hartmann 1987). Lada (1987) developed a scheme to classify energy distributions of stars

based on the severity of the infrared excess at the near to mid-infrared wavelengths. The spectral index (*i.e.*, slope) of the 2 - 20μm range of the energy distribution of IRS15a, shown in Figure E.3, places the star, according to Lada's criterion, in the class II group of lightly embedded protostars or T-Tauri stars. Presumably the 2μm emission is dominated by reddened photospheric starlight and the mid-infrared emission is dominated by reradiated starlight from hot dust grains in a circumstellar disk (the reader is referred to an excellent discussion of the photometric properties of protostars in Wilking, Lada and Young, 1989). It is not clear whether the faint companion to IRS15a is a protostar since there is no mid-infrared photometry available for this star. Nevertheless, its close proximity to IRS15a (~9″, or ~1500 a.u.) and its sharply rising flux density, similar to IRS15a, strongly implies that this star is associated with the group of newly forming stars around the bipolar molecular outflow source, IRAS 1629a.

In summary, the apparent nature of IRS15a,b is its association with recent star formation in the L1689 filament of ρ Ophiuchi.

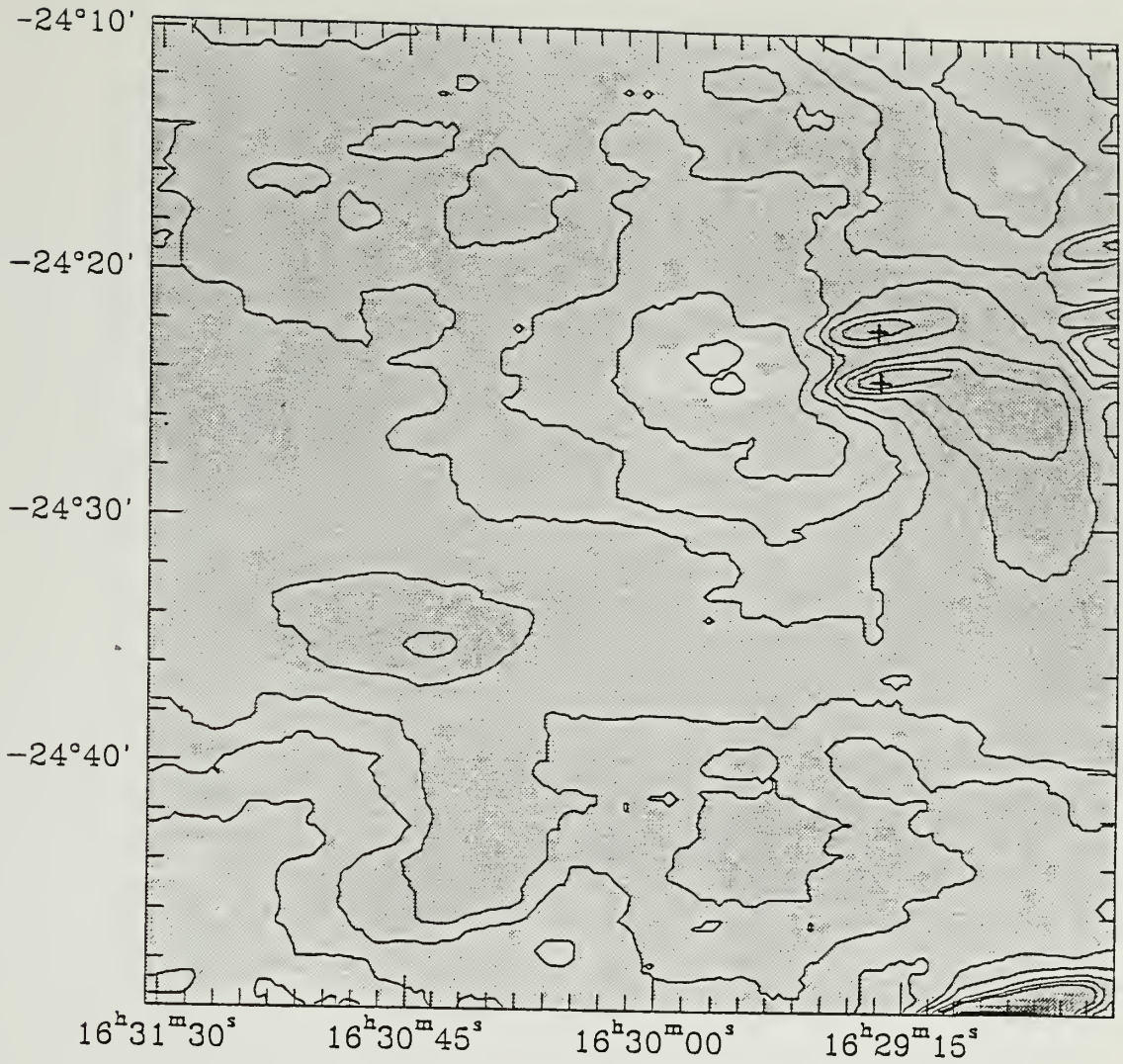

Figure E.1 Co-added IRAS 25μm intensity image of a 40′ × 40′ field centered at (16^h 30^s, -24° 30′). Contour levels in units of the median noise, are as follows: ($\langle n \rangle = 1.1 \times 10^4$ Jy sr^{-1}); 5, 10, 15, 20, 30, 40, 50. The + symbols mark the locations of IRAS point sources 16293-2424 and 16293-2422.

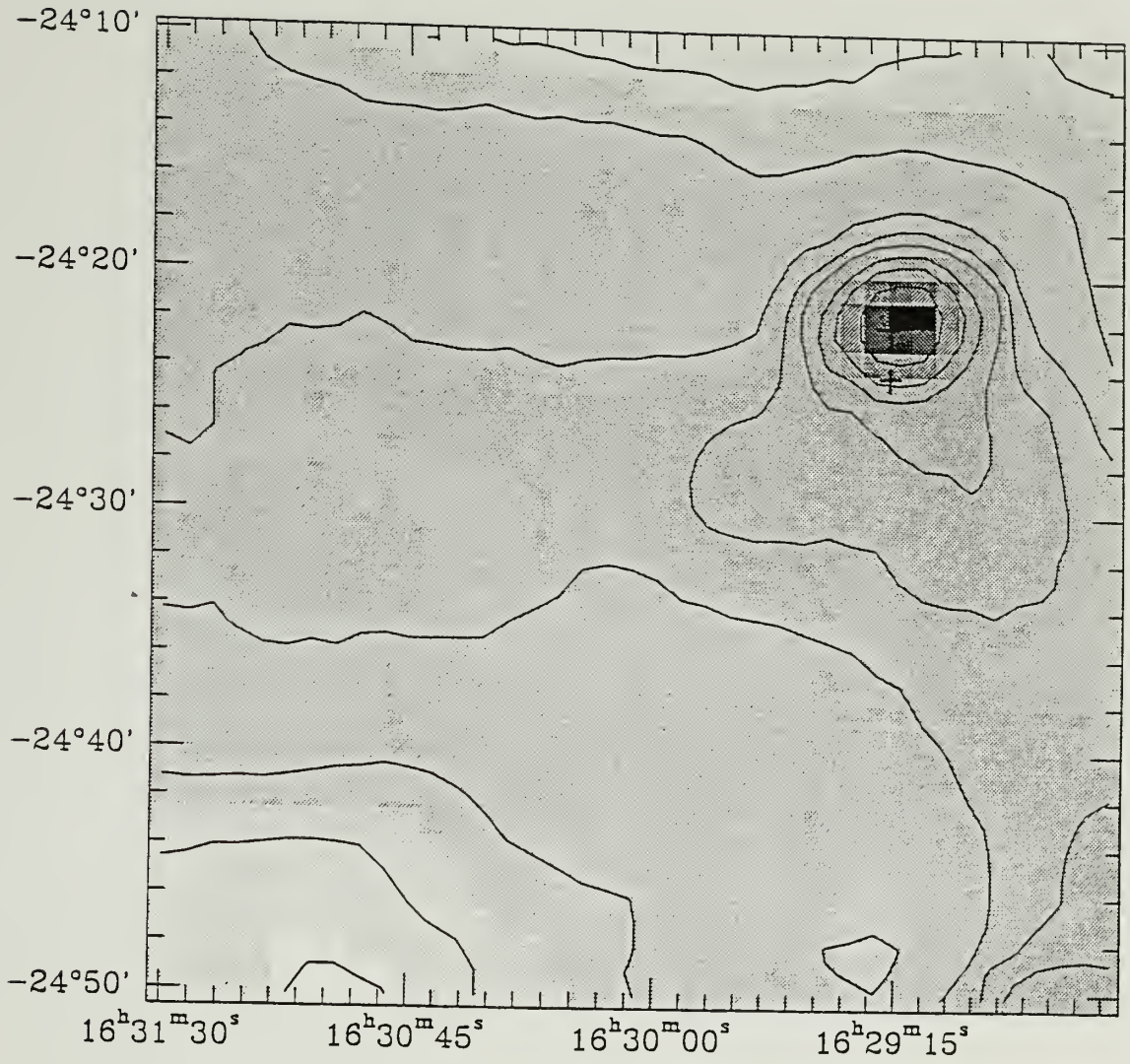

Figure E.2 Co-added 100μm IRAS intensity image of a 40′ × 40′ field centered at (16^h 30^s, -24° 30′). Contour levels in units of the median noise, are ($\langle n \rangle = 1.50 \times 10^6$ Jy sr^{-1}); 1, 10, 25, 50, 75, 100, 150, 200, 300, 400. The + symbols mark the locations of IRAS point sources 16293-2424 and 16293-2422. The image is taken from Jarrett, Dickman and Herbst (1989).

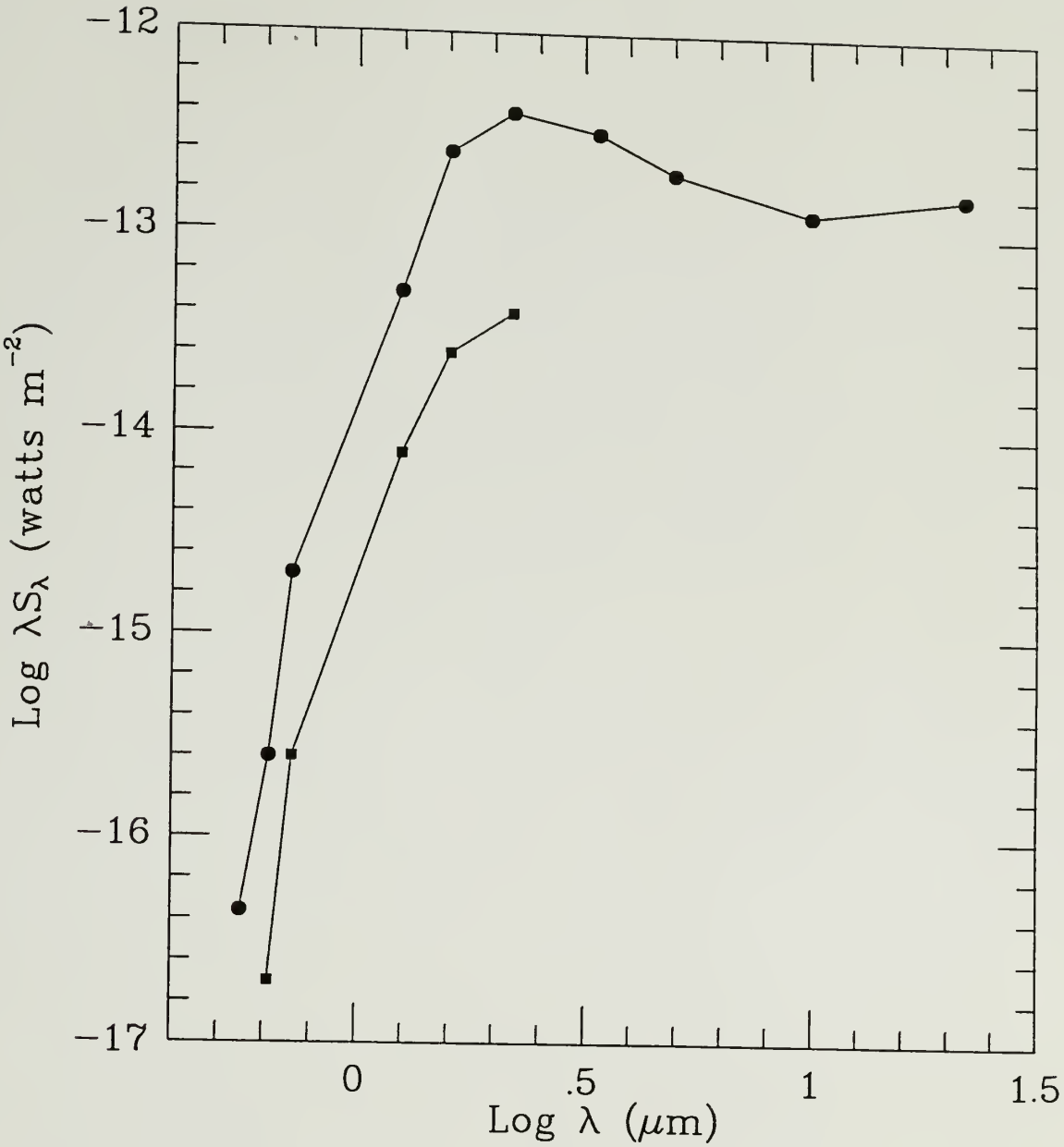

Figure E.3 Optical and infrared spectral energy distribution of IRS15a,b (#42a,b). The flux density is plotted as λS_λ (watts m^{-2}). The source IRS15a is represented by filled circles, and IRS15b by filled squares. The infrared data is from B. Wilking (private communication).

APPENDIX F

SPATIAL DISTRIBUTION MODELS OF THE GALAXY

In this appendix a description of contemporary models simulating the spatial distribution of stars in the Galaxy is presented, including a version of the "standard" model used in this thesis. Our model (and those like it) attempt to predict the stellar surface density in a given direction from the Sun. Specifically, the model predicts the total number of stars per square degree, brighter than apparent magnitude m_λ in a direction whose Galactic coordinates are (ℓ,b). This quantity is usually designated $N(m_\lambda,\ell,b)$. The stellar surface density is determined by the spatial contributions from the Galactic disk and spheroid populations. Accordingly,

$$N(m_\lambda,\ell,b) = N_{disk}(m_\lambda,\ell,b) + N_{sph}(m_\lambda,\ell,b) \ .$$

In addition to disk and spheroid stars, some models include components due to a faint halo population and a "thick" disk population.

Numerical distribution models have been developed by Elias (1978) and Bahcall and Soneira (1980; henceforth B&S) assuming a purely exponential density of stars in the disk (Elias applied this model to near-infrared wavelengths) and in the spheroid (B&S added this component to their optical model). Later Jones *et al.* (1981) and Garwood and Jones (1987) modified the Elias (1978) model to include a spheroidal component, so that their infrared simulation resembled the B&S model.

This appendix is organized as follows. In the first section, a review of the Galactic stellar distribution, including the disk and spheroid populations, is given. A brief

discussion of the controversial thick disk model is also included. In section F.2, we discuss the effects of interstellar extinction and its application within the standard model. A detailed discussion of the model and numerical algorithm used in this thesis is presented in section F.3. In the last section, we validate the stellar distribution model by comparing the results of the model, applied toward several diverse directions, with observed data and the B&S model.

F.1 The Stellar Distributions

Seen from the vantage point of the Sun, our home Galaxy is clearly a flattened structure, with the Solar system situated within a disk of stars, and well offset from the center of this spiral "wheel". It is more difficult to view stars above or below the Galactic disk (globular clusters are a notable exception) especially toward the Galactic center, so we must look to nearby galaxies in order to infer the distributions of other spatial components that may be important in building a model of our galaxy. De Vaucouleurs (1958; 1959; 1977) reported a spheroidal population of stars in spiral galaxies; these stars have a distribution not unlike that of elliptical galaxies that is well-approximated by a flattened exponential. This component is further divided into an inner "bulge", which can also be seen in the Milky Way at far-infrared wavelengths (*cf.* Habing *et al.* 1985), extending ~3 kpc from the Galactic center. A third component, the so-called "halo", has been proposed as a solution to the non-Keplerian, flat rotation curves observed in our Galaxy and in other spiral galaxies (*cf.* Bahcall 1984 for a discussion on the mass to light deficit). However, while halo stars are critical to dynamical models, their intrinsic faintness moderates their overall importance as a spatial component; thus, they are usually omitted from distribution models. We are left with a two component model of the Galaxy, containing an exponential disk and spheroid.

F.1.1 The Galactic Disk Contribution

The disk population is composed of a mixed ensemble of main sequence stars and evolved stars of varying mass and age. Each spectral type belonging to the dwarf and giant populations[1] can be characterized by a scale height, which is basically an indicator of age. The older the star, the more dynamical interactions it has suffered with other stars and giant molecular clouds (Spitzer and Schwarzschild 1951). The result is an increase in the spatial velocity of older stars (particularly along the vertical axis of the disk).

At fixed Galacticentric distance, the number density of stars of spectral type s along the vertical or z direction can be written as

$$\rho_{\perp}(z,s) \propto \exp\left[-\frac{z}{\beta(s)}\right] \qquad \textbf{(F.1)}$$

where the scale height, β, is a function of spectral type. For example, M dwarfs have relatively large scale heights, $\beta \sim 300$ pc, in contrast to the younger A-type stars with $\beta \sim 100$ pc (Faber *et al.* 1976). Giants and subgiants have scale-heights typically between 200 and 500 pc, though their uncertainty is greater than that of the dwarf luminosity class (*cf.* B&S).

Within the plane of the disk, B&S express the radial density function similarly,

$$\rho_{\parallel}(x) \propto \exp\left[-\frac{(x-R_0)}{\alpha}\right] \qquad \textbf{(F.2)}$$

where x is the distance from the Galactic center (in the plane of the disk), R_0 is the Solar distance from the center, and α is the Galactic disk scale length. The latter parameter varies as a function of galactic morphological type (Freeman 1970). For the Milky Way,

---

[1] To simplify the numerical model, distinctions between the differing luminosity classes are not made. Instead, we designate generic dwarf and giant populations. This assumption is adequate, since the total number density of stars in the Galaxy is dominated by luminosity classes V (dwarfs) and III (giants).

published values of α range from 2.5 to 3.5 kpc (De Vaucouleurs and Pence 1978; Knapp *et al.* 1978; McCuskey 1969). B&S adopt a mean value of 3.5 kpc (with R_0 = 8 kpc), whereas Jones *et al.* (1981) treat the scale length as a free parameter ranging from 2.2 to 3 kpc (where R_0 = 8.7 kpc).

Combining the two density functions we arrive at the disk spatial density function

$$\rho(x,z,s) \propto \exp\left[-\frac{(x-R_0)}{\alpha} - \frac{z}{\beta(s)}\right] \qquad \textbf{(F.3)}$$

To transform Equation F.3 into a distribution formula per spectral type, one must normalize using the appropriate luminosity functions. The luminosity function per spectral type can be modelled as a gaussian, where each spectral type has an intrinsic uncertainty in its luminosity or absolute magnitude due to calibration assumptions (*i.e.*, discretely grouping stars together) and systematic errors within the calibration (*cf.* Mihalas and Binney 1981):

$$\Phi(M,s) = \frac{\Phi_0(s)}{\sqrt{2\pi\sigma(s)^2}} \exp\left[\frac{|M - M_0(s)|^2}{2\sigma(s)^2}\right] \qquad \textbf{(F.4)}$$

where M_0 is the mean absolute magnitude per spectral type, σ is the intrinsic dispersion and Φ_0 is the luminosity function in the Solar vicinity (*i.e.*, the local number density per spectral type). Now we may write the disk distribution function in complete form:

$$\rho(x,z,M,s) = \frac{\Phi_0(s)}{\sqrt{2\pi\sigma(s)^2}} \exp\left[\frac{|M - M_0(s)|^2}{2\sigma(s)^2}\right] \exp\left[\frac{-(x - R_0)}{\alpha} - \frac{z}{\beta(s)}\right] \qquad \textbf{(F.5)}$$

F.1.2 The Spheroid Contribution

Following the example of de Vaucouleurs (1959), B&S characterized the spatial distribution of spheroidal stars in the Galaxy with a $r^{1/4}$ exponential measured radially from the Galactic center, as follows:

$$\rho(r) \propto \left(\frac{r}{r_e}\right)^{-\frac{7}{8}} \exp\left[-7.669\left(\frac{r}{r_e}\right)^{\frac{1}{4}}\right] \qquad \text{(F.6)}$$

where r_e is analogous to a scale length, approximately equal to R_0 / 3 (de Vaucouleurs and Buta 1978). A virtue of this density formula is that it assumes spherical symmetry, while other models involve a more complex oblate symmetry (*cf.* King 1966). In a later paper, Bahcall and Soneira (1984) turn to an oblate distribution with an axis ratio of 0.8, to better fit the observational data.

It is by no means an easy task to determine the local luminosity function for spheroidal stars owing to the Sun's relative position with respect to the spheroid, and the rarity of these stars compared to the disk population. Stars in globular clusters are often used to compare with (or add to) those of the field spheroid ensemble[2]. Schmidt (1975) was able to isolate a sample of sub-dwarf stars, presumably belonging to the spheroid population, because of their remarkable space velocities (100 to 250 km s^{-1}). Although the statistics are poor, Schmidt computed the resultant luminosity function and found that the general shape of the luminosity function belonging to the high proper motion stars resembles that of the disk. The overall number density is, however, about 3 orders of magnitude smaller. Combining the data of Schmidt (1975) and Wielen (1974) with the star

---

[2] Although globular clusters are located within the realm of the spheroid, they are usually treated as separate entities. However, Bahcall and Soneira (1984) conclude that the luminosity functions of globular clusters and spheroid stars are the same within the accuracy of the data (the exception being a depression "feature" between $2 < M_v < 4$ in the globular cluster luminosity function).

count data of Bahcall and Soneira (1980), the spheroidal luminosity function is best described using the shape of the disk luminosity function, normalized with a value between 500^{-1} to 800^{-1} (Bahcall, Schmidt and Soneira 1983), where the larger value corresponds to a spheroid with oblate symmetry. Further tuning the spheroid density function in the vicinity of the Galactic center, Bahcall and Soneira (1984) express the density function in complete form:

$$\rho(r) = 800^{-1} \left(\frac{r}{R_0}\right)^{-\frac{7}{8}} \exp\left[-10.093\left(\frac{r}{R_0}\right)^{\frac{1}{4}} + 10.093\right] \times \left[1 - 0.0867\,(r/R_0)^{-\frac{1}{4}}\right], \quad r \geq 0.03R_0 \tag{F.7}$$

F.1.3 A Thick Disk?

It should be noted there is a fair amount of controversy as to the overall nature of the spheroid population. Gilmore and Reid (1983) claim that many high proper motion stars are in fact a tracer of a *thick* disk component. They point out that if one increases the disk scale heights ($\beta \sim 1500$ pc), the resultant distribution matches that of the subdwarf stars. Their stellar surface density simulations include the disk and spheroid populations, as well as a third, "intermediate" population which contains metal-poor subdwarf stars with a z-distribution characteristic of a thick disk (Reid 1983). However, Bahcall and Soneira (1983; 1984) maintain that Gilmore and Reid did not include evolved spheroid stars in their simulation, consequently arriving at a false conclusion. These giant stars are very bright and very far away from the Sun. If one mistakenly identifies them as dwarfs, their intrinsic brightness is vastly changed, the result being that their placement is ~1000 pc off the disk — mimicking a thick disk — as opposed to ~10 kpc where the giants would lie.

Gilmore and Reid question the overall abundance of evolved spheroid giants, suggesting that selection effects[3] may be deceiving their true numbers. Nonetheless, Bahcall and Soneira (1984) are confident the observational evidence for these subgiants is firm (*cf.* Ratnatunga 1982). The fact remains that the B&S model adequately simulates the observed Galactic distribution in several diverse directions (as is shown in section F.4), proving the robust nature of the two-component model. The existence of a thick disk shall probably remain in the sphere of debate for some time. The reader is referred to a spirited discussion between the two camps in a talk by Bahcall and Soneira (1983), and to the comprehensive review by Gilmore, Wyse, and Kuijken (1989) in which they build a strong case — based on the most recent observational evidence — for the existence of a thick disk.

F.2 Interstellar Extinction

A final ingredient to consider in modelling surface density is interstellar extinction. Starlight is absorbed by grains of dust and light at shorter wavelengths is preferentially blocked, resulting in a selective reddening of the starlight (for more details, see Appendix C). The spatial distribution of dust is usually modeled similarly to that of the young disk population, namely, an exponential with a scale height severely restricted to the plane of the disk (~100 pc; Spitzer 1978). Jones *et al.* (1981) expanded this relation to include an

[3] Given a small viewing cone/beam, the sample of stars within the beam will be biased toward very distant stars (thus, luminous giants) because of the solid-angle effect; recall the volume of a cone is proportional to the distance cubed.

absorption scale length in the disk, α_a, which they determine to be ~ 4 kpc. The equation in differential form follows:

$$\delta A_V(x,z,R) \propto \exp\left[-\frac{(x-R_0)}{\alpha_a} - \frac{z}{\beta_a}\right]\delta R \qquad \textbf{(F.8)}$$

where R is the distance from the Sun. The normalization constant is the local absorption in magnitudes per kpc. The canonical value is typically quoted between 1 and 2 mag kpc^{-1} at visual wavelengths (*cf.* Elias 1978). The absorption function described above does not take into account dense clumps arising from molecular clouds and giant molecular clouds in the disk. This omission may become a problem when modelling the stellar distribution at low galactic latitudes ($b < 10°$).

F.3 Model Developed in this Work

In the following discussion, a version of the model described above used in this dissertation is outlined. Numerical simulations are carried out to validate the model with the results of B&S and real data. The results are described in the section that follows.

Begin by transforming the number density equations into a frame centered about the Sun. Recall that the variable x is measured from the Galactic center in the plane of the disk, and that R is measured from the Sun to the source (or viewing direction); they are related using galactic coordinates, ℓ and b, as follows:

$$x^2(R) = R_0^2 + R^2\cos^2 b - 2RR_0\cos b\cos l \qquad \textbf{(F.9)}$$

and z, measured perpendicular to the disk, is related to R,

$$z(R) = R\sin b \qquad \textbf{(F.10)}$$

The variable r, measured radially from the Galactic center to the source is

$$r^2(R) = x^2(R) + z^2(R) \qquad \textbf{(F.11)}$$

Finally a viewing cone of angular radius θ, extending distance R has volume

$$Vol(R,\theta) = \frac{2\pi}{3} (1 - \cos\theta) R^3 \qquad \textbf{(F.12)}$$

B&S define the luminosity, scale height and local density parameters for each spectral type in analytic form as a matter of numerical convenience. In this study, a discrete format using the values in Elias (1978), Jones *et al.* (1981) and Garwood and Jones (1987) is applied. This allows for more flexibility in modifying or adding new spectral types to the sample. For example, the Wielen luminosity function is added to account for the late M-dwarfs ($M_v > 13$ mag); also included is a Hawkins and Bessell (1988) upturn in the luminosity function at the very faint end ($M_v > 16$), which can be compared with the nominal values given by Wielen. The models developed by Elias, Jones *et al.*, and Garwood and Jones are specifically applied to K-band (2.2 μm) data. Therefore the magnitude and number density values that are adopted here will be different because the spatial distribution model was developed for the visual and red wavebands. The transformation involves color corrections (*i.e.*, V - K) and interpolation of the luminosity function. In the case of evolved stars, the V-band luminosity function given in Mamon and Soneira (1982) is used. The scale height and absolute magnitude dispersion values given by Garwood and Jones remain the same. Table F.1 lists the spectral type, brightness, colors, local number density, dispersion and scale height. The optical colors are in the Kron-Cousin system (from Bessell 1990), and the infrared colors are from Koornneef (1983). The spheroid population has the same parameters except their number density decreases by a factor of 800, and owing to their intrinsic metal poor composition, their

colors tend to be blue with respect to main sequence dwarfs, as follows (from Mamon and Soneira 1982):

$$\delta(B\text{-}V) \approx 0.15,\ \delta(V\text{-}R) \approx 0.15,\ \delta(V\text{-}I) \approx 0.25,\ \delta(R\text{-}I) \approx 0.1,\ \delta(V\text{-}K) \approx 0.4$$

The spatial distribution model embodies a numerical algorithm that follows 4 basic steps: 1) integrate the surface density functions for each spectral type over a differential volume defined by stepping an incremental distance through the viewing cone (that is, a volume bounded by a specified field of view, whose direction is given by the Galactic coordinates), 2) assign the appropriate mean absolute magnitude and its dispersion to the stars given by step 1, 3) compute the total interstellar absorption within the volume by integrating the extinction surface density function, and 4) calculate the apparent brightness, $5\log d - 5 + A_\lambda + M_\lambda$, for each star given by step 1. It is then a simple matter to derive colors and construct cumulative star counts curves (see section F.5).

Consider the disk population. Integrate the density function, Equation F.5, out to some distance d:

$$N_T(d,s) = 2\pi(1 - \cos\theta)\,\frac{\Phi_0(s)}{\sqrt{2\pi\sigma(s)^2}} \int_{-\infty}^{\infty} dM\, \exp\left[\frac{|M - M_0(s)|^2}{2\sigma(s)^2}\right] \times \int_0^d dR\, R^2 \exp\left[\frac{-(x(R) - R_0)}{\alpha} - \frac{z(R)}{\beta(s)}\right] \qquad \text{(F.13)}$$

where N_T is the total number of stars of spectral type s contained in the cone volume extending distance d. We do not need to waste computer time integrating the luminosity function, Equation F.4, over magnitudes ranging from $-\infty$ to ∞. Instead, we solve for absolute magnitude based on the gaussian luminosity distribution, characterized by the mean absolute magnitude and the intrinsic magnitude dispersion, via a Monte Carlo

Table F.1

Spectral-Type Parameters

Spectral Type	M_v	B-V	V-R	R-I	V-R	log Φ_0 kpc^{-3}	σ	β kpc
B1	-3.9	-0.28	-0.11	-0.19	-0.76	2.78	0.5	0.04
B3	-1.9	-0.20	-0.08	-0.13	-0.57	3.52	0.5	0.04
B5	-0.9	-0.10	-0.05	-0.05	-0.43	4.18	0.5	0.04
A0	0.3	0.00	-0.01	-0.02	0.00	4.73	0.5	0.07
A3	1.0	0.30	0.11	0.15	0.20	6.24	0.5	0.07
F5	2.9	0.33	0.27	0.20	1.01	6.10	0.5	0.14
F8	3.5	0.54	0.32	0.28	1.12	6.24	0.5	0.14
G0	4.0	0.60	0.35	0.30	1.22	6.39	0.5	0.22
G3	5.1	0.66	0.37	0.33	1.49	6.52	0.4	0.22
G8	5.6	0.76	0.39	0.37	1.60	6.60	0.4	0.28
A0	6.0	0.80	0.45	0.40	1.75	6.64	0.5	0.30
K3	6.6	0.83	0.47	0.42	2.50	6.72	0.5	0.35
K5	7.6	1.16	0.76	0.57	3.00	6.79	0.5	0.30
M0	8.8	1.41	0.91	0.89	3.25	6.89	0.5	0.30
M4	9.46	1.48	0.94	1.02	3.50	6.87	0.5	0.30
M2	10.14	1.52	0.98	1.16	3.75	6.89	0.5	0.30
M3	11.17	1.55	1.16	1.37	4.00	6.93	0.5	0.35
M4	12.76	1.60	1.23	1.63	4.25	7.17	0.5	0.35
M5	14.70	1.82	1.5	1.9	4.50	7.25	1.0	0.30
M6	17.30	2.00	2.0	2.3	4.25	6.92	1.0	0.40
M7	18.70	2.20	2.1	2.4	5.00	6.92	1.0	0.30
M8	19	?	?	?	5.25	7.04	1.0	0.40
gG0	3.1	0.46	0.46	0.41	2.05	5.11	1.0	0.50
gG5	2.0	0.92	0.49	0.44	2.12	5.31	1.0	0.30
gG8	1.6	0.95	0.49	0.44	2.16	5.19	1.0	0.25
gK1	0.9	1.16	0.57	0.57	2.48	5.08	0.7	0.20
gK3	0.5	1.29	0.49	0.72	2.92	4.85	0.6	0.25
gK5	0.3	1.56	0.84	0.80	3.67	4.70	0.6	0.25
gM0	-0.5	1.56	0.89	0.88	3.74	4.40	0.6	0.25
gM1	-0.9	1.56	0.41	0.92	3.90	4.22	0.6	0.25
gM2	-1.5	1.60	0.95	1.00	4.16	3.90	0.6	0.25
gM3	-2.1	1.62	0.99	1.10	4.63	3.70	0.6	0.25
gM4	-2.5	1.66	1.05	1.20	5.34	3.40	0.6	0.25

technique. For a gaussian function,

$$\Delta M(s) = \sigma(s)\sqrt{2\ln\left(\frac{1}{RN1}\right)}\cos(2\pi RN2)$$
$$M_V(s) = M_0(s) - \Delta M(s) \qquad \textbf{(F.14)}$$

where RN1 and RN2 are random numbers between 0 and 1. The constants used in the optical model are indicated in Table F.2.

Table F.2

Model Parameters

Galactic Center	R_0	8 kpc
disk scale length	α	3.5 kpc
spheroid scale length	r_e	3 kpc
local absorption	$A_v(0)$	2 mag kpc^{-1}
absorption scale height	β_a	0.1 kpc
absorption scale length	α_a	4 kpc

Next integrate the density function out to a distance d + δd. The difference in total number is

$$\Delta N(d^*) = N_T(d+\delta d) - N_T(d) \qquad \textbf{(F.15)}$$

We now integrate the interstellar absorption function, Equation F.8, out to distance d*:

$$A_V(d^*) = A_V(0)\int_0^{d^*} dR\ \exp\left[-\frac{(x(R) - R_0)}{\alpha_a} - \frac{z(R)}{\beta_a}\right] \qquad \textbf{(F.16)}$$

The apparent magnitude is given by the distance modulus,

$$\begin{aligned} m_V(s) &= M_V(s) + 10 + 5\log(d^*) + A_V(d^*) \\ m_R(s) &= M_v(s) - (V-R) + 10 + 5\log(d^*) + A_R(d^*) \\ m_I(s) &= M_v(s) - (V-I) + 10 + 5\log(d^*) + A_I(d^*) \end{aligned} \qquad \textbf{(F.17)}$$

where d^* is measured in kpc, A_R and A_I are derived using reddening curves and the ratio of total to selective extinction (see Appendix C, Interstellar Reddening). The apparent (reddened) colors are calculated using the above magnitudes. In addition, we may apply a random error to the colors, which will mimic uncertainties due to signal to noise, poor seeing conditions and calibration to standard colors. For example, suppose the random errors for V, R and I are determined to be σ_v, σ_R and σ_I. The color dispersions are then

$$\begin{aligned} \sigma^2_{(V-R)} &= \sigma^2_V + \sigma^2_R \\ \sigma^2_{(R-I)} &= \sigma^2_R + \sigma^2_I \end{aligned} \qquad \textbf{(F.18)}$$

and the color errors are computed, as before, using a gaussian Monte-Carlo technique:

$$\begin{aligned} \Delta(V-R) &= \sigma_{(V-R)}\sqrt{2\ln\left(\frac{1}{RN1}\right)}\cos(2\pi\, RN2) \\ \Delta(R-I) &= \sigma_{(R-I)}\sqrt{2\ln\left(\frac{1}{RN3}\right)}\cos(2\pi\, RN4) \end{aligned} \qquad \textbf{(F.19)}$$

where RN1, RN2, RN3 and RN4 are random numbers between 0 and 1.

The simulation using a spheroid component follows the same procedure. Integrate the density function, Equation F.7, out to some distance d:

$$N_T(d) = 800^{-1} \frac{2\pi(1 - \cos\theta)}{\sqrt{2\pi\sigma^2(s)}} \int_{-\infty}^{\infty} dM \exp\left[-\frac{|M - M_0(s)|^2}{2\sigma^2(s)}\right]$$

$$\times \int_0^d dR\, R^2 \left(\frac{r(R)}{R_0}\right)^{-\frac{7}{8}} \exp\left[-10.093\left(\frac{r(R)}{R_0}\right)^{\frac{1}{4}} + 10.093\right] \qquad \text{(F.20)}$$

$$\times \left[1 - 0.0867\left(\frac{r(R)}{R_0}\right)^{-\frac{1}{4}}\right], \qquad r \geq 0.03R_0$$

and integrate out to distance d + δd. Compute the number difference, apply an extinction and color correction. It should be noted that the volumes are integrated out to some maximum distance depending on the direction the model is attempting to simulate. Bahcall, Schmidt and Soneira (1983) tabulate R_{max} as a function of galactic coordinates (see Table 1 in their paper). This value is constrained by the requirement to clearly separate the two major stellar components, the disk and spheroid; the range is approximately given as

$$4 \leq r(R) \leq 12 \text{ kpc}$$

For the disk, the maximum distance to which the surface density function is integrated depends on the Galactic coordinates and geometry of the disk. Here we are assuming a perfectly flat, circular disk of thickness $2z_H$, and diameter 2X. The Milky Way Galaxy appears to have a total diameter of about 25 kpc (*cf.* Bok 1979) and, based on

stellar spatial scale heights, a thickness of about 2 kpc or so. The maximum distance, d_{max}, is given within the geometric relation,

$$0 = X^2 - R_0^2 - [d_{max}\cos b]^2 + 2R_0 d_{max}\cos b\cos l$$
$$z_{max} = d_{max}\sin b \qquad \text{(F.21)}$$

unless z_{max} is greater than z_H, in which case the maximum distance is given by

$$d_{max} = \frac{z_H}{\sin b} \qquad \text{(F.22)}$$

F.4 Validating the Model

In this section, a brief description of numerical tests conducted by Bahcall and Soneira (1984) in five different fields is presented. Simulations are performed using the model described in the last section for these five fields, comparing these results with those of Bahcall and Soneira, and real data. The fields lie in the directions: 1) north Galactic pole (NGP); 2) SA 57: ℓ = 65°, b = 86°; 3) SA 68: b = -46°, ℓ = 111°; 4) Aquarius: b = -57°, ℓ = 36°; and 5) SA 51: b = +21°, Galactic anticenter. The fields were chosen by Bahcall and Soneira to minimize confusion and interstellar extinction (*i.e.*, by avoiding locations anywhere near the plane of the Galaxy), as well as to test the degree of oblateness in the spheroid.

Both SA 57 and the NGP offer an excellent test of the spheroid parameters because disk stars are considerably less numerous well off the plane, whereas spheroid stars can be seen several kpc from the Sun. Bahcall and Soneira were able to fit their simulated differential starcounts to the data with better than 20% accuracy. They found that spheroid stars begin to dominate the total number observed at visual magnitudes fainter than ~17. Disk giants diminish rapidly beyond V ~ 12, and disk dwarfs vanish at V ~ 25. In Figures F.1a and F.1b plots of the differential starcounts using the model described in section F.3 is

shown for these two regions. The total contribution is drawn with a solid line, disk dwarfs are shown with a short dashed line, disk giants with a dotted line, and the total contribution due to the spheroid population is drawn with long dashed line. Real data is represented by filled circles. In Figure F.1a it is apparent that the predicted starcounts fit the data by Reid and Gilmore (1983) with an accuracy ~10% for visual magnitudes fainter than 10. At the bright end the fit begins to deviate substantially, due in part to Poisson statistics. This effect can be seen in Figure F.1b as well, where the predicted counts do not follow a smooth line or the data of Weistrop (1972). Overall the fit in Figure F.1b is good to ~20%, where some deviation settles in at V > 16 mag. As in the case with the B&S model fits, it can be seen that the spheroid stars begin to dominate the total numbers beginning at V ~ 17. The dominant spectral component in the spheroid population are distant K giants.

As we move down in galactic latitude, the importance of spheroid stars lessens relative to disk dwarfs. This effect can be seen in Figures F.2a (SA 68) and F.2b (Aquarius). The main difference between the two plots is that the direction of Aquarius lies substantially closer than SA 68 to the Galactic center; consequently, more spheroid stars are seen (*cf.* the "bulge" sub-component of the spheroid). In the case of SA 68, the model fits the data (taken from Bahcall and Soneira 1984) to an accuracy of 10 - 25%, which is about the accuracy of the photometry itself. The predicted counts for Aquarius have an even better fit, ~10%, with only two data points deviating by about 20% (Tritton and Morton, 1983, taken from Bahcall and Soneira 1984). Likewise, B&S were also able to fit the predicted starcounts to the data with accuracies better than 20%.

Finally, consider the case of SA 51. In Figure F.3, a plot of the predicted differential starcounts versus observed data (by King, taken from Bahcall and Soneira 1984) is shown. Notice that at low galactic latitudes the total number density increases, while the contributions due to disk giants and spheroid stars substantially decreases. The fit is

accurate to ~20% between $12 < V < 21$, with greater deviation occurring at the bright end, (again, due to statistics) and the faint end, where only ~30% accuracy is achieved. The model fits by B&S do a little better at the faint end, with 20% accuracy.

It has been shown that both the B&S and spatial distribution models of this dissertation adequately fit, to the accuracy of the observational data, starcounts in five different Galactic fields. The fact that these fields are located toward diverse galactic latitudes and longitudes attests to the robustness of the models. The models can thus be applied, with a satisfactory degree of confidence, toward fields lying between $30° < \ell < 330°$ and $b > 20°$. Beyond these limits there is uncertainty, since no tests were performed by Bahcall and Soneira; however, given the apparently robust character of the models, extension to latitudes ~ 10° and $\ell \sim 10°$ should not present a significant problem.

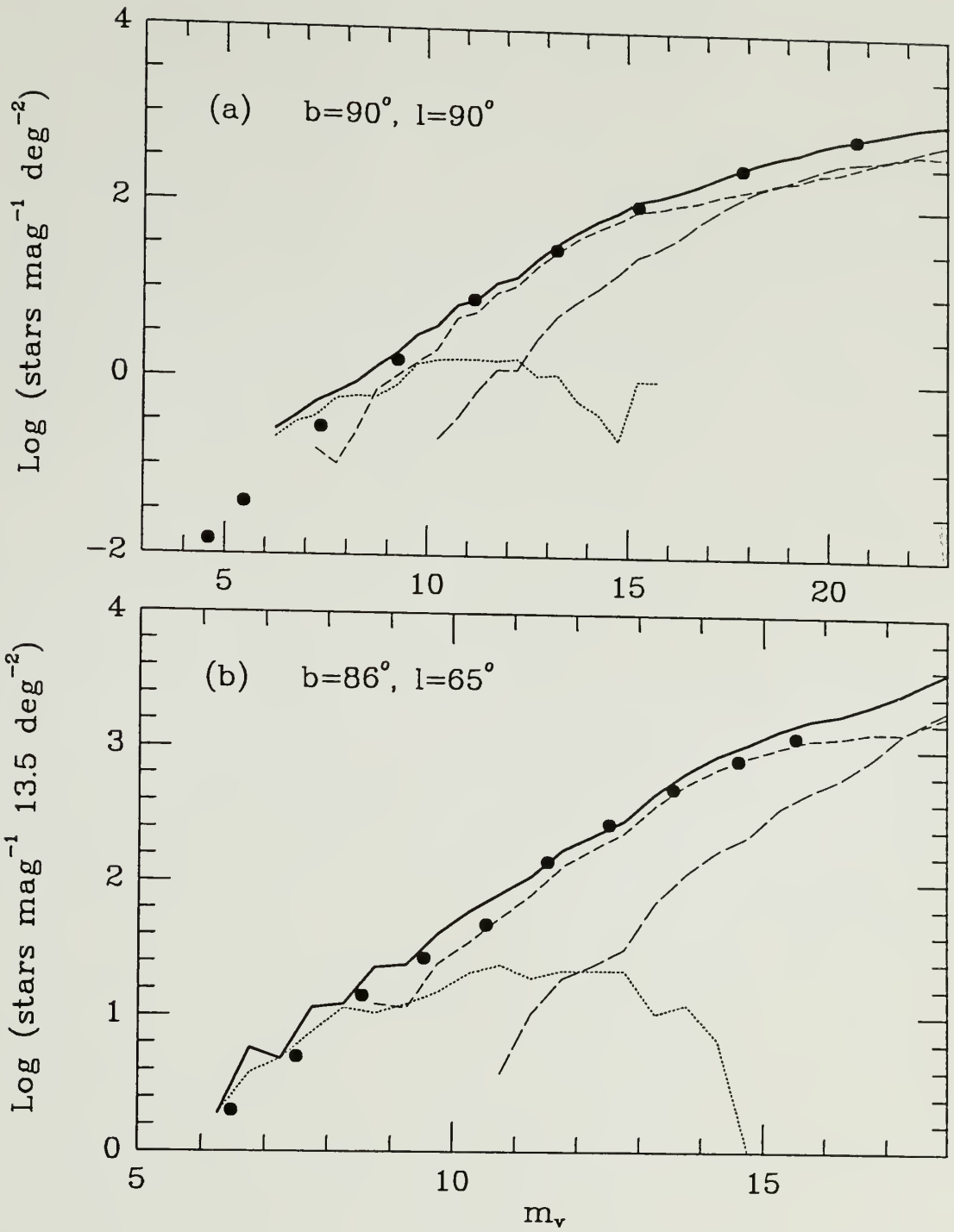

Figure F.1 Differential starcounts *versus* apparent visual magnitude toward fields (a) north Galactic pole, and (b) SA 57, b = 86°, ℓ = 65°. Model predictions drawn with lines according to: solid denotes the total contribution, short dashed the disk dwarfs, dotted the disk giants, and long dashed denotes the total contribution of the spheroid stars. Observed data from Reid and Gilmore (1983) and Weistrop (1972) is represented by filled circles.

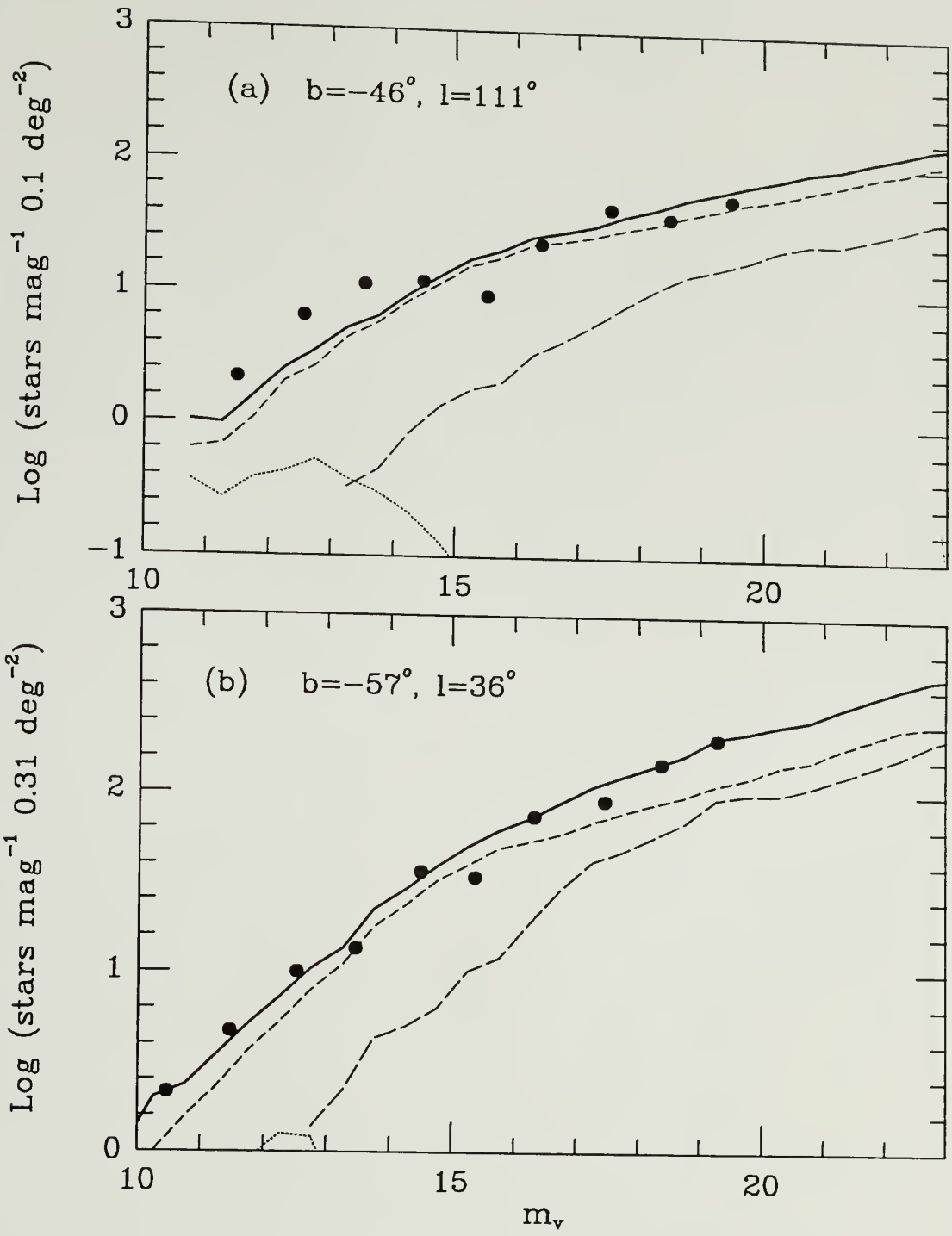

Figure F.2 Differential starcounts *versus* apparent visual magnitude toward fields (a) SA 68, b = -46°, ℓ = 111°, and (b) Aquarius, b = -57°, ℓ = 36°. Model predictions drawn with lines according to: solid denotes the total contribution, short dashed the disk dwarfs, dotted the disk giants, and long dashed denotes the total contribution of the spheroid stars. Observed data from Bahcall and Soneira (1984) and Tritton and Morton (1983) is represented by filled circles.

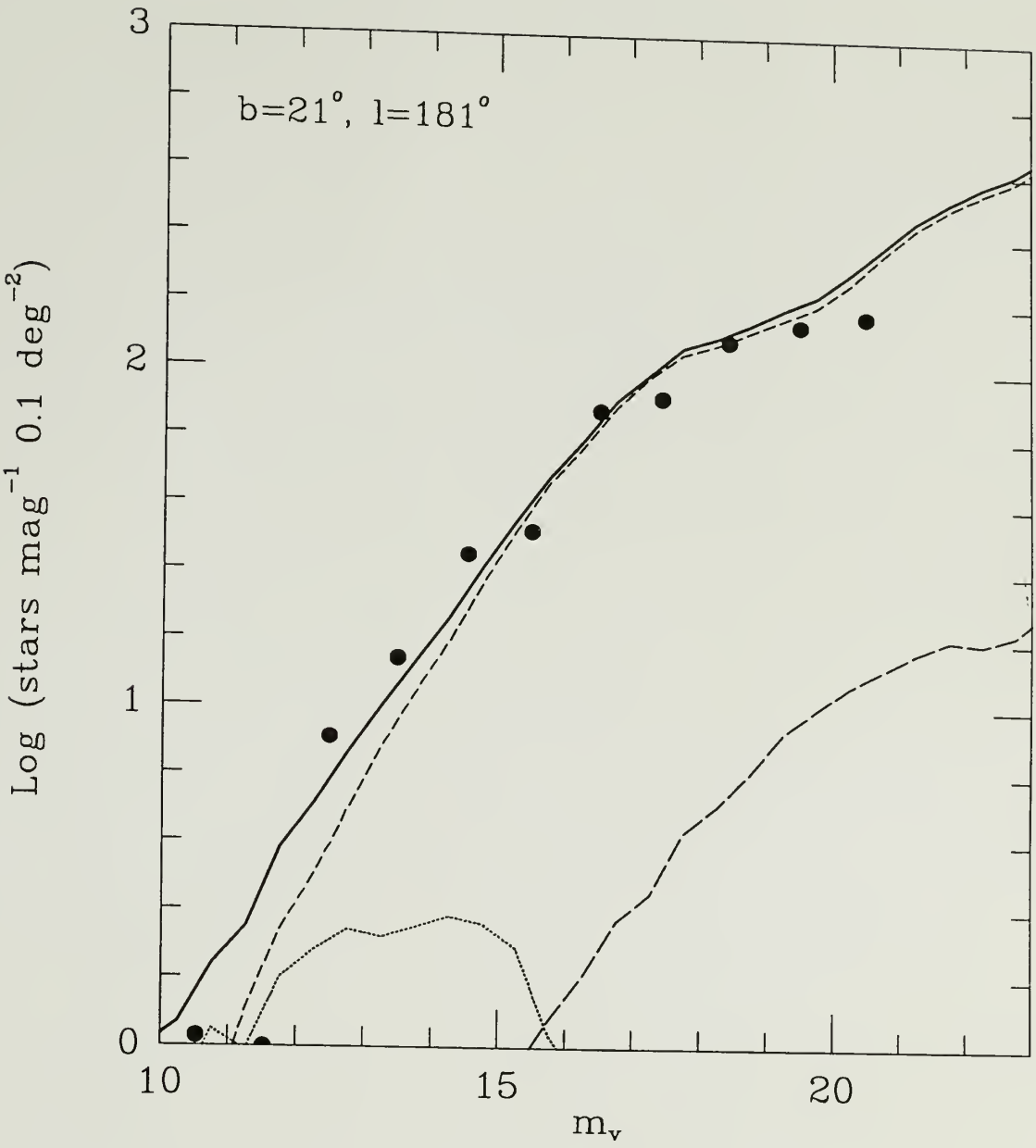

Figure F.3 Differential starcounts *versus* apparent visual magnitude toward SA 51, b = 21°, ℓ = 181°. Model predictions drawn with lines according to: solid denotes the total contribution, short dashed the disk dwarfs, dotted the disk giants, and long dashed denotes the total contribution of the spheroid stars. Observed data taken from Bahcall and Soneira (1984) is represented by filled circles.

BIBLIOGRAPHY

Andre, P., Montmerle, T., and Feigelson, E.D. 1987, *A. J.*, **93**, 1182.

Bahcall, J.N. 1984, *Ap. J.*, **276**, 169.

Bahcall, J.N., Schmidt, M., and Soneira, R.M. 1983, *Ap. J.*, **265**, 730.

Bahcall, J.N. and Soneira, R.M. 1980, *Ap. J. Suppl.*, **44**, 73.

Bahcall, J.N. and Soneira, R.M. 1983, in *The Nearby Stars and the Stellar Luminosity Function*, ed. A.G. Davis Philip and A.R. Upgren (Schenectady: L. Davis Press), p. 209.

Bahcall, J.N. and Soneira, R.M. 1984, *Ap. J. Suppl.*, **55**, 67.

Beckert, D.C. and Newberry, M.V. 1989, *Publ. Astron. Soc. Pac.*, **101**, 849.

Beichman, C.A., Myers, D.C., Harris-Law, S., Mathieu, R., Benson, P.J., and Jennings, R.E. 1986, *Ap. J.*, **307**, 337.

Beichman, C.A., Boulanger, F., and Moshir, M. 1991, *IPAC Preprint No. 0076.*

Bessell, M.S. 1983, *Publ. Astron. Soc. Pac.*, **95**, 480.

Bessell, M.S. 1986, *Publ. Astron. Soc. Pac.*, **98**, 1303.

Bessell, M.S. 1990, *Astron. Astrophys. Suppl.*, **83**, 357.

Bessell, M.S. 1991, *A. J.*, **101**, 662.

Bless, R.C. and Savage, B.D. 1972, *Ap. J.*, **171**, 293.

Boeshaar, P.C. and Tyson, J.A. 1985, *A. J.*, **90**, 817.

Bok, B.J. 1937, *The Distribution of Stars in Space* (Chicago: University of Chicago Press).

Bok, B.J. 1956, *A. J.*, **61**, 309.

Bowen, I.S. 1963, in *Stars and Stellar Systems*, **I**, ed. G.P. Kuiper and B.M. Middlehurst (Chicago: University of Chicago Press), p. 43.

Bruzual, G.A. 1966, Ph.D. Thesis, University of California, Berkeley.

Carrasco, L., Strom, S.E., and Strom, K.M. 1973, *Ap. J.*, **182**, 95.

Cernicharo, J. and Guelin, M. 1987, *Astron. Astrophys.*, **176**, 299.

Code, A.D. and Bless, R.C. 1970, in IAU Symp. 36, p. 173.

Cousins, A.W.J. 1976, *Mem. Roy. Astron. Soc.*, **81**, 25.

Cousins, A.W.J 1980, *S. African Astr. Obs. Circ.*, **1**, 166.

Dahn, C.C., Liebert, J., and Harrington, R.S. 1986, *A. J.*, **91**, 621.

D'Antona, F. and Mazzitelli, I. 1985, *Ap. J.*, **296**, 502.

Dearborn, D., Tinsley, B.M., and Schramm, D.N. 1978, *Ap. J.*, **223**, 557.

de Geus, Eugene 1988, Ph.D. Thesis, University of Leiden.

DeVaucouleurs, G. 1958, *Ap. J.*, **128**, 465.

DeVaucouleurs, G. 1959, in *Handbuch der Physik*, **53**, ed. S. Fluegge (Berlin: Springer-Verlag), p. 311.

DeVaucouleurs, G. 1977, *Astron. Astrophys.*, **56**, 91.

DeVaucouleurs, G. and Buta, R.J. 1978, *A. J.*, **83**, 1383.

DeVaucouleurs, G. and Pence, W.D. 1978, *A. J.*, **83**, 1163.

Dickman, R.L. 1978, *A. J.*, **83**, 363.

Dickman, R.L. and Herbst, W. 1990, *Ap. J.*, **357**, 531.

Dorman, B., Nelson, L.A., and Chau, W.Y. 1989, *Ap. J.*, **342**, 1003.

Eggen, O.J. 1980, *Ap. J. Suppl.*, **43**, 457.

Elias, J.H. 1978, *Ap. J.*, **223**, 859.

Elias, J.H. 1978, *Ap. J.*, **224**, 453.

Elias, J.H. 1978, *Ap. J.*, **224**, 857.

Faber, S.M., Burstein, D., Tinsley, B.M., and King, I.R. 1976, *A. J.*, **81**, 45.

Feigelson, E.D. 1987, in *Protostars and Molecular Clouds*, ed. T. Montmerle and C. Bertout (Saclay: CEA), p.123.

Fernie, J.D. 1983, *Publ. Astron. Soc. Pac.*, **95**, 782.

Freeman, K.C. 1970, *Ap. J.*, **160**, 811.

Garwood, R. and Jones, T.J. 1987, *Publ. Astron. Soc. Pac.*, **99**, 453.

Gilmore, G. and Reid, N. 1983, *Mon. Not. Roy. Astron. Soc.*, **202**, 1025.

Gilmore, G., Wyse, R., and Kuijken, K. 1989, *Ann. Rev. Astron. Astrophys.*, **27**, 555.

Greenberg, J.M. 1968, in *Nebulae and Interstellar Matter*, ed. L.H. Aller and B.M. Middlehurst (Chicago: University of Chicago Press), p. 221.

Greenstein, J.L. 1984, *Ap. J.*, **276**, 602.

Gunn, J.E. and Stryker, L.L. 1983, *Ap. J. Suppl.*, **52**, 121.

Habing, H.J., Olnon, F.M., Chester, T.J., Gillett, F.C., Rowen-Robinson, M., and Neugebauer, G. 1985, *Astron. Astrophys.*, **152**, L1.

Hanson, R.B. 1983, in *The Nearby Stars and the Stellar Luminosity Function*, ed. A.G. Davis Philip and A.R. Upgren (Schenectady: L. Davis Press), p. 51.

Hawkins, M.R.S. and Bessell, M.S. 1988, *Mon. Not. Roy. Astron. Soc.*, **234**, 177.

Hayes, D.S. 1974, in *Multicolor Photometry and the Theoretical HR Diagram*, ed. A.G. Davis Philip and D.S. Hayes (Albany: Dudley Observatory), p. 309.

Henden, A.A. and Kaitchuck, R.H. 1982, *Astronomical Photometry*, (New York: Van Nostrand Reinhold Co.).

Henry, T.J. and McCarthy, D.W. 1990, *Ap. J.*, **350**, 334.

Herbst, W. and Dickman, R.L. 1983, in *The Nearby Stars and the Stellar Luminosity Function*, ed. A.G. Davis Philip and A.R. Upgren (Schenectady: L. Davis Press), p. 187.

Heyer, M.H., Snell, R.L., Goldsmith, P.F., and Myers, P.C. 1987, *Ap. J.*, **321**, 370.

Hill, G, Hilditch, R.W., and Barnes, J.V. 1979, *Mon. Not. Roy. Astron. Soc.*, **186**, 813.

Ichikawa, T. and Nishida, M. 1989, *A. J.*, **97**, 1074.

Jarrett, T.H., Dickman, R.L., and Herbst, W. 1989, *Ap. J.*, **345**, 881.

Johnson, H.L., Mitchell, R.I., Iriarte, B., and Wisniewski, W.Z. 1966, *Comm. Lunar and Planetary Lab.*, **4**, 99.

Jones, T.J., Ashley, M., Hyland, A.R., and Ruelas-Mayorga, A. 1981, *Mon. Not. Roy. Astron. Soc.*, **197**, 413.

Jones, B.F. and Herbig, G.H. 1979, *A. J.*, **84**, 1872.

Kenyon, S.J. and Hartmann, L. 1987, *Ap. J.*, **323**, 714.

King, I.R. 1966, *A. J.*, **71**, 131.

Knapp, G.R., Tremaine, S.D., and Gunn, J.E. 1978, *A. J.*, **83**, 1585.

Koornneef, J. 1983, *Astron. Astrophys.*, **128**, 84.

Kron, R.G. 1980, *Ap. J. Suppl.*, **43**, 314.

Lada, C.J. 1987, in *Star Forming Regions*, ed. M. Peimbert and J. Jugaku (Boston: D. Reidel), p. 1.

Lada, C.J. and Wilking, B.A. 1984, *Ap. J.*, **287**, 610.

Langer, W.D., Wilson, R.W., Goldsmith, P.F., and Beichman, C.A. 1989, *Ap. J.*, **337**, 355.

Larson, R.B. 1986, *Mon. Not. Roy. Astron. Soc.*, **218**, 409.

Leggett, S.K. and Hawkins, M.R.S. 1988, *Mon. Not. Roy. Astron. Soc.*, **234**, 1065.

Lena, Pierre 1986, *Observational Astrophysics* (Paris: Springer-Verlag).

Liebert, J. and Probst, R.G. 1987, *Ann. Rev. Astron. Astrophys.*, **25**, 473.

Luyten, W.J. 1963, *Proper Motion Survey with the 48-Inch Schmidt Telescope* (Minneapolis: University of Minnasota), No. 1.

Luyten, W.J. 1976, *Proper Motion Survey with the 48-Inch Schmidt Telescope* (Minneapolis: University of Minnasota), No. 46.

Mamon, G.A. and Soneira, R.M. 1982, *Ap. J.*, **255**, 181.

McCuskey, S.W. 1969, *A. J.*, **74**, 807.

Mihalas, D. and Binney, J. 1981, *Galactic Astronomy* (San Francisco: W.H. Freeman and Company).

Miller, G.E. and Scalo, J.M. 1979, *Ap. J. Suppl.*, **41**, 513.

Minkowski, R.L. and Abell, G.O. 1963, in *Stars and Stellar Systems*, **III**, ed. G.P. Kuiper and B.M. Middlehurst (Chicago: University of Chicago Press), p. 481.

Montmerle, T., Koch-Miramond, L., Falgarone, E., and Grindley, J.E. 1983, *Ap. J.*, **269**, 182.

Mundy, L.E., Wilking, B.A., and Myers, S.T. 1986, *Ap. J.*, **311**, L75.

Myers, P.C., Fuller, G.A., Mathieu, R.D., Beichman, C.A., Benson, P.J., Schild, R.E., and Emerson, J.P. 1987, *Ap. J.*, **319**, 340.

Myers, P.C., Linke, R.A., and Benson, P.J. 1983, *Ap. J.*, **264**, 517.

Nandy, K., Thompson, G.I., Jamar, C., Monfils, A., and Wilson, R. 1975, *Astron. Astrophys.*, **44**, 195.

Oort, J.H. 1960. *Bull. Astron. Inst. Neth.*, **15**, 45.

Probst, R.G. and Liebert, J. 1983, *Ap. J.*, **274**, 245.

Rana, N.C. 1987, *Astron. Astrophys.*, **184**, 104.

Ratnatunga, K.U. 1982, *Proc. Astr. Soc. Australia*, **4**, 422.

Reid, N. 1987, *Mon. Not. Roy. Astron. Soc.*, **225**, 873.

Reid, N. 1991, *A. J.*, **102**, 1428.

Reid, N. and Gilmore, G. 1982, *Mon. Not. Roy. Astron. Soc.*, **201**, 73.

Salpeter, E.E. 1955, *Ap. J.*, **121**, 161.

Savage, B.D. and Mathis, J.S. 1979, *Ann. Rev. Astron. Astrophys.*, **17**, 73.

Scalo, J.M. 1986, *Fund. Cosmic Phys.*, **11**, 1.

Scalo, J.M. 1988, in *Starbursts and Galaxy Evolution*, ed. T. Montmerle (Paris: Editions Frontieres).

Schild, R.E. 1977, *A. J.*, **82**, 337.

Schmidt, M. 1975, *Ap. J.*, **202**, 22.

Skrutskie, M.F. 1987, Ph.D. Thesis, Cornell University.

Skrutskie, M.F., Forrest, W.J., and Shure, M. 1989, *A. J.*, **98**, 1409.

Spitzer, L. 1978, *Physical Processes in the Interstellar Medium* (New York: Wiley).

Spitzer, L. and Schwarzschild, M. 1951, *Ap. J.*, **114**, 385.

Stine, P.C., Feigelson, E.D., Andre, P., and Montmerle, T. 1988, *A. J.*, **96**, 1394.

Stobie, R.S., Ishida, K., and Peacock, J.A. 1984, *Mon. Not. Roy. Astron. Soc.*, **238**, 709.

Strom, K.M., Strom, S.E., Carrasco, L., and Vrba, F.J. 1975, *Ap. J.*, **196**, 489.

Strom, K.M., Strom, S.E., Edwards, S., Cabrit, S., and Skrutskie, M. 1989, *A. J.*, **97**, 1451.

Taylor, B.J. 1986, *Ap. J. Suppl.*, **60**, 577.

Turnshek, D.E., Turnskek, D.A., Craine, E.R., and Boeshaar, P.C. 1985, *An Atlas of Digital Spectra of Cool Stars* (Tuscon: Western Research Company).

van de Hulst, H.C. 1949, *Rech. Astron. Obs. Utrecht*, **11**, part 2.

van de Kamp, Peter 1967, *Principles of Astrometry* (San Francisco: W.H. Freeman and Company).

Walker, C.K., Lada, C.J., Young, E., Maloney, P.R., and Wilking, B.A. 1986, *Ap. J.*, **309**, L47.

Weis, E.W. 1984, *Ap. J. Suppl.*, **55**, 289.

Weistrop, D. 1972, *A. J.*, **77**, 366.

Wielen, R. 1974, in *Highlights of Astronomy*, **3**, ed. G. Contopoulos (Dordrecht: D. Reidel), p. 395.

Wielen, R., Jahreis, H., and Krueger, R. 1983, in *The Nearby Stars and the Stellar Luminosity Function*, ed. A.G. Davis Philip and A.R. Upgren (Schenectady: L. Davis Press), p. 163.

Wilking, B.A., Lada, C.J., and Young, E.T. 1984, *Ap. J.*, **274**, 698.

Wilking, B.A., Lada, C.J., and Young, E.T. 1989, *Ap. J.*, **340**, 823.

Wing, R.F. and Dean, C.A. 1983, *The Nearby Stars and the Stellar Luminosity Function*, ed. A.G. Davis Philip and A.R. Upgren (Schenectady: L. Davis Press), p. 385.